

ATTACHMENT

**CONSUMERS POWER COMPANY
PALISADES PLANT
DOCKET 50-255**

**TOPICAL REPORT ON THE USE OF THE MCBEND CODE
FOR THE CALCULATION OF NEUTRON FLUENCES
IN THE PRESSURE VESSELS OF LWRS**

191 Pages

9611130443 961106
PDR ADOCK 05000255
P PDR

Report

AEAT-0352

Report

AEA Technology

AEAT-0352

Topical Report on the Use of the MCBEND Code for
the Calculation of Neutron Fluences in the
Pressure Vessels of LWRs

A F Avery

July 1996

	NAME	SIGNATURE	POSITION	DATE
Author	Alan Avery	<i>A. F. Avery</i>	Shielding Consultant RPSCD	4/7/96
Checker	Steve Chucas	<i>S. Chucas</i>	Shielding Product Manager RPSCD	12/7/96
Approver	Colin Cooper	<i>C. A. Cooper</i>	Department Manager, RPSCD	12.7.96

REACTOR PHYSICS, SHIELDING AND CRITICALITY DEPARTMENT
PLANT SUPPORT SERVICES GROUP
AEA TECHNOLOGY plc
WINFRITH
UNITED KINGDOM



AEA Technology

This report was prepared as an account of work carried out by AEA Technology plc in accordance with the contract between AEA O'Donnell Inc. and Consumers Power Company dated 10 October 1994.

The information which this report contains is accurate to the best knowledge and belief of AEA Technology plc, but neither AEA Technology plc nor any person acting on behalf of AEA Technology plc make any warranty or representation expressed or implied with respect to the accuracy, completeness or usefulness of this information, nor assume any liabilities with respect to the use of, or with respect to any damages which may result from the use of any information, apparatus, method or process disclosed in this report.

Topical Report on the Use of the MCBEND Code for
the Calculation of Neutron Fluences in the
Pressure Vessels of LWRs

A F Avery

ABSTRACT

The subject of this Topical Report is the application of the Monte Carlo code MCBEND9 to the calculation of neutron fluences in the pressure vessels of light water reactors. It has been prepared for submission for review and acceptance under the NRC licensing topical report program. Features of the Monte Carlo method and its application to the calculation of neutron fluxes in reactor shields are discussed. The code MCBEND9 is described and details of its verification and validation are presented. The latter include comparisons of predictions against measurements of a range of reaction rates in water, the NESDIP2 benchmark, and H B Robinson Unit 2. In the calculations nuclear data from ENDF/B-VI were used for the materials with cross-sections from the International Dosimetry File, IRDF-90, being adopted as the response functions for the detectors. The NESDIP2 experiment is a simulation of the radial shield of a PWR with measurements being made within the slabs of steel that represent the pressure vessel. The results from H B Robinson provide comparisons with measurements made in a surveillance capsule at the inner surface of the pressure vessel and also in the cavity outside the vessel. The comparisons thus meet the requirements of the Draft Regulatory Guide, DG-1025, that methods must be validated against a power reactor benchmark that provides in-vessel surveillance capsule dosimetry or ex-vessel cavity measurements or both, and a pressure vessel simulator benchmark that provides measurements at the inner surface and at the T/4 and 3T/4 positions within the vessel wall. The reports which describe the validation comparisons are included as Appendices. They give detailed analyses of the uncertainties associated with the calculations. The results confirm that MCBEND9 with the data from ENDF/B-VI and IRDF-90 gives agreement between predictions and measurements which is consistent within these uncertainties. Finally the use of the SENSACK code to adjust the calculated fluxes when reaction rate measurements are available at a plant is described.

AEA Technology plc
Plant Support Services Group
Reactor Physics, Shielding & Criticality Department
Winfrith
Dorchester
Dorset
DT2 8DH
United Kingdom

CONTENTS		Page
1	INTRODUCTION	1
2	THE MONTE CARLO METHOD	1
3	THE MCBEND9 CODE	2
	3.1 Geometry	2
	3.2 Nuclear Data	3
	3.3 Sampling	4
	3.4 Acceleration	4
	3.5 Scoring	6
	3.6 Summary	7
4	QUALITY ASSURANCE	7
5	VERIFICATION	7
6	VALIDATION	8
	6.1 Benchmark Measurements	8
	6.2 Water Benchmark	8
	6.3 NESDIP2 Benchmark	8
	6.4 H B Robinson Plant	9
7	ADJUSTMENT	11
8	SUMMARY	12
	REFERENCES	13
APPENDIX A	Analysis of the Winfrith Water Benchmark Experiment Using ENDF/B-VI and IRDF-90 Data	
APPENDIX B	The Analysis of NESDIP2 with ENDF/B-VI Nuclear Data and IRDF-90 Response Cross Sections	
APPENDIX C	Further Analysis of the H B Robinson Unit 2 PWR using the Monte Carlo Code MCBEND with ENDF/B-VI and IRDF-90 Nuclear Data	
APPENDIX D	Few-Channel Unfolding in Shielding - The SENSACK Code	

1. INTRODUCTION

MCBEND9(1) is the most recent version of the Monte Carlo code which has been developed by AEA Technology and applied to problems of neutron and gamma-ray transport over many years. The subject of this report is its use in the calculation of neutron fluences in the surveillance capsules and pressure vessels for Light Water Reactors.

The method which has usually been employed for this type of work has been based on discrete ordinates codes such as DORT(2) with the synthesis of three dimensional distributions from the results of one and two dimensional calculations. The advantage of the Monte Carlo method is that it can describe the geometry without being restricted to XYZ and R θ Z orthogonal arrays of mesh points. It also avoids the need to average the nuclear data over wide energy ranges in the preparation of multi-group libraries, and thus removes the requirement to estimate a weighting spectrum for each of the groups.

This report describes the Monte Carlo method and discusses the questions which need to be addressed in its application. It then considers how these are dealt with in calculations carried out with the MCBEND code. The Quality Assurance procedures which are followed in managing the code are described together with a summary of the user documentation. Details of the verification tests which have been performed on the code and descriptions of three validation benchmarks relevant to the pressure vessel calculations are presented. Finally the adjustment procedure which is applied when measured reaction rates are available to complement the calculations is described

2. THE MONTE CARLO METHOD

The possible application of the Monte Carlo method to calculations of neutron transport has long been recognised (3), (4), (5), but its use has become much more widespread with the rapid development of cheap computing power in recent times. This was evident at the 8th International Conference on Radiation Shielding held in April 1994 where 58 papers which referenced Monte Carlo codes were presented (6).

The Monte Carlo approach estimates the population of neutrons within regions of a given configuration of materials by creating typical tracks. If the spatial and energy distribution of the sources of neutrons are known together with the laws which govern their interactions with the nuclei comprising the materials, then it is possible by sampling from the appropriate probability function at each stage to generate a path from birth to death or leakage from the configuration. This sampling is performed by choosing random numbers in the range 0-1 and operating on them so that they correspond to a selection from the particular probability distribution. This reproduces the processes that occur in reality where a neutron path is determined by the probabilities inherent in the physical laws. At any point on its track it is therefore necessary to know the cross-sections and the associated distribution of secondary neutrons which represent these laws. In order to do this the code needs to recognise when a boundary between materials has been crossed, but these can be specified in a very general way so that the method is not restricted to regular geometries. As the energy of the neutron is known at any point along its track it is possible to refer to the cross-sections corresponding to that energy, and to sample directly from the explicit laws governing the angular distributions of scatter and the secondary energies rather than representing them by multi-group averages and parametric fits.

For any general source distribution and configuration of materials there are an infinite number of possible paths, so that both the actual migration of neutrons and the Monte Carlo simulation of the process will produce finite sets of samples from this distribution and will thus show stochastic variations. These are much more evident in the calculation where the numbers of tracks generated are far fewer than the numbers of neutrons emitted by the true sources, so that the Monte Carlo estimates of neutron fluxes have statistical uncertainties associated with them which are significant.

A key feature in the application of the method is the extent to which this statistical uncertainty can be reduced so that if possible it becomes small compared with the other uncertainties arising from the knowledge of the cross-sections, the specification of the materials, and the definition of the sources. This is achieved by concentrating the tracking on those paths which are most likely to reach the regions of interest in a problem. This artificial increase in the probability of a track contributing to the score is counterbalanced by a reduction in the weight of the particle which is included as a multiplicative factor in the scoring process. There are many techniques which have been employed for accelerating Monte Carlo calculations; in this report only that adopted when applying MCBEND to the prediction of neutron fluences in LWRs will be discussed. This is included in the description of MCBEND which is presented in the next section.

The Monte Carlo method is a powerful approach to solving neutron transport problems but when performing such calculations there are a number of features which need to be considered in order to ensure that the results are meaningful. These are listed below.

- (a) Geometry. Does the model accurately represent the practical situation? Are there any points which could lie in more than one region?
- (b) Nuclear Data. Are the cross-sections and the laws governing the emission of secondary particles adequately represented?
- (c) Sampling. Is the random number generator acceptable in its cycle length and the distribution of its numbers? Are the algorithms for sampling satisfactory?
- (d) Acceleration. Has the acceleration technique led to a class of possibly significant paths being omitted from the sampling process?
- (e) Scoring. What is the likely distribution of the scores? Are there any high score paths which are very infrequently sampled? Are the standard deviations acceptably low?

The way in which the MCBEND9 code is applied to the calculation of neutron fluences in LWRs is described in the next section where each of the above factors is considered in more detail.

3. THE MCBEND9 CODE

The facilities of the MCBEND9 code as employed in the fluence calculations for PWR pressure vessels are described in the various sub-sections which follow.

3.1 Geometry

The geometry of the problem is represented in MCBEND by dividing it into zones which are defined by specifying the surfaces which form their boundaries. The latter may be planes, spheres, ellipsoids, cylinders, cones, and tori, with sections of the surfaces being combined to form zones with complicated shapes. The Fractal Geometry system which is employed in MCBEND9(1) enables the model to be divided into "parts" with zones being specified to fill each part. This subdivision can be used to simplify construction of the model, since local co-ordinate systems can be used within each part, or to take advantage of replication which may be present. Alternatively the whole model may be one part. The combinations of surfaces are specified in most cases by constructing the model from bodies. Cylinders and cones thus have two end faces as well as their curved surfaces, whilst prisms and boxes have six plane surfaces. The zone is then defined as being outside or inside each of the bodies from which it is built. The exception to this is the plane which can be specified as a single surface with the zone being defined as being on a given side of the plane. A single material fills each zone and this is specified by means of a number which refers to compositions which are listed in another unit of the data input.

Tracking in MCBEND9 is carried out in the standard way by determining the next boundary to be crossed and the zone which is entered after that crossing. For a neutron entering a zone the distances along its path to its intersection with the surfaces defining that zone are calculated. The shortest distance is taken and if this is less than the remaining length of the flight of the neutron then this gives the next boundary crossing. If it is not then the position of the particle interaction within the zone is calculated.

Testing of the accuracy of the geometry model is an essential step in checking the input of a Monte Carlo calculation. For MCBEND9 this is performed using the programs SKETCH, VISAGE, VISTA-WIRE, and VISTA-RAY. SKETCH carries out the following functions:

- (a) it displays the material, region, or zone numbers at the mid-point of a regular spatial mesh in a selected plane,
- (b) it performs checks for multiply-defined or undefined regions to ensure that each point is uniquely associated with a zone,
- (c) it estimates zone, region, and material volumes within selected regions of a model,
- (d) it estimates body surface areas,
- (e) it performs a detailed diagnostic trace for a pre-defined track, and
- (f) it creates a file for detailed analysis using the VISAGE program.

The essential steps are those in (b) and (f), the latter being equivalent to (a) but giving a display with higher resolution.

VISAGE displays in colour the materials, regions, or zones in a two-dimensional slice through the model. By examining a number of such slices it is possible to check that the model is reproducing the required configurations.

The check for undefined or multiply-defined regions is necessary to ensure that the model is complete and unambiguous. MCBEND9 will stop if a neutron enters an undefined region, but it does not recognise the presence of two overlapping regions. In the latter case it could choose either of the two materials specified for such regions leading to errors if the wrong one is selected. SKETCH is therefore used to eliminate any doubly-defined regions from the MCBEND model through the checks in (b).

Volumes are not used in the tracking process but they are needed for track length scoring of fluxes and reaction rates. They can usually be calculated accurately by analytic methods, but facility (c) provides a check by estimating the volume from the mean length of a set of tracks, albeit with a standard deviation associated with the sampling which gives this mean.

Further checks of the geometry may be carried out using the VISTA-WIRE program which generates three-dimensional outlines or shaded views of the bodies which form the model, and VISTA-RAY which produces three dimensional pictures of the model showing materials, regions, or zones. By use of these programs it is possible to ensure that the model accurately represents the practical situation.

3.2 Nuclear Data

The neutron cross-sections for the materials in MCBEND9 calculations for LWRs are based on the ENDF/B-VI library. To facilitate sampling the data are processed into the DICE format as described by Parker (7). The ENDF/B-VI data contain doubly differential distributions in energy and angle

for Cr^{50} , Cr^{52} , Cr^{53} , Cr^{54} , Fe^{54} , Fe^{57} , Fe^{58} , Mn^{55} , Ni^{58} , Ni^{60} , Ni^{61} , Ni^{62} , Ni^{64} , U^{235} and U^{238} which are isotopes of interest in LWR calculations. These data have been converted into independent distributions in energy and angle using the SIXPAK program (8). The simplification of the data in this way is not expected to lead to significant errors because the correlations between energy and angle for the non-elastic interactions are only important at energies above 10 MeV. The data have been processed into the DICE format using the NJOY code (9) with a modified ACER module and additional modules CNMONK and MOULD. The route, methods validation, and the production of the DICE library of ENDF/B-VI data are described by Eaton and Dean (10). This library has been entered into the ANSWERS QA Set following the standard procedure (11) of AEA Technology's ANSWERS Software Service (see Section 4). The cross-sections in the validation comparisons and in the application to calculations for LWRs are represented by the mean values in 8,220 energy bands while the energy loss laws and the angular distributions are expressed as cumulative probabilities which are sampled directly at the specific energy of the neutron.

The uncertainties associated with the cross-sections have been expressed as co-variance matrices by processing the relevant files from ENDF/B-VI using the ERRORR and COVR modules of NJOY (9). However for hydrogen and oxygen there are no error files in ENDF/B-VI and in these cases the co-variances have been taken from ENDF/B-V data as processed by Kodelli and Sartori (12). The compilation of the library of co-variance data is described by Ziver and Earwicker (13).

The response cross-sections for calculating the reaction rates of detectors have been taken from IRDF-90 (14), where they are expressed as mean values in the 640 energy bands of the SAND II group scheme (15). The uncertainties associated with these response cross-sections have been derived from the IRDF-90 library using the relevant modules of NJOY. The processing of the IRDF cross-sections and co-variances into the form in which they are used in the MCBEND calculations is also described in reference 13.

3.3 Sampling

Sampling of the probabilities at each stage in the creation of the neutron tracks is performed using random numbers. The latter are generated by algorithms which give a sequence of numbers which can be identically re-generated if the same starting point is used. They are thus "pseudo" random numbers, but this is satisfactory for use in Monte Carlo calculations provided that the sequence has been shown to meet conditions of randomness. The latter involve tests in which the numbers are used to sample various probability distributions and then demonstrating that expected properties of the distribution are reproduced. The other significant feature of a random number sequence is the cycle length, i.e. the number of random numbers which are generated before the sequence starts to repeat itself. Obviously if the calculation is reproducing tracks which have already been followed by earlier samples, then it will not be generating new information and the statistical estimation of the standard deviation will be too optimistic.

In MCBEND the random numbers are produced by a combination of a Lagged Fibonacci (16) and a Linear Congruential generator. This has been shown to satisfy extensive tests of randomness, and it has a cycle length in excess of 10^{14} numbers. Each Monte Carlo calculation of the flux distribution in an LWR shield requires typically 2×10^8 random numbers so that there is no danger of track duplication.

3.4 Acceleration

The Monte Carlo calculations of the neutron fluences at LWRs are accelerated by the use of the standard technique of splitting and Russian roulette. In the MCBEND code the geometry of the problem is overlaid with an orthogonal spatial mesh in which the neutron "importances" are specified in a number of energy groups. The "importances" are approximate values of the probability of a neutron contributing to the score which is of interest in the particular calculation. Accurate values of the neutron importances are given by the solution of the adjoint transport

equation but if these were available they would enable the quantity of interest to be computed directly from a knowledge of the neutron source distribution so that there would be no need for the forward calculation. The derivation of accurate values of the importances is a problem of complexity similar to that of the forward calculation so that they are not readily available. It is found, however, that approximate values of the importances are effective in accelerating Monte Carlo calculations since they provide sufficient indication of whether a neutron is becoming more or less likely to contribute to the score of interest. The MCBEND code has an in-built facility which derives such approximate importances by solving the adjoint transport equation in the simplified form based on a multi-group diffusion treatment, although the group parameters have been adjusted to improve the accuracy at deep penetrations. The irregular three-dimensional model is translated into an orthogonal array of materials for this calculation of the importances by smearing the materials or by adopting the dominant material within a mesh. The importances are then used in the conventional way in splitting and Russian roulette; i.e. when a neutron moves to a region where its importance is increased by more than a factor of 2 it is split into a number of particles which are then tracked separately; conversely when its importance decreases it is killed off with a probability determined by the change. The weights assigned to the neutrons are adjusted after splitting or Russian roulette so that weight is conserved on average. In MCBEND calculations for LWRs, sampling of the source distribution for the initiation of tracks is also controlled by the same importance map so that the weights of all neutrons at a particular location are consistent.

The use of splitting to accelerate Monte Carlo calculations can be seen as a way of distributing the information obtained from tracking in a more uniform way over the depth of penetration of interest. In a straightforward analogue calculation most neutrons would be captured close to the source so that the density of tracks there would be high and the statistical uncertainty on the neutron fluxes would be small. Relatively few neutrons would reach deeper penetrations so that the quality of information there would be poor. By splitting neutrons as they move towards a target region the tracks are distributed more uniformly and the statistical uncertainty is reduced at deep penetrations at the expense of poorer accuracies close to the source. Because the importance map as derived by MCBEND is continuous in space and energy it is very unlikely that any important penetration path will not be sampled. (If it were sampled infrequently then this would be seen in high standard deviations.) With splitting and Russian roulette MCBEND employs natural sampling of the path lengths and the angular distributions of scatter. It does not distort the tracks and is thus more robust than techniques such as path length stretching or angular biasing of the angle of scatter where emphasis is placed on creating tracks of a particular class, and it is not always possible to justify this choice a priori. The use of adjoint solutions in MCBEND provides a standardised way of generating the importance maps which control the splitting and Russian roulette. Application of this approach in the validation comparisons, such as that for the H B Robinson plant for example, then gives confirmation of its suitability for general use in calculations of PWR fluences when the same procedure is used.

The use of splitting to give a more uniform distribution of the collisions being treated in the Monte Carlo calculation introduces one possibility for error which would not be present when there was no acceleration. The large number of collisions occurring close to the source in the latter case would generate scattered neutrons covering a wide range of energies and directions of motion. If there were a very narrow energy band in which the cross-section was exceptionally small then a scattered neutron moving in the appropriate direction in this "window" could readily penetrate deep into a shield. Such a path has a low probability of being sampled but could give a high contribution to the flux at deep penetrations. In an analogue calculation such a path would be sampled if it were important. When splitting gives fewer collisions close to the source then the probability of sampling such a path is reduced and its contribution could be omitted. This would not arise when the approximate adjoint solution recognised the presence of "streaming" in the cross-section window, but this would not be very likely given the nature of the multi-group parameters. (Similarly in discrete ordinate calculations with multigroup cross-sections the neutron would never "see" the narrow window.) It is therefore possible to postulate a situation in which splitting and Russian roulette as applied in MCBEND could underestimate the fluxes. However in practice this

has never been found to occur. It would be most likely with thick regions of single materials where the "window" would extend for distances of very many mean-free-paths for neutrons with energy outside the window. It has not been found in LWR radial shields with their layers of steel and water.

The application of splitting and Russian roulette in MCBEND calculations together with the code's in-built facility for determining the importance maps thus provide a standardised approach for acceleration. The absence of bias in the use of this technique is demonstrated in the validation calculations for the LWR fluence applications. It has also proved to be a robust and reliable method in a wide range of other calculations of neutron attenuation in shields (17), (18).

3.5 Scoring

MCBEND can score the fluxes of neutrons in any specified energy group scheme using either track length, collision density, or point estimators. The first two give the mean values of the fluxes within the volume of the scoring region. For reactor calculations track length scoring is used because it gives results in low density regions (e.g. air) and also in thin regions when spatial resolution is required. Reaction rates are scored during tracking by multiplying the track length by a reaction cross-section at the energy of neutron for that part of its track. The energy dependence of the response cross-sections is specified as a histogram, the standard IRDF library used in the calculations for LWRs being given in 640 energy groups. The sums of the contributions of the samples to the score in each bin (i.e. to the response or flux in each scoring region for each of the scoring groups) are accumulated as are the sums of the squares of the contributions. This enables the mean score and the associated standard error on the mean to be derived at the end of the calculation.

The significance which can be attached to the standard error depends upon the distribution from which the scores are sampled. The central limit theorem states that the means of samples taken from any distribution will show a normal distribution provided that sufficient samples are taken and that the second order moment of the sampled distribution about the mean is finite.

The distribution of scores in MCBEND with automated source weighting will arise from the variation in track lengths and the number of particles contributing to the score of the sample (i.e. the number of split samples which reach the scoring region). The weights of the particles will be identical in each group, and if the response function has been used as the adjoint source, that weight will be inversely proportional to the response cross-section in the group giving a constant product when the two factors are combined. When a compromise adjoint source is used to score several detector responses in the same calculation, there will, however, be an additional variation since the factors will not balance exactly for all detectors.

The main contributions to the variation will thus arise from the path lengths and the numbers of particles which score for each sample. The first will be distributed between zero and a clearly defined maximum determined by the size of the scoring region, while the second will show statistical fluctuations due to the sampling of the probabilities of particles reaching the next splitting boundary. The latter will also show sharp rises if the probability of a neutron following a particular set of tracks is much greater than is indicated by the importance map. In this case extensive splitting will take place, many secondary particles will reach the scoring regions, and a high contribution will be recorded. This will show in the high standard deviation when a large part of the score is due to one sample. The possible danger is that discussed in section 3.4 above where the probability of the high scoring path is so low that it is not sampled. As discussed in section 3.4 there is no evidence which suggests that such paths would be present in calculations for LWR vessel fluences, and none of the extensive calculations which have been carried out for this application show any sudden increase in standard deviation which would symptomise this effect.

The distribution of scores as discussed above will meet the requirement that the second moment should be finite for the central limit theorem to apply. The number of samples that are needed to meet the other condition cannot be specified a priori, but experience from calculations has shown that results with standard deviations of 20%-30% can change by many standard deviations as more samples are scored. However, when the standard deviation is less than 10% the changes are more consistent with those for a normal distribution, so that the aim is always to reduce the statistical uncertainty below this level.

MCBEND also includes a scoring option which will give the fractions of a response which are due to reactions in each of the scoring groups. This enables the uncertainty due to the response cross-sections to be estimated since these are the sensitivities which are needed to fold with the co-variance data for the response cross-section. The code will also calculate the sensitivity of a response in a given region to the cross-sections of the materials comprising the model of the reactor. This is achieved during tracking by scoring the differential of the probability of that track with respect to the specified cross-section. The latter can be for any reaction in any element of the reactor materials, and the sensitivities can be derived for a number of energy ranges of the cross-section. These can again be folded with the co-variance data for the material cross-sections in order to estimate the uncertainties in the calculation of the response due to uncertainties in the nuclear data.

3.6 Summary

The way in which the MCBEND code addresses possible errors entering into the Monte Carlo method have been discussed. Steps are taken to eliminate each of the sources of bias so that the calculation produces reliable results. The positive evidence that this has been achieved is contained in the benchmark validation comparisons, where application of the same techniques produces good agreement with measurements. These are considered in more detail in a later section. The MCBEND code is described in the comprehensive User Guide (1) which includes descriptions of features of the code and advice on their use as well as the specification of the formats for the input data.

4. QUALITY ASSURANCE

Quality Assurance (QA) is a requirement for software which is used to perform calculations associated with the safety of reactors. QA principles embrace all aspects of a software package including development, maintenance and in-service use. In the United Kingdom these requirements led to the establishment of AEA Technology's ANSWERS Software Service which has set up a comprehensive range of software management QA procedures covering the complete life-cycle including specification, design, coding, testing and in-use support and maintenance. These standards are employed in the development and validation of the MCBEND code. The Quality Management System provided by these procedures has been certified against the International Standard ISO 9001.

The source code for version 9 of MCBEND was passed to ANSWERS for testing, commissioning and final distribution as a recognised updated version of the code. The version was formally identified (version 9) and changes made since the previous version and the documentation that supports the changes were recorded and archived. ANSWERS then commissioned the code for a range of standard computer platforms, the load module for each type being fully tested at commissioning.

Any further developments of the code will be carried out under the same procedures to provide Quality Assurance.

5. VERIFICATION

Verification of MCBEND9A has been achieved by carrying out the 113 standard tests that have been assembled over a period of 10 years in order to check the various functions of the code (19).

The results were mostly compared with those given by earlier versions of the code, although in a few cases analytic solutions were available. This procedure ensures that changes made to the code have not perturbed any of its previous functions, whilst the comparisons for problems with known answers provide direct tests of the algorithms as programmed in MCBEND. Verification of a subsequent version of the code, MCBEND9B, which contained a number of minor developments has been carried out by running the 113 cases and also by the introduction of additional tests for which there are analytic solutions (20). The latter are based on the use of a library of artificial nuclear data which is written in the formats of the DICE library used in practical calculations with MCBEND, but which contains data for nuclei with simplified properties. Details of this approach are described by Shuttleworth (21). By suitable choice of such nuclei, analytic solutions can be obtained for problems which enable more routines within the code to be tested in a direct manner rather than against previous results. As MCBEND9B is mostly identical to MCBEND9A, its verification provides additional checking of the earlier version.

6. VALIDATION

6.1 Benchmark Measurements

The MCBEND code has been validated against measurements for a range of situations and this has been documented in a number of reports. Validation of the particular application of MCBEND to the calculation of neutron fluences in the pressure vessel of LWRs is provided by the comparison with the benchmarks which are described in detail in Appendices A, B and C. These cover penetration in water, the NESDIP2 array of water and steel, and the H B Robinson radial shield for Cycle 9 of the plant's operation. The NESDIP2 experiment is a simulation of the water, core barrel, and pressure vessel of a PWR shield with measurements being made within the steel slabs which represent the pressure vessel. This comparison thus provides validation of the method for points within the vessel wall as required in reference 22. The results from the individual benchmarks are summarised in the sections below.

6.2 Water Benchmark

The detailed description of the comparison of measurements and calculations for the water benchmark is given in Appendix A. The neutron source for this experiment was provided by spontaneous fission in Cf^{252} and the attenuation of high energy neutrons, $E > 2\text{MeV}$, was measured with the $\text{S}^{32}(\text{n},\text{p})\text{P}^{32}$ reaction. The ratios of the calculated to experimental reaction rates (C/E) for points on the plane of the sources lie between 0.965 and 1.035, with no consistent trend with increasing penetration. The uncertainties on the values of C/E (one standard deviation) are estimated to be between 7.4% and 8.1% with the largest contribution of 6% arising from the measurements. The largest uncertainty in C/E due to the cross-sections of water as calculated using the co-variance data (13) is at the deepest measurement position of 355.6mm where it is $\pm 2.4\%$. The agreement of measurement and calculation to within 4% at all five penetrations suggests that the uncertainty on the measurements was less than was estimated, confirms that the calculation of fast neutron attenuation is accurate to within 4% over a penetration of 355mm, and suggests that the uncertainties assigned to the cross-sections of hydrogen and oxygen in the library of co-variance data are appropriate with no significant under-estimation of the errors.

6.3 NESDIP2 Benchmark

The NESDIP2 Benchmark was a series of measurements carried out in the ASPIS facility with the source provided by a fission plate which was driven by neutrons from the NESTOR low power reactor operated by AEA Technology at Winfrith. This plate was approximately disc-shaped with a radius of 50cm and it was composed of enriched U/Al coupons of 2mm overall thickness. The distribution of the source across the plate was measured with manganese foils whilst the absolute source was determined from the analysis of the fission products in selected coupons. The shield array was a series of water tanks and steel slabs of lateral dimensions 1.83m x 1.91m which

simulated the radial shield of a PWR, with measurements being made within the region of steel which represented the pressure vessel. The benchmark is described more fully in Appendix B.

The measurements were carried out using the three detectors $S^{32}(n,p)P^{32}$, $In^{115}(n,n')In^{115m}$, and $Rh^{103}(n,n')Rh^{103m}$.

The sulphur and indium measurements were only made within the pressure vessel region and the cavity region outside of the vessel. For the sulphur detector the values of C/E range from 0.89 ± 0.10 to 0.99 ± 0.12 with the major contributions to the estimated uncertainties arising from the cross-sections for iron, the detector cross-sections, and the spectrum of the fission neutron source. The values of C/E do not show any consistent trend with penetration, and the mean value for the five positions is 0.94 with the individual departures from unity being -1.1, -0.36, -0.08, -0.62, and -0.29 when expressed as fractions of the standard deviations. Similarly for indium the mean value of C/E at the five locations is 0.95 with the discrepancies being -0.88, -0.63, -0.11, -0.44 and -1.0 when expressed in terms of the standard deviations.

The rhodium measurements were made at the same five locations in the vessel as those using sulphur and indium, but in addition detectors were irradiated in the two regions which simulated the downcomer water on either side of the steel slab representing the thermal shield. In the two regions of water the values of C/E for the twelve measuring positions ranged from 0.88 to 1.08 with a mean of 0.92 and discrepancies of -0.86, -1.0, +0.62, -1.23, -1.7, -0.50, -1.00, -1.13, -1.38, -1.5, -1.38 and -1.13 standard deviations. In the pressure vessel location the values of C/E were between 0.88 and 1.02 with a monotonic increase with penetration through the vessel followed by a fall for the measuring position in the cavity. The discrepancies expressed as fractions of the standard deviations for these locations were -1.5, -0.67, -0.11, +0.2, -1.2.

The mean values of C/E for the three detectors are 0.94, 0.95, and 0.93 which suggests that the absolute normalisation is low by about 6%. The uncertainty on the measurement of the power of the fission plate was estimated to be 3.5% (1 standard deviation). However if the source strength of the plate is increased by 6% then the mean C/Es for the three detectors are very close to unity and only 4 of the 27 individual values differ from unity by more than one standard deviation, the contributions from the source uncertainty having been removed from the latter. The comparisons of the measurements and calculations in NESDIP2 thus confirm the accuracy of the code and the data for calculations in PWR radial shields, and in particular in the simulated pressure vessel for neutrons in the energy range 0.37MeV to 10 MeV over which the three detectors are sensitive.

6.4 H B Robinson Plant

Measurements of neutron reaction rates were made during cycle 9 at Unit 2 of the H B Robinson plant with detectors being irradiated in a surveillance capsule at the inner surface of the pressure vessel and in the cavity between the vessel and the primary shield. The reactor is a three loop PWR so that the measurements provide data against which the accuracy of calculations can be tested in a practical situation. MCBEND calculations have been carried out using the ENDF/B-VI data and IRDF-90 dosimetry cross-sections, and the results have been compared with the measured reaction rates. Full descriptions of the calculations and the results of the comparisons are given in Appendix C.

The detectors that were used were $Ti^{46}(n,p)Sc^{46}$, $Fe^{54}(n,p)Mn^{54}$, $Fe^{58}(n,g)Fe^{59}$, $Ni^{58}(n,p)Co^{58}$, $Co^{59}(n,g)Co^{60}$, $Cu^{63}(n,a)Co^{60}$, $U^{235}(n,fx)$, $U^{238}(n,fx)$, $Np^{237}(n,fx)$, and $Sc^{45}(n,g)Sc^{46}$. The n,p and n,a reactions are sensitive to neutrons at energies above about 2MeV while the n,g reactions are due mostly to neutrons at thermal or near-thermal energies. The fission reactions cover a range of energies; U^{235} is sensitive to low energy neutrons, U^{238} to those above 1MeV, and Np^{237} mostly to those above 0.2MeV although some 5% of its response can be due to energies below this. In the surveillance capsule the Ti, Co, Cu and fission foils were covered with gadolinium to reduce any

response to thermal neutrons. (In the fast neutron detectors this can alleviate possible problems with burn-up of the product nuclei or activation through alternative reactions.) Similarly in the cavity detectors Fe⁵⁴, Ni⁵⁸, Cu⁶³, U²³⁸, and Np²³⁷ foils were encased in cadmium.

Calculations for cycle 9 of the operation of the plant were initially carried out with a source distribution for fissions within the core which corresponded to a time close to the mid-point of the cycle. This distribution was specified as relative powers in each fuel pin together with absolute powers for each fuel assembly. There are 15x15 pin locations in each assembly which were grouped into 25 arrays of 3x3 with a uniform source strength being specified within each array. The relationship between the reactor power and the neutron fluxes in the radial shield varies during the course of a cycle for two reasons. Firstly the power distribution changes with burn-up so that a greater proportion of the fissions occur in the peripheral fuel assemblies thus increasing the fluxes in the shield. Secondly the fraction of the power which is being generated by fissions in plutonium also increases with burn-up. This in turn has a number of effects on the neutron source. Firstly the energy released per fission is higher for Pu²³⁹ than it is for U²³⁵ so that the number of fissions per watt of reactor power decreases. Secondly the number of neutrons emitted in fission is greater for Pu²³⁹ than it is for U²³⁵, the combined effect giving an increase of 13% in the neutrons per watt for Pu²³⁹. The third difference is in the spectra of the neutrons emitted in fission in the two isotopes, that for Pu²³⁹ being harder and thus giving greater penetration in water than that for U²³⁵. For the calculation of the fluences (flux x time) at the pressure vessel for the cycle it would be possible to use mean values for the neutron source distributions for the cycle but this is not acceptable for the calculation of the activation of the detectors. The decay of the induced activity during the cycle will make the activation of different detectors dependent upon the power distribution at a particular time in ways which will be influenced by the half-lives of the product nuclei. It is therefore necessary to consider the variation with time during the cycle of the reaction rate per unit reactor power when calculating the activation produced in the various detectors at the end of the cycle. In earlier MCBEND calculations for H B Robinson plant (23) the reaction rates were obtained for the power distributions and fractions of fissions in plutonium corresponding to the beginning and the end of the cycle as well as for those close to the middle of the cycle. These calculations also used ENDF/B-VI data for the materials but the cross-sections for the detectors were taken from IRDF-85. The factors which related the mid-cycle reaction rates to the end-of-cycle activations of the detectors were derived from the results of the earlier calculations and applied to the mid-cycle results obtained with ENDF/B-VI and IRDF-90 data. It is thus assumed that the calculation of the relative time dependence of the reaction rates through the cycle is not sensitive to the changes in the detector cross sections. This assumption is valid because the differences between the cross-sections in the two compilations are small and they would only produce any effect if there were changes in the neutron spectrum during the cycle. The largest contribution to the time dependence is due to the increase in the flux/unit power during the cycle arising from the change in the power distribution within the core; the changes in the neutron spectrum at the pressure vessel are small. The combination of these two small effects makes the time variation effectively independent of the change in the detector cross-sections and justifies the use of the time factors from the earlier calculations.

Uncertainties were estimated for the ratios of Calculation/Experiment (C/E) which were derived when the results were compared. Contributions for the calculation arose from the nuclear data, the detector cross-sections, reactor dimensions, material compositions, source strengths, the source spectrum, and the statistical standard deviations from the Monte Carlo method. Typically the latter were less than 4% which was much smaller than the total of those estimated for the other contributing factors. Uncertainties for the measured reaction rates were provided with the published results.

At the surveillance position the comparison of calculation and measurement gave values of C/E between 0.9 and 1.0 for seven of the nine detectors with the values of 0.85 and 0.89 for the other two reactions, Ti⁴⁶(n,p)Sc⁴⁶ and U²³⁸(n,fx)Zr⁹⁵ respectively. Comparisons were not made for the low energy detectors which were covered with gadolinium because of the difficulty of calculation.

the effect of the casing. The uncertainties on C/E are between 23.4% and 26.5% for the detectors at this position with the dominant contribution of 20% arising from the imprecise knowledge of the location of the capsule. This would affect all of the detectors to approximately the same degree. The mean value of C/E was 0.94 which suggests that factors which affect all the detectors in a similar way, i.e. the capsule position, the source data, and the water density, give a small underestimation which is much less than one standard deviation. Uncertainties which apply to the C/E values for individual detectors, and which contribute to the spread about the mean, are those from the measurements and from the reaction cross-sections. For the Ti foils these are 10% and 5.3% respectively with corresponding values of 5% and 0.7% for the U²³⁸ results. The discrepancies between the mean value of C/E and the values for the individual detectors are less than one standard deviation from the combined uncertainties due to measurement and detector cross-section for all detectors. The calculations thus give results which are consistent with the measurements to within the estimated uncertainties.

The values of C/E for the comparisons of calculated and measured reaction rates in the cavity range from 0.90 to 1.14 for thirteen of the sixteen detectors with the values for the three neptunium detectors ranging from 0.82 to 0.88. For the fast neutron detectors the standard deviations on these ratios lie between 19.13% and 25.28% with the largest contributions of 11% to 19% being due to the uncertainties in the cross-sections for iron. For the low energy detectors the latter contributions are less than 4.0% with the overall uncertainties being between 14.7% and 17.5%. The values of C/E for the ten fast neutron detectors are between 0.82 and 1.05 with a mean of 0.93, whilst those for the low energy detectors are between 1.04 and 1.14 with a mean of 1.08. This indicates that the fast neutron reaction rates are predicted much more accurately than would be suggested by the standard deviations whilst the low energy fluxes are overestimated. The spread in the results for the individual reactions about the two means exceeds the standard deviations from the combined uncertainties due to the measurements and the response cross-sections in only one case, the C/M being 0.82 for Np²³⁷(n,fx) Cs¹³⁷ with a difference from the mean of 1.05 x the standard deviation. The fact that the results for the high and the low energy detectors fall into two clear groups is attributed to the greater sensitivity of the low energy neutron fluxes to the composition of the concrete. The uncertainty due to the latter has not been quantified but it will have a greater influence on the low energy reaction rates because in this case the neutron fluxes arise from backscatter from the concrete. The results suggest that this backscatter was overestimated with the composition that was adopted for the calculations.

The agreement observed between calculations and measurements is thus better than that which would be expected with the estimated uncertainties at both positions and for all detectors. The results suggest that the uncertainties due to the position of the surveillance capsule were overestimated as were those for the cross-sections for iron as obtained from the ENDF/B-VI covariance files. The consistency between calculation and measurement therefore provides validation for the application of the MCBEND code to the prediction of neutron fluxes in the radial shields of PWRs.

7 ADJUSTMENT

When calculations of the neutron fluxes are carried out for operating plant they are frequently combined with the results obtained from measurements in order to derive the best estimates of the neutron doses received by the pressure vessel and by specimens in surveillance capsules. The uncertainties on measured reaction rates are usually much less than those associated with the calculation so that confidence in the values of the doses is increased when the two are taken together. The results of the calculation are adjusted to improve their consistency with the measurements and this process usually reduces the uncertainties. (It is not possible to use measurements alone because they cannot be made at all the positions of interest, nor can the dose expressed either as fluence above 1MeV or atomic displacements per atom be measured directly in the practical situation.) The process of adjustment of the calculations is not dependent on the method used to calculate the fluxes so that it is not necessary to employ any special technique for treating the

results from Monte Carlo. In this section details of the SENSACK code (25) which is used in AE Technology for performing such adjustments are given in order to complete the description of the approach which is applied to the calculation of pressure vessel fluences. The report specifying the equations which are solved by SENSACK is included as Appendix D.

The SENSACK code follows the maximum likelihood procedure as discussed in ASTM Standard Guide E 944 (26). The results of the MCBEND calculation are presented as the neutron fluxes and the mean detector cross-sections in a number of energy groups as specified by the user in his input. These are fed into SENSACK together with their associated uncertainties. For the fluxes the latter are expressed separately as the components arising from the source, and those due to other factors with correlations between the groups being provided for this second type of data. Similarly co-variance data are specified for the detector cross-sections. Typical values of these uncertainties as estimated for the H B Robinson calculations are given in Appendix C. The measurements and their associated uncertainties are also specified. The SENSACK code then adjusts the group fluxes to improve the agreement between the measured and calculated reaction rates and it generates co-variances for the adjusted data. The adjusted fluxes can then be folded with response cross-sections to provide revised values of quantities such as the flux above 1MeV and the displacement rate together with their uncertainties. The latter will be based on the consistency of the measurements and the adjusted calculated reaction-rates together with the size of the adjustments that were required. Because the accuracies of the measurements are usually much better than those of the calculations in the practical situation, this procedure leads to reduced uncertainties on the neutron doses. Also in practice the uncertainties on the fluxes are much larger than those on the detector cross-sections so that it is the fluxes which are changed in the adjustment procedure. An example of the use of SENSACK to improve the accuracy of some very coarse calculations is included in Appendix D.

8 SUMMARY

The features of the Monte Carlo method have been discussed and the way in which the method has been implemented in the MCBEND code has been described. Quality Assurance and verification of the code have been described and the results of validation benchmarks for the calculation of neutron fluxes in the pressure vessels of LWRs have been presented, with the more detailed reports of the benchmark comparisons with measurements being included in Appendices A, B, and C. The adjustment code SENSACK which can be used to improve the accuracies of the predicted neutron doses when measurements are available at the operating plant has also been described.

This report thus provides validation for the application of the MCBEND9 Monte Carlo code to provide accurate calculations of neutron fluxes in the radial shields of LWRs when the nuclear data are taken from ENDF/B-VI for materials and from IRDF-90 for detector cross-sections.

REFERENCES

- [1] MCBEND User Guide to Version 9A, ANSWERS/MCBEND(94)15.
- [2] TORT-DORT Manual for Two/Three-Dimensional Discrete Ordinates Transport ORNL/RSIC-CCC-543. Version 2.8.14
- [3] Cashwell E and Everett C J. A Practical Manual on the Monte Carlo Method for Random Walk Problems. Pergamon Press 1959
- [4] Hammersley J M and Handscomb D C. Monte Carlo Methods. Methuen 1964
- [5] Goldstein H. Fundamental Aspects of Reactor Shielding. Addison-Wesley 1959
- [6] Proceedings of the 8th International Conference on Radiation Shielding, Arlington, USA 1994.
- [7] Parker J B. DICE MkV. The Preparation of Nuclear Data into a Form Suitable for Monte Carlo Calculations using an Electronic Computer. AEEW-27/66
- [8] Cullen D E. SIXPAK: A Code Designed to Check Double-Differential Correlated Data and Calculate "Equivalent" Uncorrelated Data. UCRL-ID-110241
- [9] MacFarlane R E & Muir D W. The NJOY Nuclear Data Processing System, Version 91. LA-12740-M
- [10] Dean C J & Eaton C R. The 1994 DICE Nuclear Data Library AEA-RS 5697
- [11] Production of Nuclear Data Libraries for Applied Purposes. Reactor Physics, Shielding and Criticality Department Procedure 2.306 AEA Technology
- [12] Kodelli I and Sartori E. Co-variance Data Library. ZZ-VITAMIN-J/COVA, NEA1264, OECD/NEADB 1990
- [13] Ziver A K and Earwicker J. Generation of Variance-Covariance Data from the ENDF-B/VI and IRDF-90 Nuclear Data Libraries. AEA-TSD-0387
- [14] Kocherov N P and McLaughlin P K. The International Dosimetry File (IRDF-90), IAEA-NDS-141 October 1993.
- [15] McElroy W N, Berg S and Crockett T A. Computer Automated Iterative Method for Neutron Flux Spectra Determined by Foil Activation. AFWL-TR-67-4
- [16] Marsaglia G and Zaman A. Toward a Universal Random Number Generator. Supercomputer Computations Research Institute and Department of Statistics. The Florida State University, Tallahassee
- [17] Locke H F. NEACRP Intercomparison of Codes for the Assessment of Transport Packages: Solution for the TN12 Benchmark Problem. AEA-RS-1063

- [18] Wright G A. Analysis of the Winfrith Graphite Benchmark Experiment
AEA-RS-5628
- [19] The Verification of MCBEND 9A.
NCD/MCANO/TT.1/9. AEA Technology
- [20] Shuttleworth E. MCBEND Verification. Review of Tests
NCD/MCANO/TT.1/14. AEA Technology
- [21] Shuttleworth E. The Verification of Monte Carlo Codes in Middle Earth.
Proceedings of the 8th International Conference on Radiation Shielding, Arlington, USA
1994. p1148
- [22] Draft Regulatory Guide DG-1025 Calculation and Dosimetry Methods for Determining
Pressure Vessel Neutron Fluence. USNRC September 1993
- [23] Locke (Mrs) H F. Further Analysis of the H B Robinson Unit 2 PWR using the Monte
Carlo Code MCBEND with ENDF/B-VI Nuclear Data.
AEA RS 5579
- [24] Lippincott E.P. et al. Evaluation of Surveillance Capsule and Reactor Cavity Dosimetry
from H B Robinson Unit 2, Cycle 9
WCAP-11104, NUREG/CR-4576
- [25] McCracken A K. Few-Channel Unfolding in Shielding - The SENSAK Code.
Proceedings of the Third ASTM-EURATOM Symposium on Reactor Dosimetry,
1975. pp 732-742
- [26] Standard Guide for Application of Neutron Spectrum Adjustment Methods in Reactor
Surveillance. ASTM E 944

APPENDIX A

AEA-TSD-0392

ANALYSIS OF THE WINFRITH WATER
BENCHMARK EXPERIMENT USING
ENDF/B-VI AND IRDF-90 DATA

A K Ziver

December 1994

AEA Technology
Technical Services Division
Reactor Physics, Shielding and Criticality Department
Winfrith Technology Centre
Dorchester
Dorset DT2 8DH
United Kingdom
Telephone 0305 251888
Facsimile 0305 202194

AUTHORISATION

	NAME	POSITION	SIGNATURE	DATE
Author	A K Ziver	Senior Analyst	<i>A K Ziver</i>	17/1/1995
Checked	A F Avery	Section Head	<i>A F Avery</i>	17/1/95
Approved	CA Cooper	Department Manager	<i>CA Cooper</i>	18/1/95

AEA-TSD-0392

ANALYSIS OF THE WINFRITH WATER BENCHMARK
EXPERIMENT USING THE ENDF/B-VI AND IRDF-90 DATA

A K Ziver

December 1994

Summary

This report describes the analysis of the Winfrith water benchmark experiment as part of the validation of MCBEND9A and its associated point data cross-section library based on the ENDF-B/VI compilation. Results are presented for the high energy S32(n,p)P32 reaction rates which are calculated using the IRDF-90 dosimetry library. It is shown that MCBEND9A predictions are within one standard deviation of the experimental results.

AEA Technology
Technical Services Division
Reactor Physics, Shielding and Criticality Department
Winfrith Technology Centre
Dorchester
Dorset DT2 8DH
United Kingdom
Telephone 0305 251888
Facsimile 0305 202194

Contents

		<u>Page</u>
1.	INTRODUCTION	1
2.	EXPERIMENTAL DESCRIPTION	1
3.	THE MCBEND MODEL	1
4.	RESULTS	2
5.	UNCERTAINTIES	2
6.	CONCLUSIONS	4
	REFERENCES	5

List of Tables

Table 1 Options Used in the MCBEND Input Files

Table 2 Californium-252 Source Spectrum

Table 3 The Sulphur $S^{32}(n,p)P^{32}$ Reaction-rates

Table 4 Relative Sensitivities from MCBEND (DUCKPOND) Calculations

Table 5 Experimental and Calculational Uncertainties

Table 6 Analysis of C/E for the Sulphur Reaction Rates

List of Figures

Figure 1 Schematic View of the Experimental Set up

Figure 2 Model of the Source Capsule

Figure 3 Values of C/M for the $S^{32}(n,p)P^{32}$ Reaction Rate in the Source Plane

Figure 4 $S^{32}(n,p)P^{32}$ Reaction Rate Cross-sections (IRDF-90)

Appendix

A The MCBEND9 Input Data for the Source Detector Separation 10.16 cm

1. INTRODUCTION

This report describes the analysis of the single material water benchmark experiment performed as part of the validation study for MCBEND9A [1] with the ENDF-B/VI [2] point energy nuclear data in conjunction with the IRDF-90 [3] dosimetry library.

The water benchmark experiment was performed at AEA Technology, Winfrith in the U.K [4] in the early 1980s. The aim of the experiment was to test calculational methods and the validity of cross-section data for materials of importance in PWR dosimetry analysis. The experiment was set up in a water tank in which eight individual accurately calibrated Californium (Cf^{252}) capsules were used as neutron sources. The Cf^{252} sources provided spontaneous fission neutrons with a well-known energy distribution. The fast neutron flux was measured using sulphur detectors with the $\text{S}^{32}(\text{n,p})\text{P}^{32}$ reaction rate being determined at distances ranging from 100 to 400mm from the source. This experiment has been studied previously [5], [6] to test the JEF2.2, UKNDL and the ENDF-B/VI nuclear data with the IRDF-85 dosimetry library.

A brief description of the experimental set up is given, followed by a full description of the MCBEND input model. The results from the calculations using the ENDF-B/VI and IRDF-90 data are compared against the measurements.

2. EXPERIMENTAL DESCRIPTION

A water-filled tank containing a light support structure from which various source configurations were suspended was used to perform the experiment. Figure 1 shows a schematic view of the experimental set up. The tank was 2280mm by 1770mm in cross section and 1720mm high. Because the shortest distance between a source and any external boundary was 380mm, which is more than four times the migration length of a 5MeV neutron in water, the whole source - detector arrangement could be considered to be in an infinite bath of water. The detector was placed in an air-filled measurement tube made of aluminium situated at the centre of the support structure, the tube being 75.1mm in radius with a wall thickness of 4.04mm. Measurements were made in the plane of the sources and at 150 and 300mm above and below this plane. The support structure has eight arms from which up to eight sources were symmetrically suspended by thin steel wires at accurately known distances around the measurement tube. The source to detector spacing could be increased by 50.08mm steps from 100.16mm to 500.80mm.

The Californium sources were contained in special capsules. Each consisted of an inner double walled stainless steel capsule (1.6mm in total thickness) holding the source which was inserted via a plug into an outer cylindrical stainless steel container of 9.5mm radius. The neck of the latter contained a steel screw which was connected by a very fine steel wire to an arm of the support structure. The central region of the source capsule contains a very small amount of air and aluminium. Figure 2 shows the MCBEND9A model of the source container. The absolute calibration of the sources was carried out at the National Physical Laboratory. The estimated standard deviation on the source strengths is 0.5%, with appropriate corrections being made for the decay following calibration. The angular variation of the neutron output of one source was also measured and departures from the average value were found to be well below 10%. The Cf^{252} source spectrum was taken from reference [4].

3. THE MCBEND MODEL

The experiment was modelled accurately apart from omitting the light support structure and thin steel support wires. This is not considered significant because of their small volume. Figure 1 shows a schematic view of the experimental model and Figure 2 shows a schematic view of the

model of the source container. The model differed from that used in earlier calculations because the detector was explicitly included; previously it had been treated as a scoring region in the void within the measurement tube [5] [6]. The sulphur was in the form of a cylindrical block of density 1.86g/cm^3 with its height and diameter both equal to 28mm. As data for sulphur from ENDF-B/VI had not been processed into the library for MCBEND, the detector was represented by aluminium. Supporting calculations for this model using data from UKNDL showed that there were negligible differences in the predicted reaction rates when the detector was represented as sulphur or aluminium. (Inclusion of the detector reduced the reaction rate by 7% below that obtained when the scoring region was a void.) Version 9A of the code has been used in this work to predict the detector reaction-rates in the measurement tube at the centre of the source array. MCBEND's complex source option, where the source is described using bodies similar to those used to construct the model of the system, was used to define the source geometry and spectrum. Splitting and Russian roulette were applied to accelerate the calculation, with the MAGIC adjoint diffusion module in MCBEND being used to determine the importances in the R, Z and energy dimensions, the calculation being accelerated towards the sulphur detector on the source plane. The cross-sections for the $S^{32}(n,p)P^{32}$ reaction were taken from the IRDF-90 response library [3]. Figure 4 shows the variation of $S^{32}(n,p)P^{32}$ cross-sections with neutron energy. The input data options used in setting up the MCBEND model are listed in Table 1. The Cf^{252} source spectrum used in the calculations is presented in Table 2.

The calculations were run until the majority of the Monte Carlo standard deviations on the responses were less than 5%. The input data necessary to perform sensitivity calculations have been included in the model. The sensitivities to nuclear data (hydrogen, oxygen and detector cross-sections) are required to determine the uncertainties due to these parameters.

4. RESULTS

The results are given in Table 3 which compares the calculated $S^{32}(n,p)P^{32}$ reaction-rates with the experimental values for each source-detector configuration. The results show good agreement with the measurements giving C/E (ie Calculation/Experiment) ratios ranging from 0.95 to 1.00. However the calculations were concentrated on predicting reaction rates on the source plane (Axial displacement = 0) so that the uncertainties due to the Monte Carlo statistics are least for these points. The measurements and calculations all agree to within 3.6% at these points. The attenuation between 101.6mm and 355.6mm is calculated to be 4.9×10^{-3} compared with the measured value of 4.5×10^{-3} . For a point kernel in spherical geometry this would imply that the attenuation cross-section is known to an accuracy of 3%.

A full analysis of the significance of the comparison, however, requires a detailed sensitivity and uncertainty analysis. This is presented in the next section.

5. UNCERTAINTIES

5.1 Experimental

The main uncertainty quoted by the experimentalists arises from the dispersion introduced into the measurements due to the technique of burning the irradiated sulphur to concentrate the P^{32} activity thereby increasing the sensitivity of the detector. When combined with the smaller contribution from the counting statistics the uncertainty is estimated to be 6% on each measurement. In addition the experimentalists mention uncertainties in the source strength (0.5%), and in the sulphur density (5%). An error in the source-detector separation is also quoted as $\pm 0.25\text{mm}$. The error in the vertical position of the sources is $\pm 0.4\text{mm}$. The changes in the sulphur reaction rate due to

additional errors are negligible when compared with the uncertainty arising from the burning technique. This is consistent with the experimentalists' report that every effort was made to minimise the overall uncertainties.

5.2 Computational

The calculational uncertainties are mainly due to the nuclear data (hydrogen and oxygen cross-sections) and the sulphur $S^{32}(n,p)P^{32}$ reaction rate cross-sections. The MCBEND model of the experiment is an exact representation of the geometry in three-dimensions, therefore no modelling approximations are present in the analysis. The MCBEND model was checked by the SKETCH geometry visualisation program [7] to ensure that no errors were present in the parameters defining the model. There is an additional uncertainty arising from the errors in the Cf^{252} source spectrum used in the calculations which has a mean neutron energy at 2.164 ± 0.062 MeV. The effect of this on the sulphur reaction rates is calculated to be less than 1%.

The nuclear data uncertainties for hydrogen and oxygen have been determined using the relative sensitivity profiles obtained from MCBEND folded with the variance-covariance data obtained from the ZZ-VITAMIN COVA library [8]. The sensitivities as calculated by the DUCKPOND module of MCBEND are presented in Table 4. The uncertainties estimated using the WINCOV program [9] to combine the sensitivities and the variance-covariance data are given in Table 5. It was found that the main uncertainty is due to the hydrogen elastic scattering cross-section which becomes more significant with increasing separation of the sources and the detector. Below 13MeV the total macroscopic cross-section for hydrogen in water is greater than that of oxygen even at the narrow resonance peaks in oxygen. At 8 MeV the cross-section is twice as large for hydrogen as for oxygen and at lower energies the average ratio is even higher. Therefore most of the collisions in water are with the hydrogen nuclei. Further, an elastic collision with oxygen does not significantly degrade the neutron energy, whilst at high energies there is a large probability of small angle elastic scattering which has little effect on the penetration. Collisions with hydrogen however will tend to degrade the neutron energy so as to remove it below the threshold for the $S^{32}(n,p)P^{32}$ reaction. Hydrogen collisions therefore play the dominant role in the penetration of fast neutrons through water. Hence calculations performed for the water benchmark are a test of the accuracy of the hydrogen cross-section. The latter decreases with increasing energy and therefore for greater source - detector spacings, higher energy neutrons are more important. Table 4 is given to show the relative sensitivities of the $S^{32}(n,p)P^{32}$ reaction to the cross-sections of hydrogen and oxygen.

The uncertainties in the calculated reaction rates which arise from the response cross-sections for the sulphur detectors have been calculated using the contributions to the sulphur reaction rate from neutrons in 4 energy groups above 0.7 MeV folded with the co-variances obtained from the IRDF-90 data after processing with the NJOY [10] system. The results showed that a 4% uncertainty is due to the sulphur $S^{32}(n,p)P^{32}$ cross-sections at the positions presented in Table 5.

The overall uncertainties on the ratios of the calculated and measured reaction rates range from 7.4% at 101.6mm from the source to 8.1% at 355.6mm. The large contribution to the uncertainty which arises from the measurements means that it is not possible to provide positive confirmation of the accuracies ascribed to the hydrogen and oxygen cross-sections on the basis of the comparisons. However the consistency of the better than expected agreement suggests that the contribution of the dispersion from burning to the uncertainty in the measurements has been overestimated. Similarly the absence of any consistent bias suggests that the likely errors in the sulphur reaction cross-sections are less than the 4% standard deviation given in Table 5. This is illustrated further by the data presented in Table 6. The mean value of C/E is 0.997 and the standard deviation for the distribution of the individual values is 3.27%. The discrepancies between calculation and measurement are less than 0.5 of the standard deviations as derived in Table 5 by combining all of the estimated contributions. In the light of these observations and the absence of any consistent

trend in the ratio of calculation to measurement with increasing penetration, the results as plotted in Figure 3 suggest that the attenuation cross-section for water is accurate to within the standard deviations given by the co-variance data from reference 9. These data give an uncertainty of $\pm 2.4\%$ in the fast flux detected by the sulphur reaction after a penetration of 355.6mm of water.

6. CONCLUSIONS

The single material water benchmark has been analysed using the Monte Carlo code MCBEND9A with the ENDF/B-VI and IRDF-90 nuclear data as part of a validation programme for the nuclear data library and the calculational method. The accuracy of the model ensures that there are no errors introduced when modelling the experimental system.

The comparison of the sulphur reaction rates calculated by MCBEND9A against the measurements showed good agreement with maximum discrepancies of 3.5% on the source plane. Figure 3 gives the values of the ratios of calculated to experimental reaction rates (C/E) for this plane together with the calculated uncertainties. The total maximum uncertainty has been calculated to be around 8% (1 standard deviation) with the major contributions being those from the measurements and the cross-sections for the sulphur reaction rate. The agreement is closer and more consistent than would be expected from the calculated uncertainties and it suggests that the uncertainties on the measurements and the detector cross-sections are overestimated. The variance-covariance data for the cross-sections for oxygen and hydrogen give an uncertainty of 2.4% in the predicted sulphur reaction rate at a penetration of 355.6mm due to the calculated attenuation in the water. While the comparisons cannot provide confirmation of this degree of accuracy, they do indicate that the variance-covariance data are not seriously underestimating the possible errors in the cross-sections at these energies.

The results presented in this report can be used as part of the validation of MCBEND9A code for the prediction of fast neutron attenuation in water.

REFERENCES

- [1] MCBEND User Guide to Version 9A, ANSWERS/MCBEND(94)15.
- [2] Eaton C R and Dean C J
Report on the Extension of the Monte Carlo Nuclear Data Generation Route.
AEA-RS-1246
- [3] Kocherov N P and Mclaughlin P K
The International Dosimetry File (IRDF-90), IAEA-NDS-141 October 1993.
- [4] Carter M D and Packwood A
The Winfrith Water Benchmark Experiment
NEACRP-A-628
- [5] Locke H F and Wright G A
Benchmark Testing of JEF2.2 Data for Shielding Applications. Analysis of the Winfrith
Water Benchmark Experiment. AEA-RS-1232.
- [6] McGuinness J M
MCBEND Validation Report No. 3. ANSWERS/VALIDATION/MCBEND/3/1.
- [7] SKETCH. A Program for Checking Geometry Models used in MCBEND, RANKERN
and MONK. ANSWERS/VISTA(94)2.
- [8] Kodelli I and Sartori E
Co-variance Data Library. ZZ-VITAMIN-J/COVA, NEA1264, OECD/NEADB 1990
- [9] Ziver A K and Earwicker J
Generation of Variance-Covariance Data from the ENDF-B/VI and IRDF-90 Nuclear
Data Libraries. AEA-TSD-0387
- [10] MacFarlane R E & Muir D W.
The NJOY Nuclear Data Processing System, Version 91.
LA-12740-M

Table 1. Options used in the MCBEND input files.
 (All of the files used the same options.)

Option.	Details of option.
Geometry.	A large rectangular volume of water.
Type of source particle.	Neutron.
Thermal treatment.	None used.
Source.	Complex source.
Energy Variation	Cf-252 user supplied spectrum.
Source weighting.	None.
Acceleration.	MAGIC in R, Z and Energy.
Scoring.	Track length estimation.
Responses.	From the IRDF-90 response library [3].
Sensitivities	Elastic and non-elastic cross-sections of hydrogen, oxygen and detector cross-sections.
Nuclear Data	From the ENDF/B-VI [2].

Table 2 Californium-252 Neutron Source Spectrum

Upper Energy (MeV)	Neutrons per second	Upper Energy (MeV)	Neutrons per second
1.284E+01	7.119E-04	8.208E-01	2.945E-02
1.133E+01	1.625E-03	7.244E-01	3.097E-02
1.000E+01	3.304E-03	6.393E-01	2.747E-02
8.825E+00	6.059E-03	5.642E-01	2.417E-02
7.788E+00	1.014E-02	4.979E-01	2.112E-02
6.873E+00	1.565E-02	4.394E-01	1.833E-02
6.065E+00	2.222E-02	3.877E-01	1.583E-02
5.353E+00	2.941E-02	3.422E-01	1.361E-02
4.724E+00	3.684E-02	3.020E-01	1.164E-02
4.169E+00	4.398E-02	2.655E-01	9.835E-03
3.679E+00	5.033E-02	2.352E-01	8.134E-03
3.247E+00	5.547E-02	2.075E-01	6.660E-03
2.865E+00	5.914E-02	1.832E-01	5.456E-03
2.528E+00	6.123E-02	1.616E-01	4.473E-03
2.231E+00	6.177E-02	1.426E-01	3.670E-03
1.969E+00	6.090E-02	1.259E-01	3.014E-03
1.738E+00	5.884E-02	1.111E-01	2.476E-03
1.534E+00	4.715E-02	9.804E-02	2.036E-03
1.353E+00	3.633E-02	8.652E-02	1.676E-03
1.194E+00	3.329E-02	7.635E-02	1.380E-03
1.054E+00	3.015E-02	6.738E-02	1.137E-03
9.301E-01	2.702E-02	5.946E-02	
			1.0

Table 3 The Sulphur Reaction Rates (S32(n,p)P32)

Axial Position (mm)	Experimental reaction-rate. (Bq/atom/source neutron)		Calculated reaction-rate. (Bq/atom/source neutron)		C/E
		1 s.d.		1 s.d.	
1. Source = 1.256E7 n/s 101.6mm from detector.					
300	6.71E-31	6.0%	6.46E-31	7.4%	0.963
150	5.37E-30	6.0%	5.28E-30	1.9%	0.983
0	3.13E-29	6.0%	3.02E-29	1.5%	0.965
2. Source = 2.540E7 n/s 152.4mm from detector.					
300	3.22E-31	6.0%	3.06E-31	8.4%	0.950
150	2.25E-30	6.0%	2.28E-30	4.0%	1.013
0	7.56E-30	6.0%	7.78E-30	2.2%	1.029
3. Source = 5.260E7 n/s 203.2mm from detector.					
300			1.79E-31	6.7%	
150			9.96E-31	3.5%	
0			2.45E-30	2.4%	
4. Source = 1.048E7 n/s 254.0mm from detector.					
300	9.5E-32	6.0%	9.41E-32	7.2%	0.991
150	4.36E-31	6.0%	4.31E-31	2.9%	0.989
0	8.55E-31	6.0%	8.39E-31	2.4%	0.981
5. Source = 1.046E7 n/s 304.8mm from detector.					
300	5.16E-32	6.0%	4.98E-32	8.4%	0.965
150	1.94E-31	6.0%	1.96E-31	3.8%	1.010
0	3.43E-31	6.0%	3.34E-31	2.6%	0.974
6. Source = 1.048E7 n/s 355.6mm from detector.					
300	2.81E-32	6.0%	2.96E-32	6.6%	1.053
150	8.92E-32	6.0%	9.06E-32	2.8%	1.015
0	1.42E-31	6.0%	1.47E-31	2.6%	1.035
7. Source = 1.045E7 n/s 508.0mm from detector.					
300			4.48E-33	7.6%	
150			1.02E-32	2.9%	
0			1.41E-32	2.5%	

The errors quoted are due to the dispersion due to the experimental method (experiment) and Monte Carlo stochastic error (calculated).

Table 4 Relative Sensitivities from MCBEND (DUCKPOND) Calculations

Group	Upper Energy (MeV)	Sensitivity		Sensitivity		Sensitivity	
		Hydrogen Elastic	1 s.d	Oxygen Elastic	1 s.d	Oxygen Non-Elastic	1 s.d
Source - Detector Spacing = 10.16 cm							
1	14.92	-0.168	0.01	0.011	0.004	-0.017	0.001
2	4.4	-0.333	0.01	-0.03	0.007	-0.004	0.001
3	2.6	-0.079	0.01	-0.007	0.001	0	
	1.35						
Source - Detector Spacing = 25.4 cm							
1	14.92	-0.987	0.06	-0.138	0.02	-0.096	0.01
2	4.4	-0.837	0.06	-0.188	0.02	-0.013	0.01
3	2.6	-0.123	0.02	-0.016	0.01	0	
	1.35						
Source-Detector Spacing = 35.56 cm							
1	14.92	-1.641	0.09	-0.280	0.03	-0.186	0.01
2	4.4	-0.881	0.04	-0.231	0.02	-0.013	0.01
3	2.6	-0.172	0.04	-0.025	0.01	0	
	1.35						
Source - Detector Spacing = 50.8 cm							
1	14.92	-2.801	0.11	-0.602	0.04	-0.359	0.02
2	4.4	-0.776	0.03	-0.218	0.01	-0.012	0.01
3	2.6	-0.141	0.04	-0.018	0.02	0	
	1.35						

Table 5. Experimental and Calculational Uncertainties

Source of Uncertainty	Error 1 s.d %
Source - Detector Spacing 10.16 cm	
Experimental	6.00
Monte Carlo Statistics	1.50
Sulphur Reaction Cross Sections	3.94
Nuclear Data - Hydrogen	0.50
Nuclear Data - Oxygen	0.02
Total on C/E	7.37
Source - Detector Spacing 25.40 cm	
Experimental	6.00
Monte Carlo Statistics	2.40
Sulphur Reaction Cross Sections	3.98
Nuclear Data - Hydrogen	1.67
Nuclear Data - Oxygen	0.29
Total on C/E	7.78
Source - Detector Spacing 35.56 cm	
Experimental	6.00
Monte Carlo Statistics	2.60
Sulphur Reaction Cross Sections	4.10
Nuclear Data - Hydrogen	2.30
Nuclear Data - Oxygen	0.50
Total on C/E	8.07

Note. Nuclear data uncertainties are calculated using the co-variance data from reference [8]
 Uncertainties due to Sulphur reaction rate cross-sections are calculated from reference [9]

Table 6 Analysis of C/E for the Sulphur Reaction Rates

Distance (mm)	C/E	Uncertainty on C/E 1 std dev σ	$(C/E-1)/\sigma$
101.6	0.965	0.0737	-0.4749
152.4	1.029	0.0750	0.3867
254.0	0.981	0.0778	-0.2442
304.8	0.974	0.0790	-0.3291
355.6	1.035	0.0807	0.4337

Mean Value of C/E = 0.9968

Standard Deviation of the values of C/E = 0.0327

Figure 1 Schematic View of Experimental Set up

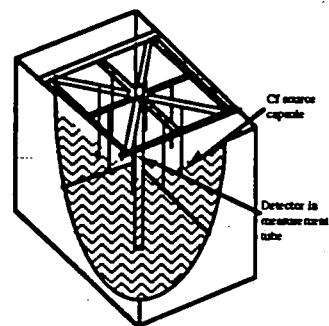
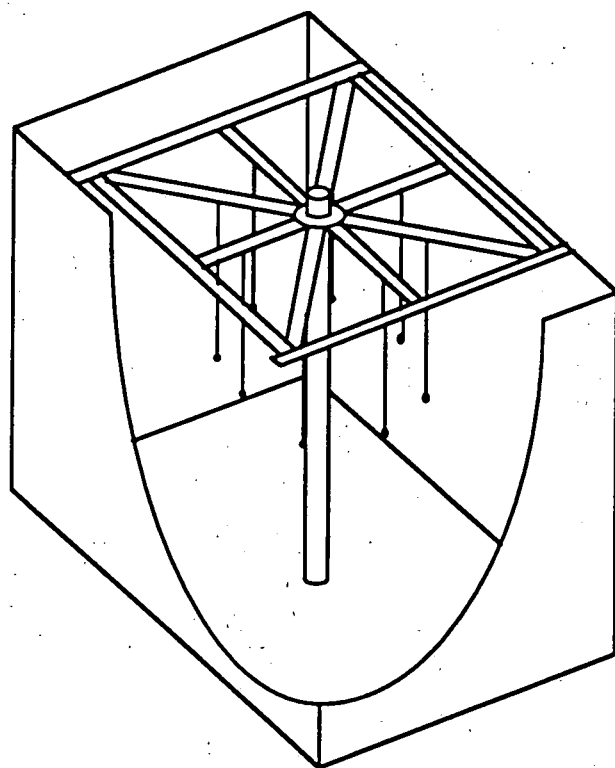
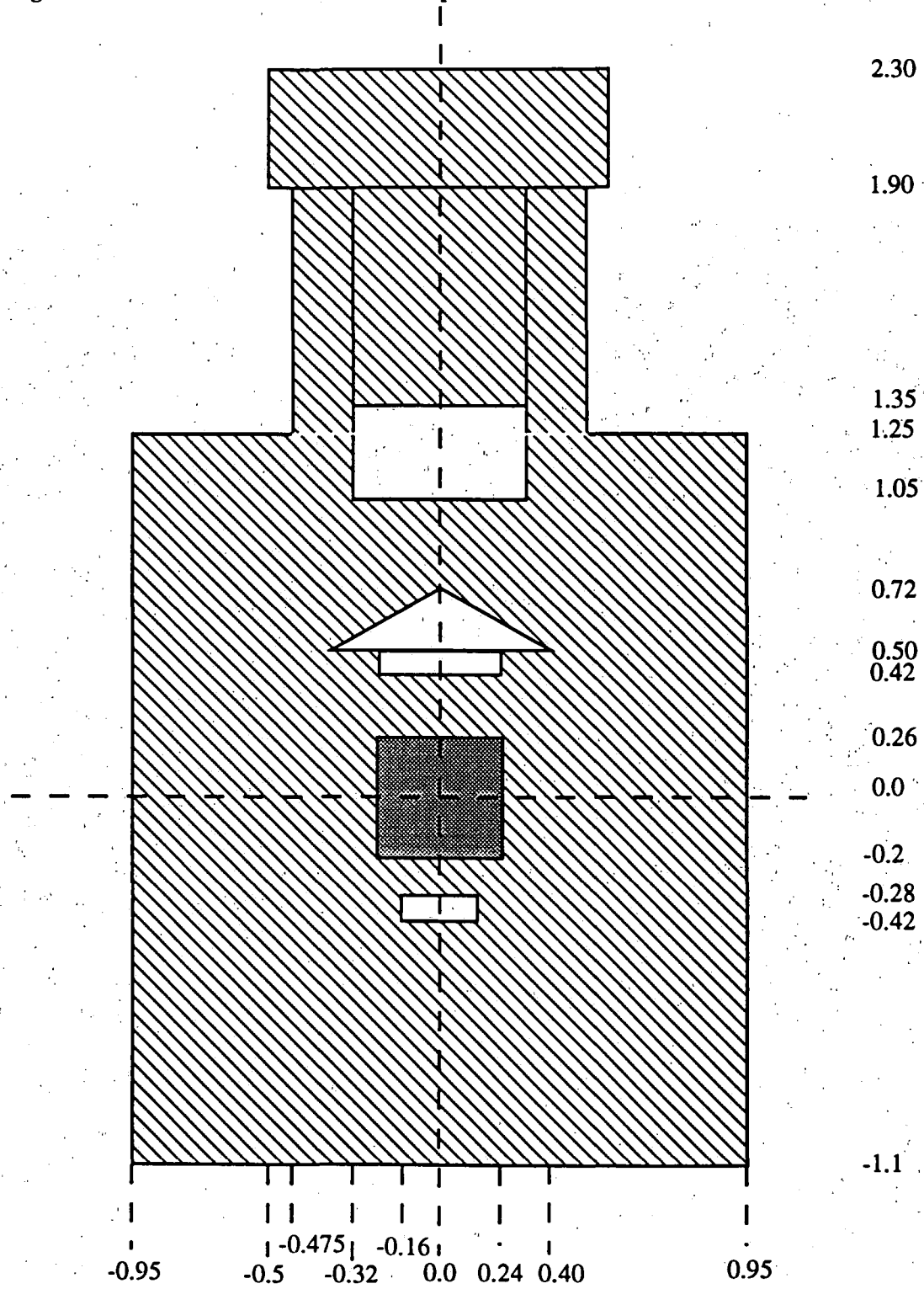


Figure 2 Model of the Source Capsule



-  Stainless steel
-  Californium-252
-  Void

All dimensions in cm

Figure 3 Values of C/E for the $S^{32}(n,p)P^{32}$ Reaction Rate in the Source Plane

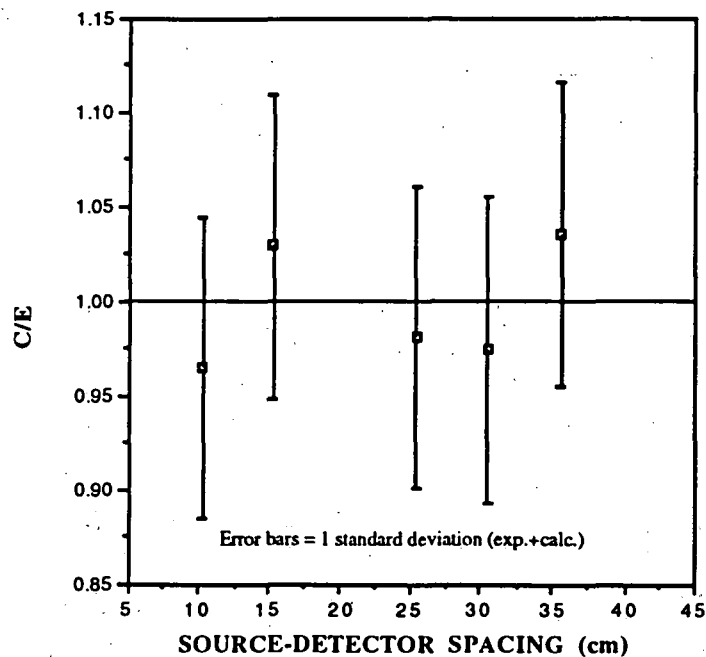
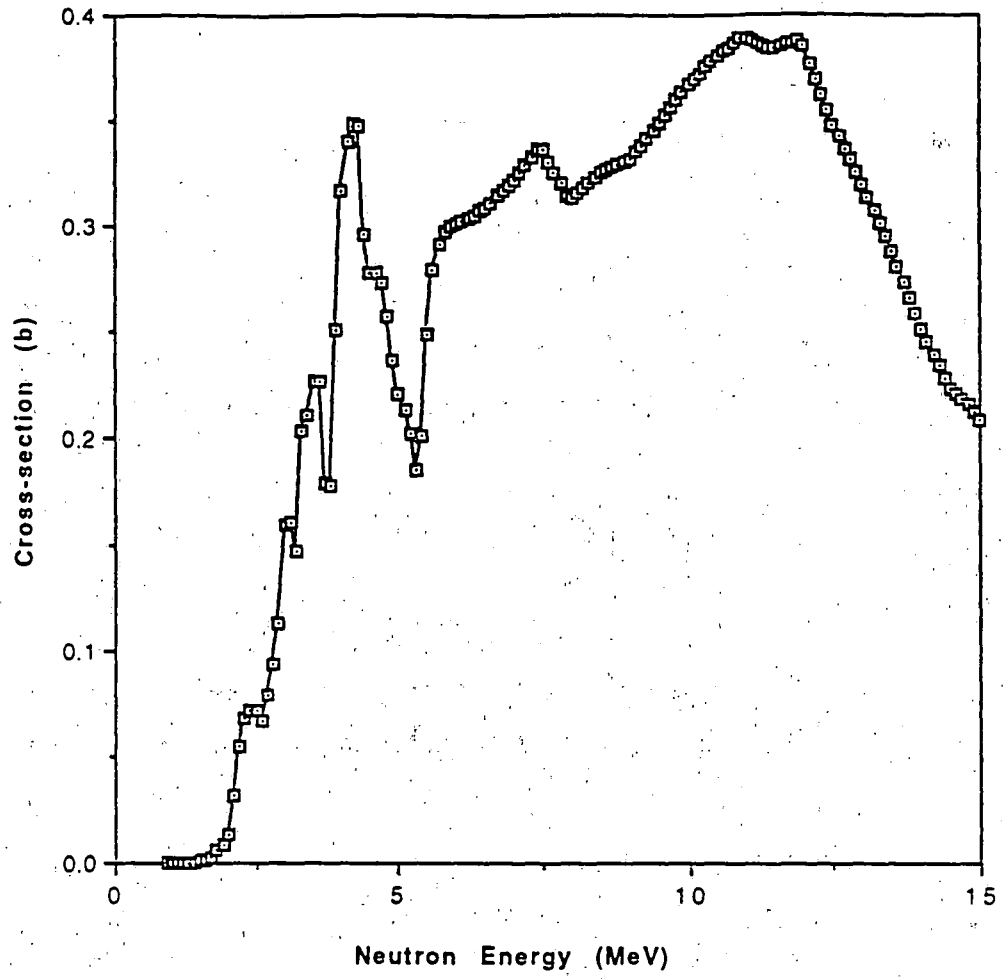


Figure 4 $S^{32}(n,p)P^{32}$ Reaction Rate Cross-sections (IRDF-90)



APPENDICES

A MCBEND INPUT DATA

```
&*****
&
&          WATER BENCHMARK ----- CASE 1
&
&          SOURCE 10.16CM FROM DETECTOR
&
&*****
&
&UNIT 1
BEGIN CONTROL DATA
    PROCESS TO STAGE THREE
    SPLITTING
END
&UNIT 2
BEGIN DATASET DEFINITIONS
    DUMP A 25
    DUMP B 26
END
&UNIT 4
BEGIN MATERIAL GEOMETRY
    CG
&AL MEASUREMENT TUBE (OUTER)
    RCC1 0.0 0.0 -90.0
        0.0 0.0 180.0
        3.755
&AL MEASUREMENT TUBE (INNER)
    RCC2 0.0 0.0 -90.0
        0.0 0.0 180.0
        3.351
&AL TANK
    RPP3 -114.0 114.0 -88.5 88.5 -86.0 86.0
&SCORING REGIONS
    RCC4 0.0 0.0 -31.4
        0.0 0.0 2.8
        1.4
COPY 4
Z 4*15.0
&SOURCE CAPSULES (RPP DEFINING CELL)
    C 1
    RPP9 -0.95 0.95 -11.11 -9.21 -1.1 2.3
&BODIES WITHIN SOURCE CAPSULE
    CELL 1
&SOURCE
    RCC1 0.95 0.95 0.9
        0.0 0.0 0.46
        0.24
&LOWER VOID
    RCC2 0.95 0.95 0.68
        0.0 0.0 0.14
        0.16
```

&UPPER VOID

RCC3 0.95 0.95 1.52
 0.0 0.0 0.09
 0.24

&VOID CAP

TRC4 0.95 0.95 1.61
 0.0 0.0 0.21
 0.4 0.0

&BULK OF CAPSULE

RCC5 0.95 0.95 0.0
 0.0 0.0 2.35
 0.95
 RCC6 0.95 0.95 2.35
 0.0 0.0 0.65
 0.475

&LID OF CAPSULE

RCC7 0.95 0.95 3.0
 0.0 0.0 0.4
 0.5

&SCREW VOID

RCC8 0.95 0.95 2.15
 0.0 0.0 0.3
 0.32

&SCREW SSTEEL

RCC9 0.95 0.95 2.45
 0.0 0.0 0.55
 0.32

&

ZONES

ALTUBE 20 +1 -2
 MEASVOID 20 +2 -4 -5 -6 -7 -8
 WATER 20 +3 -1 -9
 SCOR-30 20 +4
 SCOR-15 20 +5
 SCOR0 20 +6
 SCOR+15 20 +7
 SCOR+30 20 +8
 EXTVOID 20 -3

&

CELL 1

&

SSCASE 20 +5 -2 -1 -3 -4 -8
 SSCASETOP 20 +6 -8 -9
 SSLID 20 +7
 SOURCE 20 +1
 VOIDLOW 20 +2
 VOIDUP 20 +3
 VOIDCAP 20 +4
 VOIDSCREW 20 +8
 SSSCREW 20 +9
 WATER 20 +0 -5 -6 -7

&

REGIONS
 SEQUENCE
 CELL 1

```
COMMON
SEQUENCE
MATERIALS
1 0 2 5*5 -2000
CELL 1
3*3 4 4*0 3 2
VOLUMES
&EQUAL 1.0 EXCEPT SCORING REGIONS
3*1.0 5*17.24 1.0
CELL 1
UNITY
END
&UNIT 5
BEGIN SPLITTING GEOMETRY
R 3
0.0 2.5 5.0 150.0
THETA DUMMY
Z 5
-90.0 -20.0 -5.0 5.0 20.0 90.0
END
&UNIT 6
END
&UNIT 7
BEGIN ENERGY DATA
NEUTRON
SPLITTING
GROUPS 12
14.6 13.5 12.5 11.25 10.0 8.5 7.0 6.07 4.72
3.68 2.87 1.74 0.639
SCORING
GROUPS 20
12.84 8.825 7.788 6.873 6.065 5.353 4.724
4.169 3.679 3.247 2.865 2.528 2.231 1.969
1.738 1.534 1.353 1.194 1.054 0.930 0.639
THERMAL TREATMENT
NONE
COMPLEX SOURCE
END
&UNIT 8
BEGIN IMPORTANCE MAP
DIMENSIONS 3 1 5 12 1
CALCULATE
TARGETS 1
ZONES 6
STRENGTHS
1.0
USE METHOD D
PRINT IMPORTANCE VALUES
END
&UNIT 9
BEGIN SCORING DATA
MESH SYSTEM CG
DIMENSIONS 19 1 1
MATERIAL MESH
TRACK LENGTH
```

FLUX ALL NOT SOME
1
1 2 3 9 10 11 12 14 15 16 17 18 19
RESPONSES DITTO
SENSITIVITY OF FLUX
DITTO
SENSITIVITY OF RESPONSES
DITTO
CONTRIBUTIONS TO RESPONSES
DITTO

END

&UNIT 10

BEGIN RESPONSE DATA

FUNCTION

S32(N,P)

& S32(N,P) IRDF90

FUNCTION PAIRS

See Figure 4 of this report

END

&UNIT 11

BEGIN SENSITIVITY DATA

COMBINATIONS 36

1250296 0

EXC 1 2

1250296 0

INC 1 2

825 0

EXC 1 2

825 0

INC 1 2

2631 0

EXC 1 2

2631 0

INC 1 2

1325 0

EXC 1 2

1325 0

INC 1 2

2525 0

EXC 1 2

2525 0

INC 1 2

2431 0

EXC 1 2

2431 0

INC 1 2

2825 0

EXC 1 2

2825 0
INC 1 2

9237 0
EXC 1 2
9237 0
INC 1 2

2625 0
EXC 1 2
2625 0
INC 1 2

2634 0
EXC 1 2
2634 0
INC 1 2

2637 0
EXC 1 2
2637 0
INC 1 2

2425 0
EXC 1 2
2425 0
INC 1 2

2434 0
EXC 1 2
2434 0
INC 1 2

2437 0
EXC 1 2
2437 0
INC 1 2

2831 0
EXC 1 2
2831 0
INC 1 2

2834 0
EXC 1 2
2834 0
INC 1 2

2837 0
EXC 1 2
2837 0
INC 1 2

2843 0
EXC 1 2

2843 0
INC 1 2

GROUPS 16

1.492E+1 4.400E+0 2.600E+0 1.350E+0 7.080E-1
5.800E-1 4.100E-1 3.095E-1 2.620E-1 6.200E-2 3.000E-2
1.500E-2 1.585E-2 2.145E-2 1.068E-5 5.043E-6
5.500E-7

END

&UNIT 14

BEGIN MATERIAL DATA

MINNIE
MIXTURES 1
WEIGHT

M1 MN 1.5986E-2
FE54 0.0401 FE56 0.6458 FE57 0.0150 FE58 0.0021
CR50 0.0078 CR52 0.1564 CR53 0.0180 CR54 0.0046
NI58 6.387E-2 NI60 2.545E-2 NI61 1.12E-3
NI62 3.64E-3 NI64 9.6E-4

MATERIALS 5

VOLUME

1 AL 2.7 1.0
2 WATER 1.0
3 M1 7.9 1.0
4 U238 18.7 1.0
5 AL27 1.86 1.0

USE MOULD 28 FOR H IN ALL MATERIALS
USE MOULD 21 FOR O IN ALL MATERIALS
USE DFN 1625 FOR S32 IN ALL MATERIALS
USE ADCN FE FOR FE56 IN ALL MATERIALS
USE ADCN FE FOR FE57 IN ALL MATERIALS
USE ADCN FE FOR FE54 IN ALL MATERIALS
USE ADCN FE FOR FE58 IN ALL MATERIALS
USE ADCN CR FOR CR50 IN ALL MATERIALS
USE ADCN CR FOR CR52 IN ALL MATERIALS
USE ADCN CR FOR CR53 IN ALL MATERIALS
USE ADCN CR FOR CR54 IN ALL MATERIALS
USE ADCN NI FOR NI58 IN ALL MATERIALS
USE ADCN NI FOR NI60 IN ALL MATERIALS
USE ADCN NI FOR NI61 IN ALL MATERIALS
USE ADCN NI FOR NI62 IN ALL MATERIALS
USE ADCN NI FOR NI64 IN ALL MATERIALS
USE ADCN AL FOR AL27 IN ALL MATERIALS

END

&UNIT 23

BEGIN CG SOURCE DATA

RCA 0.0 -10.16 -0.2
0.0 0.0 0.46
0.0 0.24

1.0 1 1

VOLUME SOURCE

ENERGY BOUNDARIES

43

12.84 11.33 10.0 8.825 7.788
6.873 6.065 5.353 4.724 4.169

3.679 3.247 2.865 2.528 2.231
1.969 1.738 1.534 1.353 1.194
1.054 9.301E-1 8.208E-1 7.244E-1 6.393E-1
5.642E-1 4.979E-1 4.394E-1 3.877E-1 3.422E-1
3.020E-1 2.665E-1 2.352E-1 2.075E-1 1.832E-1
1.616E-1 1.426E-1 1.259E-1 1.111E-1 9.804E-2
8.652E-2 7.635E-2 6.738E-2 1.0E-20

GROUP IMPORTANCES

10.0 9.6 8.3 7.5 7.0 6.1 5.0 4.1 3.0 2.2
1.5 1.0 0.8 0.6 0.5 0.3 8*0.001 19*0.0

SOURCE GENERATION GROUPS 1

FLUXES

1.510E8

CROSS SECTIONS

7.119E-4 1.625E-3 3.304E-3 6.059E-3 1.014E-2
1.565E-2 2.222E-2 2.941E-2 3.684E-2 4.398E-2
5.033E-2 5.547E-2 5.914E-2 6.123E-2 6.177E-2
6.090E-2 5.884E-2 4.715E-2 3.633E-2 3.329E-2
3.015E-2 2.702E-2 2.945E-2 3.097E-2 2.747E-2
2.417E-2 2.112E-2 1.833E-2 1.583E-2 1.361E-2
1.164E-2 9.835E-3 8.134E-3 6.660E-3 5.456E-3
4.473E-3 3.670E-3 3.014E-3 2.476E-3 2.036E-3

1.676E-3 1.380E-3 1.137E-3

END

AEA Technology

AEAT-0355

**The Analysis of NESDIP2 with ENDF-B/VI Nuclear
Data and IRDF90 Response Cross Sections.**

A F Avery, S Newbon and A K Ziver

June 1996

**Reactor Physics, Shielding and Criticality Department
Plant Support Services Group
AEA Technology
Winfrith
Dorset DT2 8DH**

AUTHORISATION

	NAME	POSITION	SIGNATURE	DATE
Author	A F Avery	Shielding Consultant	<i>A. F. Avery</i>	12/6/96
Checked	S J Chucas	Product Manager	<i>S. J. Chucas</i>	12/6/96
Approved	C A Cooper	Department Manager	<i>C A Cooper</i>	17.6.96

AEAT-0355

AEA Technology

The Analysis of NESDIP2 with ENDF-B/VI Nuclear Data
and IRDF90 Response Cross Sections.

A F Avery, S Newbon, and A K Ziver

June 1996

Summary

This report describes a comparison with measurements to validate the Monte Carlo code MCBEND for the determination of neutron penetration through typical PWR radial shields. Calculations were carried out for the NESDIP2 experiment performed in the ASPIS facility of the NESTOR reactor at Winfrith, using MCBEND9A with ENDF-B/VI nuclear data and IRDF-90 response cross-sections. Results for three reaction rates, ie $S^{32}(n,p)P^{32}$, $In^{115}(n,n')In^{115m}$ and $Rh^{103}(n,n')Rh^{103m}$ have been compared with measurements. A detailed analysis of uncertainties using the covariances from the ENDF-B/VI library is included.

In general MCBEND accurately predicts the reaction rates in the region representing the RPV and the cavity and underpredicts in the water regions inboard of the RPV. At the important T/4 and 3T/4 positions in the RPV, the C/M values are within 12% of those at the cavity, showing that accurate predictions of the neutron fluence at these positions can be derived from measurements made in the cavity.

The results provide validation for the use of MCBEND and the ENDF-B/VI library for this type of calculation, and confirm that the uncertainties assigned to the material cross-sections are appropriate.

Reactor Physics, Shielding and Criticality Department
Plant Support Services Group
AEA Technology
Winfrith
Dorset DT2 8DH

CONTENTS

	Page No.
1 INTRODUCTION	1
2 THE EXPERIMENTAL CONFIGURATION	1
3 THE FISSION PLATE	2
3.1 The Fission-Rate Distribution within the NESDIP Fission Plate Located in the NESDIP 2 Radial Shield Array	2
3.2 The Low-Energy Neutron Flux Profile Over the Fission Plate	3
3.3 The Fission Plate Profile	3
3.4 The Z Dependence of the Fission-Rate Distribution	3
3.5 The Absolute Calibration of the Fission Plate	4
4 THRESHOLD REACTION-RATE MEASUREMENTS	4
4.1 Rhodium Activation Measurements	4
4.2 Sulphur Activation Measurements	4
4.3 Indium Activation Measurements	4
4.4 Core Background Corrections	4
4.5 Activation Results	5
4.6 Perturbation in the RPV Region	5
5 MONTE CARLO CALCULATIONS	5
5.1 The Geometric Model	5
5.2 The Fission Plate Source Distribution	5
5.3 The Scoring Data	5
5.4 Nuclear Data	6
5.5 Variance-Covariance Data	6
5.6 Acceleration of the Monte Carlo Calculations	6
6 MONTE CARLO RESULTS	6
6.1 Corrections to the Calculated Reaction-Rates	6
6.2 Uncertainties	7
6.3 Comparison of Calculation with Experiment	8
7 SUMMARY	9
8 REFERENCES	11

TABLES

- 1 Dimensions and Materials in the NESDIP2 Array
- 2 Material Compositions
- 3 The Neutron Source Distribution in the NESDIP Fission Plate Located in the NESDIP2 Array
- 4 Measured Reaction-Rates through the NESDIP2 Radial Shield
- 5 $S^{32}(n,p)$ Reaction-Rate Profile in the Cavity
- 6 Comparison of Activation Measurements in the Cavity with RPV Plates Open and Closed
- 7 Calculated Responses with ENDF-B/VI Data
- 8 Calculated Reaction-Rates and Uncertainties for $Rh^{103}(n,n')Rh^{103m}$
- 9 Calculated Reaction-Rates and Uncertainties for $In^{115}(n,n')In^{115m}$
- 10 Calculated Reaction-Rates and Uncertainties for $S^{32}(n,p)P^{32}$
- 11 Ratio of Calculated and Measured Reaction Rates

FIGURES

- 1 NESDIP2 Configuration
- 2 NESDIP2 Enriched U/Al Alloy Fission Plate
- 3 ASPIS U/Al Alloy Fuel Element
- 4 Detail of Fuel Loading Pattern
- 5 Co-ordinate System
- 6 Fuel Element Configuration and Manganese Foil Measurement Positions
- 7 NESDIP2 Fission Plate Source Profile
- 8 Source Mesh Boundaries
- 9 Measurement Locations in the NESDIP2 Array
- 10 Relative $S^{32}(n,p)P^{32}$ Reaction-Rate Axial Profile in the Cavity of the NESDIP2 Array
- 11 MCBEND Model of the NESDIP2 Array

APPENDIX

- A MCBEND Input

1 INTRODUCTION

The NESTOR Shielding and Dosimetry Improvement Programme (NESDIP) (1) was conceived to study neutron penetration through typical PWR radial shields. The programme encompassed both penetration through the radial shield from the core boundary to the cavity external to the reactor pressure vessel (RPV) and the subsequent transport within the cavity. An important feature of these experiments was the ability to make measurements at positions within the simulated vessel wall, since in practice the fluxes at penetrations of T/4 and 3T/4, where T is the thickness of the RPV, are required. The first three phases of NESDIP studied the radial penetration to the cavity while Phases 4 and 5 studied streaming within the cavity and in a simulated nozzle and coolant duct configuration.

In Phase 1 of NESDIP an exact replica of the Oak Ridge PCA radial shield benchmark (2) was constructed in a large water tank mounted in the ASPIS trolley of the NESTOR facility at Winfrith in order to investigate discrepancies in the PCA between measurement and calculation. The second phase of NESDIP was a natural extension of the PCA and REPLICIA experiments whereby the lateral extent of the configuration was expanded to the full height and width of the ASPIS trolley. The PCA configuration was thereby represented by a combination of slabs and water tanks of 1.8m x 1.8m cross-sectional area, the thickness of each region remaining unchanged. To fulfil a major concept of the NESDIP studies, the move away from the REPLICIA configuration was carried out in well defined stages. In this phase of NESDIP two series of measurements were conducted. The first series retained the small rectangular fission plate used in the REPLICIA experiment; this configuration is known as the NESDIP1 radial shield. The second series utilised a large circular fission plate with an effective radius of 56cm; this configuration is known as the NESDIP2 radial shield. Both configurations have common slab components outboard of their respective fission plates. With a spatially large source as in the NESDIP2 configuration the effect of the lateral leakage on the centre-line fluxes is substantially reduced.

The results of measurements made within the shields using fast neutron threshold activation foils and neutron spectrometers, along with comparisons against analysis with the Monte Carlo code MCBEND using UKNDL point energy neutron data were reported in reference 3, which considered both NESDIP1 and NESDIP2. A later (4) report described the analysis of NESDIP2 with the latest version of the code, MCBEND7B, using the new DICE data library based on ENDF-B/VI data. The latter calculations have been repeated using the IRDF-90 library of response functions (5) in place of the IRDF-85 data (6) used previously. In addition the analysis of the uncertainties in these later calculations is based on co-variances derived from the ENDF-B/VI files and IRDF-90.

2 THE EXPERIMENTAL CONFIGURATION

The NESDIP2 configuration is shown in Figure 1. It consisted of a combination of slabs and water tanks contained within a trolley of mild steel with an aluminium window on the NESTOR side to allow passage of neutrons into the trolley. The region between the window and the fission plate consisted of void and a graphite slab to allow further thermalisation of the neutrons from the NESTOR source. Beyond the fission plate the array consisted of a water cell divided into two compartments by a thermal baffle, a mild steel block representing the reactor pressure vessel, a 29.4cm wide cavity, a second water cell and a 61cm thick concrete slab forming a biological shield. The positioning of the array within the trolley was constrained in order that the front (NESTOR side) of the cavity was aligned with the front face of the roof slot of the ASPIS facility thus allowing the cavity region to extend beyond the height of the trolley so that streaming measurements could be taken. The 12/13 configuration (i.e 12cm of water between the core and the thermal shield and 13 cm between thermal shield and the reactor pressure vessel) was constructed from a single water tank

which contained the 6.3cm thick stainless steel thermal baffle. The above thicknesses of water are nominal dimensions because the end faces of the cell bowed when the cell was filled with water. The baffle was located to maintain the front water gap at 12.1 cm and the expansion due to bowing was mostly taken up in the rear water compartment which has a thickness of 13.2 cm, both dimensions being measured on the centre line. To allow the use of stock components the mild steel block representing the pressure vessel was constructed from 5.08cm thick plates and the 2.5cm plate which formed the rear wall of the water cell. Hence the total steel thickness was 22.8cm. The dimensions of the NESDIP2 configuration are given in Table 1. It should be noted that this table differs from that in reference 3 due to a correction to the thickness of the thermal baffle. This can also be seen in the dimensions of Figure 11. The material specifications are given in Table 2.

The thicknesses of steel and water in NESDIP2 simulated typical arrangements of the barrel, thermal shield, pressure vessel, and downcomer water in a PWR power plant. The outer surface of the cavity however was defined by a tank of water. Whilst some PWRs do have steel and water primary shields, it is more common to find concrete forming the outer wall of the cavity. Thus while steel and water gave well-defined materials for the primary shield in the NESDIP benchmark, it should be noted that in many practical situations the lack of an accurate composition for the concrete would introduce additional uncertainties.

3 THE FISSION PLATE

The large circular fission plate used in NESDIP2, known as the NESDIP fission plate, is shown in Figure 2. It comprised an aluminium frame which filled the height and width of the ASPIS trolley. Located within the frame were 13 separate fuel elements. An exploded view of an individual fuel element is shown in Figure 3. Each element had two 12mm thick aluminium cover plates which attached on either side of the top and bottom locating pieces leaving a 5mm separation in which U/Al alloy fuel strips were located. The fuel strips were of density $3.256\text{g}\cdot\text{cm}^{-3}$ and were 80% by weight of Al and 20% by weight of U enriched to 93%. They were nominally 30.5mm wide and 1mm thick and were screwed to the rear cover plate.

There was depth for four fuel strips within each element leaving a 1mm clearance gap next to the front cover plate. Three columns of fuel strips laid side by side filled the width of the element. In the NESDIP configuration only the central two strips in each column contained U/Al alloy, the outer two were both blanks manufactured from aluminium. To approximate to a disc source the axial fuel loading within each element had been arranged to the specification of Figure 4 by the substitution of aluminium blanks where necessary.

3.1 The Fission-Rate Distribution within the NESDIP Fission Plate Located in the NESDIP 2 Radial Shield Array

The approach taken to obtain the absolute power distribution throughout the fission plate in this phase of NESDIP follows the procedure set out in reference 3. In summary this is :

- (a) The measurement of manganese reaction-rates over the front surface of the fission plate to define a thermal flux profile in the X and Y coordinates of the system defined in Figure 5 ;
- (b) A measurement of the distribution of the U^{235} content within the fuel;
- (c) Combining (a) and (b) to provide a relative fission-rate profile in X and Y;

- (d) The definition of a relative fission profile in the Z direction through the fuel from fission product decay measurements in irradiated fuel;
- (e) Normalisation of the fission-rate profile to absolute measurements of the fission-rate per NESTOR Watt in the plate.

3.2 The Low-Energy Neutron Flux Profile Over the Fission Plate

Measurements of the $Mn^{55}(n,\gamma)Mn^{56}$ reaction-rate on the front and back faces of the fission plate were made with 12.7mm diameter Mn foils. The distribution of foils on the front face of the fission plate is shown in Figure 6. The foils on the back face were positioned directly behind the foils on the front face at the locations which are encircled in Figure 6. The definition of the X-Y flux profile was made using the manganese measurements made on the front face. The fission-rate attenuation in the Z direction through the plate is assumed to be independent of X and Y, allowing a considerable simplification of the treatment with little loss of accuracy. To support this assumption it is noted that the average difference in the ratios of the manganese measurements at the front to those at the back is less than 3% between positions at the centre of the plate and at its edge.

The manganese reaction-rate measurements on the front face of the plate were input to the CRISP code (7) which fitted a continuous surface to them to define the manganese reaction-rate covering the plate. The surface fit is shown in Figure 7. From this surface the average manganese reaction-rate can be defined within the elements of any source mesh overlaid onto the fission plate. To model exactly the boundaries of the plate and to provide adequate spatial resolution, the source mesh shown in Figure 8 was used. The fractional uncertainty on the mean manganese reaction-rate in each source mesh due to the surface fitting and integration is estimated to be 2%.

3.3 The Fission Plate Profile

The fission-rate profile in X and Y is taken as the manganese reaction-rate profile on the front face of the fuel plate, as shown in Figure 7. In the definition of the fission-rate in each mesh the Z dependence is irrelevant provided it is independent of X and Y. This assumption has been made and justified in Section 3.2. The uncertainty estimate on the average fission-rate in each source mesh is mostly due to the uncertainty of the surface fitting and integration procedures of the CRISP code with a much smaller contribution from the uncertainty on the U^{235} content, giving a total of $\pm 2.1\%$ (2).

3.4 The Z Dependence of the Fission-Rate Distribution

The relative fission rates in the two layers of fuel contained within the plate have been derived from measurements performed to establish the absolute power of the plate. The ratio of fission rates in the front and back fuel plates was 1.044 ± 0.015 . For the calculational analysis of the NESDIP2 radial shield this variation is neglected and the fission-rate in the Z direction is assumed to be uniform over the 2mm depth of the fuel.

It has become customary to provide a spatial neutron source definition which integrates to a total plate power of 1 Watt. Table 3 contains the neutron source distribution for the NESDIP plate in the NESDIP2 array normalised in this way; constants of $3.121E10$ fissions per Watt and 2.437 neutrons per fission have been used in its derivation.

3.5 The Absolute Calibration of the Fission Plate

The absolute power in the fission plate, expressed per NESTOR watt, has been determined by combining spot measurements of the absolute fission-rate made by counting fission product decay rates with corresponding absolute measurements of the $Mn^{55}(n,\gamma)$ reaction-rate and the fission-rate profile data derived in CRISP. This is fully described in reference 3. The fission plate power per NESTOR Watt is calculated to be $8.67E-4$ Watts, the standard deviation on this value being 3.5%. The latter is due mostly to the 3% uncertainty in the measurement of the absolute fission rate.

4. THRESHOLD REACTION-RATE MEASUREMENTS

The reaction-rates of three fast neutron threshold detectors have been measured along the nuclear axis of the shields. They are the $S^{32}(n,p)P^{32}$, $In^{115}(n,n')In^{115m}$ and $Rh^{103}(n,n')Rh^{103m}$ reactions. The rhodium reaction-rate was measured over four decades of attenuation through the water cell, RPV and into the cavity. For measurements in the RPV region, 0.6cm air gaps were opened up between the slab components to allow the insertion of the activation detectors. The indium and sulphur measurements were made in the RPV region and the cavity. In addition, during all irradiations of activation detectors within the shields, three sulphur pellets were placed in locations at the centre of the front face of the fission plate to monitor its run-to-run power via the $S^{32}(n,p)P^{32}$ reaction.

4.1 Rhodium Activation Measurements

The rhodium measurements were made under cadmium to reduce impurity activation. The foils were located within the water cells on a thin perspex jig which was sprung against the cell wall. The positional uncertainty was ± 1 mm. In the RPV and cavity the foils were located on a thin aluminium carrier. The uncertainty associated with the calibration of the NaI spectrometer counting system is 3%.

4.2 Sulphur Activation Measurements

In the RPV and cavity 20g sulphur samples were located on thin aluminium carriers. To facilitate their inclusion in the RPV, 0.6cm voids were introduced between the 5.1cm thick mild steel components. The activated sulphur is first slowly burnt in a thin aluminium cup which is subsequently collapsed to a disc. The residue containing the P^{32} activity is then counted. The calibration of the counting system including counter efficiency, losses due to burning, and reference data has a systematic uncertainty of 4%.

4.3 Indium Activation Measurements

The indium samples were located on the thin aluminium carrier in the RPV and Cavity. The calibration of the counting system for these foils, including Ge(Li) efficiency and reference data has a systematic uncertainty of 2%.

4.4 Core Background Corrections

A small fraction of neutrons present in the arrays originate from leakage from the NESTOR core. The NESTOR reactor is fitted with a boral shutter which is located outside the thermal column, ie adjacent to the front of the ASPIS trolley. It is composed of 1.27cm of boral and when closed it absorbs thermal neutrons which could otherwise enter the trolley. This boral shutter, to a first approximation, shuts down the fission plate leaving only fast neutron leakage from the NESTOR core. Work conducted to study the true shutdown factor of

plate power when the boral shutters are closed (8) led to value for the background correction of $(2\pm 1)\%$. This background correction applies in both the RPV and cavity regions. In the water cells the value of $(1\pm 1)\%$ is appropriate.

4.5 Activation Results

The reaction-rates measured on axis in the NESDIP2 array with the corrections and uncertainties described above are shown in Table 4. The foil irradiation locations are defined in Figure 9. The results of the lateral scans made with the sulphur detectors are shown in Table 5 and Figure 10.

4.6 Perturbation in the RPV Region

The RPV region is constructed from four 5.1cm thick mild steel plates and the rear wall of the water cell. To obtain activation measurements through the RPV region four air gaps of width 0.6cm were opened up between these components. The perturbation of activation measurements made at a position 4cm into the cavity when these voids are introduced is given in Table 6 (note that the measurements were made at a constant distance from the rear face of the RPV region irrespective of whether the RPV plates were separated by air gaps or closed up). The ratios suggest a slight reduction in the measured reaction-rates caused by opening the plates as would be expected, but the reduction is not statistically significant.

5 MONTE CARLO CALCULATIONS

The analysis of the NESDIP2 measurements has been performed using version 9A of the Monte Carlo code MCBEND (9). A listing of the input data is given in Appendix A.

5.1 The Geometric Model

A precise geometric representation of the NESDIP2 radial shield configuration in the ASPIS trolley was achieved using the combinatorial geometry package of MCBEND. The calculational model is shown in Figure 11. The only approximation in the model is the exclusion of the 0.6cm wide voids between the mild steel plates in the RPV region. It is assumed from the evidence presented in Section 4.6 that the activation rates in the cavity are insensitive to the absence of the voids between the plates.

5.2 The Fission Plate Source Distribution

The derivation of the source distribution for the fission plate has been described in detail in Section 3. The Z dependence of the source between the two fuel strips in the NESDIP plate has not been modelled and a uniform source across the thickness of the plate has been used. The effect of this approximation on the calculated fluxes is trivial but it does allow a halving of the number of source regions required to 225. The output from the CRISP program which derives the source distribution in the fission plate is formatted in accordance with the input requirements for the source module in MCBEND and has been included directly into the input data. The fission neutron energy spectrum for U^{235} due to Story and Miller (10) has been used in this analysis.

5.3 The Scoring Data

Scoring is in rectangular regions having a 20cm x 20cm cross-sectional area and 2mm depth. The regions are centred on the measurement positions through the shield which have been defined in Figure 9. An additional scoring region at 23.9cm into the cavity region was included. This was used as the target for the MAGIC calculation(see below). In addition to

the three measured reaction-rates the reactions $Al^{27}(n,\alpha)$, $Fe^{54}(n,p)$, ASTM displacement and total flux $>0.11\text{MeV}$ were scored for comparison with the calculated results of reference 3. The cross-section data were taken from IRDF-90 (5).

5.4 Nuclear Data

Reference 3 used UKNDL data presented at 8220 energy points. This exercise uses ENDF-B/VI data in the same DICE format in which the nuclear data are represented as averaged partial cross-sections at 8220 energy points, a point being a very fine group, with explicit representation of the energy loss laws and angular distributions of scatter. The data libraries are produced from evaluated nuclear data by processing codes contained in the NJOY suite of codes. In the case of ENDF-B/VI data the processing includes replacing the doubly differential distribution for angle and energy, which is present for some isotopes, by uncorrelated angular and energy distributions. The production of the DICE Library of ENDF-B/VI data is described by Eaton and Dean [12]

5.5 Variance-Covariance Data

The variance-covariance data used for material cross-sections were based on the ENDF-B/V (hydrogen and oxygen) and ENDF-B/VI library (iron). The co-variances for the detector cross-sections were generated from the IRDF-90 (5) library which is based on the ENDF-B/VI compilation. In estimating uncertainties these co-variance data were folded with the sensitivities of the responses to the appropriate cross-section calculated by MCBEND in 10 energy groups above 0.028MeV .

5.6 Acceleration of the Monte Carlo Calculations

The MCBEND module MAGIC was invoked to calculate the importance map for use in accelerating the MCBEND calculation. This performs an adjoint diffusion theory calculation in an orthogonal mesh, in this case RZ, in order to provide the importances used in splitting and Russian roulette. The spatial mesh was the same as in reference 3 with 11 R intervals and 33 Z intervals. Material compositions for each mesh were automatically determined by MAGIC. The importances were calculated in 16 energy groups ranging from 14.6MeV to 0.03MeV . The source for the adjoint calculation was positioned at the outermost scoring region, with the adjoint source spectrum being specified to be identical in all energy groups in an attempt to score all responses with equal statistical accuracy.

6 MONTE CARLO RESULTS

The calculation was performed on a microVAX3 running for about 15 hours with approximately 1.15 million particles being started. The results of the calculation using the ENDF-B/VI data in conjunction with the IRDF-90 dosimetry cross-sections are shown in Table 7. The statistical errors are expressed in terms of one standard deviation (sd).

6.1 Corrections to the Calculated Reaction-Rates

In order to compare the calculated and measured results it is necessary to make the following corrections to the calculated results

- (a) To correct for the size of the Monte Carlo scoring regions compared to the size of the measurement foils.

The ratio of the fluxes on the axis to the mean fluxes over the Monte Carlo scoring regions varies slightly with energy and position, becoming flatter with lower energy.

and sharper near the source. The ratio for the NESDIP2 calculation has been determined from the axial measurements of the $S^{32}(n,p)P^{32}$ reaction in the cavity already shown in Table 5. A cosine distribution of width 140cm was fitted to the measured profile and from this the maximum to mean ratio of 1.014 for the $S^{32}(n,p)P^{32}$ reaction-rate in the scoring zone was derived with an uncertainty of 1%. This ratio is assumed to apply for all reactions at all positions.

- (b) To normalise the calculation to 1 NESTOR watt.

The fission-plate calibrations detailed in Section 3 give the fission plate power per NESTOR Watt as $8.67E-4$ Watts.

6.2 Uncertainties

In addition to the corrections described above there are other considerations which contribute to the overall uncertainty of the calculation. These are discussed below.

- (a) Uncertainty due to the correction for the size of the scoring region

A value of 1% as described in section 6.1 is adopted.

- (b) Uncertainties due to material cross-sections

There are uncertainties in the nuclear data libraries. As part of the MCBEND calculations the sensitivities of the various responses to changes in the total cross-sections of hydrogen and oxygen and in the inelastic cross-section of iron were determined in 10 energy groups ranging from 14.9 to 0.03 MeV. The calculated sensitivities were folded with co-variance matrices obtained from the ENDF-B/VI (iron inelastic) and the ENDF-B/V (hydrogen and oxygen) to produce the uncertainties which are recorded in Tables 8, 9 and 10. (Currently there are no co-variance data in ENDF-B/VI for hydrogen and oxygen).

- (c) Uncertainties due to material dimensions

- (i) Front and rear water gaps in cell 1

Spot measurements made of the front and rear water gaps in cell 1 show a maximum difference from the input water thickness of -0.16cm and +0.1cm and -0.16cm and +0.37cm respectively. Uncertainties on the calculated results based on the maximum uncertainty in cell width have been determined by extrapolating the calculated results for the input water thickness assuming an exponential attenuation for the response function. This uncertainty applies to the reaction-rates downstream of the water cells and can be seen in Tables 8, 9 and 10.

- (ii) Air gaps

The air gaps between the mild steel plates were not modelled. Section 4.6 states that the slight reduction in the measured reaction-rate with the gaps open is not statistically significant.

(d) Uncertainties due to detector cross-sections

The detector cross-sections used in the calculation were taken from the International Reactor Dosimetry File IRDF-90 (5) which also contains co-variance matrices for the cross-sections in reduced energy group schemes. An uncertainty for each calculated response for the three measured reactions was derived from the co-variance data and the contributions to each response from 27 energy groups.

(e) Uncertainties due to the representation of the fission spectrum

The calculations used MCBEND's built-in option for providing a U^{235} fission spectrum. The formula used to represent the spectrum is the Watt-Cranberg expression

$$\chi(E) = K e^{-AE} \sinh\sqrt{BE}$$

where E is the neutron energy in MeV, $\chi(E)$ is the fraction of neutrons at E per MeV, and A and B are constants which vary with nuclide. K is a normalisation constant. Uncertainties in the values of A and B lead to uncertainties in the spectrum and hence in the results. The uncertainties in the spectrum are negligible at the peak energy of about 2MeV, and increase with decreasing energy to about 4% at 0.11MeV. However, the uncertainties are more significant at higher energies, being about 7% at 10MeV.

The effect of the uncertainty in the representation of the fission spectrum has been investigated in an analysis of NESDIP2 with JEF2.2 nuclear data (11). In the cavity, the uncertainty was 4.3% for sulphur, 3.7% for indium and 3.5% for rhodium. Just inside the RPV, the uncertainty was 4.1% for sulphur, 3.3% for indium and 3.2% for rhodium. Near the fission plate the uncertainty on the rhodium result was 2.3%, at zone 36 immediately beyond the baffle the uncertainty was 2.6%. Uncertainties at other positions have been determined by linear interpolation between these values. Uncertainties inboard of the RPV have not been determined for sulphur and indium as no measurements for these two reactions were taken there.

The calculated results for the rhodium, indium, and sulphur reaction-rates, along with the corrections detailed in section 5.8 are shown in Tables 8, 9 and 10 together with the calculated uncertainties detailed above.

6.3 Comparison of Calculation with Experiment

The ratios of calculated and measured reaction-rates are shown in Table 11. In the RPV and cavity regions, the average C/M values for the sulphur, rhodium and indium reactions are 0.94, 0.94 and 0.95 respectively. Inboard of the RPV, the C/M values for rhodium along the centre-line of the system vary from 1.08 near the source to 0.89 in the water cells with a mean value of 0.92. This suggests that the absolute normalisation of the calculation is low by about 6%, the estimated uncertainty on the source strength being $\pm 3.5\%$.

All values of C/M for indium and sulphur are within one standard deviation of unity, the rhodium results being within two standard deviations throughout the system. The major components of the uncertainty on the C/M values are due to the detector cross-sections, the iron inelastic cross-section, and the fission spectrum.

In the RPV position T/4 corresponds approximately to measurement position 15, and the values of C/M at this point are within 5% of those for the cavity. At position 3T/4, corresponding to measurement position 17, the values of C/M are within 4% of those for the cavity for sulphur and indium, and 14% for rhodium. Therefore normalising calculation

measurements made in the cavity of an operating PWR allows accurate prediction of the neutron fluence at the T/4 and 3T/4 positions.

Of the 27 values of C/M given in Table 11 none differ from unity by as much as two standard deviations, whilst in 10 cases the discrepancy exceeds one standard deviation. The expected number for a normal distribution would be 9. Most of the instances of large discrepancies are for the rhodium detector where in 53% of the comparisons the differences exceed one standard deviation, compared with 20% for the other two detectors. This suggests that the uncertainty in the rhodium measurements and the detector cross-section have been underestimated and that the remaining uncertainties, including those due to the material cross-sections, are if anything overestimated. The measurements therefore support the uncertainties that have been assigned to the cross-sections for hydrogen, oxygen and iron in the ENDF-B/V and ENDF-B/VI files.

7 SUMMARY

The NESDIP programme has been briefly described, and details of the NESDIP2 experimental configuration presented. Measurements of three reaction-rates, ie $S^{32}(n,p)P^{32}$, $In^{115}(n,n')In^{115m}$ and $Rh^{103}(n,n')Rh^{103m}$, have been tabulated and compared with the results of analysis using the Monte Carlo code MCBEND with ENDF-B/VI nuclear data. MCBEND predicts the reaction rates with maximum discrepancy of 12%. Within the wall of the simulated vessel the mean value of C/M for the three detectors at four positions is 0.95. At the important T/4 and 3T/4 positions in the RPV, the C/M values are all within 5% of those at the cavity except for the rhodium at 3T/4, showing that accurate predictions of the neutron fluence at these positions could be derived from measurements in the cavity and calculated ratios. It should be noted that the outer wall of the cavity in the NESDIP2 array was a water tank thus giving well defined materials. In a practical reactor the primary shield is usually composed of concrete with additional uncertainties arising in the fluxes calculated in the cavity because of the lack of an accurate chemical analysis.

The results are consistent with the uncertainties assigned to cross-sections in the ENDF-B/V and ENDF-B/VI, and they provide validation for the application of MCBEND with its ENDF-B/VI library to the calculation of fluences in PWR vessels.

REFERENCES

- [1] Review of the NESTOR Shielding and Dosimetry Improvement Programme (NESDIP)
J Butler et al
Reactor Dosimetry: Methods, Applications and Standardisation (Farrar and Lippincott, ed.), STP 1001, ASTM, Philadelphia, PA, USA, 1989
- [2] The PCA Replica Experiment Part 1. Winfrith Measurements and Calculations.
AEEW - R 1736
- [3] NESDIP Phase 2. The ASPIS PCA Slab Geometry Benchmarks
Carter M D, Curl I J
PRPWG(SH)P(85)34
- [4] The Analysis of NESDIP2 with ENDF-B/VI Nuclear Data
Newbon S
AEA-RS-5591
- [5] The International Reactor Dosimetry File (IRDF-90)
Kocherov N P and McLaughlin P K.
IAEA-NDS-141
- [6] The International Reactor Dosimetry File (IRDF-85)
Cullen D.E. & McLaughlin P.K.
IAEA-NDS-41
- [7] CRISP - A Computer Code to Define Fission-Plate Source Profiles
Curl I J
RPD/IJC/934
- [8] ASPIS: Correction for NESTOR Core Background
Carter M D
RPD/MDC/1048
- [9] MCBEND9 User Guide
ANSWERS/MCBEND(94)15
- [10] Fission Neutron Spectra for Shielding Calculations
Story J S and Miller P C
ARPWG/P(81)12
- [11] Benchmark Testing of JEF2.2 Data for Shielding Applications
Analysis of the NESDIP2 Benchmark Experiment
G.A Wright , S.Newbon and J.M Earwicker
AEA-RS-5629
- [12] Eaton C R and Dean C J
Report on the Extension of the Monte Carlo Nuclear Data Generation Route
AEA-RS-1246

Assembly	Component	Thickness (cm)	Material	Material Reference Number ³
Trolley Face		3.2	Mild Steel with Aluminium Window of radius 56.1cm	3,8
	Void	6.0		0
	Graphite	15.0	Graphite	1
	Void	1.2		0
Fission Plate	coverplate	1.2	Aluminium	9
	void	0.1		0
	blank	0.1	Aluminium	9
	fuel	0.2	Fuel	7
	blank	0.1	Aluminium	9
	coverplate	1.2	Aluminium	9
	Void	0.4		0
Water Cell No. 1	front face	1.9	Aluminium	9
	water gap	12.1 ¹	Water	10
	thermal baffle	6.3	Stainless Steel	6
	water gap	13.2 ¹	Water	10
	rear face	2.5	Mild Steel	4
RPV	plate 1	5.1 ²	Mild Steel	5
	plate 2	5.1 ²	Mild Steel	5
	plate 3	5.1 ²	Mild Steel	5
	plate 4	5.1 ²	Mild Steel	5
	Cavity	29.4		0
Water Cell No. 2		1.9	Aluminium	9
		22.5	Water	10
		2.5	Mild Steel	5
Biological Shield		61.0	Concrete	2

- ¹ This dimension is greater than the specification due to cell bowing.
² A 0.6cm void was opened up in front of this component for activation foil measurements.
³ See Table 2.

Table 1 Dimensions and Materials in the NESDIP2 Array

Material	Material Reference No.	Density (g.cm ⁻³)	Element	Atom Fraction
Graphite	1	1.65	C	1.00
Concrete	2	2.30	Si Fe H O Al Ca Na K	0.2044 0.0043 0.169 0.5633 0.0215 0.0161 0.0119 0.0096
Mild Steel	3	7.835	Fe Mn C Si	0.9781 0.011 0.0102 0.0007
Mild Steel	4	7.862	Fe Mn C	0.9958 0.0024 0.0018
Mild Steel	5	7.85	Fe Mn C H	0.9816 0.0075 0.0106 0.0003
Stainless Steel	6	7.90	Fe C Ni Cr Ti Si Mn	0.6914 0.0011 0.0934 0.1856 0.0021 0.0121 0.0143
Fuel	7	3.256	Al U235 U238	0.9721 0.026 0.0019
Aluminium	8	2.70	Al	1.00
Aluminium	9	2.666	Al Si Fe	0.9959 0.0014 0.0027
Water	10	1.00	H O	0.6667 0.3333

Table 2 Material Compositions

		X-Coordinate (cm)																
		-49.75	-46.85	-43.32	-37.08	-33.92	-27.58	-11.75	-2.25	7.25	16.75	32.58	38.92	42.08	48.42	51.58	54.75	
Y C o o r d i n a t e c m	51.44	0	0	0	0	0	0	0	3.236E+07	3.277E+07	3.236E+07	0	0	0	0	0	0	
	47.63	0	0	0	0	0	0	3.333E+07	3.572E+07	3.642E+07	3.591E+07	3.327E+07	0	0	0	0	0	
	40.64	0	0	0	0	3.232E+07	3.693E+07	4.021E+07	4.115E+07	4.052E+07	3.711E+07	3.245E+07	0	0	0	0	0	
	35.56	0	0	0	3.356E+07	3.551E+07	3.994E+07	4.375E+07	4.484E+07	4.412E+07	4.022E+07	3.483E+07	3.205E+07	0	0	0	0	0
	31.75	0	0	3.489E+07	3.729E+07	3.983E+07	4.531E+07	4.985E+07	5.110E+07	5.022E+07	4.561E+07	3.921E+07	3.587E+07	3.231E+07	0	0	0	0
	19.69	0	3.502E+07	3.784E+07	4.079E+07	4.380E+07	5.009E+07	5.517E+07	5.651E+07	5.549E+07	5.032E+07	4.317E+07	3.941E+07	3.539E+07	3.125E+07	0	0	0
	15.88	3.440E+09	3.651E+07	3.973E+07	4.302E+07	4.632E+07	5.307E+07	5.842E+07	5.977E+07	5.861E+07	5.316E+07	4.562E+07	4.166E+07	3.741E+07	3.304E+07	3.011E+07	3.011E+07	3.011E+07
	5.29	3.482E+07	3.731E+07	4.070E+07	4.428E+07	4.779E+07	5.484E+07	6.029E+07	6.159E+07	6.035E+07	5.468E+07	4.697E+07	4.295E+07	3.866E+07	3.425E+07	3.129E+07	3.129E+07	3.129E+07
	-5.29	3.319E+07	3.553E+07	3.910E+07	4.264E+07	4.610E+07	5.296E+07	5.819E+07	5.937E+07	5.808E+07	5.255E+07	4.518E+07	4.139E+07	3.738E+07	3.331E+07	3.062E+07	3.062E+07	3.062E+07
	-15.88	0	3.335E+07	3.672E+07	4.007E+07	4.334E+07	4.982E+07	5.472E+07	5.578E+07	5.450E+07	4.926E+07	4.238E+07	3.889E+07	3.524E+07	3.159E+07	0	0	0
	-19.69	0	0	3.309E+07	3.603E+07	3.891E+07	4.465E+07	4.898E+07	4.986E+07	4.866E+07	4.393E+07	3.789E+07	3.489E+07	3.183E+07	0	0	0	0
	-31.75	0	0	0	3.157E+07	3.393E+07	3.869E+07	4.228E+07	4.296E+07	4.186E+07	3.782E+07	3.282E+07	3.043E+07	0	0	0	0	0
	-35.56	0	0	0	0	3.113E+07	3.518E+07	3.825E+07	3.880E+07	3.779E+07	3.423E+07	2.994E+07	0	0	0	0	0	0
	-40.64	0	0	0	0	0	3.071E+07	3.296E+07	3.330E+07	3.243E+07	2.963E+07	0	0	0	0	0	0	0
	-47.63	0	0	0	0	0	0	2.870E+07	2.883E+07	2.811E+07	0	0	0	0	0	0	0	0
	-51.44	0	0	0	0	0	0	0	0	0	0	0	0	0	0	0	0	0

Table 3. The Neutron Source Distribution in the NESDIP Fission Plate Located in the NESDIP2 Array (n.cm⁻³s⁻¹/Plate Watt)

Reference Location	Position	Reaction Rates (dps.atom ⁻¹ per NESTOR Watt)		
		Rh ¹⁰³ (n,n')Rh ^{103m}	In ¹¹⁵ (n,n')In ^{115m}	S ³² (n,p)P ³²
Monitor	1			9.94E-22±5.41%
Front Compartment of water Cell no.1	2	8.24E-21±4.7%		
	3	4.84E-21±4.7%		
	4	1.88E-21±4.7%		
	5	1.45E-21±4.7%		
	6	7.16E-22±4.7%		
	7	6.15E-22±4.7%		
	Rear Compartment of water Cell no.1	8	2.13E-22±4.8%	
9		1.06E-22±4.8%		
10		5.82E-23±5.0%		
11		3.86E-23±5.0%		
12		2.39E-23±5.6%		
13		1.87E-23±5.3%		
RPV	14	1.66E-23±5.1%	3.39E-24±4.3%	1.05E-24±5.8%
	15	9.16E-24±5.1%	1.66E-24±4.2%	4.05E-25±6.2%
	16	5.04E-24±5.6%	7.93E-25±4.4%	1.59E-25±5.8%
	17	2.71E-24±5.9%	3.75E-25±4.5%	6.42E-26±5.8%
Cavity	18	1.18E-24±6.2%	1.36E-25±4.6%	2.02E-26±5.8%

Table 4 Measured Reaction-Rates through the NESDIP2 Radial Shield

Distance from Nuclear Centre (cm)+	Reaction-Rate (dps.atom-1 per NESTOR Watt)	Profile (Normalised to 1.0 at Nuclear Centre)
75	3.11E-27	0.15
50	9.05E-27	0.44
25	1.76E-26	0.86
0	2.06E-26	1.00
-25	1.71E-26	0.83
-50	9.28E-27	0.45
-75	2.75E-27	0.13

* Measurements made on vertical axis intersecting the nuclear centre of the trolley and 4cm off the front wall of the cavity.

+ Nuclear Centre is 88.9cm from the floor of the trolley

Table 5 S³²(n,p) Reaction-Rate Profile in the Cavity*

Reaction	Reaction-Rate Ratio (Plates Open/Plates closed)
Rh ¹⁰³ (n,n')Rh ^{103m}	0.98±0.04
In ¹¹⁵ (n,n')In ^{115m}	0.95±0.04
S ³² (n,p)P ³²	0.98±0.03

Table 6 Comparison of Activation Measurements in the Cavity with the RPV Plates Open and Closed

Location	Measurement position ref. Number	MCBEND Zone Number	Reaction-Rates (dps.atom ⁻¹ per PlateWatt)										Flux>0.11MeV (n.cm ⁻² s ⁻¹ per Plate Watt)			
			Al ²⁷ (n,a)		Rh ¹⁰³ (n,n')		In ¹¹⁵ (n,n')		S ³² (n,p)		ASTM 800 steel			Fe ⁵⁴ (n,p)		
			ad%	ad%	ad%	ad%	ad%	ad%	ad%	ad%	ad%	ad%				
Front Water Compartment	2	30	4.50E-21	1.2	8.86E-18	2.6	1.97E-18	1.4	5.32E-19	1.0	1.069E-14	4.1	6.611E-19	1.0	1.80E+07	14.4
	3	31	3.12E-21	1.2	5.14E-18	2.4	1.20E-18	1.5	3.42E-19	1.2	6.396E-15	2.5	4.267E-19	1.0	9.85E+06	6.2
	4	32	1.45E-21	1.5	2.31E-18	11	4.80E-19	2.7	1.43E-19	1.9	2.398E-15	3.9	1.728E-19	1.5	3.53E+06	9.9
	5	33	1.20E-21	1.6	1.49E-18	4.2	3.61E-19	2.1	1.12E-19	1.5	1.809E-15	3.2	1.383E-19	1.4	2.58E+06	9.5
	6	34	6.69E-22	1.7	7.13E-19	2.8	1.79E-19	2.2	5.65E-20	1.7	8.915E-16	2.6	6.846E-20	1.5	1.32E+06	6.3
	7	35	5.44E-22	1.8	6.65E-19	7.3	1.49E-19	2.7	4.49E-20	1.8	7.788E-16	3.2	5.496E-20	1.6	1.30E+06	10.1
	8	36	1.51E-22	2.0	2.23E-19	3.5	4.56E-20	2.1	1.19E-20	1.7	2.664E-16	2.1	1.507E-20	1.6	4.75E+05	3.7
Rear Water Compartment	9	37	1.05E-22	2.1	1.11E-19	2.8	2.48E-20	2.1	7.43E-21	1.7	1.333E-16	2.1	9.355E-21	1.6	2.15E+05	3.5
	10	38	7.20E-23	2.1	5.86E-20	2.7	1.42E-20	2.3	4.59E-21	1.9	7.278E-17	2.2	5.860E-21	1.7	1.10E+05	4.1
	11	39	5.44E-23	2.1	3.86E-20	2.3	9.55E-21	2.0	3.29E-21	1.8	4.780E-17	1.9	4.113E-21	1.6	6.72E+04	3.0
	12	40	3.84E-23	2.1	2.42E-20	2.3	5.98E-21	2.0	2.14E-21	1.8	3.074E-17	2.0	2.796E-21	1.8	4.21E+04	3.5
	13	41	2.78E-23	2.2	1.94E-20	1.9	4.59E-21	1.9	1.54E-21	1.9	2.455E-17	1.9	1.960E-21	1.7	3.72E+04	2.3
	14	42	1.83E-23	2.4	1.66E-20	1.7	3.57E-21	1.8	1.06E-21	1.9	2.075E-17	1.7	1.361E-21	1.8	3.63E+04	2.0
RPV	15	43	7.71E-24	2.8	9.78E-21	1.6	1.80E-21	1.7	4.42E-22	2.0	1.214E-17	1.6	5.573E-22	1.7	2.66E+04	1.7
	16	44	3.27E-24	3.3	5.71E-21	1.5	8.84E-22	1.7	1.78E-22	2.2	7.096E-18	1.4	2.179E-22	1.7	1.83E+04	1.5
	17	45	1.31E-24	3.7	3.13E-21	1.4	4.11E-22	1.6	6.74E-23	2.4	4.019E-18	1.4	8.633E-23	1.7	1.18E+04	1.5
Cavity	18	46	4.83E-25	4.0	1.18E-21	1.2	1.39E-22	1.4	2.19E-23	2.5	1.556E-18	1.4	2.800E-23	1.4	4.92E+03	1.6
	-	47	3.71E-25	3.9	8.36E-22	1.2	9.96E-23	1.3	1.66E-23	2.5	1.129E-18	1.3	2.092E-23	1.3	3.57E+03	1.4

Table 7 Calculated Responses with ENDF-B/VI Data

Location	Measurement position ref number	MCBEND Zone Number	MCBEND calculated reaction-rates/ NESTOR Watt		scoring region size %	Uncertainties						Total uncertainty %
			sd %	%		material cross sections			material dimensions	detector	fission spectrum	
						iron inelastic %	oxygen total %	hydrogen total %	water gaps %	cross sections %	cross sections %	
Front Water Compartment	2	30	7.79E-21	2.6	1.0	0.00	0.1	0.1	0.0	3.5	2.3	5.0
	3	31	4.52E-21	2.4	1.0	0.00	0.1	0.4	0.0	3.5	2.3	4.9
	4	32	2.03E-21	10.9	1.0	0.00	0.2	0.8	0.0	4.1	2.4	12.0
	5	33	1.31E-21	4.2	1.0	0.01	0.2	0.9	0.0	3.6	2.4	6.2
	6	34	6.27E-22	2.8	1.0	0.05	0.4	1.4	0.0	3.4	2.5	5.4
	7	35	5.85E-22	7.3	1.0	0.12	0.5	1.4	0.0	4.0	2.5	8.9
	Rear Water Compartment	8	36	1.96E-22	3.5	1.0	0.70	0.5	1.5	0.5	3.9	2.6
9		37	9.76E-23	2.8	1.0	0.92	0.5	1.8	0.5	3.6	2.7	5.8
10		38	5.15E-23	2.7	1.0	1.07	0.6	2.1	0.5	3.3	2.8	5.8
11		39	3.39E-23	2.3	1.0	1.12	0.7	2.3	0.5	3.4	2.9	5.8
12		40	2.13E-23	2.3	1.0	1.22	0.9	2.6	0.5	3.4	3.0	6.0
13		41	1.71E-23	1.9	1.0	1.33	1.0	2.7	0.5	3.4	3.1	6.0
RPV	14	42	1.46E-23	1.7	1.0	1.69	1.0	2.7	2.2	3.6	3.2	6.6
	15	43	8.60E-24	1.6	1.0	2.38	1.0	2.7	2.2	4.0	3.3	7.0
	16	44	5.02E-24	1.5	1.0	2.86	1.0	2.7	2.2	4.4	3.3	7.4
	17	45	2.75E-24	1.4	1.0	3.11	1.1	2.7	2.2	4.9	3.4	7.8
Cavity	18	46	1.04E-24	1.2	1.0	3.28	1.1	2.7	2.2	5.2	3.5	8.1
	-	47	7.35E-25	1.2	1.0	4.30	1.0	2.7	2.2	5.2	3.5	8.6

Table 8 Calculated Reaction-Rates and Uncertainties for Rh¹⁰³(n,n')Rh^{103m}

Location	Measurement position ref number	MCBEND Zone Number	MCBEND calculated reaction-rates/ NESTOR Watt		scoring region size %	Uncertainties					Total uncertainty %	
			sd %	%		material cross sections			material dimensions water gaps %	detector cross sections %		fission spectrum %
						iron inelastic %	oxygen total %	hydrogen total %				
Front Water Compartment	2	30	1.73E-21	1.4	1.0	0.0	0.1	0.1	0.0	2.2		2.8
	3	31	1.05E-21	1.5	1.0	0.0	0.1	0.4	0.0	2.2		3.0
	4	32	4.22E-22	2.7	1.0	0.0	0.2	0.9	0.0	2.2		3.7
	5	33	3.17E-22	2.1	1.0	0.0	0.2	1.0	0.0	2.2		3.2
	6	34	1.57E-22	2.2	1.0	0.2	0.4	1.4	0.0	2.2		3.6
	7	35	1.31E-22	2.7	1.0	0.2	0.5	1.5	0.0	2.2		3.7
	Rear Water Compartment	8	36	4.01E-23	2.1	1.0	1.1	0.4	1.5	0.6	2.2	
9		37	2.18E-23	2.1	1.0	1.2	0.5	1.8	0.6	2.2		3.8
10		38	1.25E-23	2.3	1.0	0.9	0.6	2.1	0.6	2.2		4.0
11		39	8.40E-24	2.0	1.0	1.3	0.7	2.3	0.6	2.2		4.2
12		40	5.26E-24	2.0	1.0	1.4	0.9	2.6	0.6	2.2		4.4
13		41	4.04E-24	1.9	1.0	1.5	1.0	2.8	0.6	2.2		4.6
RPV	14	42	3.14E-24	1.8	1.0	2.1	1.0	2.7	2.6	2.2	3.3	6.3
	15	43	1.58E-24	1.7	1.0	3.3	1.0	2.7	2.6	2.2	3.4	6.8
	16	44	7.77E-25	1.7	1.0	4.2	1.0	2.7	2.6	2.2	3.5	7.3
	17	45	3.61E-25	1.6	1.0	5.0	1.0	2.6	2.6	2.2	3.6	7.8
Cavity	18	46	1.22E-25	1.4	1.0	5.5	1.0	2.6	2.6	2.2	3.7	8.3
	-	47	8.76E-26	1.3	1.0	5.5	1.0	2.7	2.6	2.2	3.7	8.3

Table 9 Calculated Reaction-Rates and Uncertainties for In¹¹⁵(n,n')In^{115m}

Location	Measurement position ref number	MCBEND Zone Number	MCBEND calculated reaction-rates/ NESTOR Watt		scoring region size %	Uncertainties						Total uncertainty %
			sd %	%		material cross sections			material dimensions	detector	fission spectrum	
						iron inelastic	oxygen total	hydrogen total	water gaps	cross sections		
Front Water Compartment	2	30	4.68E-22	1.0	1.0	0.0	0.1	0.1	0.0	3.7		4.0
	3	31	3.01E-22	1.2	1.0	0.0	0.0	0.4	0.0	3.7		4.1
	4	32	1.26E-22	1.9	1.0	0.0	0.2	0.8	0.0	3.7		4.2
	5	33	9.85E-23	1.5	1.0	0.0	0.3	0.9	0.0	3.7		4.3
	6	34	4.97E-23	1.7	1.0	0.1	0.5	1.3	0.0	3.7		4.4
	7	35	3.95E-23	1.8	1.0	0.1	0.6	1.4	0.0	3.7		4.5
	Rear Water Compartment	8	36	1.05E-23	1.7	1.0	1.7	0.5	1.3	0.8	3.7	
9		37	6.53E-24	1.7	1.0	1.7	0.6	1.6	0.8	3.7		5.0
10		38	4.04E-24	1.9	1.0	1.8	0.7	1.9	0.8	3.7		5.2
11		39	2.89E-24	1.8	1.0	1.8	0.8	2.0	0.8	3.7		5.2
12		40	1.88E-24	1.8	1.0	1.8	1.0	2.3	0.8	3.7		5.4
13		41	1.35E-24	1.9	1.0	1.9	1.1	2.4	0.8	3.7		5.5
RPV	14	42	9.32E-25	1.9	1.0	3.0	1.1	2.4	3.2	3.7	4.1	7.9
	15	43	3.89E-25	2.0	1.0	4.8	1.2	2.3	3.2	3.7	4.1	8.8
	16	44	1.56E-25	2.2	1.0	6.7	1.2	2.3	3.2	3.7	4.2	10.0
	17	45	5.93E-26	2.4	1.0	8.1	1.1	2.2	3.2	3.7	4.2	11.1
Cavity	18	46	1.93E-26	2.5	1.0	9.8	1.1	2.2	3.2	3.7	4.3	12.6
	-	47	1.46E-26	2.5	1.0	9.8	1.1	2.3	3.2	3.7	4.3	12.6

Table 10 Calculated and Measured Reaction-Rates and Uncertainties for S32(n,p)P32

Location	Measurement position ref number	MCBEND Zone Number	$Rh^{103}(n,n')Rh^{103m}$	$In^{115}(n,n')In^{115m}$	$S^{32}(n,p)P^{32}$
			C/M	C/M	C/M
Front Water Compartment	2	30	0.94 ±0.07		
	3	31	0.93 ±0.07		
	4	32	1.08 ±0.13		
	5	33	0.90 ±0.08		
	6	34	0.88 ±0.07		
Rear Water Compartment	7	35	0.95 ±0.10		
	8	36	0.92 ±0.08		
	9	37	0.91 ±0.08		
	10	38	0.89 ±0.08		
	11	39	0.88 ±0.08		
RPV	12	40	0.89 ±0.08		
	13	41	0.91 ±0.08		
	14	42	0.88 ±0.08	0.93 ±0.08	0.89 ±0.10
	15	43	0.94 ±0.09	0.95 ±0.08	0.96 ±0.11
Cavity	16	44	0.99 ±0.09	0.99 ±0.09	0.99 ±0.12
	17	45	1.02 ±0.10	0.96 ±0.09	0.92 ±0.13
	18	46	0.88 ±0.10	0.90 ±0.10	0.96 ±0.14

Table 11. Ratio of Calculated and Measured Reaction-Rates

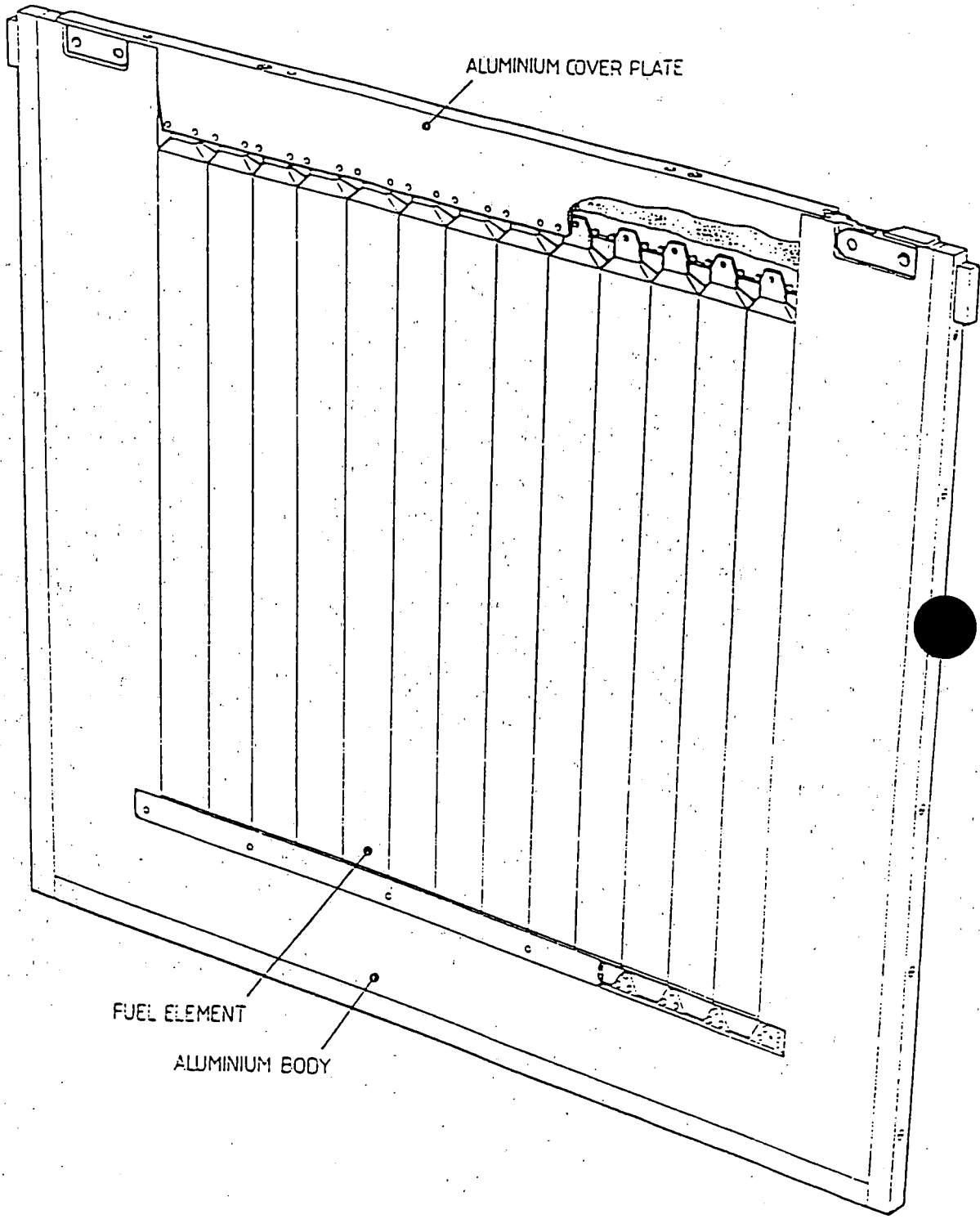


Fig 2 NESDIP2 Enriched U/Al Alloy Fission Plate

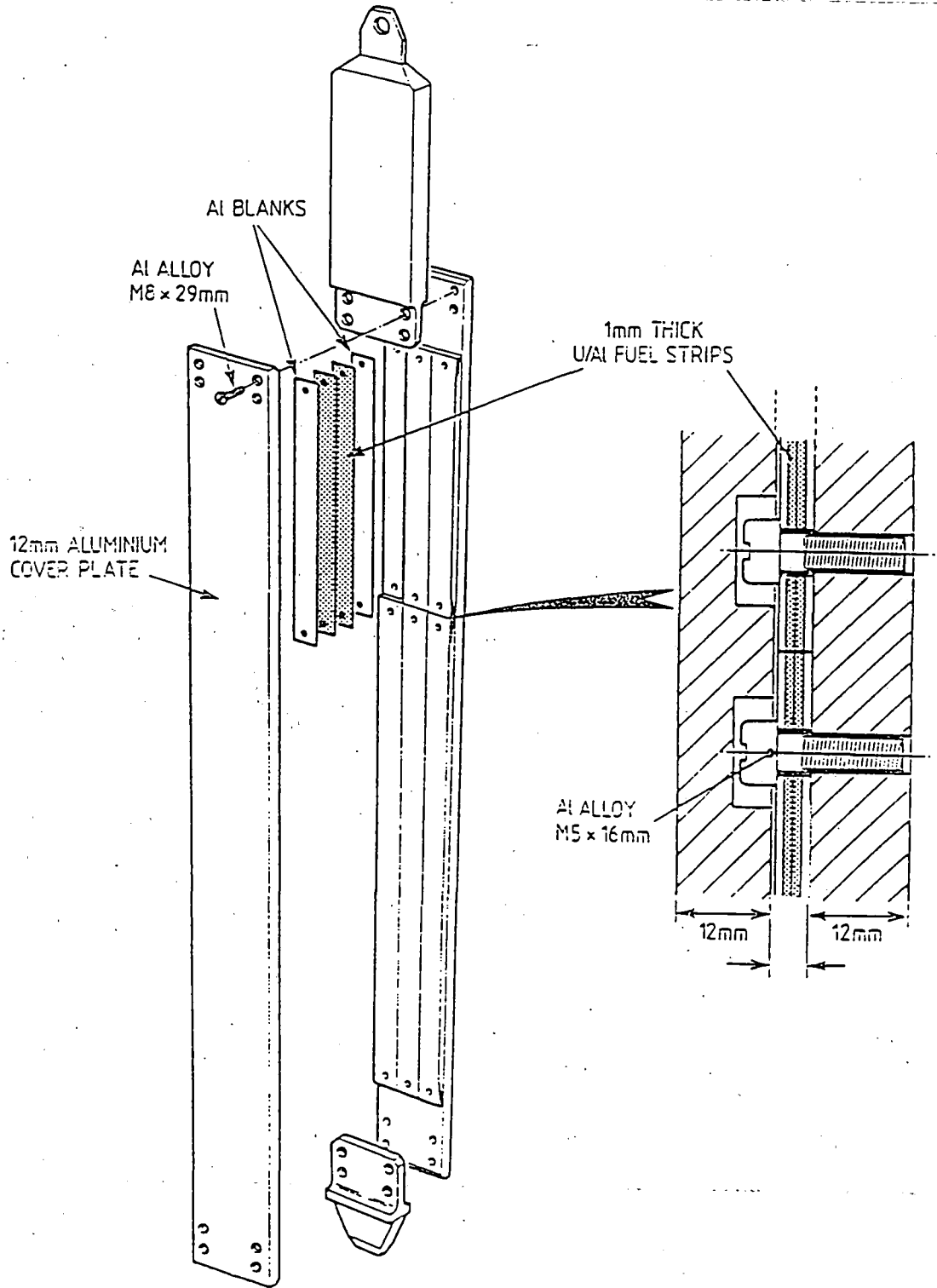


Fig 3 ASPIS U/AI Alloy Fuel Element

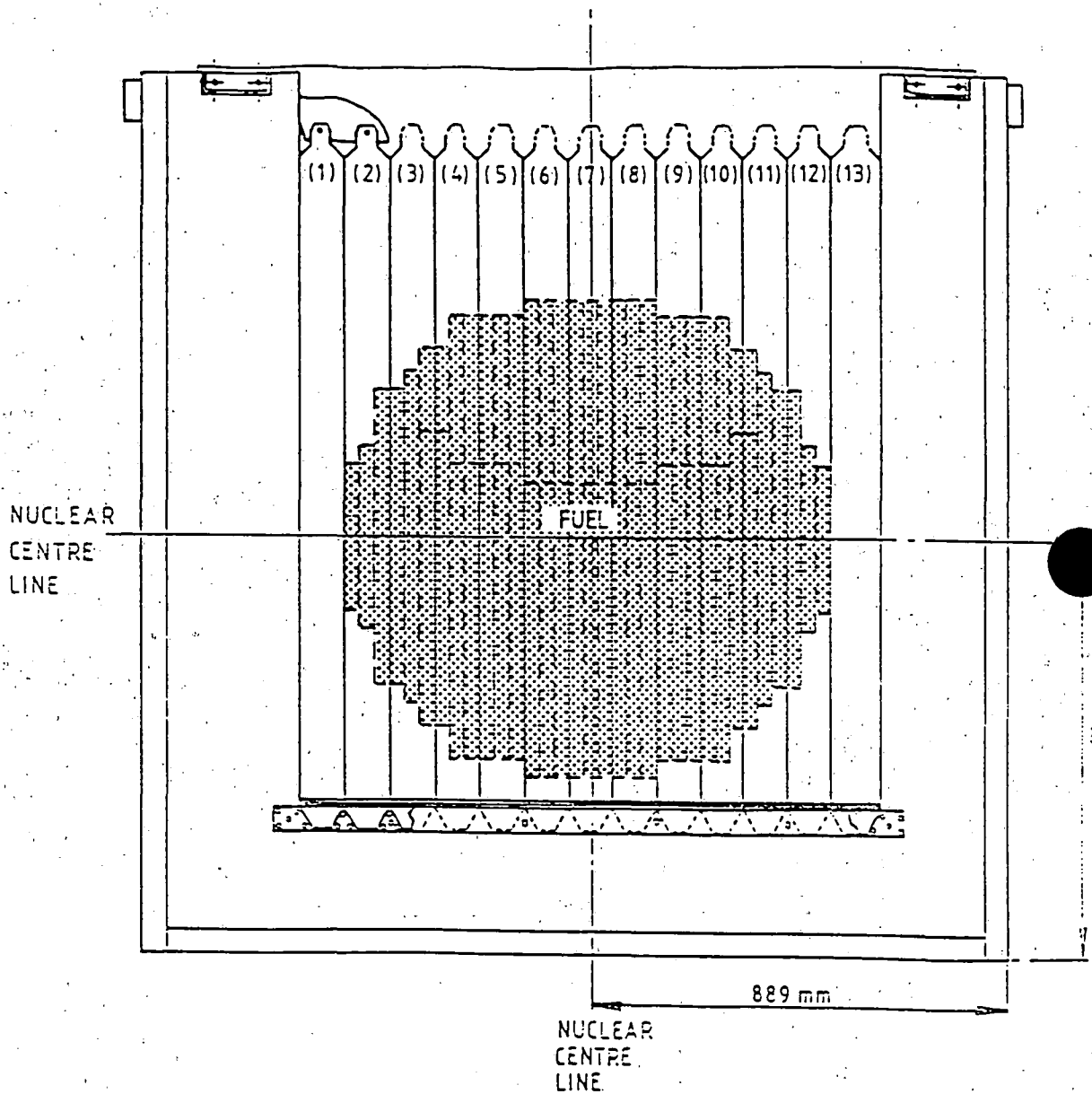


Fig 4 Detail of Fuel Loading Pattern

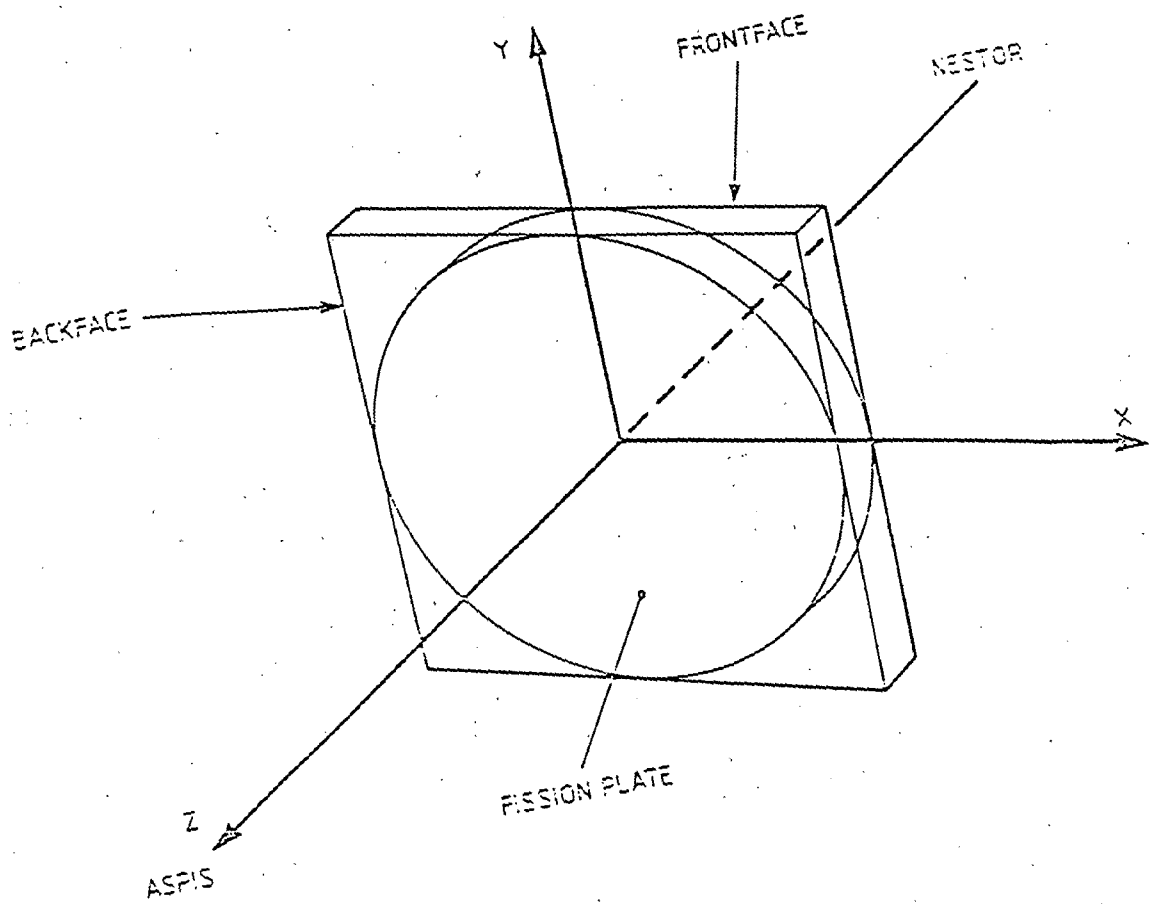


Fig 5 Co-ordinate System

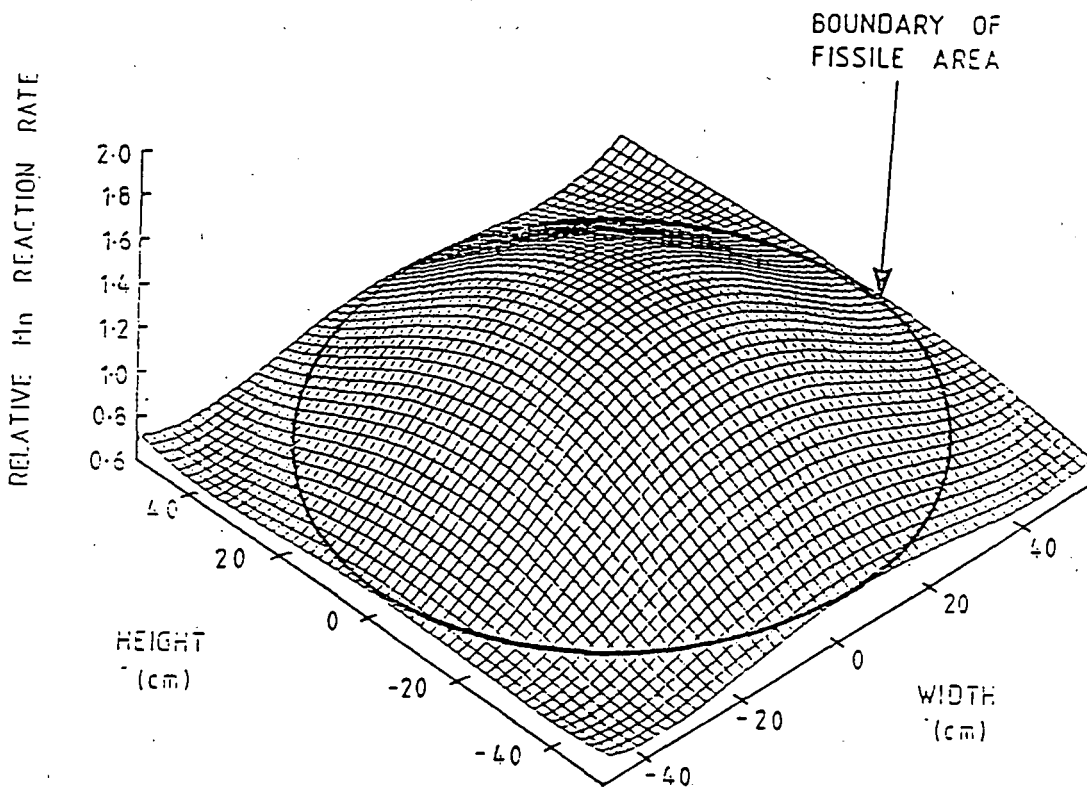


Fig 7 NESDIP2 Fission Plate Source Profile

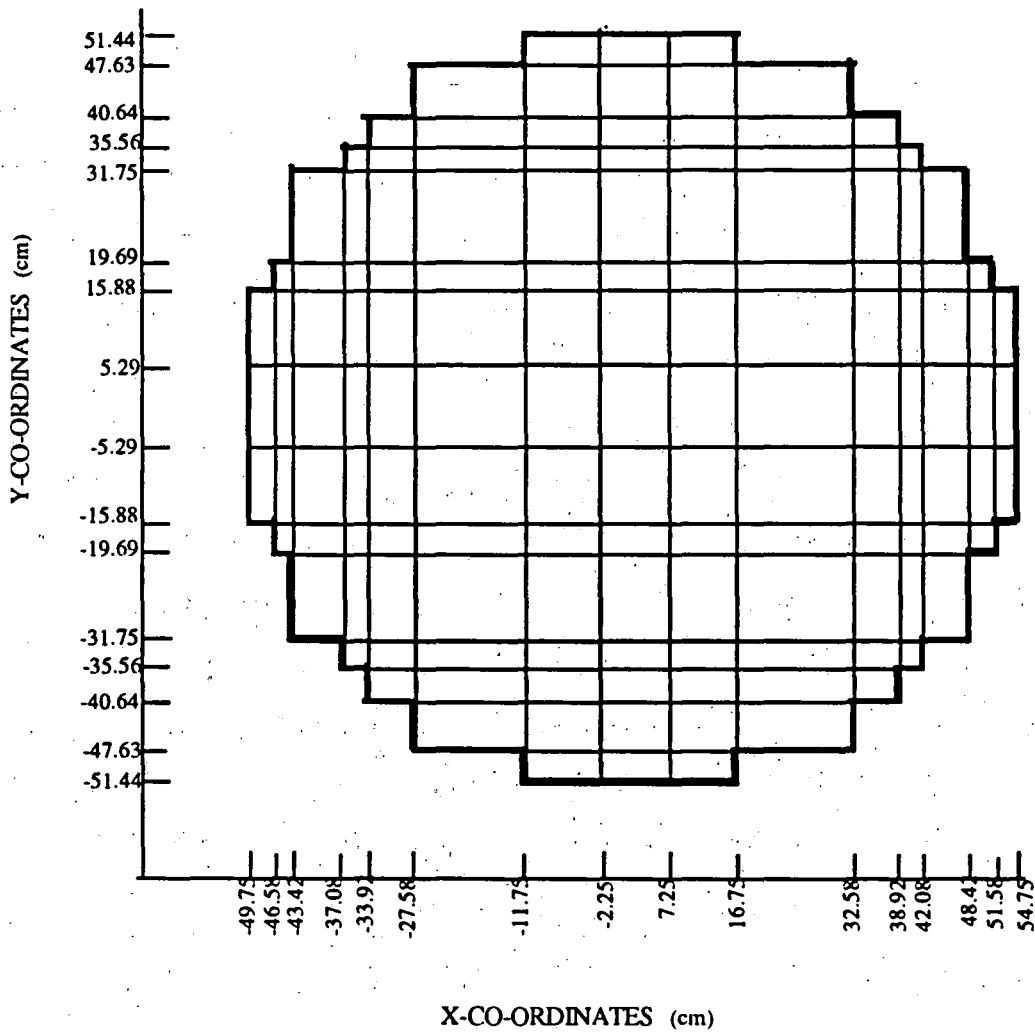
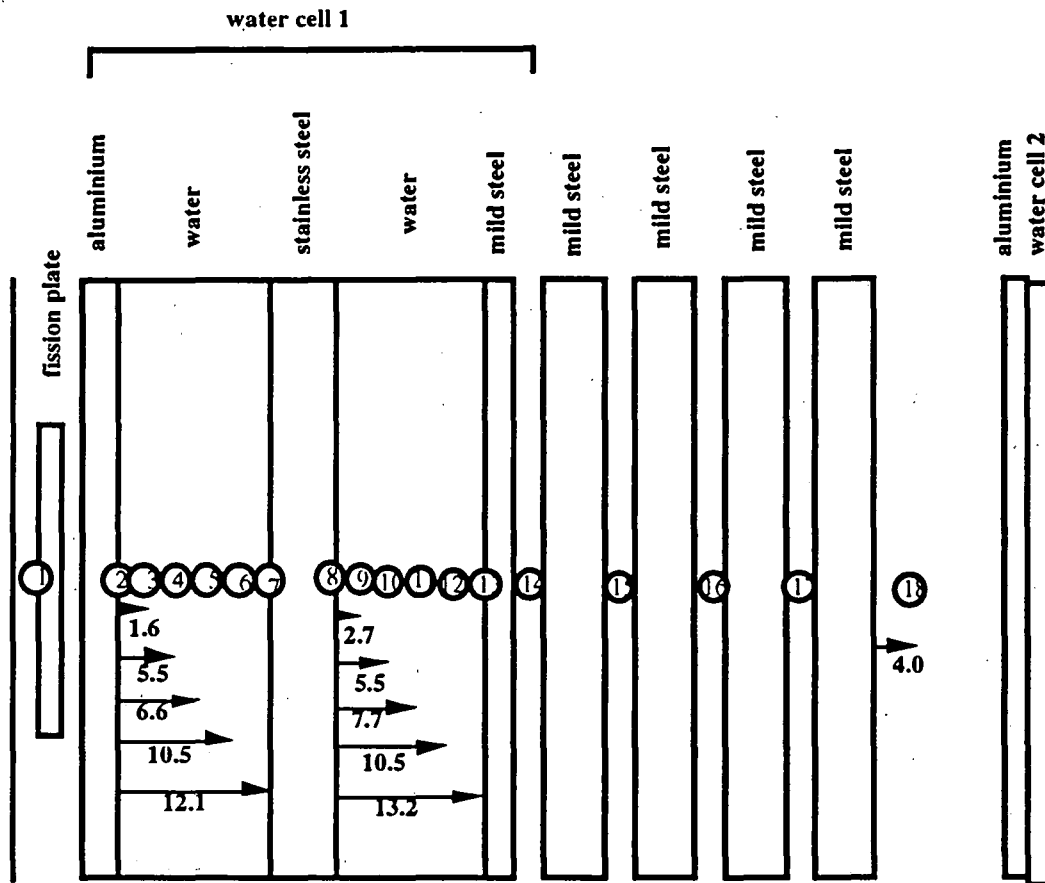


Fig 8 Source Mesh Boundaries



Ⓝ position reference number

All measurement positions are on an axis that extends through the centre of the fission plate

dimensions in cm

Fig 9 Measurement Locations in the NESDIP2 Array

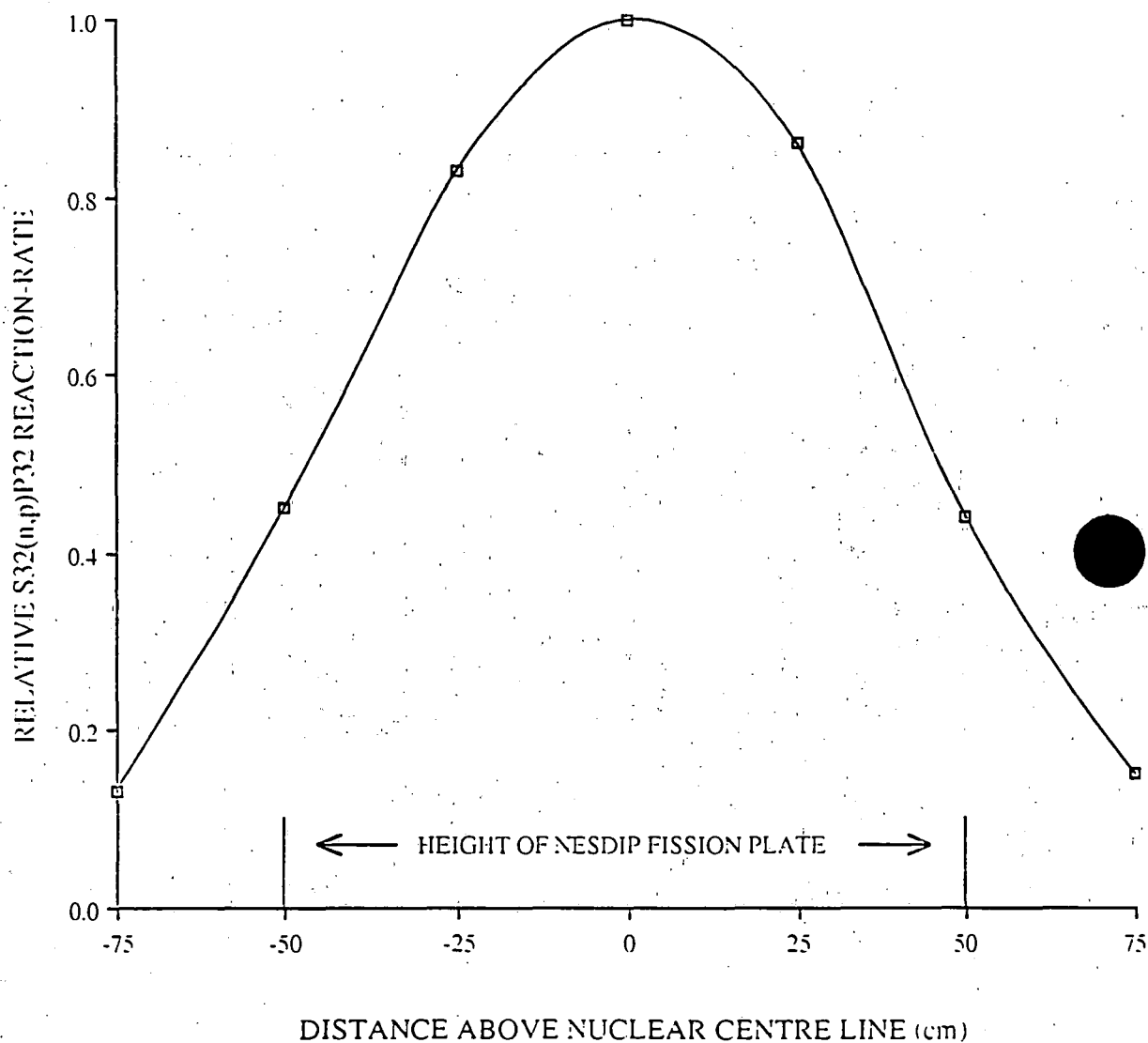
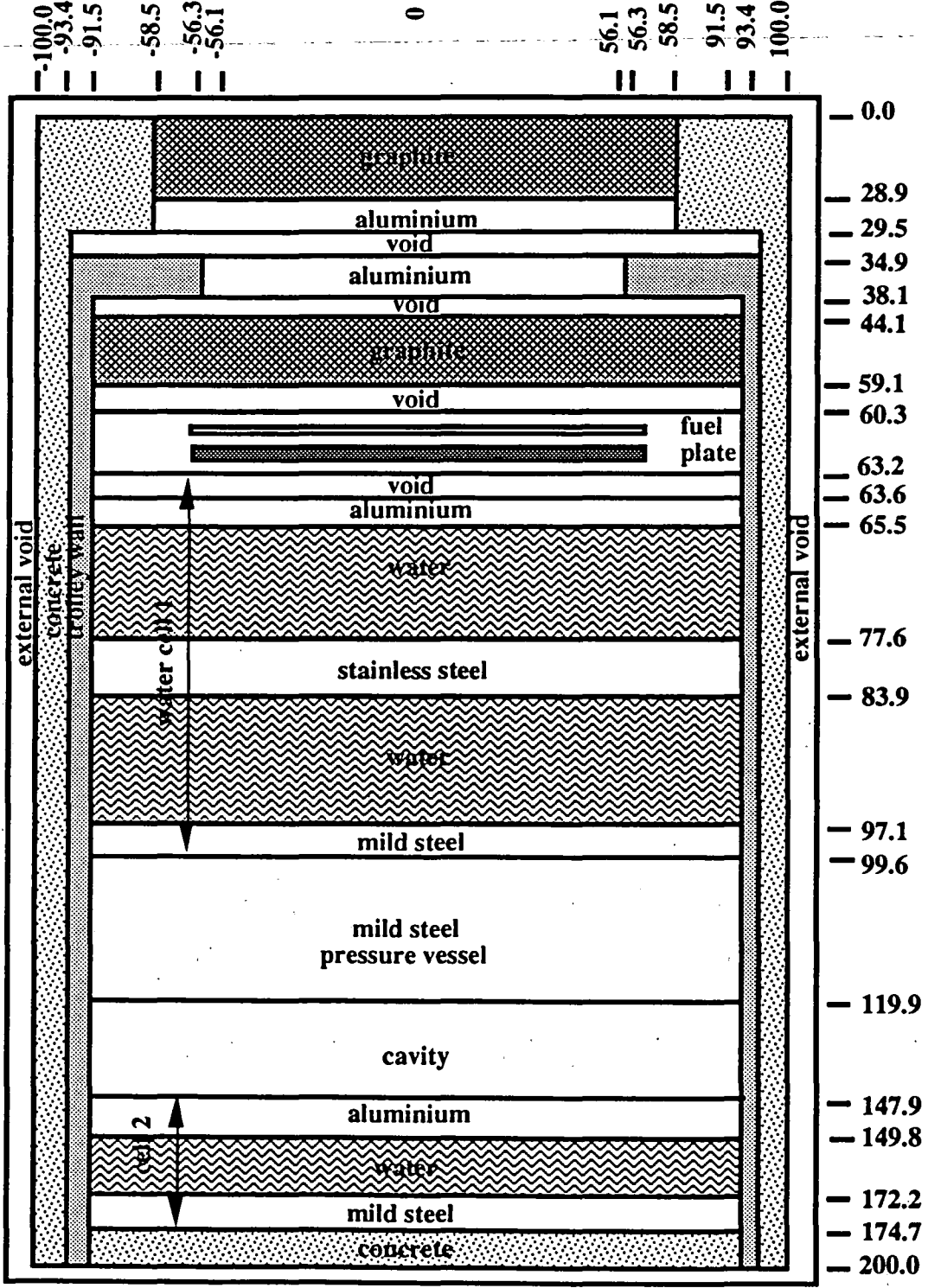


Fig 10

Relative $S^{32}(n,p)P^{32}$ Reaction-Rate Axial Profile in the Cavity of the NESDIP2 Array



all dimensions in cm - not to scale

Fig 11 MCBEND Model of the NESDIP2 Array

APPENDIX

A
 & *****
 & NESDIP BENCHMARK EXPERIMENT
 & MCBEND ANALYSIS
 & *****
 & ENDF/B-VI and IRDF-90 DATA
 &

CARD COLUMN LIMIT 1 80
 BEGIN CONTROL DATA
 PROCESS TO STAGE THREE
 DUMP INTERVALS 5
 SPLITTING

END
 & UNIT 2
 BEGIN DATASET DEFINITIONS
 DUMP A 40

END
 & UNIT 3
 BEGIN OUTPUT CONTROL
 SUPPRESS INFLOWS

END
 & UNIT 4
 BEGIN MATERIAL GEOMETRY
 CG

RPP1	-150.0	150.0	-150.0	155.0	-10.0	210.0
RPP2	-155.0	155.0	-155.0	160.0	-15.0	0.0
RPP3	-155.0	155.0	-155.0	160.0	-15.0	28.90
RPP4	-155.0	155.0	-155.0	160.0	-15.0	29.50
RPP5	-155.0	155.0	-155.0	160.0	-15.0	34.90
RPP6	-155.0	155.0	-155.0	160.0	-15.0	38.10
RPP7	-155.0	155.0	-155.0	160.0	-15.0	44.10
RPP8	-155.0	155.0	-155.0	160.0	-15.0	59.10
RPP9	-155.0	155.0	-155.0	160.0	-15.0	60.30
RPP10	-155.0	155.0	-155.0	160.0	-15.0	63.20
RPP11	-155.0	155.0	-155.0	160.0	-15.0	63.60
RPP12	-155.0	155.0	-155.0	160.0	-15.0	65.50
RPP13	-155.0	155.0	-155.0	160.0	-15.0	77.60
RPP14	-155.0	155.0	-155.0	160.0	-15.0	83.90
RPP15	-155.0	155.0	-155.0	160.0	-15.0	97.10
RPP16	-155.0	155.0	-155.0	160.0	-15.0	99.60
RPP17	-155.0	155.0	-155.0	160.0	-15.0	119.90
RPP18	-155.0	155.0	-155.0	160.0	-15.0	147.90
RPP19	-155.0	155.0	-155.0	160.0	-15.0	149.80
RPP20	-155.0	155.0	-155.0	160.0	-15.0	172.20
RPP21	-155.0	155.0	-155.0	160.0	-15.0	174.70
RPP22	-155.0	155.0	-155.0	160.0	-15.0	200.00
RCC23	0.0	0.0	-15.0	0.0	0.0	230.00
RPP24	-58.50	58.50	-58.50	58.50	-15.0	215.00
RPP25	-91.50	91.50	-88.90	96.50	-15.0	215.00
RPP26	-93.40	93.40	-92.70	98.60	-15.0	215.00
RPP27	-100.00	100.00	-100.00	110.00	-15.0	215.00

56.10

RPP28	-59.20	64.20	-51.40	51.40	61.50	61.60	
RCC29	2.50	0.00	61.70	0.0	0.0	0.20	56.30
RPP30	-7.50	12.50	-10.00	10.00	65.00	65.70	
RPP31	-7.50	12.50	-10.00	10.00	67.00	67.20	
RPP32	-7.50	12.50	-10.00	10.00	70.90	71.10	
RPP33	-7.50	12.50	-10.00	10.00	72.00	72.20	
RPP34	-7.50	12.50	-10.00	10.00	75.90	76.10	
RPP35	-7.50	12.50	-10.00	10.00	77.40	78.00	
RPP36	-7.50	12.50	-10.00	10.00	83.40	84.10	
RPP37	-7.50	12.50	-10.00	10.00	86.50	86.70	
RPP38	-7.50	12.50	-10.00	10.00	89.30	89.50	
RPP39	-7.50	12.50	-10.00	10.00	91.50	91.70	
RPP40	-7.50	12.50	-10.00	10.00	94.30	94.50	
RPP41	-7.50	12.50	-10.00	10.00	96.90	97.40	
RPP42	-7.50	12.50	-10.00	10.00	98.40	99.80	
RPP43	-7.50	12.50	-10.00	10.00	104.60	104.80	
RPP44	-7.50	12.50	-10.00	10.00	109.70	109.90	
RPP45	-7.50	12.50	-10.00	10.00	114.70	114.90	
RPP46	-7.50	12.50	-10.00	10.00	123.80	124.00	
RPP47	-7.50	12.50	-10.00	10.00	143.80	144.00	

ZONES

& EXTERNAL VOID

1 20 +1 +22 -2 -27

2 20 +1 +2

3 20 +1 -22

& CONCRETE TROLLEY SHIELD

4 20 +27 -26 +22 -4

5 20 +4 -2 +27 -24

6 20 +22 -21 +25

& GRAPHITE BLOCK OUTSIDE OF THE TROLLEY

7 10 +3 -2 +24

& ALUMINIUM PLATE ON BODY 7

8 10 +4 -3 +24

& VOID BEFORE TROLLEY

9 10 +5 -4 +26

& MILD STEEL TROLLEY WALLS

10 40 +22 -6 +26 -25

11 40 +6 -5 +26 -23

& ALUMINIUM TROLLEY WINDOW

12 10 +6 -5 +23

& VOID AT FRONT OF TROLLEY

13 10 +7 -6 +25

& GRAPHITE BLOCK INSIDE OF TROLLEY

14 10 +8 -7 +25

& VOID CORE SIDE OF FISSION PLATE

15 20 +9 -8 +25

& ALUMINIUM FISSION PLATE SURROUND

16 20 +10 -9 +25 -28 -29

& VOID IN THE FISSION PLATE

17 10 +28

& FISSION PLATE

18 10 +29

& VOID SHIELD SIDE OF THE FISSION PLATE

19 10 +11 -10 +25

& CELL 1 1.9cm ALUMINIUM PLATE

20 10 +12 -11 +25
 & CELL 1 12.1cm WATER
 21 10 +13 -12 +25 -30 -31 -32 -33 -34 -35
 &CELL 1 5.9 CM STAINLESS STEEL (THERMAL SHIELD)
 22 10 +14 -13 +25
 & CELL 1 13.2cm WATER
 23 10 +15 -14 +25 -36 -37 -38 -39 -40 -41
 &CELL 1 2.5cm MILD STEEL
 24 10 +16 -15 +25
 & 4*5.1 cm MILD STEEL BLOCKS (RPV WALL)
 25 30 +17 -16 +25 -42 -43 -44 -45
 &CAVITY
 26 10 +18 -17 +25 -46 -47
 & CELL 2 1.9 cm ALUMINIUM
 27 10 +19 -18 +25
 & CELL 2 22.4 cm WATER
 28 10 +20 -19 +25
 & CELL 2 2.5 cm MILD STEEL
 29 10 +21 -20 +25
 & 30 -47 ARE 20 cm SQUARE SCORING REGIONS
 30 10 +30 -12
 31 10 +31
 32 10 +32
 33 10 +33
 34 10 +34
 35 10 +35 +13
 36 10 +36 -14
 37 10 +37
 38 10 +38
 39 10 +39
 40 10 +40
 41 10 +41 +15
 42 10 +42 -16
 43 10 +43
 44 10 +44
 45 10 +45
 46 10 +46
 47 10 +47

REGIONS

1	2	3	4	5
6	7	8	9	10
11	12	13	14	15
16	17	18	19	20
21	22	23	24	25
26	27	28	29	30
31	32	33	34	35
36	37	38	39	40
41	42	43	44	45
46	47			

MATERIALS

-2000	-2000	-2000	2	2
2	1	8	0	3
3	8	0	1	0
9	0	7	0	9
10	6	10	4	5

0	9	10	4	10
10	10	10	10	10
10	10	10	10	10
10	5	5	5	5
0	0			

VOLUMES

1.0	1.0	1.0	1.0	1.0
1.0	1.0	1.0	1.0	1.0
1.0	1.0	1.0	1.0	1.0
1.0	1.0	1.0	1.0	1.0
1.0	1.0	1.0	1.0	1.0
1.0	1.0	1.0	1.0	80.0
80.0	80.0	80.0	80.0	80.0
80.0	80.0	80.0	80.0	80.0
80.0	80.0	80.0	80.0	80.0
80.0	80.0			

END
 & UNIT 5
 BEGIN SPLITTING GEOMETRY
 & RADIAL SPLITTING BOUNDARIES

R 11
 0.0 5.0 12.5 20.0 30.0 40.0 50.0 60.0 80.0 100.0 120.0 149.0
 Z 33
 -10.0 -2.0 10.0 20.0 29.5 34.9 38.1 44.1 49.1 54.1
 59.1 63.6 65.5 71.6 77.6 83.5 90.1 96.7 99.2 104.3
 109.4 114.4 119.5 128.8 138.2 143.3 143.7 147.5 149.4 156.9 164.7
 171.8
 174.3 205.0

END
 & UNIT 7
 BEGIN ENERGY DATA
 NEUTRON
 SPLITTING
 GROUPS 16
 1.46E+1 1.35E+1 1.25E+1 1.12E+1 1.00E+1
 8.50 7.00 6.07 4.72 3.68 2.87
 1.74 6.39E-1 3.88E-1 1.11E-1 6.74E-2 2.48E-2
 SCORING AS SPLITTING
 THERMAL TREATMENT NONE
 COMPLEX SOURCE

END
 & UNIT 8
 BEGIN IMPORTANCE MAP
 DIMENSIONS 11 1 33 16 1
 CALCULATE TARGETS 1
 ZONES 47 STRENGTHS 1.0
 USE METHOD D
 DOMINANT MATERIAL
 NO PRINT
 END

& UNIT 9
 BEGIN SCORING DATA
 MESH SYSTEM CG
 DIMENSIONS 47 1 1

MATERIAL MESH
TRACK LENGTH
FLUX

SOME 1
30 31 32 33 34
35 36 37 38 39
40 41 42 43 44
45 46 47

RESPONSES
DITTO
SENSITIVITY OF RESPONSES DITTO
CONTRIBUTIONS TO RESPONSES DITTO
END

& UNIT 10
BEGIN RESPONSE DATA
& RESPONSE FUNCTIONS FROM IRDF90
& rh103(N,N') irdf90

END
& UNIT 11
BEGIN SENSITIVITY DATA
7
&FE
2631 0 2 1 2 -1 2
&NI
2825 0 2 1 2 -1 2
&CR
2431 0 2 1 2 -1 2
& H
125 0 3 TOTAL 1 2 -1 2
&O
825 0 4 TOTAL 1 2 -1 2 1 107
&AL
1325 0 2 1 2 -1 2
&C
600 0 2 1 2 -1 2
& NO OF ENERGY GROUPS BOUNDARIES

16
1.492E+1 4.400E+0 2.600E+0 1.350E+0 7.080E-1 5.800E-1 4.100E-1
3.095E-1 2.620E-1 6.200E-2 3.000E-2 1.500E-2 1.585E-3 2.145E-4
1.068E-5 5.043E-6 5.500E-7
END

& UNIT 23
BEGIN CG SOURCE DATA
BOX -49.75 -51.44 61.70 104.5 0.0 0.0 0.0 102.88 0.0 0.0 0.0 0.2
1.0 1 1

VOLUME SOURCE
SUBDIVIDE
15 0.0303 0.0303 0.0606 0.0303 0.0606 0.1515 0.0909 0.0910
0.0909 0.1515 0.0606 0.0303 0.0606 0.0303 0.0303
15 0.03703 0.06794 0.04938 0.03703 0.11722 0.03703 0.10294 0.10286
0.10294 0.03703 0.11722 0.03703 0.04938 0.06794 0.03703
1 1.0

IMPORTANCES
0. 0. 0. 0. 0. 0. 1. 1. 1. 0. 0. 0. 0. 0. 0.

0. 0. 0. 0. 0. 1. 1. 1. 1. 1. 0. 0. 0. 0. 0.
 0. 0. 0. 0. 1. 1. 1. 1. 1. 1. 1. 0. 0. 0. 0.
 0. 0. 0. 1. 1. 1. 1. 1. 1. 1. 1. 1. 0. 0. 0.
 0. 0. 1. 1. 1. 1. 1. 1. 1. 1. 1. 1. 1. 0. 0.
 0. 1. 1. 1. 1. 1. 1. 1. 1. 1. 1. 1. 1. 1. 0.
 1. 1. 1. 1. 1. 1. 1. 1. 1. 1. 1. 1. 1. 1. 1.
 1. 1. 1. 1. 1. 1. 1. 1. 1. 1. 1. 1. 1. 1. 1.
 1. 1. 1. 1. 1. 1. 1. 1. 1. 1. 1. 1. 1. 1. 1.
 0. 1. 1. 1. 1. 1. 1. 1. 1. 1. 1. 1. 1. 1. 0.
 0. 0. 1. 1. 1. 1. 1. 1. 1. 1. 1. 1. 1. 0. 0.
 0. 0. 0. 1. 1. 1. 1. 1. 1. 1. 1. 1. 0. 0. 0.
 0. 0. 0. 0. 1. 1. 1. 1. 1. 1. 1. 0. 0. 0. 0.
 0. 0. 0. 0. 0. 1. 1. 1. 1. 1. 1. 0. 0. 0. 0.
 0. 0. 0. 0. 0. 0. 1. 1. 1. 1. 0. 0. 0. 0. 0.

SOURCES

1 1 2 1 3 1 4 1 5 1 6 1 7 1 8 1 9 1 10 1
 11 1 12 1 13 1 14 1 15 1 16 1 17 1 18 1 19 1 20 1
 21 1 22 1 23 1 24 1 25 1 26 1 27 1 28 1 29 1 30 1
 31 1 32 1 33 1 34 1 35 1 36 1 37 1 38 1 39 1 40 1
 41 1 42 1 43 1 44 1 45 1 46 1 47 1 48 1 49 1 50 1
 51 1 52 1 53 1 54 1 55 1 56 1 57 1 58 1 59 1 60 1
 61 1 62 1 63 1 64 1 65 1 66 1 67 1 68 1 69 1 70 1
 71 1 72 1 73 1 74 1 75 1 76 1 77 1 78 1 79 1 80 1
 81 1 82 1 83 1 84 1 85 1 86 1 87 1 88 1 89 1 90 1
 91 1 92 1 93 1 94 1 95 1 96 1 97 1 98 1 99 1 100 1
 101 1 102 1 103 1 104 1 105 1 106 1 107 1 108 1 109 1 110 1
 111 1 112 1 113 1 114 1 115 1 116 1 117 1 118 1 119 1 120 1
 121 1 122 1 123 1 124 1 125 1 126 1 127 1 128 1 129 1 130 1
 131 1 132 1 133 1 134 1 135 1 136 1 137 1 138 1 139 1 140 1
 141 1 142 1 143 1 144 1 145 1 146 1 147 1 148 1 149 1 150 1
 151 1 152 1 153 1 154 1 155 1 156 1 157 1 158 1 159 1 160 1
 161 1 162 1 163 1 164 1 165 1 166 1 167 1 168 1 169 1 170 1
 171 1 172 1 173 1 174 1 175 1 176 1 177 1 178 1 179 1 180 1
 181 1 182 1 183 1 184 1 185 1 186 1 187 1 188 1 189 1 190 1
 191 1 192 1 193 1 194 1 195 1 196 1 197 1 198 1 199 1 200 1
 201 1 202 1 203 1 204 1 205 1 206 1 207 1 208 1 209 1 210 1
 211 1 212 1 213 1 214 1 215 1 216 1 217 1 218 1 219 1 220 1
 221 1 222 1 223 1 224 1 225 1

ENERGY BOUNDARIES 52

1.3499E+1 1.2214E+1 1.1052E+1 1.0000E+1 9.0484E+0 8.1873E+0
 7.4082E+0
 7.0469E+0 6.7032E+0 6.3763E+0 6.0653E+0 5.4881E+0 4.9659E+0
 4.7240E+0 4.4933E+0
 4.0657E+0 3.6788E+0 3.3287E+0 3.0112E+0 2.7253E+0 2.4660E+0
 2.3460E+0 2.2313E+0
 2.0190E+0 1.8268E+0 1.6530E+0 1.4957E+0 1.3534E+0 1.2246E+0
 1.1080E+0 1.0026E+0
 9.0718E-1 8.2085E-1 7.4274E-1 6.7206E-1 6.0810E-1 5.5023E-1
 4.9787E-1 4.5049E-1
 4.0762E-1 3.6883E-1 3.3373E-1 3.0197E-1 2.7324E-1 2.4724E-1
 2.2371E-1 2.0242E-1
 1.8316E-1 1.6573E-1 1.4996E-1 1.3569E-1 1.2277E-1 1.1109E-1

GROUP IMPORTANCES

2.30E-1 7.3E-2 2.60E-2 2*8.10E-3 2*3.2E-03 3*1.80E-3
 3*9.00E-4 3*3.90E-4 3*2.10E-4 6*1.0E-04 10*3.0E-05

5*7.60E-6 12*2.1E-06
SOURCE GENERATION GROUPS 1
FLUXES

&
& Y BOUNDS -51.44 -47.63 -40.64 -35.56 -31.75 -19.69 -15.88 -5.29
& 5.29. 15.88 19.69 31.75 35.56 40.64 47.63 51.44

& X-MESH BETWEEN -49.75 AND -46.58

1.0000E-10
1.0000E-10
1.0000E-10
1.0000E-10
1.0000E-10
1.0000E-10
3.3194E+07
3.4821E+07
3.4471E+07
1.0000E-10
1.0000E-10
1.0000E-10
1.0000E-10
1.0000E-10
1.0000E-10

& X-MESH BETWEEN -46.58 AND -43.32

1.0000E-10
1.0000E-10
1.0000E-10
1.0000E-10
1.0000E-10
3.3347E+07
3.5528E+07
3.7134E+07
3.6506E+07
3.5023E+07
1.0000E-10
1.0000E-10
1.0000E-10
1.0000E-10
1.0000E-10

& x-MESH BETWEEN -43.32 AND -37.08

1.0000E-10
1.0000E-10
1.0000E-10
1.0000E-10
3.3094E+07
3.6719E+07
3.9095E+07
4.0704E+07
3.9732E+07
3.7844E+07

3.4890E+07
1.0000E-10
1.0000E-10
1.0000E-10
1.0000E-10

& X-MESH BETWEEN -37.08 AND -33.92

1.0000E-10
1.0000E-10
1.0000E-10
3.1570E+07
3.6028E+07
4.0073E+07
4.2640E+07
4.4277E+07
4.3025E+07
4.0791E+07
3.7289E+07
3.3557E+07
1.0000E-10
1.0000E-10
1.0000E-10

& X-MESH BET-EEN -33.92 AND -27.58

1.0000E-10
1.0000E-10
3.1129E+07
3.3930E+07
3.8913E+07
4.3345E+07
4.6100E+07
4.7791E+07
4.6322E+07
4.3802E+07
3.9826E+07
3.5509E+07
3.3234E+07
1.0000E-10
1.0000E-10

& X-MESH BETWEEN -27.58 AND -11.75

1.0000E-10
3.0709E+07
3.5185E+07
3.8688E+07
4.4654E+07
4.9825E+07
5.2964E+07
5.4838E+07
5.3073E+07
5.0094E+07
4.5306E+07

3.9940E+07
3.6932E+07
3.3333E+07
1.0000E-10

& X-MESH BETWEEN -11.75 AND -2.25

2.8695E+07
3.2959E+07
3.8254E+07
4.2275E+07
4.8979E+07
5.4722E+07
5.8190E+07
6.0290E+07
5.8416E+07
5.5174E+07
4.9853E+07
4.3755E+07
4.0207E+07
3.5724E+07
3.2358E+07

& X-MESH BETWEEN -2.25 AND 7.25

2.8830E+07
3.3303E+07
3.8804E+07
4.2959E+07
4.9864E+07
5.5779E+07
5.9368E+07
6.1594E+07
5.9771E+07
5.6531E+07
5.1100E+07
4.4841E+07
4.1154E+07
3.6423E+07
3.2773E+07

& X-MESH BETWEEN 7.25 AND 16.75

2.8110E+07
3.2434E+07
3.7793E+07
4.1862E+07
4.8658E+07
5.4505E+07
5.8081E+07
6.0350E+07
5.8641E+07
5.5491E+07
5.0223E+07
4.4119E+07

4.0522E+07
3.5909E+07
3.2360E+07

& X-MESH BETWEEN 16.75 AND 32.58

1.0000E-10
2.9626E+07
3.4234E+07
3.7822E+07
4.3934E+07
4.9257E+07
5.2551E+07
5.4676E+07
5.3160E+07
5.0322E+07
4.5609E+07
4.0216E+07
3.7112E+07
3.3266E+07
1.0000E-10

& X-MESH BETWEEN 32.58 AND 38.92

1.0000E-10
1.0000E-10
2.9939E+07
3.2819E+07
3.7886E+07
4.2376E+07
4.5182E+07
4.6970E+07
4.5619E+07
4.3169E+07
3.9214E+07
3.4832E+07
3.2446E+07
1.0000E-10
1.0000E-10

& X-MESH BETWEEN 38.92 AND 42.08

1.0000E-10
1.0000E-10
1.0000E-10
3.0427E+07
3.4889E+07
3.8886E+07
4.1391E+07
4.2951E+07
4.1660E+07
3.9411E+07
3.5870E+07
3.2047E+07
1.0000E-10

1.0000E-10
1.0000E-10

& X-MESH BETWEEN 42.08 AND 48.42

1.0000E-10
1.0000E-10
1.0000E-10
1.0000E-10
3.1830E+07
3.5244E+07
3.7384E+07
3.8657E+07
3.7415E+07
3.5388E+07
3.2315E+07
1.0000E-10
1.0000E-10
1.0000E-10
1.0000E-10

& X-MESH BETWEEN 48.42 AND 51.58

1.0000E-10
1.0000E-10
1.0000E-10
1.0000E-10
1.0000E-10
3.1588E+07
3.3310E+07
3.4245E+07
3.3043E+07
3.1252E+07
1.0000E-10
1.0000E-10
1.0000E-10
1.0000E-10
1.0000E-10

& X-MESH BETWEEN 51.58 AND 54.75

1.0000E-10
1.0000E-10
1.0000E-10
1.0000E-10
1.0000E-10
1.0000E-10
3.0616E+07
3.1292E+07
3.0108E+07
1.0000E-10
1.0000E-10
1.0000E-10
1.0000E-10
1.0000E-10

1.0000E-10

&

&

CROSS SECTIONS

1.364E-4 3.257E-4 7.019E-4 1.377E-3 2.485E-3 4.156E-3 2.911E-3
3.585E-3
4.349E-3 5.203E-3 1.329E-2 1.761E-2 1.054E-2 1.178E-2 2.718E-2
3.195E-2 3.637E-2
4.032E-2 4.326E-2 4.566E-2 2.338E-2 2.375E-2 4.772E-2 4.757E-2
4.666E-2 4.520E-2
4.325E-2 4.097E-2 3.844E-2 3.570E-2 3.296E-2 3.019E-2 2.749E-2
2.489E-2 2.243E-2
2.012E-2 1.797E-2 1.599E-2 1.419E-2 1.255E-2 1.107E-2 9.743E-3
8.553E-3 7.497E-3
6.561E-3 5.731E-3 4.998E-3 4.354E-3 3.789E-3 3.293E-3 2.862E-3
2.481E-3

ENDSOURCE

END

&***** UNIT 14 *****

BEGIN MATERIAL DATA

MINNIE

MIXTURES 10

& MAT 1 GRAPHITE

WEIGHT

M 1 C 1.0

& MAT 2 CONCRETE

WEIGHT

M 2 SI .36205

FE54 .000863

FE56 .013914

FE57 .000324

FE58 .000044

H .010743

O16 .51753

AL .036585

CA .040696

NA .017254

& MAT 3 TROLLEY MILD STEEL

WEIGHT

M 3 FE54 .562316E-01

FE56 .906316

FE57 .211115E-01

FE58 .286091E-02

MN .010914

C .22126E-02

SI .35507E-03

& MAT 4 WATER CELL MILD STEEL

WEIGHT

M 4 FE54 .056846

FE56 .916220

FE57 .021342

FE58 .002892

MN .22662E-02

C .43084E-03

& MAT 5 STANDARD 2 INCH MILD STEEL PLATES

WEIGHT
 M 5 FE54 .564425E-01
 FE56 .909743
 FE57 .211914E-01
 FE58 .287177E-02
 C .22999E-02
 H .54624E-05
 MN .007443

& MAT 6 WATER CELL STAINLESS STEEL

WEIGHT
 M 6 FE54 .4014E-01
 FE56 .6469
 FE57 .1507E-01
 FE58 .2042E-02
 C .24021E-03
 NI58 .66996E-01
 NI60 .26699E-01
 NI61 .11764E-02
 NI62 .38184E-02
 NI64 .10069E-02
 CR50 .007316
 CR52 .14685
 CR53 .01697
 CR54 .004299
 SI .61786E-02
 MN .014283

& MAT 7 FUEL IN FISSION PLATE

WEIGHT
 M 7 AL .79988
 U235 .18633
 U238 .01379

& MAT 8 PURE ALUMINIUM

WEIGHT
 M 8 AL 1.0

& MAT 9 WATER CELL ALUMINIUM

WEIGHT
 M 9 AL .99297
 SI .001453
 FE54 .31761E-03
 FE56 .51191E-02
 FE57 .11924E-03
 FE58 .16159E-04

& MAT 10 WATER CELL WATER

WEIGHT
 M 10 H .11192
 O16 .88808

MATERIALS 10

1 M 1 1.650 1.0
 2 M 2 2.300 1.0
 3 M 3 7.835 1.0
 4 M 4 7.862 1.0
 5 M 5 7.850 1.0
 6 M 6 7.900 1.0
 7 M 7 3.256 1.0

8 M 8 2.700 1.0
9 M 9 2.666 1.0
10 M 10 1.000 1.0

USE MOULD 12 FOR H IN ALL MATERIALS
USE ADCN FE FOR FE54 IN ALL MATERIALS
USE ADCN FE FOR FE56 IN ALL MATERIALS
USE ADCN FE FOR FE57 IN ALL MATERIALS
USE ADCN FE FOR FE58 IN ALL MATERIALS
USE ADCN NI FOR NI58 IN ALL MATERIALS
USE ADCN NI FOR NI60 IN ALL MATERIALS
USE ADCN NI FOR NI61 IN ALL MATERIALS
USE ADCN NI FOR NI62 IN ALL MATERIALS
USE ADCN NI FOR NI64 IN ALL MATERIALS
USE ADCN CR FOR CR50 IN ALL MATERIALS
USE ADCN CR FOR CR52 IN ALL MATERIALS
USE ADCN CR FOR CR53 IN ALL MATERIALS
USE ADCN CR FOR CR54 IN ALL MATERIALS
USE ADCN O FOR O16 IN ALL MATERIALS

END

AEA Technology

AEAT 0468

Further Analysis of the H B Robinson Unit 2 PWR
using the Monte-Carlo Code MCBEND with
ENDF/B-VI and IRDF-90 Nuclear Data.

A F Avery, H F Locke and A K Ziver

June 1996

Reactor Physics Shielding and Criticality Department
Plant Support Services Group
AEA Technology plc
Dorset DT2 8DH
United Kingdom

The information which this report contains is accurate to the best knowledge and belief of AEA Technology, but neither AEA Technology nor any person acting on behalf of AEA Technology make any warranty or representation expressed or implied with respect to the accuracy, completeness or usefulness of this information, nor assume any liabilities with respect to the use of, or with respect to any damages which may result from the use of any information, apparatus, method or process disclosed in this report.

| | Name | Position | Signature | Date |
|----------|------------|----------------------|-------------------|---------|
| Author | A F Avery | Shielding Consultant | <i>A F Avery</i> | 23/6/96 |
| Checked | S J Chucas | Product Manager | <i>S J Chucas</i> | 1/7/96 |
| Approved | C A Cooper | Department Manager | <i>C A Cooper</i> | 2.7.96 |

AEAT-0468

**Further Analysis of the H B Robinson Unit 2 PWR
using the Monte-Carlo Code MCBEND with
ENDF/B-VI and IRDF-90 Nuclear Data.**

A F Avery, H F Locke and A K Ziver

Summary

This report describes the validation of the Monte Carlo code MCBEND for determining neutron fluence in the radial shield of PWRs. Calculations were performed for the H.B.Robinson Unit 2 PWR, at dosimetry positions in the reactor cavity and the surveillance capsule, using MCBEND with ENDF/B-VI nuclear data and the predicted reaction rates are compared with extensive measurements. This report is an extension of the work reported in AEA-RS-5579 with the use of data from IRDF-90 for the calculation of the detector responses and their associated uncertainties. A detailed analysis of all the uncertainties in the calculation route is included.

MCBEND accurately predicts the reaction rates in the cavity and surveillance position, with the ratio of calculated reaction rate to measurement (C/M) lying within one standard deviation of unity. The average value of C/M is 0.94 at the surveillance position whilst in the cavity it is 0.93 for the threshold reactions which detect high energy neutrons ($E > 0.1$ MeV) and 1.08 for those which are sensitive to the low energy fluxes.

Reactor Physics Shielding and Criticality Department
Plant Support Services Group
AEA Technology plc
Dorset DT2 8DH
United Kingdom

CONTENTS

| | Page |
|---|------|
| 1 INTRODUCTION | 1 |
| 2 THE MEASUREMENTS | 1 |
| 3 THE MCBEND MODEL | 3 |
| 3.1 Geometry | 3 |
| 3.2 Materials | 3 |
| 3.3 Source | 3 |
| 3.3.1 X-Y Source Intensities | 4 |
| 3.3.2 Z Profile | 5 |
| 3.3.3 Source Spectrum | 5 |
| 3.4 Scoring | 6 |
| 3.4.1 Cavity Scoring Region | 6 |
| 3.4.2 Surveillance Capsule Scoring Region | 7 |
| 3.4.3 Detector Responses | 7 |
| 3.5 Nuclear Data | 7 |
| 3.6 Variance Reduction | 7 |
| 4 TIME DEPENDENCE | 8 |
| 5 CORRECTION FACTOR | 9 |
| 6 RESULTS OF THE CALCULATIONS | 10 |
| 7 UNCERTAINTIES | |
| 7.1 Cross-Sections | 10 |
| 7.1.1 Surveillance Capsule | 10 |
| 7.1.2 Cavity Position | 11 |
| 7.2 Dimensions | 11 |
| 7.3 Radial Variation of the Flux | 11 |
| 7.4 Material Compositions | 11 |
| 7.5 Core Smearing | 12 |
| 7.6 Source Intensity | 12 |
| 7.7 Core Source Data | 13 |
| 7.8 Fission Spectrum | 13 |
| 7.9 Detector Response Functions | 13 |
| 7.10 Total Uncertainties | 13 |
| 8 COMPARISON OF CALCULATION AND MEASUREMENT | |
| 8.1 Surveillance Position | 14 |
| 8.2 Cavity Position | 14 |
| 9 SUMMARY | 15 |
| REFERENCES | |

TABLES

- 1 Power History for Cycle 9
- 2 Derivation of Activations Measured at the End of the Cycle.
- 3 Material Compositions
- 4 Initial and Final Burn-up Distributions for the 9th Cycle
- 5 Fuel Composition at the Beginning, Middle and End of the 9th Cycle
- 6 Calculation of Source Intensity
- 7 Source Spectra for Fresh Fuel Assemblies in Peripheral Locations
- 8 Comparison of Reaction-rates at the Beginning, Middle and End of the 9th Cycle
(Taken from Calculations with IRDF-85 data (Ref 5))
- 9 Ratios of the End-of-Cycle Activities to the Reaction Rates at Mid-cycle
- 10 Calculated Reaction Rates
- 11 Calculated Uncertainties arising from Cross-sections
- 12 Uncertainties Due to the Detector Cross-sections
- 13 Correction Factors and Uncertainties
- 14 Comparison of Calculated and Measured Activations

FIGURES

- 1 Plan View showing Sector Modelled and Measurement Positions
- 2 Plan View of the Model showing Materials
- 3 Plan View of the Model showing Dimensions
- 4 Side View of the Model showing Materials
- 5 Side View of the Model showing Dimensions
- 6 Core Sources Modelled
- 7 Scoring Regions Modelled
- 8 Power Variation through the 9th Cycle for Assemblies adjacent to the Cavity and
Surveillance Positions
- 9 Variation of Response through the 9th cycle - Cavity Position
- 10 Variation of Response through the 9th cycle - Surveillance Position

APPENDIX

MCBEND9 INPUT DATA

1 INTRODUCTION

The H B Robinson Unit 2 (HBR-2) station is a three-loop 665 MW(e) Westinghouse PWR. It is owned by the Carolina Power & Light Company (CP&L), and is located on the shore of Lake Robinson at Hartsville, South Carolina, USA. It has been identified as a reactor likely to be susceptible to pressurised thermal shock. This susceptibility occurs when irradiation by neutrons causes embrittlement of the pressure vessel wall. To ameliorate this problem previously burned fuel was loaded into the locations on the flats of the core at the start of cycle 9. As the neutron sources in these regions contribute heavily to the fluence in the pressure vessel wall, the introduction of the irradiated fuel reduces this fluence level significantly. In order to validate the effectiveness of this low-leakage core arrangement, special dosimetry was introduced into the surveillance position in the downcomer annulus and into the reactor cavity.

The extensive range of measurements carried out during cycle 9 provides an opportunity to evaluate the Monte Carlo code MCBEND (reference 1) for radial shield calculations on PWRs. Previous calculations for the reactor cavity (reference 2) and the surveillance capsule (reference 3) used cross-sections from the UKNDL. Calculations for both dosimetry positions carried out with ENDF/B-VI data and detector response cross sections from IRDF85 (reference 4) were reported by Locke (reference 5). This report describes a repeat of those calculations using MCBEND9 with response cross-sections from IRDF-90 (reference 6) and compares the results with the measurements. In contrast with the earlier comparisons, the present results are given as the activities of the detectors at the end of the cycle rather than the reaction rates at mid-cycle.

2 THE MEASUREMENTS

Measurements were made in the reactor cavity and in a surveillance capsule located between the thermal shield and the pressure vessel. The sensor packages were inserted at the start of cycle 9. In the cavity they were placed at 4 azimuthal positions and 5 axial positions centred on the reactor core mid-plane; however those of interest to this analysis are at the mid-height of the core at the 0° position shown in figure 1. The surveillance capsule was positioned at 20°.

The measurements are presented in reference 7 as the saturation reaction rates derived from the activations of the detectors by making the assumption that the ratios between reaction rates and the power of the reactor remained constant through the cycle. Estimated corrections were subsequently applied to account for changes in this ratio for the results for the detectors in the cavity, these being based on the measurement of the activities of several fission products with differing half lives, and the adoption of a linear variation with burn-up for the flux/power ratio. It was shown in reference 5 that the changes in the power distribution within the core during the cycle gave a non-linear variation for this ratio. For the comparisons with the present calculations the uncorrected measurements have been converted back into the activations at the end of the cycle by carrying out a reversal of this process.

Thus

$$A(T) = \int_0^T R(t)P(t)\lambda e^{-\lambda(T-t)} dt$$

where

- $A(T)$ = Activation at the end of the cycle,
 $R(t)$ = Reaction rate for full power (2300MW) at time t in the cycle,
 $P(t)$ = Reactor power (fraction of full power) at time t
 λ = Decay constant for the activity, and
 T = Duration of the cycle.

The assumption made previously for the uncorrected results in reference 7 was that R was independent of burn-up. The cycle history is given in that reference as the mean powers in 18 time intervals, and this is reproduced in Table 1. The above equation for the cycle is then reduced to a summation over the intervals.

$$A(T) = R e^{-\lambda T} \sum_1^{18} P_i \int_{t_i}^{t_{i+1}} \lambda e^{\lambda t} dt$$

$$= R e^{-\lambda T} \sum_1^{18} P_i (e^{\lambda t_{i+1}} - e^{\lambda t_i})$$

where

- P_i = Mean power in the i_{th} interval,
 t_i = Time at the start of the i_{th} interval, and
 t_{i+1} = Time at the end of the i_{th} interval ($t_{19}=T$).

Values of the ratio $A(T)/R$ were derived using the power history of Table 1. The resulting ratios are given in Table 2 as scaling factors for each detector. Also presented in Table 2 are the measured values of R taken from reference 7 together with the resulting values of $A(T)$ when the calculated factors are applied. The table also gives the estimated standard deviations on the measurements as taken from reference 7.

The measurements were made with some of the detectors being covered with gadolinium in the surveillance position and with cadmium in the cavity. This provided shielding against low energy neutrons and thus reduced

- (i) reactions which would arise from impurities in the detectors e.g. Co59(n,g)Co60 from cobalt in the copper foils and U235(n,fx) from traces of U235 in U238,
- (ii) the background count from other reactions e.g. Fe59 for the Fe54(n,p) reaction, and
- (iii) the burn-up of Co58 by the (n,g) reactions.

The accuracy of the high energy measurements will be improved by the presence of the covering and therefore, where there is a choice, the results which are included in Table 2 for these detectors are those given with the covers present. For the low energy reactions the results given in the table are for the bare detectors except for Co59(n,g)Co60 and U235(n,fx) in the surveillance position where the only measurements were made with gadolinium covers.

3 The MCBEND Model

3.1 Geometry

A 45° sector of the reactor core and shield was modelled using combinatorial geometry, as shown in figures 1 to 5. The reactor has eight-fold symmetry, so that it may be modelled by a 45° slice with reflective boundaries at its sides. The full height of the reactor was modelled, although approximations were made at regions away from the core mid-height. (Most of the measurements were taken at the mid-height.) Most of the dimensions were taken from reference 8, although some of the heights were taken from reference 9. Although the shield, baffles, and pressure vessel were modelled exactly, the core region was smeared.

3.2 Materials

The materials data and compositions were taken directly from reference 8 which specifies them in terms of number densities. The core region consists of fuel (UO₂), fuel pin cladding (Zircaloy), fuel assembly supports and sheathing (Inconel and SST304), and boronated water smeared together. The material compositions are given in Table 3. Iron, nickel and chromium are present in the ENDF/B-VI library in isotopic form and so the composition of each material is defined using the relevant isotopes.

3.3 Source

The calculation was performed for a single time interval with burn-up and power distribution appropriate to the core at a time which was close to half way through the cycle. Neutron source data were provided in reference 10 for one quarter of the reactor core at a near-mid-cycle burn-up of 5,500 MWd/Te, this being representative of a cycle averaged distribution. Not all of this source was needed for the 45° sector, as can be seen in figure 6. The effect of the variation of the source due to changes in the burn-up and power distribution through the cycle were examined in reference 5 where additional calculations were performed with sources appropriate to the beginning and end of the cycle as well as for those corresponding to the near mid-cycle condition. The time dependence of the ratio of reaction rate to power was thus calculated in reference 5 for each of the detectors, the nuclear data being taken from ENDF/B-VI for the material cross-sections and IRDF-85 for the response functions. The present calculations were restricted to the burn-up of 5,500MWd/Te and the effects of the variation of the source distribution during the cycle were derived from the results given in reference 5. The assumption is thus made that the factors which allow for the time dependence of the source distribution are not sensitive to the changes in the response functions between IRDF-85 and IRDF-90. This is valid because the corrections are mostly due to the increase in the absolute fluxes per unit power and the

effect of the latter would be independent of the response cross-section. There are changes in the neutron spectra during the cycle which could be given different weightings by the two sets of dosimetry cross-sections but these are both small differences which in combination are expected to produce an insignificant effect.

An XYZ source configuration was used, with Z being the vertical axis. In Monte Carlo calculations the efficiency is improved if sampling of the source is biased in energy and position to concentrate on those neutrons which are most likely to contribute to the fluxes of interest. MCBEND's option for "Automatic" source weighting was used which meant that the importance map specified for accelerating the tracking was also used to generate source importances. The source intensity was specified as two components, namely intensities for each source area in the X and Y directions, combined with a single Z profile.

3.3.1 X-Y Source Intensities

Two sets of data were produced by CP&L and provided in reference 10. They were:

- 1) Relative pin powers, calculated using the code PDQ7.
- 2) Assembly averaged relative powers measured at a reactor power of 1782.9MW(t), processed using INCORE.

These measurements are considered to be better than the calculated assembly averaged powers (reference 11). The PDQ7 pin powers were re-normalised to the INCORE assembly averaged powers by using the following equation for each pin:

$$r_{xy} = p_{xy} \frac{I_a}{Q_a}$$

where p_{xy} is the relative pin power for pin x,y as calculated using PDQ7. Division of p_{xy} by Q_a , the mean pin power in the assembly containing pin x,y as calculated using PDQ7, normalises the calculation to unit mean pin power in the assembly. Multiplication by I_a , the mean pin power in the assembly containing pin x,y as calculated using INCORE with normalisation to unit mean pin power for the whole core, results in r_{xy} being the relative pin power for pin x,y normalised to unit mean pin power over the whole core.

The values of r_{xy} were multiplied by the mean absolute power per pin (S, measured in MW), and by a factor n relating the number of neutrons emitted to the power produced (measured in neutrons $s^{-1} MW^{-1}$), to give source strengths in neutrons s^{-1} per pin. Because source strengths are specified for MCBEND in terms of neutrons $s^{-1} cm^{-3}$, the strength for each pin needs to be divided by the volume of the MCBEND source for the pin. At this stage, the source strengths for each pin were divided by the area of the source, the height of the pin being considered with the axial profile (see below).

Therefore,

$$s_{xy} = \frac{n S r_{xy}}{A_{xy}}$$

where s_{xy} is the absolute source density for pin x,y (neutrons $s^{-1} cm^{-2}$) and A_{xy} is the area occupied by pin x,y including the space around it which forms the MCBEND source mesh (cm^2).

There are 32028 pins in the full source and the total reactor power was 1782.9MW(t), giving a mean pin power of 0.05567 MW. The source for each pin occupied an area 1.43cm square. The pin powers were converted to source rate densities using a value of $(7.96 \pm 0.13)E16$ neutrons $s^{-1} MW^{-1}$ as described in section 7.6.

To reduce the amount of data required to describe the source, groups of 3 pins by 3 pins were combined into single large source regions. Thus each assembly (containing 15×15 pins) was modelled by a 5 by 5 array of sources. Therefore,

$$S_r = \sum_{y=1}^3 \sum_{x=1}^3 \frac{S_{x,y}}{9}$$

where S_r is the absolute source density for the region r containing the 9 pins with $x=1$ to 3 and $y=1$ to 3 (neutrons $s^{-1} cm^{-2}$).

3.3.2 Z Profile

The axial (Z) profiles are stated in reference 10 to be independent of Y, and almost independent of X. For the purpose of the calculation, the Z profile was assumed to be independent of both X and Y, and a mean figure was taken. The profile was supplied in 57 vertical intervals, but to reduce the amount of data required to describe the source, these intervals were combined into sets of three to give 19 larger intervals over the full height of the source. The Z profile was then normalised to unity.

Because source strengths must be specified for MCBEND in terms of neutrons $s^{-1} cm^{-3}$, the factor for each vertical interval was divided by the height of the interval (the other dimensions of the sources having been considered with the X-Y component). Combining the source strengths for each XY region (neutrons $s^{-1} cm^{-2}$), with the factors for each Z interval (cm^{-1}), gives the complete source for the core.

Although the source was produced for one quarter of the core, only one eighth of the core was modelled. The source was reduced in area to omit those regions in the X direction lying entirely outside the eighth modelled. This still leaves some source regions outside the model. MCBEND will automatically ensure that any particles started outside the model are absorbed immediately, thus not affecting the source normalisation. Figure 6 shows the source areas used.

3.3.3 Source Spectrum

MCBEND9 has the capability of generating sources with spectra arising from a mixture of fission in U^{235} and Pu^{239} , the fraction of neutrons created from each of the two spectra being specified for each source mesh. This facility was adopted for the present calculations. The fractions of the fissions occurring in each of the isotopes were obtained from the calculations described below.

In cycle 9 for H B Robinson some of the fuel assemblies had considerable burn-ups hence contained substantial proportions of plutonium, so the source will have consisted of some neutrons with a plutonium fission spectrum, with the remainder having that appropriate to uranium. The additional information that is required for input to MCBEND is the fraction of neutrons with a plutonium spectrum in each source mesh. It is assumed that U^{238} produces the same fission spectrum as U^{235} with the plutonium spectrum applying to both Pu^{239} and Pu^{241} , these being the four main fissionable isotopes.

Table 4 shows the distribution of burn-up within the core at the beginning and end of the 9th cycle. It can be seen that there are regions of very high burn-up on the flats, which are nearest to the main 0° dosimetry position, and low burn-up at the other edge regions. The remainder of the core consists of a range of burn-up histories. The assemblies were considered in groups with comparable histories as follows:

High burn-up assemblies on the flats:-

| | | | |
|-------|---------|----|-------------------|
| Inner | ~22,000 | to | ~26,500 MWd/tonne |
| Outer | ~29,000 | to | ~33,000 MWd/tonne |

Low burn-up assemblies near surveillance capsule:-

| | | | |
|-------|---|----|-------------------|
| Inner | 0 | to | ~10,000 MWd/tonne |
| Outer | 0 | to | ~7,700 MWd/tonne |

Rest of the core:-

| | | |
|---------|----|-------------------|
| ~7,500 | to | ~20,000 MWd/tonne |
| ~11,000 | to | ~23,000 MWd/tonne |
| ~18,500 | to | ~30,000 MWd/tonne |
| ~0 | to | ~8,000 MWd/tonne |
| ~0 | to | ~11,000 MWd/tonne |

Fission fractions were obtained from burn-up calculations carried out with the nuclide inventory code FISPIN (reference 12) for 3.1% enriched fuel for this range of burn-up histories. Table 5 gives the fission fractions at the beginning, middle and end of the 9th cycle for the five regions above (the "rest of the core" is treated as one region), with average values being presented for the fifth region. The fraction of neutrons with a plutonium spectrum was then determined, knowing the neutrons produced per fission (reference 13), and this is also shown. The calculated fission rates for the highest rated fuel are in reasonable agreement with those given in Table 33 of reference 14, for 3.2% U^{235} with fuel discharged at burn-ups approaching 30,000 MWd/tonne. The variation of the source per MW with plutonium content is shown in Table 6 for fuel assemblies at the positions illustrated in figure 6, these being based on the energy released per fission taken from reference 15. Table 7 gives the variation in the neutron spectrum emitted during cycle 9 by a fresh fuel assembly which was loaded into a peripheral core position at the start of the cycle.

3.4 Scoring

The reaction rates were scored in the reactor cavity and at the surveillance capsule position, as shown in figure 7.

3.4.1 Cavity Scoring Region

For scoring, the cavity was divided by planes at the following distances above and below the core centre line: ± 91 cm, ± 122 cm, ± 145 cm, ± 175 cm, ± 206 cm and ± 221 cm. Only the mid-height region is of interest in this exercise. The cavity was also divided into wedges around the circumference of the reactor. These included a 12° wedge centred on the 0°

position, an 8° wedge centred on 30° and a 12° wedge centred on 45°. The 0° and 45° wedges were actually only 6° wide, the reflection planes giving the effect of the other half. Each scoring region covered the full width of the cavity. Most of the measurements were made at 0° at the core mid-height. The scoring regions were chosen to provide as large a scoring volume as possible around each measurement position, but with 10% or less variation in measured detector response across them (based on the axial and azimuthal measurements of reference 7).

3.4.2 Surveillance Capsule Scoring Region

The surveillance capsule was modelled accurately as shown in figure 7. The measurements of reference 7 show that there is little variation in flux over the 60cm height of the capsule, so the scoring region covered the entire central carbon steel region of the capsule.

3.4.3 Detector Responses

The following detector responses were scored:

| | | | | |
|------------------------|-------------------------|-------------------------|--------------------------|------------------------|
| Ti ⁴⁶ (n,p) | Fe ⁵⁴ (n,p) | Fe ⁵⁸ (n,γ) | Ni ⁵⁸ (n,p) | Co ⁵⁹ (n,γ) |
| Cu ⁶³ (n,α) | U ²³⁵ (n,fx) | U ²³⁸ (n,fx) | Np ²³⁷ (n,fx) | Sc ⁴⁵ (n,γ) |

The cross-sections for these reactions were taken from the International Reactor Dosimetry Files IRDF-90 (reference 6). They are used in MCBEND in the 640 energy group scheme in which they are presented in the files. These data do not take the gadolinium or cadmium covering into account, the effect of which is discussed later.

3.5 Nuclear Data

The nuclear data were processed from ENDF/B-VI into the DICE format used by MCBEND, which expresses cross-sections at 8220 energy points and has an explicit representation of the angular distributions and the energy loss laws. The doubly-differential representation of the energy and angle dependency of the scatter laws present for some isotopes in the ENDF/B-VI data was replaced by two independent distributions, the former representation being incompatible with the DICE format. The route for preparing the data was that described by Dean and Eaton (16) in which the SIXPAK (17) code is used to change the doubly-differential data, and the files are then processed with NJOY (18) to convert them to the DICE format designed for Monte Carlo tracking of neutrons. The calculations also included a detailed treatment of thermal neutron scattering using S(α,β) data (reference 19).

3.6 Variance Reduction

The MCBEND module MAGIC was invoked to calculate the importance map for use in accelerating the MCBEND calculation. This performs an adjoint diffusion theory calculation in an orthogonal mesh, in this case XYZ, in order to provide the importances used in splitting and Russian roulette. The spacing of the mesh was determined from consideration of the attenuating properties of the materials in the system and of the penetration path from source to detector, e.g. coarser meshes were used at the axial extremities of the model because the importances are not required to be very accurate in these regions. Material compositions for each mesh were automatically determined by MAGIC by identifying the material in the MCBEND model at a number of points within the mesh, and combining the materials in the appropriate proportions. The importances were calculated in 28 energy groups.

Importance maps were generated for both detector positions separately. The source for the adjoint calculation was specified at either the 0° cavity position or the surveillance capsule, the adjoint source spectrum being identical in all energy groups in an attempt to score the high and low energy responses with equal statistical accuracy.

4 TIME-DEPENDENCE

During the cycle the source distribution changes, with more power being produced by the peripheral assemblies towards the end of the cycle. This leads to an increase in the ratio of the flux levels outboard of the core to reactor power over the duration of the cycle, the effect being greater near the assemblies with high burn-up than near those containing fresh fuel (reference 20). When there is this variation with time there is no straightforward definition of a mean reaction rate for the cycle and the results in the present comparisons are therefore given as the activations of the detectors at the end of the cycle.

The source terms used in the calculations with ENDF/B-VI and IRDF-90 data corresponded to a burn-up of 5500MWd/tonne, i.e. about half way through the 9th cycle. The effects of the time dependence were taken from the calculations described in reference 5 and the relevant results and data are reproduced from that report. In those calculations MCBEND cases were run with source strengths appropriate to the power distributions at the beginning and end of the 9th cycle as well as for those at 5500MWd/Te. The mid-cycle sources were adjusted by multiplying them by the ratio of the appropriate assembly powers at the beginning/end of the cycle to those in the middle of the cycle to give the relevant source strengths. No allowance was made for the change in neutrons released per MW through the cycle due to the increased plutonium content. This is considered separately (see section 7.6). The power distribution was that supplied in reference 21, and figure 8 shows the variation for assemblies adjacent to the cavity and surveillance positions. The effects on the source spectra of differences in the amount of plutonium through the cycle were taken into account by specifying the fractions of the sources arising from plutonium at the beginning and end of the cycle calculated as described in section 3.3.3. The reactor power was kept constant for these calculations at 1782.9MW(t).

Table 8 and figures 9 and 10 are reproduced from reference 5. They compare the results of the MCBEND calculations for 1782.9MW(t) at the beginning, middle and end of cycle 9 for both detector positions. It can be seen that the responses in general do not vary linearly with time, as is often assumed, although this could be considered valid for the surveillance capsule.

The plutonium contents in assemblies adjacent to the cavity position, i.e. those on the flats at the edge of the core, show little change throughout the cycle (see Table 5) and so the variation in the reaction rates is due to differences in the source strength. Figure 8 shows that the power, and hence source strength, in the assemblies adjacent to the cavity, increases linearly over the first ~350 days (from 70% to 110% of the value at mid-cycle) and then flattens out. The calculated reaction rates show the same variation. The peripheral assemblies adjacent to the surveillance position were fresh at the start of cycle 9 so that the plutonium content increases during the cycle. The calculated reaction rates will thus be dependent on the change in both spectrum (for high energy reactions) and source strength over the cycle. The maximum change in spectrum however (see Table 7) is ~6% at the very high energies which is less than the source strength variation. The change in the spectrum is much less than 6% for the lower energies at which most of the neutrons are emitted. The source strength for the assemblies close to the surveillance position shows less increase (from 85% to 103%) than did those relevant to the cavity reaction rates and this is reflected in the calculated time profile through the cycle.

Following the equation given in Section 2 above the activation A(T) at the end of the cycle is given by

$$A(T) = \int_0^T R(t)P(t)\lambda e^{-\lambda(T-t)} dt$$

where

| | | |
|-----------|---|---|
| $A(T)$ | = | Activation at the end of the cycle, |
| $R(t)$ | = | Reaction rate for full power (2300MW) at time t in the cycle, |
| $P(t)$ | = | Reactor power (fraction of full power) at time t |
| λ | = | Decay constant for the activity, and |
| T | = | Duration of the cycle. |

When this is re-written for the representation of the power history by the mean powers in 18 intervals it becomes

$$A(T) = e^{-\lambda T} \sum_1^{18} P_i R_i (e^{\lambda t_{i+1}} - e^{\lambda t_i})$$

where

| | | |
|-----------|---|--|
| R_i | = | Mean reaction rate at full power in the i^{th} interval |
| P_i | = | Mean power (fraction of full power) in the i^{th} interval, |
| t_i | = | Time at the start of the i^{th} interval, and |
| t_{i+1} | = | Time at the end of the i^{th} interval ($t_{19}=T$). |

The ratio of the end-of-cycle activation to the reaction rate in interval 9, i.e. that corresponding to 5500MWd/Te, is then given by

$$\frac{A(T)}{R_9} = \frac{e^{-\lambda T}}{R_9} \sum_1^{18} P_i R_i (e^{\lambda t_{i+1}} - e^{\lambda t_i})$$

The results from reference 5 have been used to evaluate the relationships between A(T) and R_9 for each detector at the surveillance position and in the cavity and the ratios are given in Table 9. These ratios, which are based on the IRDF-85 dosimetry cross-sections, are then applied to the current results for the R_9 reaction rates obtained with IRDF-90 data in order to derive the end of cycle activations. As discussed in Section 3.3 above the ratios are expected to show only small sensitivities to the differences between the two sets of response cross-sections so that this procedure should not introduce any significant error.

5 CORRECTION FACTOR

The calculations were for one eighth of the core, and did not take account of any asymmetry. This is not significant for the surveillance capsule; however the 0° measurement position is right on the reflection plane in the MCBEND model, so half the flux reaching it will be due to the eighth that was not modelled. Of the three assemblies nearest the measurement position (A7, A8 and A9 in figure 6), the right hand one (A9), which was included in the calculation, had a power 3.5% higher than the left hand one (A7), which was not included. Assuming that sources from these three assemblies dominate the fluxes and that each contributes equally to the responses measured in the cavity, a correction can be derived.

$$\begin{aligned} \text{Effective relative source in calculation} &= \text{centre source} + 2 \times \text{right hand source} \\ &= 0.468 + 2 \times 0.355 \\ &= 1.178 \end{aligned}$$

$$\begin{aligned} \text{True source} &= \text{left source} + \text{centre source} + \text{right source} \\ &= 0.342 + 0.468 + 0.355 \\ &= 1.165 \end{aligned}$$

Comparing the two indicates that the calculated responses should be multiplied by a factor of 0.989.

6 RESULTS OF THE CALCULATIONS

The results of the MCBEND9 calculations with data from ENDF/B-VI and IRDF-90 are given in columns 2 and 5 of Table 10. These are the reaction rates calculated for a reactor power of 2300MW(t) with the source distribution corresponding to the burn-up of 5500MWd/Te. The standard deviations that are given in columns 3 and 6 of that table are those derived by MCBEND from the statistics of the Monte Carlo scores. Also included in the table are the end-of-cycle activations as derived from the reaction rates by applying the factors of Table 9. For the activations in the cavity the correction factor from Section 5 has also been applied.

7 UNCERTAINTIES

There are several factors which contribute to the overall uncertainty of the calculation in addition to those arising from the Monte Carlo statistics as given in Table 10. These are uncertainties associated with the cross-sections of the materials in the reactor, dimensions of its components, material compositions, smearing of the model of the core, source data and the detector cross-sections. These are considered individually in the following sections where the analysis is mostly taken from reference 5 with modified values for the uncertainties arising from the data for iron in ENDF/B-VI and for the detectors in IRDF-90.

7.1 Cross-Sections

To determine the uncertainty in the results due to uncertainties in the ENDF/B-VI cross-section data for the reactor materials, each MCBEND calculation generated the sensitivities of the various responses to changes in the total cross-sections of hydrogen and oxygen and for the elastic and non-elastic cross-sections of iron, the latter being of particular importance. For iron the calculated sensitivities were folded with the covariance matrices derived by Ziver from the data in the ENDF/B-VI library (22) to produce the uncertainties presented in Table 11 for both the cavity position and surveillance capsule, the correlations between the two partial cross-sections being taken into account in this process. The remaining uncertainties in Table 11 are those derived previously using co-variances from ENDF/B-V because these data are not present for hydrogen and oxygen in ENDF/B-VI. The uncertainties due to the cross-sections of iron were considered separately in two areas of steel: the pressure vessel and the material comprising the barrel, baffle and thermal shield.

7.1.1 Surveillance Capsule

The most important contribution to the total uncertainty for fluxes in the surveillance capsule comes from the uncertainty in the cross-sections of iron in the stainless steel of the barrel, baffle and thermal shield. The relative importance of this material compared with the steel

the pressure vessel is due to the positioning of the surveillance capsule between the two regions. The smaller uncertainties due to the iron cross-section assigned to the low energy reactions are due to the lower sensitivity of these fluxes in the surveillance capsule to changes in the inelastic scatter cross-section because neutrons below the inelastic scatter threshold can migrate large distances. The contributions to the total uncertainties from hydrogen and oxygen are both less than that from the iron and apply equally to all reactions.

7.1.2 Cavity Position

The most important contribution to the total uncertainty in the fluxes in the cavity comes from the uncertainty in the cross-section of iron in the pressure vessel for the high energy reactions, with a significant contribution over all energies from the iron in the stainless steel of the barrel, baffle and thermal shield. The low energy reactions are not sensitive to the cross-section in the pressure vessel because the thermal flux in the cavity is determined by local downscatter of neutrons with energies below the inelastic scatter threshold. Such neutrons can migrate large distances in iron and the fluxes emerging into the cavity at these energies are not therefore sensitive to the positions of inelastic scatter events. In contrast, any increase in the inelastic cross-section leads directly to a decrease in the high energy responses. The contributions to the total uncertainties from hydrogen and oxygen are both less than that from the iron and apply equally across all energies.

7.2 Dimensions

No information was available on the as-built dimensions of the reactor, and nominal dimensions were used in the model. Reference 8 examines the effect of varying the dimensions within the given manufacturing tolerances, and concludes that the maximum effect on the neutron fluence at the surveillance position is $\pm 2.5\%$. This value is taken as the uncertainty at both measurement locations.

Reference 20 states that the radial position of the surveillance capsule is known to within 0.5in, resulting in an uncertainty of approximately 20% being applied to the fluxes in the capsule. In the cavity, measurements had been made at several axial and azimuthal positions (reference 7) so the MCBEND scoring regions were chosen such that there was 10% or less variation in measured detector response across them (section 3.4.1) and this uncertainty is applied to the fluxes in the cavity.

7.3 Radial Variation of the Flux

Radial variation of the fluxes within a scoring region is only significant for the surveillance capsule which has a radial width of 3.175cm. The MCBEND result represents the mean flux over the radial width and this may be different to the true flux at the mid-point where the detectors are located. If the flux is assumed to vary exponentially through the steel capsule with distance from the core then there is a ~3% difference between the mean and the mid-point value (calculated using a cross-section for iron averaged over the fission spectrum). It is recognised that this effect is energy dependent but, as it is small, the above value is applied to all results.

The axial variation in flux is taken into account in the uncertainties applied to the measurements.

7.4 Material Compositions

Reference 8 examines the plant-specific atomic number densities for the steels in the reactor, and concludes that using these would have no significant effect on the neutron fluences. Reference 20 considers the effect of uncertainties in the coolant density and ascribes a

standard deviation of approximately 6% for flux predictions at both measurement locations. The results of the sensitivity analysis described in section 7.1 imply that all responses are equally sensitive to the hydrogen and oxygen total cross-sections and so this value has been applied to all of the results. Similarly taking the analysis from reference 20 for the effect of the density of the steel, a 3% uncertainty is applied to the responses at the surveillance position with corresponding values in the cavity of 6% for the high energy detectors and 3% for those at low energies.

Measurements made in the cavity will be influenced by the backscatter of neutrons from the concrete of the primary shield particularly for those detectors which are sensitive to neutrons at thermal or near thermal energies. No data are available at present which enable an estimate to be made of the uncertainty in the calculated reaction rates due to possible errors in the composition of the concrete. The existence of a likely contribution from this source should however be noted.

7.5 Core Smearing

The core components (fuel, clad, supports, and water) were smeared in the model because including all fuel pins explicitly would be impractical (there are more than 35,000 pin locations in the reactor). However this approximation is not expected to introduce any significant error because neutrons reaching the detectors leave the core with high energies where there is very little fine structure in the flux in the pins and moderator. Smearing is therefore justified. Moreover, as most of the flux received at both measurement locations is from those assemblies on the edge of the core where there has been only a short penetration through the core material, any small error in the treatment of attenuation will not be magnified by being applied over large distances. Evidence on the validity of smearing the fuel pins is provided in reference 23.

7.6 Source Intensity

The estimated uncertainties on the calculation of the neutron source per MW are given in Table 6. The FISPIN uncertainty on the calculation of the fission fractions is estimated as 5% (reference 24). The fission fractions quoted for the "rest of the core" are average values (see section 3.3.3) and therefore the uncertainty stated in Table 6 includes the standard deviation on the values used to determine the average. The calculated total source intensity is $(7.96 \pm 0.13) \times 10^{16} \text{ ns}^{-1} \text{ MW}^{-1}$. This value is used to convert pin powers to source rate densities so that an uncertainty of 1.6% is appropriate for the source strength per unit power.

There is an increase in neutrons released per unit power throughout the cycle due to the increase in plutonium content. This was not taken into account in the change in source strength used in calculations at the beginning and end of the cycle (see section 4). The resultant uncertainty on total source strength can be estimated from the values given for n/MW in Table 6. For assemblies adjacent to the surveillance capsule, which contribute about 78% of the result at that position, it can be seen that the mid-cycle source is lower than the adopted mean value of $7.96 \times 10^{16} \text{ ns}^{-1} \text{ MW}^{-1}$ by about 3% and there is a ~2% variation from the mid-cycle value. Thus an additional uncertainty of 4% should be applied to the results. For assemblies adjacent to the cavity position the number of neutrons emitted per unit power does not change significantly during the cycle, but at $8.2 \times 10^{16} \text{ ns}^{-1} \text{ MW}^{-1}$ the source is higher than the adopted mean by 3%. An uncertainty of 3% is therefore assigned to the results for the cavity due to this variation in the source of neutrons per unit power.

7.7 Core Source Data

In reference 8 the uncertainties on the measured power distributions from INCORE are considered: the assembly-averaged powers are ascribed a standard deviation of $\pm 2.3\%$ and the axial distributions a standard deviation of $\pm 1.0\%$. The accuracy of the PDQ7 calculated pin powers is estimated as $\pm 1.5\%$.

In defining the source data each assembly was divided into groups of 3x3 pins. This introduces an averaging of the source over the group with an associated uncertainty. By estimating the contributions made by individual pins to the result in the scoring regions, uncertainties due to the averaging have been quantified and found to be $\sim 0.5\%$ at both scoring positions. Thus the total uncertainty due to core source data is 2.9%.

7.8 Fission Spectrum

The calculations used MCBEND's built-in option for providing a U^{235} and Pu^{239} fission spectrum. The formula used to represent the spectra is the Watt-Cranberg expression

$$\chi(E) = K e^{-AE} \sinh\sqrt{BE}$$

where E is the neutron energy in MeV, $\chi(E)$ is the fraction of neutrons at E per MeV, and A and B are constants which vary with nuclide. K is a normalisation constant. Uncertainties in the values of A and B lead to uncertainties in the spectrum and hence in the results. The uncertainties in the spectrum are negligible at the peak energy of about 2MeV, and increase, with decreasing energy to about 4% at 0.11MeV. The uncertainties are more significant at higher energies, being about 7% at 10MeV.

The effect of the uncertainty in the representation of the fission spectra has been investigated in a study of an experimental benchmark whose configuration was similar to the radial shield of a PWR (reference 25). For high energy reactions, the uncertainty on results in positions equivalent to the cavity was about 4%. The value for locations equivalent to the surveillance position was about 3.5%. These values have been used for the high energy reactions in this study, with no uncertainties being applied to the low energy reactions as they are much less sensitive to the detailed structure of the fission spectrum.

7.9 Detector Response Functions

The cross-sections for the reactions for which measurements were made were taken from the International Reactor Dosimetry File IRDF-90 (reference 6) which also contains variance-covariance data. The uncertainties on the calculated reaction rates due to the IRDF-90 response cross-sections have been derived by folding the energy dependence of the reaction rates with these covariance data as presented in matrix form by Ziver (22). The covariance data for the $Fe^{58}(n,\gamma)Fe^{59}$ reaction in IRDF-90 however contain errors and the uncertainty of 5% has been taken from reference 5 for this reaction. The uncertainties obtained in this way are given in Table 12.

7.10 Total Uncertainties

The uncertainties due to the above factors are summarised in Table 13. The data from Tables 11, 12 and 13 have been combined in quadrature with the variances arising from the Monte Carlo calculation to give the total uncertainties on the calculated reaction rates.

8 COMPARISON OF CALCULATION AND EXPERIMENT

The calculated activations at the end of cycle 9 are compared with the measured values in Table 14 where values of the ratio of Calculation/Measurement (C/M) are presented together with the uncertainties based on the analysis given in Section 7. The results are discussed separately for the surveillance position and the cavity.

8.1 Surveillance Position

The measured values which are included in Table 14 for the $U^{235}(n,fx)$ and $Co^{59}(n,\gamma)$ reactions at the surveillance position are for the gadolinium covered detectors. As this was not taken into account in the calculated responses, it is not possible to make meaningful C/M comparisons for these detectors.

Of the remaining nine responses, the MCBEND results show values of C/M in the range 0.90 to 1.00 for seven of the detectors. The remaining two, $Ti^{46}(n,p)$ and $U^{238}(n,fx)Zr^{95}$, give ratios of 0.85 and 0.89 respectively. The average C/M value is 0.94. All of the responses have values of C/M which are within one standard deviation of unity, the values of the standard deviation for the ratios being about 25%. The uncertainties mostly arise from the 20% assigned to the doubt about the radial position of the capsule which, as suggested in reference 20, may be too large. The variation of C/M between the detectors with the mean value of 0.94 for C/M suggests that the factors which contribute to the uncertainties for all detectors in an approximately similar way, such as the those due to the material cross-sections, the source data, the capsule position, and the material densities/dimensions, give a small underestimate with the remaining spread being due to the uncertainties associated with particular reactions, i.e. the measurements and the detector cross-sections. For $Ti^{46}(n,p)$ these are 10% and 5.3% which gives a combined uncertainty of 11.3%, so that the departure from the mean is 0.85 standard deviations. The values of C/M for the other reactions are closer to the mean and the differences are all less than one standard deviation due to the combined measurement and detector cross-section uncertainties. The measured and calculated reaction rates are thus consistent within the uncertainties assigned to the input parameters.

8.2 Cavity Position

The results for the detectors in the cavity as given in Table 14 show values of C/M in the range 0.82 to 1.05 for the fast neutron reactions with a mean of 0.93. The differences between the values of C/M and the mean for this group of detectors are again less than one standard deviation due to the combined uncertainties arising from the measurements and the detector cross-sections except in one case. For the neptunium reaction the uncertainty on the measurement is 5% whilst the uncertainty due to the detector is 9.2% giving a standard deviation of 10.5% for the combined uncertainties pertaining solely to that detector. The C/M for the $Np^{237}(n,f)Cs^{137}$ reaction is 0.82 so that its departure from the mean is just greater than one standard deviation. The mean of 0.93 for the high energy detectors in the cavity is close to the value of 0.94 at the surveillance position so that the results suggest that the attenuation through the vessel is being calculated more accurately than is indicated by the uncertainties of 11.5% to 18.45% due to the iron cross-sections which were obtained from the ENDF/B-VI co-variance data.

The results for the six low energy reactions, $Fe^{58}(n,\gamma)Fe^{59}$, $Co^{59}(n,\gamma)Co^{60}$, $U^{235}(n,f)Zr^{95}$, $U^{235}(n,f)Cs^{137}$, $U^{235}(n,f)Ru^{103}$, and $Sc^{45}(n,\gamma)Sc^{46}$ give values of C/M of 1.14, 1.13, 1.04, 1.10, 1.03, and 1.04 respectively. These show that the low energy fluxes are overestimated with a mean value of C/M of 1.08. The fluxes in the cavity at low energies arise from back scatter of the neutrons leaking from the pressure vessel at intermediate energies and

therefore more sensitive to the composition of the concrete primary shield than those which contribute to the reaction rates of the high energy detectors. The composition of the concrete, and in particular its hydrogen content, is not known precisely so that there is an additional uncertainty in the calculated results for the low energy detectors which it was not possible to quantify in the analysis of section 7.4. The comparisons suggest that the back-scatter of low energy neutrons is overestimated with the composition of the concrete that has been adopted in the present calculations. The embrittlement of the pressure vessel is usually correlated against neutron fluxes either through the fluxes above 1MeV or the atomic displacement rate (dpa). The cross-section for the production of displacements falls with decreasing energy down to 1keV and then shows a $1/v$ variation at energies below this, with the cross-section at thermal energies being lower than that at 1MeV by a factor 0.015. The embrittlement in the pressure vessels of PWRs is thus dominated by the higher energy neutrons so that it is the values of C/M for the threshold detectors which are the more relevant indicators of the accuracy of the calculations for predicting such damage effects.

9 SUMMARY

Calculations have been performed for the H B Robinson Unit 2 PWR, at dosimetry positions in the reactor cavity and the surveillance capsule, using MCBEND with ENDF/B-VI nuclear data. The calculations show a slight underestimation of the reaction rates at the inner surface of the vessel at the surveillance position with a mean value of C/M of 0.94 ± 0.02 , where the uncertainty is the standard error on the mean. In the cavity there is a similar underestimation of the reaction rates of the threshold detectors with a mean value of C/M of 0.93 ± 0.02 .

The values of C/M for the low energy detectors in the cavity are all above 1.0 with a mean of 1.08 ± 0.02 . This distinct difference between the results for the high and low energy detectors is attributed to the greater sensitivity of the latter to uncertainties in the composition of the concrete which forms the outer region bounding the cavity. The results suggest that the back-scatter of neutrons by the concrete is overestimated in the calculations with the composition that is currently specified.

The uncertainties in the calculational route have been quantified. The major contributions are the uncertainties due to the iron inelastic cross-section, the water density, and the radial position of the surveillance capsule. The similarity of the mean values of C/M in the two measurement positions suggests that the error is most likely due to a common cause such as the water density or the source data. The departure of the mean C/Ms from unity is less than one standard deviation arising from such common uncertainties. The agreement suggests that the uncertainties assigned to the radial position of the surveillance detectors and the cross-sections of iron which each affect one position more than the other are too large.

In most cases the discrepancies between the values of C/M for the individual detectors and the mean values are less than one standard deviation based on the combined uncertainties due to the measurements and the detector cross-sections, i.e. the uncertainties which are relevant to that C/M alone. The only exception is the result for one of the three neptunium fission measurements in the cavity where the difference is just over one such standard deviation. The measurements and calculations are therefore consistent with each other.

These results show that MCBEND with data from ENDF/B-VI can be used to predict the neutron fluence in PWR pressure vessels to a high degree of accuracy.

REFERENCES

- 1 MCBEND User Guide for Version 9
ANSWERS /MCBEND(94)15
- 2 S.W. Power. An Analysis of the H B Robinson Unit 2 PWR using the Monte Carlo Code
MCBEND
RSWG/P(89)25
- 3 S. Newbon & S.J. Chucas. Further Analysis of the H B Robinson Unit 2 PWR using the
Monte Carlo Code MCBEND
SESD/6028/3.17
- 4 The International Reactor Dosimetry File (IRDF-85)
Cullen D.E. & McLaughlin P.K.
IAEA-NDS-41
- 5 Locke (Mrs) H F. Further Analysis of the H B Robinson Unit 2 PWR using the Monte
Carlo Code MCBEND with ENDF/B-VI Nuclear Data.
AEA RS 5579
- 6 Kocherov N P and McLaughlin P K. The International Dosimetry File (IRDF-90),
IAEA-NDS-141 October 1993.
- 7 Lippincott E.P. et al. Evaluation of Surveillance Capsule and Reactor Cavity Dosimetry
from H B Robinson Unit 2, Cycle 9
WCAP-11104, NUREG/CR-4576
- 8 Anderson S.L. Summary of H B Robinson PTS Analysis
RSAC-CPL-170
- 9 IAEA Directory of Reactors
- 10 Maerker R.E.
Private Communication
- 11 Kam F.B.K.
Private Communication.
- 12 Burstall R.F. & Webb S.G. FISPIN-6
IMAC/P(82)106
- 13 Nash G.
Private Communication
- 14 Nash G. A Fuel Management Study on a Pressurised Water Reactor
AEEW -R802
- 15 James M.F. The Relation between Power and Flux in Inventory Codes
IMAC(83)/P120

- 16 Dean C J & Eaton C R. The 1994 DICE Nuclear Data Library
AEA-RS 5697
- 17 Cullen D E. SIXPAK: A Code Designed to Check Double-Differential Correlated Data and Calculate "Equivalent" Uncorrelated Data.
UCRL-ID-110241
- 18 MacFarlane R E & Muir D W.
The NJOY Nuclear Data Processing System, Version 91.
LA-12740-M
- 19 Bendall D.E. New Thermal Treatment for MONK
Proceedings of the ICNC 91. International Conference on Nuclear Criticality Safety.
- 20 Maerker R.E. LEPRICON Analysis of Pressure Vessel Surveillance Dosimetry Inserted into
H B. Robinson-2 during Cycle 9
NUREG/CR-4439
- 21 Maerker R.
Private Communication
- 22 Ziver A K and Earwicker J
Processing of the Variance-Covariance Data from the ENDF/B-VI and IRDF-90 Nuclear
Data Libraries for use with the MCBEND Code.
AEA-TSD-0387
- 23 NEACRP Comparison of Codes for the Radiation Protection Assessment of Transportation
Packages. Solutions to Problems 1-4.
NEACRP-L-331 Table 43 (i)
- 24 Burstall R.F. Thermal Reactor Validation Work for the FISPIN Code
AEA RS 1138 (March 1992)
- 25 Newbon S.(Mrs.) The Analysis of NESDIP2 with ENDF/B-VI Nuclear Data.
AEA RS 5591 (February 1994)

Table 1 - Power History for Cycle 9

| Period | Days | Cumulative days | Mean Power MW(e) | MWd(e) | Cumulative MWd(e) | Fraction of Cycle |
|--------|------|-----------------|------------------|----------|-------------------|-------------------|
| 1 | 20 | 20 | 334.94 | 6698.8 | 6699 | 0.03 |
| 2 | 3 | 23 | 0 | 0 | 6699 | 0.03 |
| 3 | 78 | 101 | 511.96 | 39932.88 | 46632 | 0.22 |
| 4 | 2 | 103 | 48.98 | 97.96 | 46730 | 0.22 |
| 5 | 29 | 132 | 533.92 | 15483.68 | 62213 | 0.30 |
| 6 | 2 | 134 | 75.24 | 150.48 | 62364 | 0.30 |
| 7 | 89 | 223 | 496.78 | 44213.42 | 106577 | 0.51 |
| 8 | 4 | 227 | 45.79 | 183.16 | 106760 | 0.51 |
| 9 | 24 | 251 | 465.76 | 11178.24 | 117939 | 0.57 |
| 10 | 29 | 280 | 0.1 | 2.9 | 117942 | 0.57 |
| 11 | 100 | 380 | 507.67 | 50767 | 168709 | 0.81 |
| 12 | 16 | 396 | 11.95 | 191.2 | 168900 | 0.81 |
| 13 | 4 | 400 | 323.75 | 1295 | 170195 | 0.82 |
| 14 | 39 | 439 | 521.79 | 20349.81 | 190545 | 0.92 |
| 15 | 36 | 475 | 1.83 | 65.88 | 190610 | 0.92 |
| 16 | 16 | 491 | 286.15 | 4578.4 | 195189 | 0.94 |
| 17 | 7 | 498 | 503.43 | 3524.01 | 198713 | 0.95 |
| 18 | 26 | 524 | 363.22 | 9443.72 | 208157 | 1.00 |

Table 2 - Derivation of Activations Measured at the End of the Cycle

| Reaction | Scaling Factor* | Surveillance Position | | | Cavity | | |
|--|-----------------|--------------------------------------|-------------------------------|-------------|--------------------------------------|-------------------------------|-------------|
| | | Measured Saturation Activity (dps/a) | End-of Cycle Activity (dps/a) | Std Dev (%) | Measured Saturation Activity (dps/a) | End-of Cycle Activity (dps/a) | Std Dev (%) |
| Ti ⁴⁶ (n,p)Sc ⁴⁶ | 0.490 | 7.08E-16 | 3.47E-16 | 10 | 6.63E-18 | 3.25E-18 | 10 |
| Fe ⁵⁴ (n,p)Mn ⁵⁴ | 0.389 | 3.86E-15 | 1.50E-15 | 10 | 3.67E-17 | 1.43E-17 | 5 |
| Fe ⁵⁸ (n,γ)Fe ⁵⁹ | 0.465 | 4.42E-14 | 2.06E-14 | 12 | 2.93E-15 | 1.36E-15 | 8 |
| Ni ⁵⁸ (n,p)Co ⁵⁸ | 0.483 | 5.35E-15 | 2.58E-15 | 10 | 5.85E-17 | 2.83E-17 | 10 |
| Co ⁵⁹ (n,γ)Co ⁶⁰ | 0.102 | 6.81E-13 | 6.92E-14 | 5 | 1.20E-13 | 1.22E-14 | 5 |
| Cu ⁶³ (n,α)Co ⁶⁰ | 0.102 | 3.98E-17 | 4.04E-18 | 10 | 3.96E-19 | 4.02E-20 | 5 |
| U ²³⁵ (n,f)Zr ⁹⁵ | 0.478 | 3.33E-12 | 1.59E-12 | 5 | 1.26E-12 | 6.03E-13 | 5 |
| U ²³⁵ (n,f)Cs ¹³⁷ | 0.019 | 3.21E-12 | 6.22E-14 | 5 | 1.10E-12 | 2.13E-14 | 5 |
| U ²³⁵ (n,f)Ru ¹⁰³ | 0.463 | | | | 1.29E-12 | 5.97E-13 | 5 |
| U ²³⁸ (n,f)Zr ⁹⁵ | 0.478 | 1.90E-14 | 9.09E-15 | 5 | 3.09E-16 | 1.48E-16 | 5 |
| U ²³⁸ (n,f)Cs ¹³⁷ | 0.019 | 1.80E-14 | 3.49E-16 | 5 | 2.87E-16 | 5.56E-18 | 5 |
| U ²³⁸ (n,f)Ru ¹⁰³ | 0.463 | | | | 3.24E-16 | 1.50E-16 | 5 |
| Np ²³⁷ (n,f)Zr ⁹⁵ | 0.478 | 1.22E-13 | 5.84E-14 | 5 | 7.34E-15 | 3.51E-15 | 5 |
| Np ²³⁷ (n,f)Cs ¹³⁷ | 0.019 | 1.18E-13 | 2.29E-15 | 5 | 7.23E-15 | 1.40E-16 | 5 |
| Np ²³⁷ (n,f)Ru ¹⁰³ | 0.463 | | | | 7.82E-15 | 3.62E-15 | 5 |
| Sc ⁴⁵ (n,γ)Sc ⁴⁶ | 0.490 | | | | 5.77E-14 | 2.83E-14 | 10 |

* The scaling factor is the ratio of the activity of a detector at the end of the cycle to the saturation activity derived assuming the power history of Table 1 and a constant proportionality of reaction rate and reactor power.

Table 3 - Material Compositions

& MATERIALS FOR H.B.ROBINSON PWR (FROM WESTINGHOUSE/CPL DOT MODEL)
& K REMOVED FROM CONCRETE
MINNIE

MIXTURES 5

WEIGHT

& CORE REGION

M 1

U235 0.20647E-01
U238 0.62565
O 0.180760
H 0.11840E-01
B10 0.65507E-04
FE54 1.32525E-04
FE56 2.13598E-03
FE57 4.9755E-05
FE58 6.74250E-06
MN 0.42278E-04
CR50 5.2033E-05
CR52 1.04441E-03
CR53 1.20662E-04
CR54 3.05711E-05
NI58 1.98361E-03
NI60 7.90492E-04
NI61 3.48312E-05
NI62 1.13054E-04
NI64 2.98312E-05
ZR 0.15447

M 2

& WATER

H 0.88799
O 0.11191
B10 0.99829E-04

M 3

& STAINLESS STEEL SST304

FE54 3.933E-02
FE56 6.339E-01
FE57 1.4766E-02
FE58 2.001E-03
MN 0.19995E-01
CR50 7.923E-03
CR52 1.5903E-01
CR53 1.8373E-02
CR54 4.655E-03
NI58 6.72067E-02
NI60 2.67827E-02
NI61 1.18012E-03
NI62 3.83038E-03
NI64 1.0101E-03

Table 3 - Material Compositions continued

M 4

& CARBON STEEL AS33B
C 0.24999E-02
MN 0.12996E-01
FE54 5.58030E-02
FE56 8.99407E-01
FE57 2.09506E-02
FE58 2.83910E-03
NI58 3.69640E-03
NI60 1.47306E-03
NI61 6.49071E-05
NI62 2.10673E-04

M 5

& CONCRETE
& POTASSIUM (K) REMOVED TO SAVE SPACE
& (ELIMINATED BY DISTRIBUTING ITS FRACTION AMONGST THE OTHER
& ELEMENTS)
H 0.50903E-02
C 0.10183E-02
O 0.51189
NA 0.16288E-01
MG 0.22130E-02
AL 0.34530E-01
SI 0.346230
CA 0.44256E-01
FE54 2.19364E-03
FE56 3.53562E-02
FE57 8.23579E-04
FE58 1.111607E-04

MATERIALS 6

& CORE REGION #100
1 M1 4.2632 1.0
& EXCORE STAINLESS STEEL #200
2 M3 8.03 1.0
& EXCORE WATER #300
3 M2 0.7886 1.0
& EXCORE CARBON STEEL #400
4 M4 7.83 1.0
& INSULATION #500
5 M3 0.241 1.0
& CONCRETE #600
6 M5 2.20 1.0

Table 4 - Initial and Final Burn-up Distributions for the 9th Cycle

Initial

| | R | P | N | M | L | K | J | H | G | F | E | D | C | B | A |
|----|-------|---|-------|-------|-------|-------|-------|-------|-------|-------|-------|-------|-------|---|-------|
| 1 | | | | | | | 29488 | 22092 | 29122 | | | | | | |
| 2 | | | | | 0 | 0 | 0 | 0 | 0 | 0 | 0 | | | | |
| 3 | | | | 0 | 7496 | 6880 | 18737 | 23046 | 18784 | 6909 | 7439 | 0 | | | |
| 4 | | | 0 | 0 | 12016 | 19632 | 7254 | 19069 | 7196 | 19457 | 11850 | 0 | 0 | | |
| 5 | | 0 | 7400 | 12236 | 22054 | 11951 | 23149 | 0 | 22983 | 11840 | 21446 | 11980 | 7528 | 0 | |
| 6 | | 0 | 6941 | 19746 | 11917 | 19513 | 10360 | 21948 | 10100 | 19755 | 11897 | 19299 | 7021 | 0 | |
| 7 | 29286 | 0 | 18786 | 7132 | 22787 | 10247 | 19607 | 8280 | 19626 | 10112 | 23248 | 7248 | 18762 | 0 | 29302 |
| 8 | 21143 | 0 | 23006 | 18885 | 0 | 22293 | 8325 | 21170 | 8474 | 21792 | 0 | 19190 | 22733 | 0 | 21351 |
| 9 | 29064 | 0 | 18920 | 7344 | 22947 | 10266 | 19454 | 8290 | 19428 | 10186 | 23054 | 7282 | 18589 | 0 | 29194 |
| 10 | | 0 | 6934 | 19819 | 11918 | 19578 | 10173 | 21729 | 10112 | 19348 | 11611 | 19619 | 7020 | 0 | |
| 11 | | 0 | 7548 | 12051 | 21592 | 11809 | 22801 | 0 | 23117 | 11807 | 21876 | 12142 | 7584 | 0 | |
| 12 | | | 0 | 0 | 11868 | 19430 | 7287 | 18794 | 7333 | 19602 | 11785 | 0 | 0 | | |
| 13 | | | | 0 | 7507 | 6949 | 18618 | 23052 | 18752 | 6844 | 7581 | 0 | | | |
| 14 | | | | | 0 | 0 | 0 | 0 | 0 | 0 | 0 | | | | |
| 15 | | | | | | | 29058 | 22727 | 29271 | | | | | | |

Final

| | R | P | N | M | L | K | J | H | G | F | E | D | C | B | A |
|----|-------|-------|-------|-------|-------|-------|-------|-------|-------|-------|-------|-------|-------|-------|-------|
| 1 | | | | | | | 33102 | 26798 | 32689 | | | | | | |
| 2 | | | | | 7705 | 10479 | 11298 | 11988 | 11179 | 10208 | 7744 | | | | |
| 3 | | | | 8622 | 19365 | 20012 | 29978 | 33468 | 30031 | 20020 | 19360 | 8588 | | | |
| 4 | | | 8646 | 12384 | 23989 | 30820 | 20290 | 30225 | 20209 | 30746 | 24075 | 12661 | 8704 | | |
| 5 | | 7830 | 19312 | 24274 | 32490 | 23678 | 33927 | 13506 | 33691 | 23701 | 32176 | 24283 | 19482 | 7658 | |
| 6 | | 10375 | 20025 | 30931 | 23658 | 30403 | 22544 | 32792 | 22241 | 30594 | 23648 | 30484 | 19908 | 10017 | |
| 7 | 32962 | 11399 | 30059 | 20070 | 33290 | 22195 | 30566 | 20758 | 30573 | 22253 | 33843 | 19838 | 29698 | 10881 | 32816 |
| 8 | 25984 | 12077 | 33556 | 30027 | 13109 | 32875 | 20790 | 31894 | 20915 | 32636 | 13396 | 29949 | 32831 | 11656 | 26080 |
| 9 | 32729 | 11284 | 30090 | 20322 | 33761 | 22171 | 30243 | 20439 | 30276 | 22220 | 33810 | 20143 | 29654 | 11058 | 32833 |
| 10 | | 10158 | 19756 | 31046 | 23921 | 30448 | 22057 | 32215 | 21963 | 30033 | 23425 | 30977 | 20133 | 10180 | |
| 11 | | 7754 | 19344 | 24165 | 32343 | 23561 | 33250 | 13152 | 33686 | 23410 | 32374 | 24205 | 19533 | 7743 | |
| 12 | | | 8663 | 12640 | 24345 | 30564 | 19870 | 29607 | 20069 | 30633 | 23781 | 12444 | 8599 | | |
| 13 | | | | 8615 | 19118 | 19680 | 29527 | 33149 | 29734 | 19689 | 19517 | 8697 | | | |
| 14 | | | | | 7691 | 10285 | 11373 | 11862 | 11076 | 10248 | 7814 | | | | |
| 15 | | | | | | | 32748 | 27443 | 32842 | | | | | | |

The numbering of the assemblies is in the scheme used by Westinghouse.

Table 5 - Fuel Composition at the Beginning, Middle and End of the 9th Cycle

| | | Fission fractions | | | | Fraction of source neutrons | | | | | n/MW |
|--|---------|-------------------|---------|---------|---------|-----------------------------|-------|-------|-------|----------|---------|
| | | U235 | U238 | Pu239 | Pu241 | U235 | U238 | Pu239 | Pu241 | Pu Total | |
| <u>Average for rest of core</u> | | | | | | | | | | | |
| | Initial | 0.658 | 0.071 | 0.240 | 0.030 | 0.620 | 0.077 | 0.267 | 0.035 | 0.302 | 7.87E16 |
| | Middle | 0.548 | 0.076 | 0.324 | 0.051 | 0.507 | 0.081 | 0.354 | 0.058 | 0.412 | 7.98E16 |
| | Final | 0.457 | 0.081 | 0.386 | 0.076 | 0.416 | 0.085 | 0.414 | 0.085 | 0.499 | 8.01E16 |
| <u>Assemblies adjacent to surveillance capsule</u> | | | | | | | | | | | |
| inner | Initial | 0.940 | 0.060 | 0.000 | 0.000 | 0.931 | 0.069 | 0.000 | 0.000 | 0.000 | 7.59E16 |
| | Middle | 0.763 | 0.066 | 0.167 | 0.004 | 0.732 | 0.073 | 0.190 | 0.005 | 0.195 | 7.77E16 |
| | Final | 0.634 | 0.071 | 0.273 | 0.022 | 0.595 | 0.077 | 0.303 | 0.025 | 0.328 | 7.90E16 |
| outer | Initial | 0.940 | 0.060 | 0.000 | 0.000 | 0.931 | 0.069 | 0.000 | 0.000 | 0.000 | 7.59E16 |
| | Middle | 0.804 | 0.064 | 0.130 | 0.002 | 0.778 | 0.072 | 0.148 | 0.002 | 0.150 | 7.72E16 |
| | Final | 0.701 | 0.068 | 0.220 | 0.011 | 0.665 | 0.075 | 0.247 | 0.012 | 0.260 | 7.83E16 |
| <u>Assemblies adjacent to 0° scoring position</u> | | | | | | | | | | | |
| outer | Initial | 0.352 | 0.087 | 0.454 | 0.107 | 0.314 | 0.089 | 0.479 | 0.117 | 0.596 | 8.20E16 |
| | Middle | 0.328 | 0.089 | 0.468 | 0.115 | 0.292 | 0.091 | 0.491 | 0.126 | 0.617 | 8.22E16 |
| | Final | 0.307 | 0.090 | 0.480 | 0.123 | 0.272 | 0.092 | 0.503 | 0.134 | 0.636 | 8.25E16 |
| inner | Initial | 0.460 | 0.080 | 0.390 | 0.070 | 0.419 | 0.084 | 0.419 | 0.078 | 0.497 | 8.08E16 |
| | Middle | 0.434 | 0.082 | 0.406 | 0.078 | 0.393 | 0.086 | 0.435 | 0.086 | 0.521 | 8.11E16 |
| | Final | 0.397 | 0.084 | 0.428 | 0.091 | 0.357 | 0.087 | 0.455 | 0.100 | 0.555 | 8.15E16 |
| Neutrons per fission | | 2.43 | 2.8 | 2.87 | 2.97 | | | | | | |
| n/s per MW | | 7.53E16 | 8.54E16 | 8.54E16 | 8.72E16 | | | | | | |

The positions of the "inner" and "outer" fuel assemblies for the 0° and 20° scoring positions are shown in figure 6.

Table 6 - Calculation of Source Intensity

| | | Fission | | Energy/fission | | Neutrons/fission | | Neutrons/MeV | | Neutrons/s/MW | |
|---------------------------------|-------|----------|-------|----------------|------|------------------|------|--------------|---------|-----------------|-----------------|
| | | fraction | unc. | (MeV) | unc. | | unc. | | unc. | | unc. |
| CORE
129* | U235 | 0.548 | 0.152 | 201.7 | 0.6 | 2.43 | 0.01 | 6.60E-03 | 3.35E-5 | 7.98E+16 | 1.57E+15 |
| | U238 | 0.076 | 0.008 | 205.0 | 0.9 | 2.80 | 0.01 | 1.04E-03 | 5.87E-6 | | |
| | Pu239 | 0.324 | 0.110 | 210.0 | 0.9 | 2.87 | 0.01 | 4.43E-03 | 2.45E-5 | | |
| | Pu241 | 0.051 | 0.035 | 212.9 | 1.0 | 2.97 | 0.01 | 7.11E-04 | 4.11E-6 | | |
| | All | 1.000 | | 205.0 | | 2.63 | | 1.28E-02 | 2.51E-4 | | |
| CAVITY
INNER
4* | U235 | 0.328 | 0.016 | 201.7 | 0.6 | 2.43 | 0.01 | 3.95E-03 | 2.01E-5 | 8.22E+16 | 3.14E+14 |
| | U238 | 0.089 | 0.004 | 205.0 | 0.9 | 2.80 | 0.01 | 1.22E-03 | 6.88E-6 | | |
| | Pu239 | 0.468 | 0.023 | 210.0 | 0.9 | 2.87 | 0.01 | 6.40E-03 | 3.53E-5 | | |
| | Pu241 | 0.115 | 0.006 | 212.9 | 1.0 | 2.97 | 0.01 | 1.60E-03 | 9.27E-6 | | |
| | All | 1.000 | | 207.2 | | 2.73 | | 1.32E-02 | 5.03E-5 | | |
| CAVITY
OUTER
8* | U235 | 0.434 | 0.022 | 201.7 | 0.6 | 2.43 | 0.01 | 5.23E-03 | 2.66E-5 | 8.10E+16 | 3.41E+14 |
| | U238 | 0.082 | 0.004 | 205.0 | 0.9 | 2.80 | 0.01 | 1.12E-03 | 6.34E-6 | | |
| | Pu239 | 0.406 | 0.020 | 210.0 | 0.9 | 2.87 | 0.01 | 5.55E-03 | 3.06E-5 | | |
| | Pu241 | 0.078 | 0.004 | 212.9 | 1.0 | 2.97 | 0.01 | 1.09E-03 | 6.29E-6 | | |
| | All | 1.000 | | 206.2 | | 2.68 | | 1.30E-02 | 5.46E-5 | | |
| SURV.
CAPSULE
INNER
8* | U235 | 0.763 | 0.038 | 201.7 | 0.6 | 2.43 | 0.01 | 9.19E-03 | 4.67E-5 | 7.76E+16 | 4.89E+14 |
| | U238 | 0.066 | 0.003 | 205.0 | 0.9 | 2.80 | 0.01 | 9.01E-04 | 5.10E-6 | | |
| | Pu239 | 0.167 | 0.008 | 210.0 | 0.9 | 2.87 | 0.01 | 2.28E-03 | 1.26E-5 | | |
| | Pu241 | 0.004 | 0.000 | 212.9 | 1.0 | 2.97 | 0.01 | 5.58E-05 | 3.22E-7 | | |
| | All | 1.000 | | 203.3 | | 2.53 | | 1.24E-02 | 7.84E-5 | | |
| SURV.
CAPSULE
OUTER
8* | U235 | 0.804 | 0.040 | 201.7 | 0.6 | 2.43 | 0.01 | 9.69E-03 | 4.92E-5 | 7.72E+16 | 5.12E+14 |
| | U238 | 0.064 | 0.003 | 205.0 | 0.9 | 2.80 | 0.01 | 8.74E-04 | 4.95E-6 | | |
| | Pu239 | 0.130 | 0.007 | 210.0 | 0.9 | 2.87 | 0.01 | 1.78E-03 | 9.81E-6 | | |
| | Pu241 | 0.002 | 0.000 | 212.9 | 1.0 | 2.97 | 0.01 | 2.79E-05 | 1.61E-7 | | |
| | All | 1.000 | | 203.0 | | 2.51 | | 1.24E-02 | 8.21E-5 | | |
| Total Neutrons/s/MW | | | | | | | | | | 7.96E+16 | 1.29E+15 |

* number of assemblies

unc. = uncertainty

The positions of the "inner" and "outer" fuel assemblies for the cavity and surveillance capsule scoring positions are shown in figure 6.

Table 7 - Source Spectra for Fresh Fuel Assemblies in Peripheral Locations

| Energy Group | Upper Energy (MeV) | Fraction in energy group | | | Initial Mid | Final Mid |
|--------------|----------------------|--------------------------|----------|----------|-------------|-----------|
| | | Initial | Midcycle | Final | | |
| | | 100% U | 20% Pu | 30% Pu | | |
| 1 | 1.46E+01 | 4.30E-05 | 4.48E-05 | 4.57E-05 | 0.960 | 1.020 |
| 2 | 1.35E+01 | 9.10E-05 | 9.48E-05 | 9.67E-05 | 0.960 | 1.020 |
| 3 | 1.25E+01 | 3.28E-04 | 3.41E-04 | 3.48E-04 | 0.961 | 1.019 |
| 4 | 1.13E+01 | 7.69E-04 | 7.96E-04 | 8.10E-04 | 0.966 | 1.017 |
| 5 | 1.00E+01 | 2.74E-03 | 2.82E-03 | 2.87E-03 | 0.969 | 1.016 |
| 6 | 8.50E+00 | 8.72E-03 | 8.97E-03 | 9.10E-03 | 0.972 | 1.014 |
| 7 | 7.00E+00 | 1.25E-02 | 1.28E-02 | 1.29E-02 | 0.976 | 1.012 |
| 8 | 6.07E+00 | 4.20E-02 | 4.28E-02 | 4.32E-02 | 0.980 | 1.010 |
| 9 | 4.72E+00 | 7.15E-02 | 7.26E-02 | 7.31E-02 | 0.986 | 1.007 |
| 10 | 3.68E+00 | 9.59E-02 | 9.68E-02 | 9.73E-02 | 0.991 | 1.005 |
| 11 | 2.87E+00 | 2.35E-01 | 2.36E-01 | 2.36E-01 | 0.997 | 1.002 |
| 12 | 1.74E+00 | 3.66E-01 | 3.64E-01 | 3.63E-01 | 1.006 | 0.997 |
| 13 | 6.00E-01 | 7.08E-02 | 7.00E-02 | 6.96E-02 | 1.012 | 0.994 |
| 14 | 3.90E-01 | 7.74E-02 | 7.63E-02 | 7.57E-02 | 1.015 | 0.993 |
| 15 | 1.10E-01
6.74E-02 | 7.99E-03 | 7.85E-03 | 7.79E-03 | 1.017 | 0.992 |

Table 8 - Comparison of Reaction-rates at the Beginning, Middle and End of the 9th Cycle (Taken from Calculations with IRDF-85 data (Ref 5)).

Surveillance position

| Response | Initial | | Middle | | Final | |
|--------------------|----------|--------|----------|--------|----------|--------|
| | dps/atom | sd (%) | dps/atom | sd (%) | dps/atom | sd (%) |
| Ti46(n,p) | 4.36E-16 | 2.2 | 4.83E-16 | 2.1 | 5.03E-16 | 1.9 |
| Fe54(n,p) | 2.56E-15 | 1.4 | 2.82E-15 | 1.3 | 2.97E-15 | 1.2 |
| Fe58(n, γ) | 2.79E-14 | 2.7 | 3.14E-14 | 2.9 | 3.32E-14 | 2.8 |
| Ni58(n,p) | 3.40E-15 | 1.3 | 3.76E-15 | 1.3 | 3.95E-15 | 1.1 |
| Co59(n, γ) | 1.25E-12 | 2.4 | 1.42E-12 | 2.3 | 1.47E-12 | 2.2 |
| Cu63(n, α) | 2.83E-17 | 3.7 | 3.18E-17 | 3.5 | 3.20E-17 | 3.1 |
| U235(n,fx) | 1.21E-11 | 3.0 | 1.36E-11 | 3.1 | 1.45E-11 | 3.0 |
| U238(n,fx) | 1.12E-14 | 1.0 | 1.24E-14 | 0.9 | 1.30E-14 | 0.8 |
| Np237(n,fx) | 8.00E-14 | 0.7 | 9.02E-14 | 0.7 | 9.36E-14 | 0.6 |
| Sc45(n, γ) | 5.81E-13 | 3.0 | 6.54E-13 | 3.2 | 6.93E-13 | 3.1 |

Cavity position

| Response | Initial | | Middle | | Final | |
|--------------------|----------|--------|----------|--------|----------|--------|
| | dps/atom | sd (%) | dps/atom | sd (%) | dps/atom | sd (%) |
| Ti46(n,p) | 3.76E-18 | 2.0 | 5.37E-18 | 1.7 | 5.65E-18 | 2.2 |
| Fe54(n,p) | 2.26E-17 | 1.4 | 3.20E-17 | 1.2 | 3.41E-17 | 1.4 |
| Fe58(n, γ) | 1.82E-15 | 2.6 | 2.35E-15 | 2.6 | 2.52E-15 | 4.2 |
| Ni58(n,p) | 3.52E-17 | 1.1 | 4.95E-17 | 0.9 | 5.29E-17 | 1.1 |
| Co59(n, γ) | 7.99E-14 | 2.1 | 1.03E-13 | 2.3 | 1.13E-13 | 3.2 |
| Cu63(n, α) | 2.71E-19 | 2.7 | 3.96E-19 | 2.5 | 4.15E-19 | 3.2 |
| U235(n,fx) | 7.44E-13 | 2.9 | 9.61E-13 | 3.1 | 1.04E-12 | 4.8 |
| U238(n,fx) | 1.53E-16 | 0.8 | 2.14E-16 | 0.7 | 2.31E-16 | 0.8 |
| Np237(n,fx) | 3.49E-15 | 0.4 | 4.81E-15 | 0.4 | 5.18E-15 | 0.4 |
| Sc45(n, γ) | 3.49E-14 | 3.0 | 4.49E-14 | 3.1 | 4.87E-14 | 5.0 |

Table 9 - Ratios of the End-of-Cycle Activities to the Reaction Rates at Mid-cycle

| Reaction | Ratio of End-of Cycle Activity to Reaction Rate at Mid-cycle | |
|--|--|--------|
| | Surveillance Position | Cavity |
| Ti ⁴⁶ (n,p)Sc ⁴⁶ | 0.5024 | 0.5029 |
| Fe ⁵⁴ (n,p)Mn ⁵⁴ | 0.3924 | 0.3832 |
| Fe ⁵⁸ (n,γ)Fe ⁵⁹ | 0.4874 | 0.4931 |
| Ni ⁵⁸ (n,p)Co ⁵⁸ | 0.4999 | 0.5045 |
| Co ⁵⁹ (n,γ)Co ⁶⁰ | 0.1003 | 0.1001 |
| Cu ⁶³ (n,α)Co ⁶⁰ | 0.0995 | 0.0966 |
| U ²³⁵ (n,f)Zr ⁹⁵ | 0.4953 | 0.5053 |
| U ²³⁵ (n,f)Cs ¹³⁷ | 0.0193 | 0.0187 |
| U ²³⁵ (n,f)Ru ¹⁰³ | 0.4824 | 0.4947 |
| U ²³⁸ (n,f)Zr ⁹⁵ | 0.5016 | 0.5067 |
| U ²³⁸ (n,f)Cs ¹³⁷ | 0.0193 | 0.0189 |
| U ²³⁸ (n,f)Ru ¹⁰³ | 0.4895 | 0.4959 |
| Np ²³⁷ (n,f)Zr ⁹⁵ | 0.4913 | 0.5044 |
| Np ²³⁷ (n,f)Cs ¹³⁷ | 0.0191 | 0.0187 |
| Np ²³⁷ (n,f)Ru ¹⁰³ | 0.4781 | 0.4937 |
| Sc ⁴⁵ (n,γ)Sc ⁴⁶ | 0.5082 | 0.5150 |

The factors in the Table were derived using the power history of Table 1 together with the variation of the ratios of reaction rates to power as calculated in Reference 5. These reaction rates were obtained with IRDF-85 data at three stages during the cycle and they are reproduced in Table 8.

Table 10 - Calculated Reaction Rates

| Reaction | Surveillance Position | | | Cavity | | |
|--|----------------------------------|-------------|--|----------------------------------|-------------|--|
| | Calculated Reaction Rate (dps/a) | Std Dev (%) | Calculated End-of-Cycle Activity (dps/a) | Calculated Reaction Rate (dps/a) | Std Dev (%) | Calculated End-of-Cycle Activity (dps/a) |
| Ti ⁴⁶ (n,p)Sc ⁴⁶ | 5.89E-16 | 0.9 | 2.96E-16 | 6.43E-18 | 2.6 | 3.19E-18 |
| Fe ⁵⁴ (n,p)Mn ⁵⁴ | 3.81E-15 | 5.6 | 1.50E-15 | 3.76E-17 | 1.5 | 1.43E-17 |
| Fe ⁵⁸ (n,γ)Fe ⁵⁹ | 4.10E-14 | 2.9 | 2.00E-14 | 3.17E-15 | 2.1 | 1.55E-15 |
| Ni ⁵⁸ (n,p)Co ⁵⁸ | 5.19E-15 | 7.6 | 2.59E-15 | 5.09E-17 | 1.3 | 2.54E-17 |
| Co ⁵⁹ (n,γ)Co ⁶⁰ | 1.78E-12 | 3.0 | 1.78E-13 | 1.39E-13 | 3.6 | 1.38E-14 |
| Cu ⁶³ (n,α)Co ⁶⁰ | 3.66E-17 | 1.0 | 3.64E-18 | 4.41E-19 | 0.8 | 4.22E-20 |
| U ²³⁵ (n,f)Zr ⁹⁵ | 1.72E-11 | 3.1 | 8.63E-12 | 1.25E12 | 2.1 | 6.26E-13 |
| U ²³⁵ (n,f)Cs ¹³⁷ | 1.72E-11 | 3.1 | 3.32E-13 | 1.25E12 | 2.1 | 2.34E-14 |
| U ²³⁵ (n,f)Ru ¹⁰³ | 1.72E-11 | 3.1 | 8.42E-12 | 1.25E12 | 2.1 | 6.13E-13 |
| U ²³⁸ (n,f)Zr ⁹⁵ | 1.63E-14 | 2.7 | 8.07E-15 | 2.87E-16 | 5.6 | 1.40E-16 |
| U ²³⁸ (n,f)Cs ¹³⁷ | 1.63E-14 | 2.7 | 3.14E-16 | 2.87E-16 | 5.6 | 5.30E-18 |
| U ²³⁸ (n,f)Ru ¹⁰³ | 1.63E-14 | 2.7 | 7.86E-15 | 2.87E-16 | 5.6 | 1.41E-16 |
| Np ²³⁷ (n,f)Zr ⁹⁵ | 1.14E-13 | 4.0 | 5.60E-14 | 6.21E-15 | 0.9 | 3.10E-15 |
| Np ²³⁷ (n,f)Cs ¹³⁷ | 1.14E-13 | 4.0 | 2.18E-15 | 6.21E-15 | 0.9 | 1.15E-16 |
| Np ²³⁷ (n,f)Ru ¹⁰³ | 1.14E-13 | 4.0 | 5.45E-14 | 6.21E-15 | 0.9 | 3.03E-15 |
| Sc ⁴⁵ (n,γ)Sc ⁴⁶ | 8.17E-13 | 3.2 | 4.15E-13 | 5.80E-14 | 2.1 | 2.95E-14 |

The standard deviations are those given by the Monte Carlo statistics.

The calculated reaction rates are for the mid-cycle power distribution normalised to 2300MW

The activations at the end of the cycle are derived by applying the factors given in Table 9.

The activations at the end of the cycle for the cavity detectors include the correction factor of 0.989 for asymmetry of the assembly power as discussed in section 5.

Table 11 - Calculated Uncertainties arising from Cross-Sections

Surveillance position

| Reaction | Oxygen
Total
% | Hydrogen
Total
% | Iron
(pressure vessel)
% | Iron
(inner steel)
% | Total
uncertainty
% |
|--------------------|----------------------|------------------------|--------------------------------|----------------------------|---------------------------|
| Ti46(n,p) | 0.89 | 1.38 | 0.47 | 5.6 | 6.29 |
| Fe54(n,p) | 0.84 | 1.63 | 0.3 | 4.6 | 5.23 |
| Fe58(n, γ) | 0.68 | 1.44 | 0.01 | 1.1 | 1.94 |
| Ni58(n,p) | 0.83 | 1.66 | 0.28 | 4.6 | 5.22 |
| Co59(n, γ) | 0.68 | 1.39 | 0.01 | 1 | 1.85 |
| Cu63(n, α) | 0.92 | 1.17 | 0.51 | 6.1 | 6.78 |
| U235(n,fx) | 0.68 | 1.44 | 0.01 | 1.1 | 1.94 |
| U238(n,fx) | 0.73 | 1.92 | 0.25 | 3.3 | 4.10 |
| Np237(n,fx) | 0.78 | 1.85 | 0.11 | 2.79 | 3.44 |
| Sc45(n, γ) | 0.68 | 1.44 | 0.01 | 1.1 | 1.94 |

Cavity position

| Reaction | Oxygen
Total
% | Hydrogen
Total
% | Iron
(pressure vessel)
% | Iron
(inner steel)
% | Total
uncertainty
% |
|--------------------|----------------------|------------------------|--------------------------------|----------------------------|---------------------------|
| Ti46(n,p) | 0.87 | 1.21 | 11.4 | 5.6 | 17.07 |
| Fe54(n,p) | 0.83 | 1.43 | 8.8 | 4.8 | 13.70 |
| Fe58(n, γ) | 0.86 | 1.88 | 0.33 | 3 | 3.92 |
| Ni58(n,p) | 0.8 | 1.51 | 8.4 | 4.7 | 13.21 |
| Co59(n, γ) | 0.86 | 1.9 | 0.44 | 2.9 | 3.94 |
| Cu63(n, α) | 0.9 | 1.05 | 12.4 | 6 | 18.45 |
| U235(n,fx) | 0.84 | 1.89 | 0.3 | 3.1 | 3.98 |
| U238(n,fx) | 0.72 | 1.74 | 6.96 | 4.4 | 11.52 |
| Np237(n,fx) | 0.77 | 1.85 | 2.80 | 3.44 | 4.87 |
| Sc45(n, γ) | 0.84 | 1.89 | 0.29 | 3.1 | 3.97 |

Table 12 - Uncertainties Due to the Detector Cross-sections

| Response | Surveillance
Uncertainty
1 s.d % | Cavity
Uncertainty
1 s.d % |
|--------------------|---|---|
| Ti46(n,p) | 5.3% | 5.2% |
| Fe54(n,p) | 4.2% | 3.1% |
| Fe58(n, γ) | 5.0% | 5.0% |
| Ni58(n,p) | 4.3% | 4.1% |
| Co59(n, γ) | 1.0% | 1.0% |
| Cu63(n, α) | 3.8% | 3.6% |
| U235(n,fx) | 0.2% | 0.2% |
| U238(n,fx) | 0.7% | 1.0% |
| Np237(n,fx) | 9.9% | 9.1% |
| Sc45(n, γ) | 3.9% | 3.9% |

Table 13 - Correction Factors and Uncertainties

Surveillance position

| Reason for Uncertainty | Described in section: | Uncertainty % |
|--|-----------------------|---------------|
| Cross-sections | 7.1 | see Table 11 |
| Dimensions | 7.2 | 2.5 |
| Radial variation of flux | 7.3 | 3.0 |
| Radial position | 7.3 | 20.0 |
| Coolant density | 7.4 | 6.0 |
| Steel density | 7.4 | 3.0 |
| Source intensity | 7.6 | 4.0 |
| Core source data | 7.7 | 2.9 |
| Fission spectra (High energy reactions only) | 7.8 | 3.5 |
| Detector response function | 7.9 | see Table 12 |

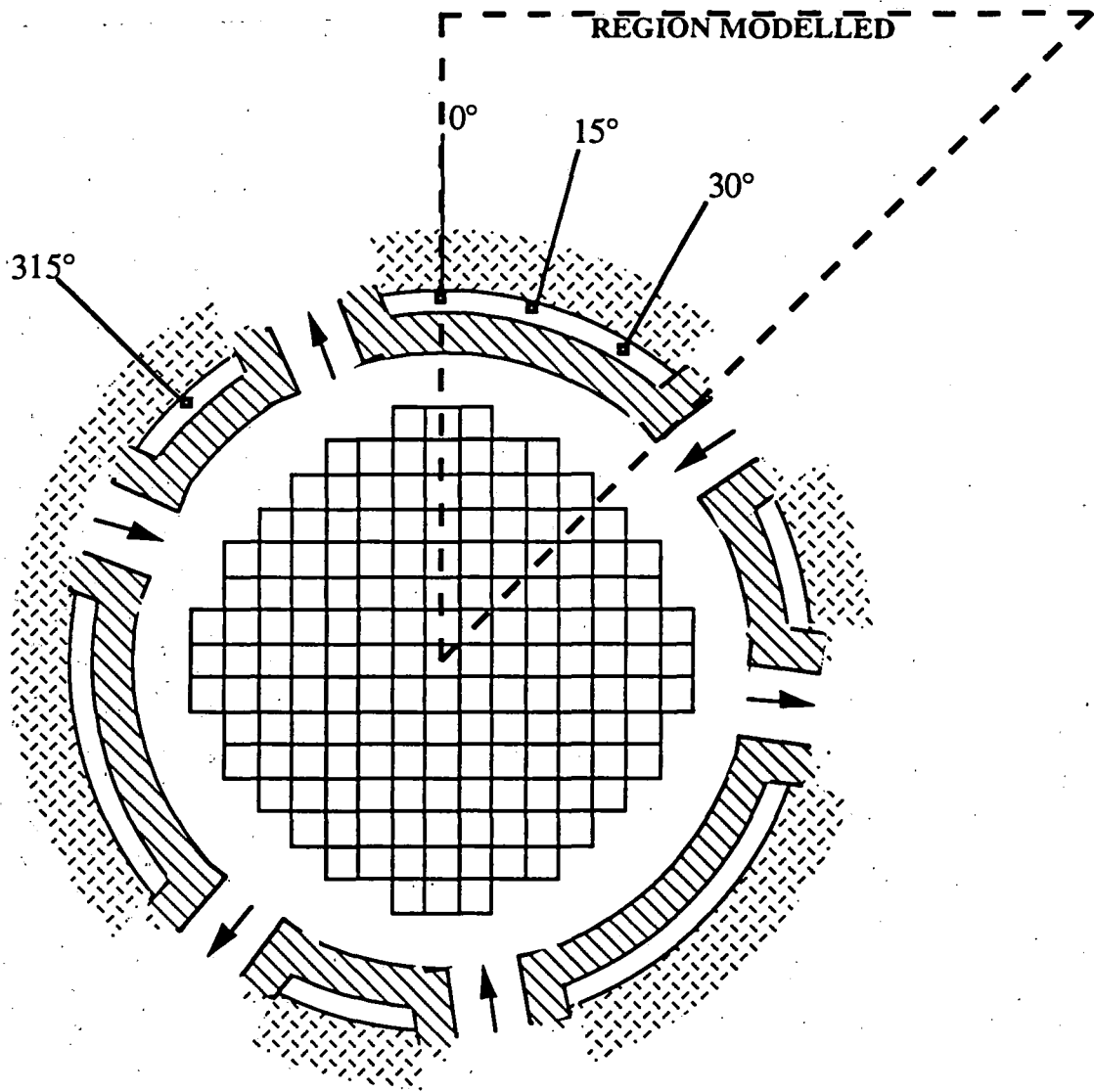
Cavity position

| Reason for Correction/Uncertainty | Described in section: | Correction factor | Uncertainty % |
|--|-----------------------|-------------------|---------------|
| Correction
Core Asymmetry | 5 | 0.989 | |
| Uncertainty
Cross-sections | 7.1 | | see Table 11 |
| Dimensions | 7.2 | | 2.5 |
| Scoring Region | 7.2 | | 10.0 |
| Coolant density | 7.4 | | 6.0 |
| Steel density High Energies | 7.4 | | 6.0 |
| Low Energies | | | 3.0 |
| Source intensity | 7.6 | | 3.0 |
| Core source data | 7.7 | | 2.9 |
| Fission spectra (High energy reactions only) | 7.8 | | 4.0 |
| Detector response function | 7.9 | | see Table 12 |

Table 14 - Comparison of Calculated and Measured Activations

| Reaction | Measurement
(dps/a) | Std Dev
(%) | Calculation
(dps/a) | Std Dev
(%) | C/M | Std Dev
(%) |
|--|------------------------|----------------|------------------------|----------------|------|----------------|
| <u>Surveillance Position</u> | | | | | | |
| Ti ⁴⁶ (n,p)Sc ⁴⁶ | 3.47E-16 | 10 | 2.96E-16 | 23.83 | 0.85 | 25.84 |
| Fe ⁵⁴ (n,p)Mn ⁵⁴ | 1.50E-15 | 10 | 1.50E-15 | 24.00 | 1.00 | 26.00 |
| Fe ⁵⁸ (n,γ)Fe ⁵⁹ | 2.06E-14 | 12 | 2.00E-14 | 22.90 | 0.97 | 25.85 |
| Ni ⁵⁸ (n,p)Co ⁵⁸ | 2.58E-15 | 10 | 2.59E-15 | 24.55 | 1.00 | 26.51 |
| Co ⁵⁹ (n,γ)Co ⁶⁰ | 6.92E-14 | 5 | 1.78E-13 | 22.37 | * | |
| Cu ⁶³ (n,α)Co ⁶⁰ | 4.04E-18 | 10 | 3.64E-18 | 23.68 | 0.90 | 25.71 |
| U ²³⁵ (n,f)Zr ⁹⁵ | 1.59E-12 | 5 | 8.63E-12 | 22.37 | * | |
| U ²³⁵ (n,f)Cs ¹³⁷ | 6.22E-14 | 5 | 3.32E-13 | 22.37 | * | |
| U ²³⁸ (n,f)Zr ⁹⁵ | 9.09E-15 | 5 | 8.07E-15 | 22.89 | 0.89 | 23.43 |
| U ²³⁸ (n,f)Cs ¹³⁷ | 3.49E-16 | 5 | 3.14E-15 | 22.89 | 0.90 | 23.43 |
| Np ²³⁷ (n,f)Zr ⁹⁵ | 5.84E-14 | 5 | 5.60E-14 | 25.02 | 0.96 | 25.51 |
| Np ²³⁷ (n,f)Cs ¹³⁷ | 2.29E-15 | 5 | 2.18E-15 | 25.02 | 0.95 | 25.51 |
| <u>Cavity</u> | | | | | | |
| Ti ⁴⁶ (n,p)Sc ⁴⁶ | 3.25E-18 | 10 | 3.19E-18 | 23.22 | 0.98 | 25.28 |
| Fe ⁵⁴ (n,p)Mn ⁵⁴ | 1.43E-17 | 5 | 1.43E-17 | 20.34 | 1.00 | 20.95 |
| Fe ⁵⁸ (n,γ)Fe ⁵⁹ | 1.36E-15 | 8 | 1.55E-15 | 14.70 | 1.14 | 16.73 |
| Ni ⁵⁸ (n,p)Co ⁵⁸ | 2.83E-17 | 10 | 2.54E-17 | 20.18 | 0.90 | 22.52 |
| Co ⁵⁹ (n,γ)Co ⁶⁰ | 1.22E-14 | 5 | 1.38E-14 | 14.17 | 1.13 | 15.02 |
| Cu ⁶³ (n,α)Co ⁶⁰ | 4.02E-20 | 5 | 4.22E-20 | 23.84 | 1.05 | 24.36 |
| U ²³⁵ (n,f)Zr ⁹⁵ | 6.03E-13 | 5 | 6.26E-13 | 13.84 | 1.04 | 14.71 |
| U ²³⁵ (n,f)Cs ¹³⁷ | 2.13E-14 | 5 | 2.34E-14 | 13.84 | 1.10 | 14.71 |
| U ²³⁵ (n,f)Ru ¹⁰³ | 5.97E-13 | 5 | 6.13E-13 | 13.84 | 1.03 | 14.71 |
| U ²³⁸ (n,f)Zr ⁹⁵ | 1.48E-16 | 5 | 1.40E-16 | 19.47 | 0.95 | 20.10 |
| U ²³⁸ (n,f)Cs ¹³⁷ | 5.56E-18 | 5 | 5.30E-18 | 19.47 | 0.95 | 20.10 |
| U ²³⁸ (n,f)Ru ¹⁰³ | 1.50E-16 | 5 | 1.41E-16 | 19.47 | 0.94 | 20.10 |
| Np ²³⁷ (n,f)Zr ⁹⁵ | 3.51E-15 | 5 | 3.10E-15 | 19.13 | 0.88 | 19.13 |
| Np ²³⁷ (n,f)Cs ¹³⁷ | 1.40E-16 | 5 | 1.15E-16 | 19.13 | 0.82 | 19.13 |
| Np ²³⁷ (n,f)Ru ¹⁰³ | 3.62E-15 | 5 | 3.03E-15 | 19.13 | 0.84 | 19.13 |
| Sc ⁴⁵ (n,γ)Sc ⁴⁶ | 2.83E-14 | 10 | 2.95E-14 | 14.37 | 1.04 | 17.51 |

* The effect of the gadolinium covers fitted to the detectors for these measurements was not included in the calculations and therefore no meaningful values of C/M can be derived.



Notes: Various directions have been used as 0° on H.B.Robinson, the system given here is that throughout this report.
In the calculation the core is assumed to be symmetrical and the 315° position is replaced by a 45° position.

Figure 1 - Plan View showing Sector Modelled and Measurement Positions

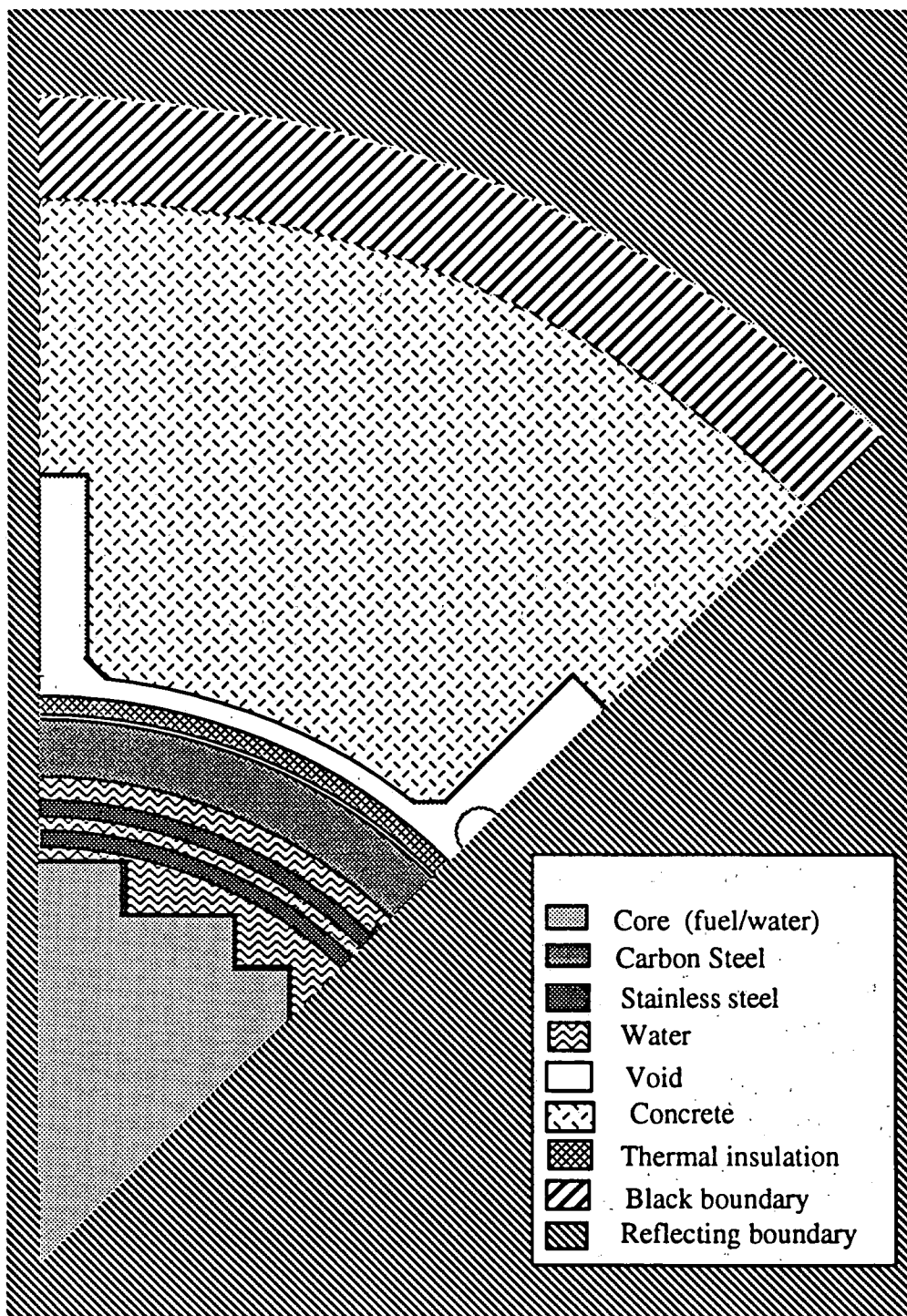


Figure 2 - Plan View of the Model showing Materials

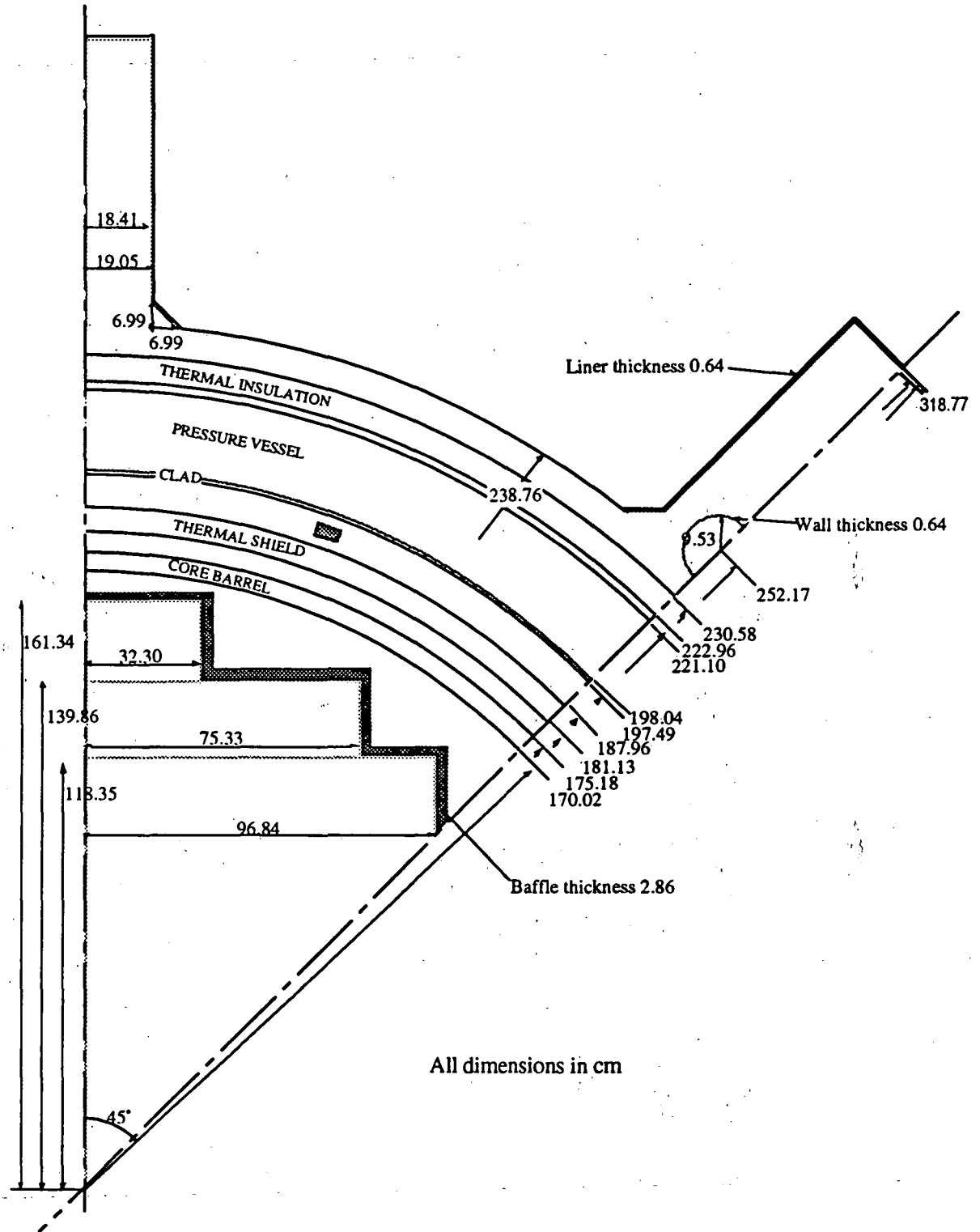


Figure 3 - Plan View of the Model showing Dimensions

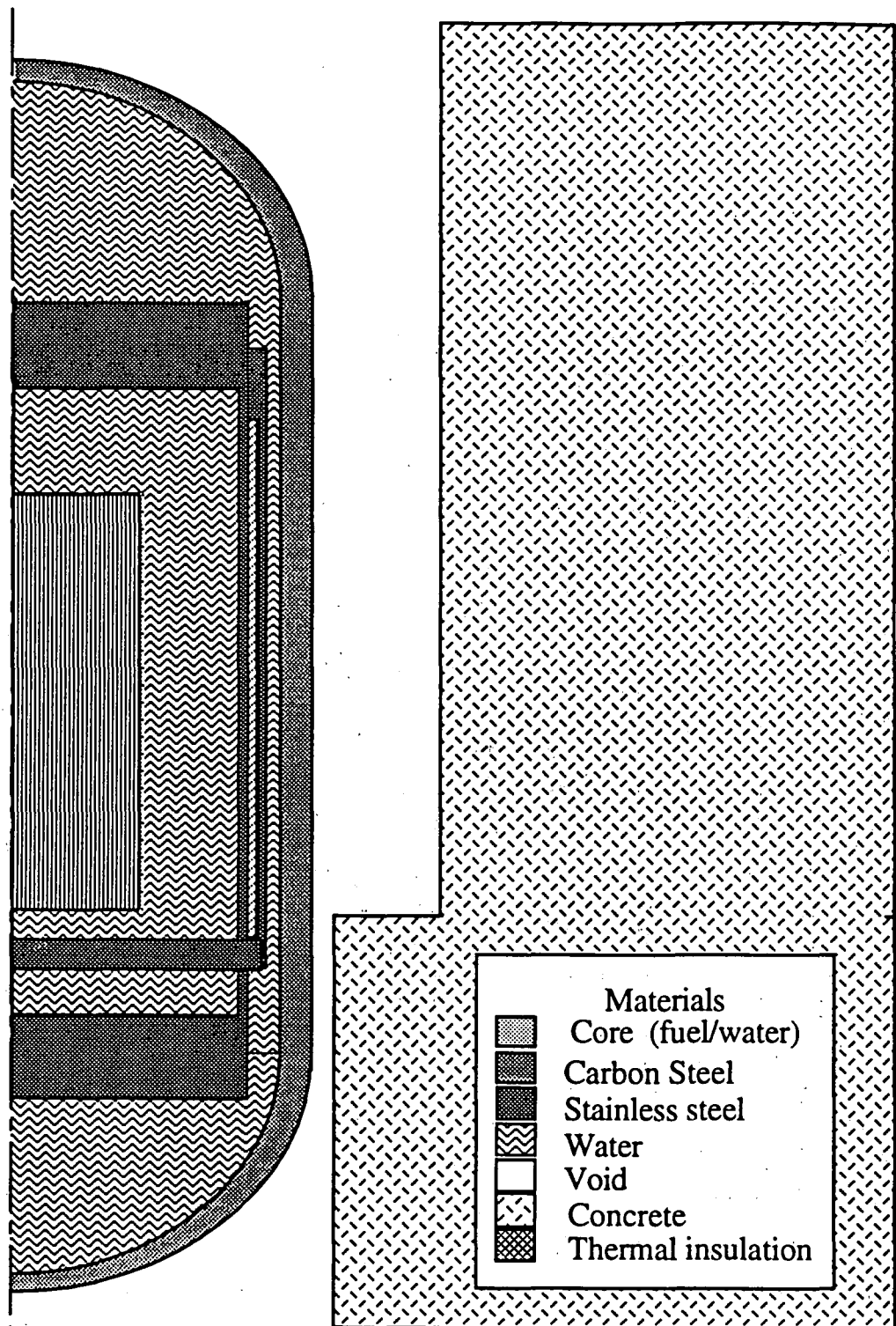


Figure 4 - Side View of the Model showing Materials

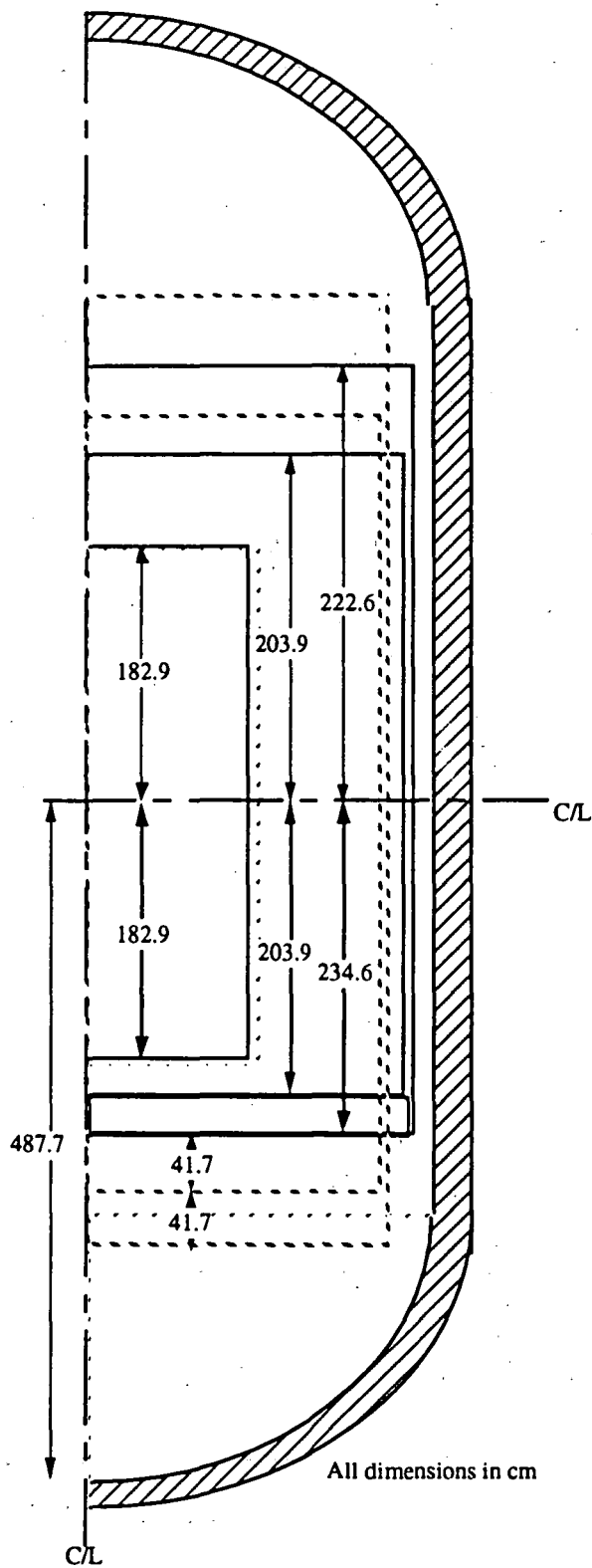
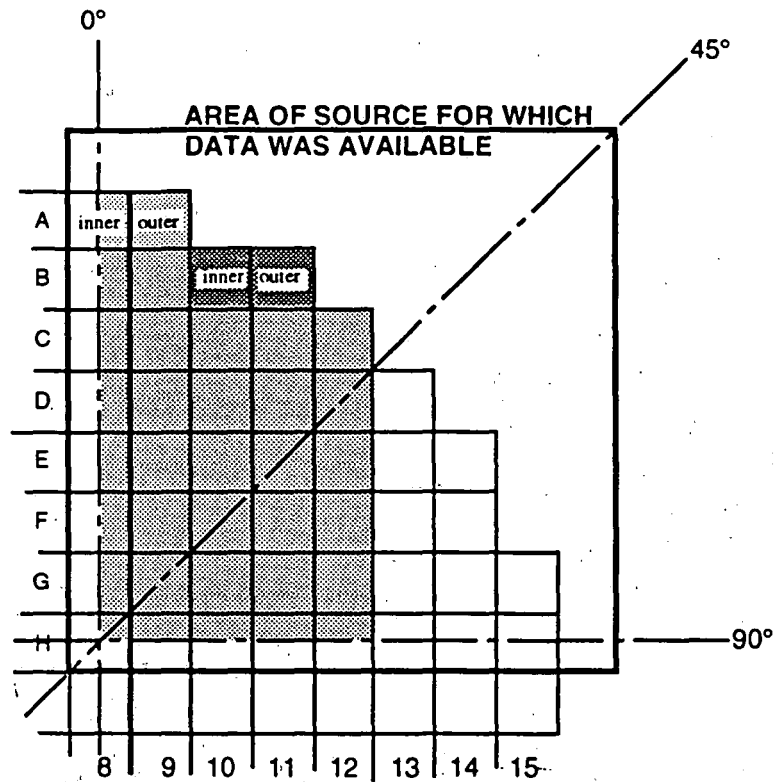


Figure 5 - Side View of the Model showing Dimensions



-  Low burn-up assemblies nearest the surveillance capsule
-  High burn-up assemblies on the flats, nearest the cavity position
-  Remainder of the core

The numbering of assemblies is in the scheme used by Westinghouse

Figure 6 - Core Sources Modelled

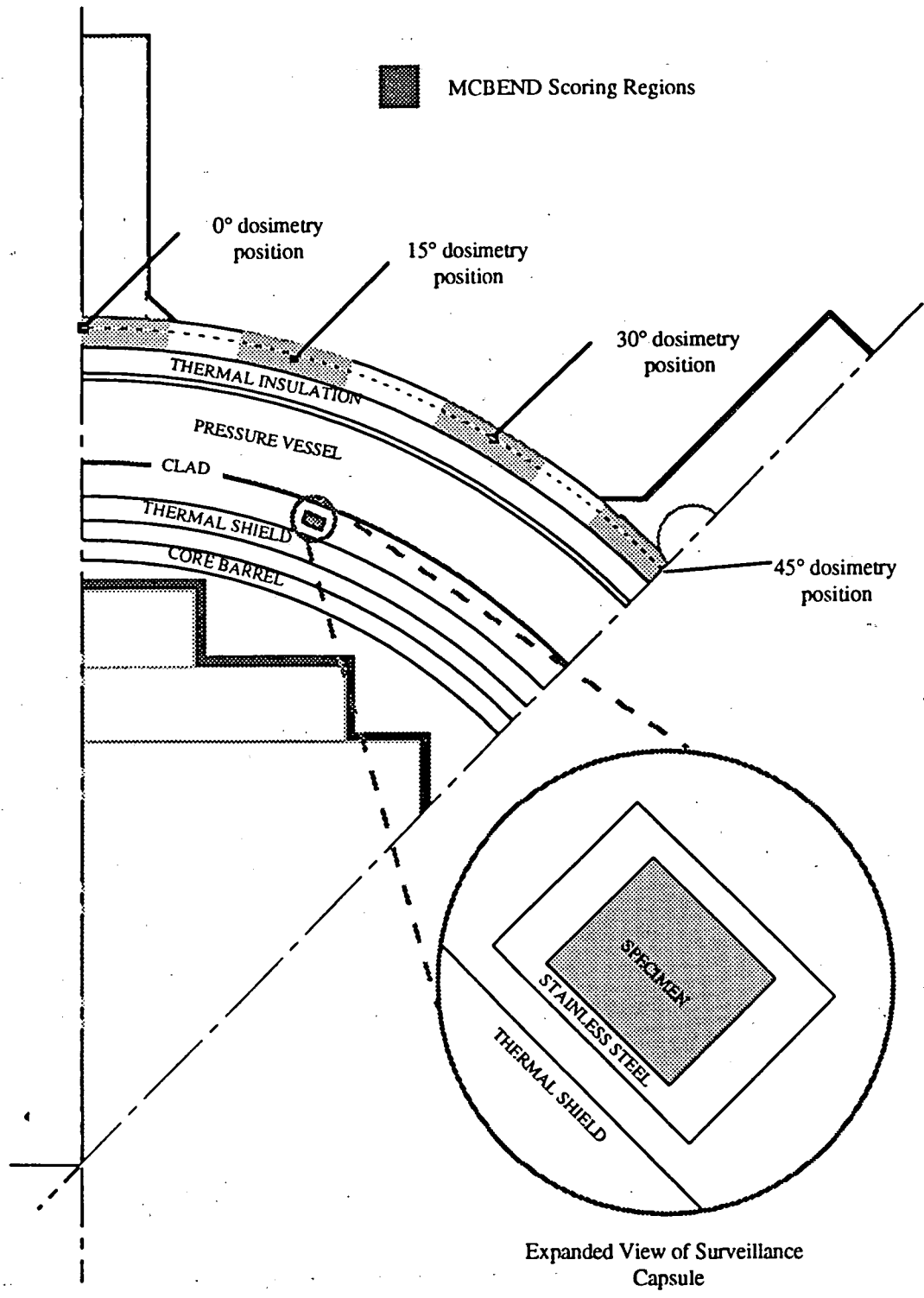
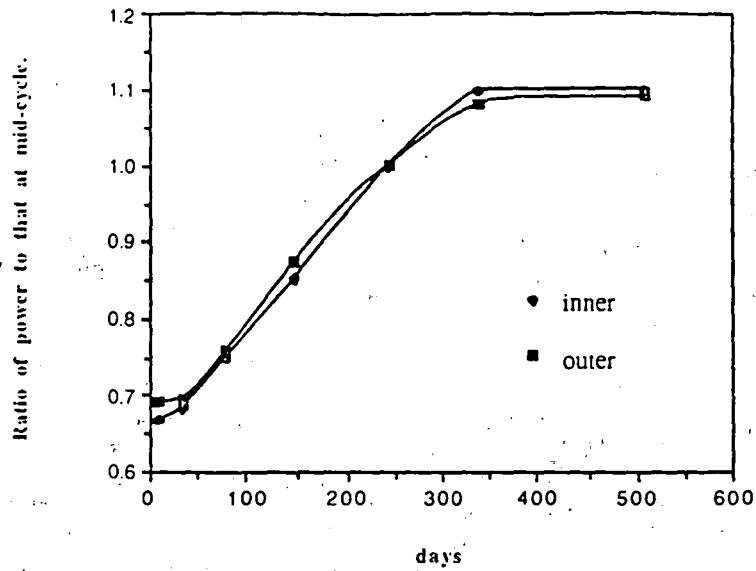


Figure 7 - Scoring Regions Modelled

Cavity position.



Surveillance capsule.

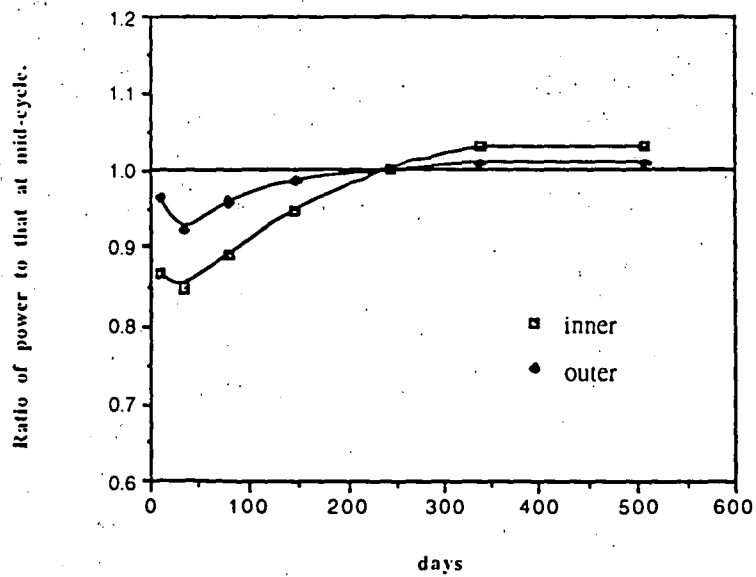


Figure 8 - Power Variation through the 9th cycle for Assemblies adjacent to the Cavity and Surveillance Positions.

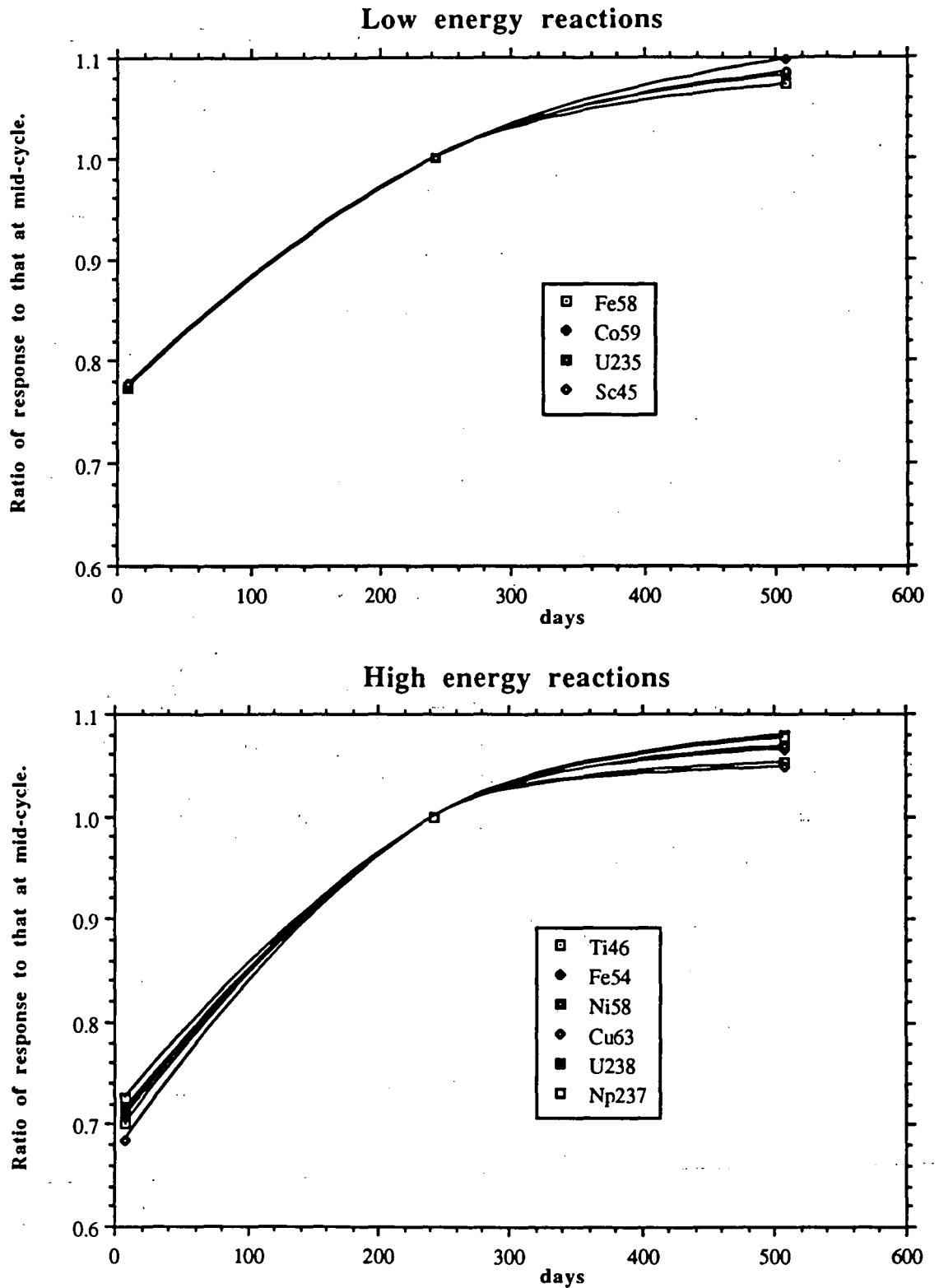


Figure 9 - Variation of Response through the 9th cycle - Cavity Position

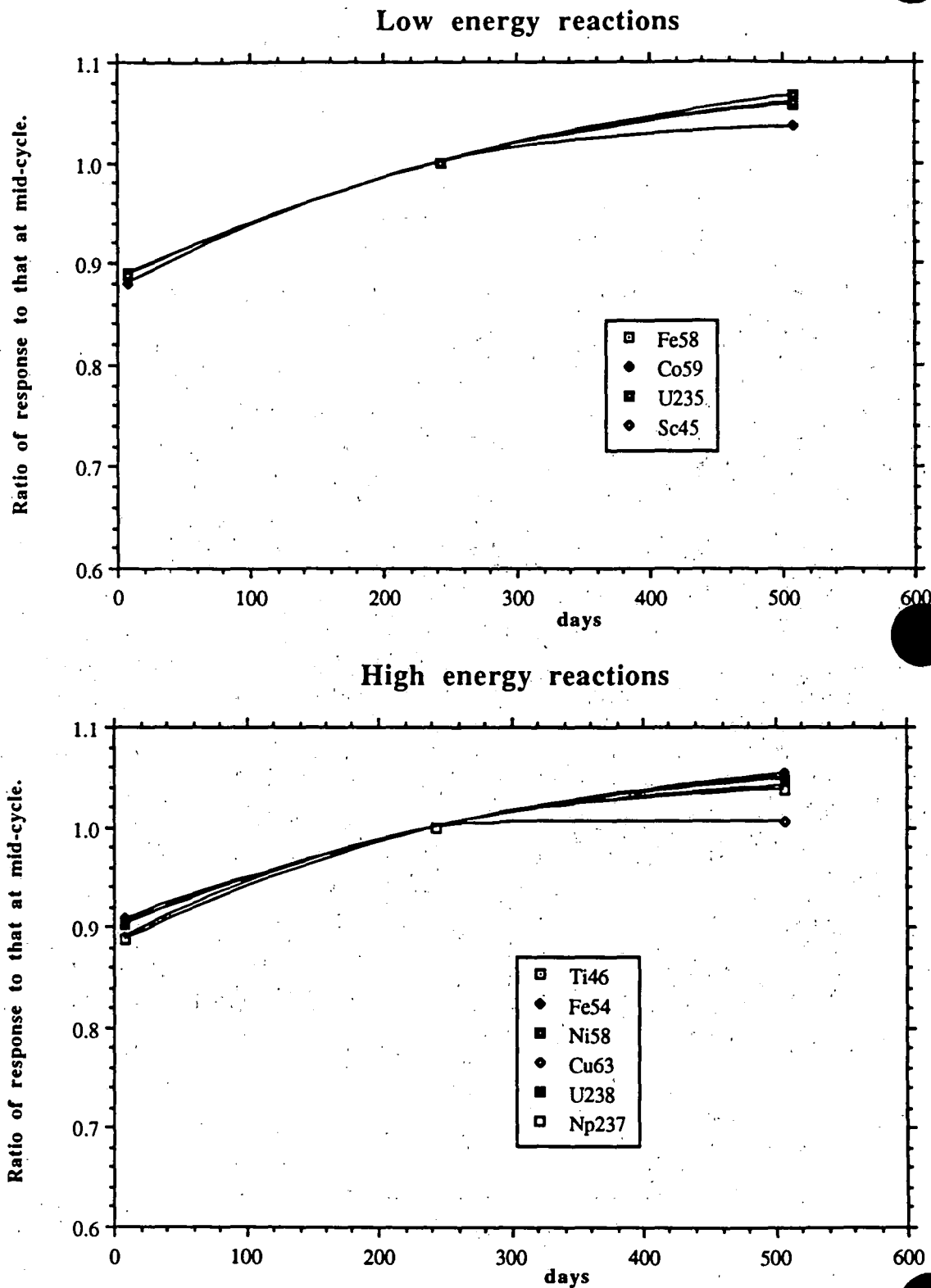


Figure 10 -Variation of Response through the 9th cycle - Surveillance Position

APPENDIX MCBEND9 INPUT DATA

```

& -----
& Case with ENDF-B/VI/IRDF-90 data
& -----
COLUMNS 1 80
BEGIN CONTROL DATA
  PROCESS TO STAGE THREE
  SAMPLE LIMIT 10
  DUMP INTERVALS 1
&   CHIME 3600
  SPLITTING
END
& UNIT 2
BEGIN DATASET DEFINITIONS
  DUMP A 25
&   SAVE NUCLEAR DATA 31
END
& UNIT 3
BEGIN OUTPUT CONTROL
SUPPRESS INFLOWS
END
& UNIT 4
BEGIN MATERIAL GEOMETRY
  CG
& H.B.ROBINSON PWR, 45 DEGREE SLICE.
&   BODIES
&
&     45 DEGREE SLICE
WED 1  0.0 1000.0 -2000.0
        0.0 -1000.0  0.0
        1000.0  0.0  0.0
        0.0  0.0 5000.0
&
&     CORE BAFFLE INNER
RPP 2 -32.304 32.304 -161.342 161.342 -210.0 210.0
RPP 3 -75.331 75.331 -139.857 139.857 -210.0 210.0
RPP 4 -96.840 96.840 -118.349 118.349 -210.0 210.0
&
&     CORE BAFFLE OUTER
RPP 5 -35.162 35.162 -164.200 164.200 -210.0 210.0
RPP 6 -78.189 78.189 -142.715 142.715 -210.0 210.0
RPP 7 -99.698 99.698 -121.207 121.207 -210.0 210.0
&
&     CORE BARREL INNER
RCC 8  0.0 0.0 -276.3  0.0 0.0 724.5  170.023
&
&     CORE BARREL OUTER
RCC 9  0.0 0.0 -318.0  0.0 0.0 766.2  175.184
&
&     THERMAL SHIELD INNER
RCC 10 0.0 0.0 -300.0  0.0 0.0 600.0  181.135
&
&     THERMAL SHIELD OUTER
RCC 11 0.0 0.0 -234.6  0.0 0.0 457.2  187.960
&
&     R.P.V. CLAD INNER
RCC 12 0.0 0.0 -400.0  0.0 0.0 1100.0  197.485
&
&     R.P.V. CLAD OUTER (MAIN VESSEL INNER)
RCC 13 0.0 0.0 -400.0  0.0 0.0 1100.0  198.041

```

| | | | | | | | | |
|---|--|---------|---------|---------|--------|-------|--------|---------|
| & | PRESSURE VESSEL OUTER | | | | | | | |
| | RCC 14 | 0.0 | 0.0 | -305.0 | 0.0 | 0.0 | 915.0 | 221.099 |
| & | INSULATION INNER | | | | | | | |
| | RCC 15 | 0.0 | 0.0 | -400.0 | 0.0 | 0.0 | 700.0 | 222.964 |
| & | INSULATION OUTER | | | | | | | |
| | RCC 16 | 0.0 | 0.0 | -385.0 | 0.0 | 0.0 | 615.0 | 230.584 |
| & | SPARE - LEFT FOR BIOLOGICAL SHIELD LINER | | | | | | | |
| | RCC 17 | 350.0 | 350.0 | 0.0 | 0.0 | 0.0 | 1.0 | 1.0 |
| & | BIOLOGICAL SHIELD INNER | | | | | | | |
| | RCC 18 | 0.0 | 0.0 | -730.0 | 0.0 | 0.0 | 3000.0 | 238.760 |
| & | 0 DEGREE EXCORE WELL LINER OUTER | | | | | | | |
| | BOX 19 | 19.050 | 319.405 | -200.0 | | | | |
| | | | | -100.0 | 0.0 | 0.0 | | |
| | | | | 0.0 | -100.0 | 0.0 | | |
| | | | | 0.0 | 0.0 | 800.0 | | |
| & | 0 DEGREE EXCORE WELL LINER INNER | | | | | | | |
| | BOX 20 | 18.415 | 318.770 | -200.0 | | | | |
| | | | | -100.0 | 0.0 | 0.0 | | |
| | | | | 0.0 | -100.0 | 0.0 | | |
| | | | | 0.0 | 0.0 | 800.0 | | |
| & | 0 DEGREE EXCORE WELL CHAMFER LINER OUTER | | | | | | | |
| | BOX 21 | 0.0 | 264.795 | -200.0 | | | | |
| | | | | -100.0 | -100.0 | 0.0 | | |
| | | | | 100.0 | -100.0 | 0.0 | | |
| | | | | 0.0 | 0.0 | 800.0 | | |
| & | 0 DEGREE EXCORE WELL CHAMFER LINER INNER | | | | | | | |
| | BOX 22 | 0.0 | 263.897 | -200.0 | | | | |
| | | | | -100.0 | -100.0 | 0.0 | | |
| | | | | 100.0 | -100.0 | 0.0 | | |
| | | | | 0.0 | 0.0 | 800.0 | | |
| & | 45 DEGREE EXCORE WELL LINER OUTER | | | | | | | |
| | BOX 23 | 212.383 | 239.324 | -200.0 | | | | |
| | | | | -100.0 | -100.0 | 0.0 | | |
| | | | | 100.0 | -100.0 | 0.0 | | |
| | | | | 0.0 | 0.0 | 800.0 | | |
| & | 45 DEGREE EXCORE WELL LINER INNER | | | | | | | |
| | BOX 24 | 212.383 | 238.426 | -200.0 | | | | |
| | | | | -100.0 | -100.0 | 0.0 | | |
| | | | | 100.0 | -100.0 | 0.0 | | |
| | | | | 0.0 | 0.0 | 800.0 | | |
| & | 45 DEGREE EXCORE WELL CHAMFER LINER OUTER | | | | | | | |
| | BOX 25 | 187.238 | 187.238 | -200.0 | | | | |
| | | | | -100.0 | 0.0 | 0.0 | | |
| | | | | 0.0 | -100.0 | 0.0 | | |
| | | | | 0.0 | 0.0 | 800.0 | | |
| & | 45 DEGREE EXCORE WELL CHAMFER LINER INNER | | | | | | | |
| | BOX 26 | 187.238 | 186.603 | -200.0 | | | | |
| | | | | -100.0 | 0.0 | 0.0 | | |
| | | | | 0.0 | -100.0 | 0.0 | | |
| | | | | 0.0 | 0.0 | 800.0 | | |
| & | INSTRUMENT CAPSULE IN 0 DEGREE WELL OUTER | | | | | | | |
| | RCC 27 | 0.0 | 252.174 | -10.635 | 0.0 | 0.0 | 21.27 | 9.525 |
| & | INSTRUMENT CAPSULE IN 0 DEGREE WELL INNER | | | | | | | |
| | RCC 28 | 0.0 | 252.174 | -10.0 | 0.0 | 0.0 | 20.0 | 8.890 |
| & | INSTRUMENT CAPSULE IN 45 DEGREE WELL OUTER | | | | | | | |

| | | | | | | | | |
|---|--|----------|----------|---------|---------|---------|--------|-------|
| | RCC 29 | 178.314 | 178.314 | -10.635 | 0.0 | 0.0 | 21.27 | 9.525 |
| & | INSTRUMENT CAPSULE IN 45 DEGREE WELL INNER | | | | | | | |
| | RCC 30 | 178.314 | 178.314 | -10.0 | 0.0 | 0.0 | 20.0 | 8.890 |
| & | BIOLOGICAL SHIELD OUTER | | | | | | | |
| | RCC 31 | 0.0 | 0.0 | -1100.0 | 0.0 | 0.0 | 1650.0 | 422.0 |
| & | SURROUNDING REFLECTOR | | | | | | | |
| | RCC 32 | 0.0 | 0.0 | -1150.0 | 0.0 | 0.0 | 4000.0 | 600.0 |
| & | SURROUNDING VOID | | | | | | | |
| | RCC 33 | 0.0 | 0.0 | 1000.0 | 0.0 | 0.0 | 2000.0 | 600.0 |
| & | TOP CLAD INNER | | | | | | | |
| | SPH 34 | 0.0 | 0.0 | 579.0 | 197.485 | | | |
| & | TOP VESSEL INNER | | | | | | | |
| | SPH 35 | 0.0 | 0.0 | 579.0 | 198.041 | | | |
| & | TOP VESSEL OUTER | | | | | | | |
| | SPH 36 | 0.0 | 0.0 | 579.0 | 218.9 | | | |
| & | BOTTOM CLAD INNER | | | | | | | |
| | SPH 37 | 0.0 | 0.0 | -285.0 | 197.485 | | | |
| & | BOTTOM VESSEL INNER | | | | | | | |
| | SPH 38 | 0.0 | 0.0 | -285.0 | 198.041 | | | |
| & | BOTTOM VESSEL OUTER | | | | | | | |
| | SPH 39 | 0.0 | 0.0 | -285.0 | 216.3 | | | |
| & | ACTIVE CORE | | | | | | | |
| | RCC 40 | 0.0 | 0.0 | -182.88 | 0.0 | 0.0 | 365.76 | 169.0 |
| & | CORE BAFFLE TOP & BOTTOM PLATES INNER | | | | | | | |
| | RCC 41 | 0.0 | 0.0 | -203.9 | 0.0 | 0.0 | 407.8 | 169.0 |
| & | CORE BAFFLE TOP & BOTTOM PLATES OUTER | | | | | | | |
| | RCC 42 | 0.0 | 0.0 | -206.8 | 0.0 | 0.0 | 413.6 | 169.0 |
| & | WEDGES FOR CAVITY SCORING REGIONS | | | | | | | |
| & | 0 DEGREES | | | | | | | |
| | WED 43 | -26.132 | 248.630 | -220.98 | | | | |
| | | 26.132 | -248.630 | 0.0 | | | | |
| | | 52.848 | 5.555 | 0.0 | | | | |
| | | 0.0 | 0.0 | 441.96 | | | | |
| & | 15 DEGREES | | | | | | | |
| | WED 44 | 47.702 | 245.407 | -220.98 | | | | |
| | | -47.702 | -245.407 | 0.0 | | | | |
| | | 34.489 | -6.704 | 0.0 | | | | |
| | | 0.0 | 0.0 | 441.96 | | | | |
| & | 30 DEGREES | | | | | | | |
| | WED 45 | 109.593 | 224.699 | -220.98 | | | | |
| | | -109.593 | -224.699 | 0.0 | | | | |
| | | 31.579 | -15.402 | 0.0 | | | | |
| | | 0.0 | 0.0 | 441.96 | | | | |
| & | 45 DEGREES | | | | | | | |
| | WED 46 | 157.330 | 194.286 | -220.98 | | | | |
| | | -157.330 | -194.286 | 0.0 | | | | |
| | | 41.297 | -33.441 | 0.0 | | | | |
| | | 0.0 | 0.0 | 441.96 | | | | |
| & | SLABS FOR CAVITY SCORING REGIONS | | | | | | | |
| & | CENTRE CAPSULE | | | | | | | |
| | RPP 47 | -250.0 | 250.0 | -250.0 | 250.0 | -91.0 | 91.44 | |
| & | UPPER CAPSULE | | | | | | | |
| | RPP 48 | -250.0 | 250.0 | -250.0 | 250.0 | 0.0 | 121.92 | |
| & | LOWER CAPSULE | | | | | | | |
| | RPP 49 | -250.0 | 250.0 | -250.0 | 250.0 | -121.92 | 0.0 | |

| | | | | | | | |
|---|------------|----------------------------|----------|--------|-------|---------|-----------|
| & | | TOP CAPSULE | | | | | |
| | RPP 50 | -250.0 | 250.0 | -250.0 | 250.0 | 205.74 | 230.0 |
| & | | BOTTOM CAPSULE | | | | | |
| | RPP 51 | -250.0 | 250.0 | -250.0 | 250.0 | -230.0 | -205.74 |
| & | | WIRE | | | | | |
| | RPP 52 | -250.0 | 250.0 | -250.0 | 250.0 | 144.78 | 175.26 |
| & | | WIRE | | | | | |
| | RPP 53 | -250.0 | 250.0 | -250.0 | 250.0 | 150.0 | 210.0 |
| & | | WIRE | | | | | |
| | RPP 54 | -250.0 | 250.0 | -250.0 | 250.0 | 120.0 | 150.0 |
| & | | WIRE | | | | | |
| | RPP 55 | -250.0 | 250.0 | -250.0 | 250.0 | -175.26 | -144.78 |
| & | | WIRE | | | | | |
| | RPP 56 | -250.0 | 250.0 | -250.0 | 250.0 | -210.0 | -150.0 |
| & | | WIRE | | | | | |
| | RPP 57 | -250.0 | 250.0 | -250.0 | 250.0 | -150.0 | -120.0 |
| & | | SURVEILLANCE CAPSULE OUTER | | | | | |
| | BOX 58 | 61.768 | 178.478 | -31.0 | | | |
| | | 5.638 | -2.052 | 0.0 | | | |
| | | 1.493 | 4.102 | 0.0 | | | |
| | | 0.0 | 0.0 | 62.0 | | | |
| & | | SURVEILLANCE CAPSULE INNER | | | | | |
| | BOX 59 | 63.095 | 178.761 | -30.48 | | | |
| | | 3.47686 | -1.26547 | 0.0 | | | |
| | | 1.08591 | 2.98352 | 0.0 | | | |
| | | 0.0 | 0.0 | 60.96 | | | |
| | END | | | | | | |
| & | | ZONES 1-5 | | | | | |
| | CORE1 | 20 | +1 | +2 | | | +40 |
| | CORE2 | 20 | +1 | +3 | -2 | | +40 |
| | CORE3 | 20 | +1 | +4 | -3 | | +40 |
| | NOZZLES1 | 20 | +1 | +2 | | | -40 +41 |
| | NOZZELS2 | 20 | +1 | +3 | -2 | | -40 +41 |
| & | | ZONES 6-10 | | | | | |
| | NOZZELS3 | 20 | +1 | +4 | -3 | | -40 +41 |
| | AXIALBAFL1 | 20 | +1 | +2 | | | -41 +42 |
| | AXIALBAFL2 | 20 | +1 | +3 | -2 | | -41 +42 |
| | AXIALBAFL3 | 20 | +1 | +4 | -3 | | -41 +42 |
| | BAFFLE1 | 20 | +1 | +5 | -2 | -6 | +42 |
| & | | ZONES 11-15 | | | | | |
| | BAFFLE2 | 20 | +1 | +6 | -3 | -2 | -7 +42 |
| | BAFFLE3 | 20 | +1 | +7 | -4 | -3 | +42 |
| | WATER1IN | 20 | +1 | +8 | -5 | -6 | -7 +9 +42 |
| | WATER1OUT | 20 | +1 | +8 | +9 | | -42 |
| | BARREL | 20 | +1 | +9 | -8 | | |
| & | | ZONES 16-20 | | | | | |
| | WATER2 | 20 | +1 | +10 | -9 | +11 | |
| | THERMALSH | 20 | +1 | +11 | -10 | | |
| | WATER3 | 20 | +1 | +12 | -11 | -9 | +14 -58 |
| | WATER3TOP | 20 | +1 | +34 | -9 | | -14 |
| | WATER3BOT | 20 | +1 | +37 | -9 | | -14 |
| & | | ZONES 21-25 | | | | | |
| | CLAD | 20 | +1 | +13 | -12 | | +14 |
| | CLADTOP | 20 | +1 | +35 | -34 | | -14 |
| | CLADBOT | 20 | +1 | +38 | -37 | | -14 |

| | | | | | | | | | | |
|-----|------------|-------|-----|-----|-----|-----|-----|--|-----|-------------|
| | VESSEL | 20 | +1 | +14 | -13 | | | | | |
| | VESSELTOP | 20 | +1 | +36 | -35 | | | | -14 | |
| & | ZONES | 26-30 | | | | | | | | |
| | VESSELBOT | 20 | +1 | +39 | -38 | | | | -14 | |
| | VOID1 | 20 | +1 | +15 | +16 | -39 | | | -14 | |
| | INSULATION | 20 | +1 | +16 | -15 | | | | | |
| 45 | CAVITY | 30 | +1 | +18 | -16 | -14 | -39 | | +31 | -43 -44 - |
| -46 | | | | | | | | | | |
| | WELLINER0 | 20 | +1 | +19 | -20 | -22 | | | +31 | |
| & | ZONES | 31-35 | | | | | | | | |
| | CHAMFLIN0 | 20 | +1 | +21 | -22 | -19 | | | -18 | +31 |
| | WELLO | 20 | +1 | +20 | -27 | | | | -18 | +31 |
| | CHAMFER0 | 20 | +1 | +22 | -20 | | | | -18 | +31 |
| | CAPSULE0 | 20 | +1 | +27 | -28 | | | | | |
| | INSTRMNT0 | 20 | +1 | +28 | | | | | | |
| & | ZONES | 36-40 | | | | | | | | |
| | WELLINER45 | 20 | +1 | +23 | -24 | -26 | | | | +31 |
| | CHAMFLIN45 | 20 | +1 | +25 | -26 | -23 | | | -18 | +31 |
| | WELL45 | 20 | +1 | +24 | -29 | | | | -18 | +31 |
| | CHAMFER45 | 20 | +1 | +26 | -24 | | | | -18 | +31 |
| | CAPSULE45 | 20 | +1 | +29 | -30 | | | | | |
| & | ZONES | 41-45 | | | | | | | | |
| | INSTRMNT45 | 20 | +1 | +30 | | | | | | |
| | CONCRETE | 20 | +1 | -19 | -23 | -21 | -25 | | -18 | +31 |
| | BLACK | 20 | +1 | +32 | -36 | -39 | | | -31 | -14 |
| | REFLECTOR | 20 | +32 | -1 | | | | | | |
| | CAV00CENTR | 10 | +1 | +18 | -16 | | | | +43 | +47 |
| & | ZONES | 46-50 | | | | | | | | |
| | CAV00TOP | 10 | +1 | +18 | -16 | | | | +43 | +50 |
| | CAV00UPPER | 10 | +1 | +18 | -16 | | | | +43 | +48 -47 |
| | CAV00LOWER | 10 | +1 | +18 | -16 | | | | +43 | +49 -47 |
| | CAV00BOTTM | 10 | +1 | +18 | -16 | | | | +43 | +51 |
| | CAV00WIRE1 | 10 | +1 | +18 | -16 | | | | +43 | +53 -50 -52 |
| & | ZONES | 51-55 | | | | | | | | |
| | CAV00WIRE2 | 10 | +1 | +18 | -16 | | | | +43 | +52 |
| | CAV00WIRE3 | 10 | +1 | +18 | -16 | | | | +43 | +54 -48 -52 |
| | CAV00WIRE4 | 10 | +1 | +18 | -16 | | | | +43 | +57 -49 -55 |
| | CAV00WIRE5 | 10 | +1 | +18 | -16 | | | | +43 | +55 |
| | CAV00WIRE6 | 10 | +1 | +18 | -16 | | | | +43 | +56 -51 -55 |
| & | ZONES | 56-60 | | | | | | | | |
| | CAV15CENTR | 10 | +1 | +18 | -16 | | | | +44 | +47 |
| | CAV15TOP | 10 | +1 | +18 | -16 | | | | +44 | +50 |
| | CAV15UPPER | 10 | +1 | +18 | -16 | | | | +44 | +48 -47 |
| | CAV15LOWER | 10 | +1 | +18 | -16 | | | | +44 | +49 -47 |
| | CAV15BOTTM | 10 | +1 | +18 | -16 | | | | +44 | +51 |
| & | ZONES | 61-65 | | | | | | | | |
| | CAV15WIRE1 | 10 | +1 | +18 | -16 | | | | +44 | +53 -50 -52 |
| | CAV15WIRE2 | 10 | +1 | +18 | -16 | | | | +44 | +52 |
| | CAV15WIRE3 | 10 | +1 | +18 | -16 | | | | +44 | +54 -48 -52 |
| | CAV15WIRE4 | 10 | +1 | +18 | -16 | | | | +44 | +57 -49 -55 |
| | CAV15WIRE5 | 10 | +1 | +18 | -16 | | | | +44 | +55 |
| & | ZONES | 66-70 | | | | | | | | |
| | CAV15WIRE6 | 10 | +1 | +18 | -16 | | | | +44 | +56 -51 -55 |
| | CAV30CENTR | 10 | +1 | +18 | -16 | | | | +45 | +47 |
| | CAV30TOP | 10 | +1 | +18 | -16 | | | | +45 | +50 |

| | | | | | | | | | |
|---|-------------|----|----|-----|-----|-----|-----|-----|-----|
| | CAV30UPPER | 10 | +1 | +18 | -16 | +45 | +48 | -47 | |
| | CAV30LOWER | 10 | +1 | +18 | -16 | +45 | +49 | -47 | |
| & | ZONES 71-75 | | | | | | | | |
| | CAV30BOTTM | 10 | +1 | +18 | -16 | +45 | +51 | | |
| | CAV30WIRE1 | 10 | +1 | +18 | -16 | +45 | +53 | -50 | -52 |
| | CAV30WIRE2 | 10 | +1 | +18 | -16 | +45 | +52 | | |
| | CAV30WIRE3 | 10 | +1 | +18 | -16 | +45 | +54 | -48 | -52 |
| | CAV30WIRE4 | 10 | +1 | +18 | -16 | +45 | +57 | -49 | -55 |
| & | ZONES 76-80 | | | | | | | | |
| | CAV30WIRE5 | 10 | +1 | +18 | -16 | +45 | +55 | | |
| | CAV30WIRE6 | 10 | +1 | +18 | -16 | +45 | +56 | -51 | -55 |
| | CAV45CENTR | 10 | +1 | +18 | -16 | +46 | +47 | | |
| | CAV45TOP | 10 | +1 | +18 | -16 | +46 | +50 | | |
| | CAV45UPPER | 10 | +1 | +18 | -16 | +46 | +48 | -47 | |
| & | ZONES 81-85 | | | | | | | | |
| | CAV45LOWER | 10 | +1 | +18 | -16 | +46 | +49 | -47 | |
| | CAV45BOTTM | 10 | +1 | +18 | -16 | +46 | +51 | | |
| | CAV45WIRE1 | 10 | +1 | +18 | -16 | +46 | +53 | -50 | -52 |
| | CAV45WIRE2 | 10 | +1 | +18 | -16 | +46 | +52 | | |
| | CAV45WIRE3 | 10 | +1 | +18 | -16 | +46 | +54 | -48 | -52 |
| & | ZONES 86-90 | | | | | | | | |
| | CAV45WIRE4 | 10 | +1 | +18 | -16 | +46 | +57 | -49 | -55 |
| | CAV45WIRE5 | 10 | +1 | +18 | -16 | +46 | +55 | | |
| | CAV45WIRE6 | 10 | +1 | +18 | -16 | +46 | +56 | -51 | -55 |
| | SURVEYINN | 10 | +1 | +59 | | | | | |
| | SURVEYOUTR | 10 | +1 | +58 | -59 | | | | |

END

| | | | | | | | | | | |
|---|------------|------------|------------|------------|------------|--|--|--|--|--|
| & | REGIONS | | | | | | | | | |
| & | CORE1 | CORE2 | CORE3 | NOZZLES1 | NOZZLES2 | | | | | |
| & | NOZZLES3 | AXIALBAFL1 | AXIALBAFL2 | AXIALBAFL3 | BAFFLE1 | | | | | |
| & | BAFFLE2 | BAFFLE3 | WATER1IN | WATER1OUT | BARREL | | | | | |
| & | WATER2 | THERMALSH | WATER3 | WATER3TOP | WATER3BOT | | | | | |
| & | CLAD | CLADTOP | CLADBOT | VESSEL | VESSELTOP | | | | | |
| & | VESSELBOT | VOID1 | INSULATION | CAVITY | WELLINER0 | | | | | |
| & | CHAMFLIN0 | WELL0 | CHAMFER0 | CAPSULE0 | INSTRMNT0 | | | | | |
| & | WELLINER45 | CHAMFLIN45 | WELL45 | CHAMFER45 | CAPSULE45 | | | | | |
| & | INSTRMNT45 | CONCRETE | BLACK | REFLECTOR | CAV00CENTR | | | | | |
| & | CAV00TOP | CAV00UPPER | CAV00LOWER | CAV00BOTTM | CAV00WIRE1 | | | | | |
| & | CAV00WIRE2 | CAV00WIRE3 | CAV00WIRE4 | CAV00WIRE5 | CAV00WIRE6 | | | | | |
| & | CAV15CENTR | CAV15TOP | CAV15UPPER | CAV15LOWER | CAV15BOTTM | | | | | |
| & | CAV15WIRE1 | CAV15WIRE2 | CAV15WIRE3 | CAV15WIRE4 | CAV15WIRE5 | | | | | |
| & | CAV15WIRE6 | CAV30CENTR | CAV30TOP | CAV30UPPER | CAV30LOWER | | | | | |
| & | CAV30BOTTM | CAV30WIRE1 | CAV30WIRE2 | CAV30WIRE3 | CAV30WIRE4 | | | | | |
| & | CAV30WIRE5 | CAV30WIRE6 | CAV45CENTR | CAV45TOP | CAV45UPPER | | | | | |
| & | CAV45LOWER | CAV45BOTTM | CAV45WIRE1 | CAV45WIRE2 | CAV45WIRE3 | | | | | |
| & | CAV45WIRE4 | CAV45WIRE5 | CAV45WIRE6 | SURVEYINN | SURVEYOUTR | | | | | |

| | | | | | | | | | |
|----|----|----|----|----|----|----|----|----|----|
| 1 | 2 | 3 | 4 | 5 | 6 | 7 | 8 | 9 | 10 |
| 11 | 12 | 13 | 14 | 15 | 16 | 17 | 18 | 19 | 20 |
| 21 | 22 | 23 | 24 | 25 | 26 | 27 | 28 | 29 | 30 |
| 31 | 32 | 33 | 34 | 35 | 36 | 37 | 38 | 39 | 40 |
| 41 | 42 | 43 | 44 | 45 | 46 | 47 | 48 | 49 | 50 |
| 51 | 52 | 53 | 54 | 55 | 56 | 57 | 58 | 59 | 60 |

| | 61 | 62 | 63 | 64 | 65 | 66 | 67 | 68 | 69 | 70 |
|---|-----------|----|-------|-------|----|----|----|----|----|----|
| | 71 | 72 | 73 | 74 | 75 | 76 | 77 | 78 | 79 | 80 |
| | 81 | 82 | 83 | 84 | 85 | 86 | 87 | 88 | 89 | 90 |
| & | MATERIALS | | | | | | | | | |
| | 1 | 1 | 1 | 2 | 2 | 2 | 2 | 2 | 2 | 2 |
| | 2 | 2 | 3 | 3 | 2 | 3 | 2 | 3 | 3 | 3 |
| | 2 | 2 | 2 | 4 | 4 | 4 | 0 | 5 | 0 | 4 |
| | 4 | 0 | 0 | 2 | 0 | 4 | 4 | 0 | 0 | 2 |
| | 0 | 6 | -2000 | -3000 | 0 | 0 | 0 | 0 | 0 | 0 |
| | 0 | 0 | 0 | 0 | 0 | 0 | 0 | 0 | 0 | 0 |
| | 0 | 0 | 0 | 0 | 0 | 0 | 0 | 0 | 0 | 0 |
| | 0 | 0 | 0 | 0 | 0 | 0 | 0 | 0 | 0 | 0 |
| | 0 | 0 | 0 | 0 | 0 | 0 | 0 | 0 | 2 | 4 |

| | VOLUMES | | | | |
|--|----------|----------|----------|---------|----------|
| | 1.0 | 1.0 | 1.0 | 1.0 | 1.0 |
| | 1.0 | 1.0 | 1.0 | 1.0 | 1.0 |
| | 1.0 | 1.0 | 1.0 | 1.0 | 1.0 |
| | 1.0 | 1.0 | 1.0 | 1.0 | 1.0 |
| | 1.0 | 1.0 | 1.0 | 1.0 | 1.0 |
| | 1.0 | 1.0 | 1.0 | 1.0 | 1.0 |
| | 1.0 | 1.0 | 1.0 | 1.0 | 1.0 |
| | 1.0 | 1.0 | 1.0 | 1.0 | 4965.73 |
| | 1.0 | 1.0 | 1.0 | 1.0 | 1.0 |
| | 4965.73 | 1.0 | 1.0 | 1.0 | 36744.89 |
| | 3062.07 | 6124.15 | 6124.15 | 3062.07 | 6124.15 |
| | 6124.15 | 4593.11 | 4593.11 | 6124.15 | 6124.15 |
| | 48993.19 | 4082.77 | 8165.53 | 8165.53 | 4082.77 |
| | 8165.53 | 8165.53 | 6124.15 | 6124.15 | 8165.53 |
| | 8165.53 | 48993.19 | 4082.77 | 8165.53 | 8165.53 |
| | 4082.77 | 8165.53 | 8165.53 | 6124.15 | 6124.15 |
| | 8165.53 | 8165.53 | 36744.89 | 3062.07 | 6124.15 |
| | 6124.15 | 3062.07 | 6124.15 | 6124.15 | 4593.11 |
| | 4593.11 | 6124.15 | 6124.15 | 716.128 | 1623.780 |

END

& UNIT 5

BEGIN SPLITTING GEOMETRY

| X 17 | | | | |
|---------------|---------------|--|---------------|---------------|
| 0.0000000E+00 | 19.353 | | 36.556 | 49.458 |
| 75.262 | 83.864 | | 92.465 | 0.1023478E+03 |
| 0.1076878E+03 | | | | |
| 0.1156978E+03 | 0.1256977E+03 | | 0.1398176E+03 | 0.1562976E+03 |
| 0.1787776E+03 | | | | |
| 0.1987776E+03 | 0.2187775E+03 | | 0.42500E+03 | |
| Y 31 | | | | |
| 0.0000000E+00 | 19.353 | | 27.955 | 40.857 |
| 58.059 | 70.961 | | 79.563 | 0.8999988E+02 |
| 0.9999986E+02 | | | | |
| 109.668 | 118.269 | | 0.1258668E+03 | 135.472 |
| 0.1427047E+03 | | | | |
| 0.1473647E+03 | 156.975 | | 0.1642027E+03 | 0.1692127E+03 |
| 0.1742227E+03 | | | | |

0.1802226E+03 0.1871226E+03 0.1928226E+03 0.2025325E+03
0.2163224E+03
0.2358624E+03 0.2458624E+03 0.2633623E+03 0.2808621E+03
0.2983618E+03
0.3208613E+03 0.42500E+03

Z 14

-1000.0 -280.0 -220.0 -200.0 -182.878
-146.956 -80.0 -20.0 20.0 80.0
146.956 182.878 200.0 260.0 2850.0

END

& UNIT 6

BEGIN SOURCE GEOMETRY

X 23

0.000 2.150 6.451 10.752
15.052 19.353 23.654 27.955 32.255
36.556 40.857 45.157 49.458 53.759
58.059 62.360 66.661 70.961 75.262
79.563 83.864 88.164 92.465 96.766

Y 38

0.000 2.150 6.451 10.752
15.052 19.353 23.654 27.955 32.255
36.556 40.857 45.157 49.458 53.759
58.059 62.360 66.661 70.961 75.262
79.563 83.864 88.164 92.465 96.766
101.066 105.367 109.668 113.968 118.269
122.570 126.870 131.171 135.472 139.773
144.073 148.374 152.675 156.975 161.277

Z 19

-182.878 -166.550 -146.956 -127.362 -107.768
-88.174 -68.580 -48.985 -29.391 -9.796
9.796 29.390 48.984 68.580 88.174
107.768 127.362 146.956 166.550 182.878

END

& UNIT 7

BEGIN ENERGY DATA

NEUTRON

SPLITTING

GROUPS 15

14.6 13.5 12.5 11.25 10.0 8.5 7.0 6.07 4.72 3.68 2.87 1.74 0.6
0.39 0.11 6.74E-02

SCORING

GROUPS 4

14.6 5.0 1.0 0.5 6.74E-02

THERMAL TREATMENT NONE

SIMPLE SOURCE

FISSION

WEIGHTING AUTOMATIC

SPECTRUM LIMITS 14.6 6.74E-02

END

& UNIT 8

BEGIN IMPORTANCE MAP

DIMENSIONS 17 31 14 15 1

CALCULATE TARGETS 1

ZONES 45 STRENGTHS 1.0

USE METHOD D

DOMINANT MATERIAL
END
& UNIT 9
BEGIN SCORING DATA
MESH SYSTEM CG
DIMENSIONS 90 1 1
MATERIAL MESH
TRACK LENGTH
FLUX

SOME 1
35 41
45 46 47 48 49
50 51 52 53 54 55
56 57 58 59 60
61 62 63 64 65 66
67 68 69 70 71
72 73 74 75 76 77
78 79 80 81 82
83 84 85 86 87 88
89

RESPONSES
DITTO
SENSITIVITY OF RESPONSES
SOME 1
45

& CONTRIBUTIONS TO RESPONSES DITTO
END

& UNIT 14
BEGIN MATERIAL DATA
& MATERIALS FOR H.B.ROBINSON PWR (FROM WESTINGHOUSE/CPL DOT MODEL)
& K REMOVED FROM CONCRETE
MINNIE

MIXTURES 5
WEIGHT
& CORE REGION
M 1

U235 0.20647E-01
U238 0.62565
O16 0.180760
H 0.11840E-01
B10 0.65507E-04
FE54 1.32525E-04
FE56 2.13598E-03
FE57 4.9755E-05
FE58 6.74250E-06
MN 0.42278E-04
CR50 5.2033E-05
CR52 1.04441E-03
CR53 1.20662E-04
CR54 3.05711E-05
NI58 1.98361E-03
NI60 7.90492E-04
NI61 3.48312E-05
NI62 1.13054E-04
NI64 2.98312E-05

ZR 0.15447
& M 2
WATER
H 0.11191
O16 0.88799
B10 0.99829E-04
& M 3
STAINLESS STEEL SST304
FE54 3.933E-02
FE56 6.339E-01
FE57 1.4766E-02
FE58 2.001E-03
MN 0.19995E-01
CR50 7.923E-03
CR52 1.5903E-01
CR53 1.8373E-02
CR54 4.655E-03
NI58 6.72067E-02
NI60 2.67827E-02
NI61 1.18012E-03
NI62 3.83038E-03
NI64 1.0101E-03
& M 4
CARBON STEEL AS33B
C 0.24999E-02
MN 0.12996E-01
FE54 5.58030E-02
FE56 8.99407E-01
FE57 2.09506E-02
FE58 2.83910E-03
NI58 3.69640E-03
NI60 1.47306E-03
NI61 6.49071E-05
NI62 2.10673E-04
NI64 5.555561E-05
& M 5
& CONCRETE
& POTASSIUM (K) REMOVED TO SAVE SPACE
& (ELIMINATED BY DISTRIBUTING ITS FRACTION AMONGST THE
OTHER
& ELEMENTS)
H 0.50903E-02
C 0.10183E-02
O16 0.51189
NA 0.16288E-01
MG 0.22130E-02
AL 0.34530E-01
SI 0.346230
CA 0.44256E-01
FE54 2.19364E-03
FE56 3.53562E-02
FE57 8.23579E-04
FE58 1.111607E-04
& MATERIALS 6
CORE REGION #100

1 M1 4.2632 1.0
 & EXCORE STAINLESS STEEL #200
 2 M3 8.03 1.0
 & EXCORE WATER #300
 3 M2 0.7886 1.0
 & EXCORE CARBON STEEL #400
 4 M4 7.83 1.0
 & INSULATION #500
 5 M3 0.241 1.0
 & CONCRETE #600
 6 M5 2.20 1.0

USE MOULD 28 FOR H IN ALL MATERIALS
 USE ADCN O FOR O16 IN ALL MATERIALS
 USE ADCN FE FOR FE54 IN ALL MATERIALS
 USE ADCN FE FOR FE54 IN ALL MATERIALS
 USE ADCN FE FOR FE56 IN ALL MATERIALS
 USE ADCN FE FOR FE57 IN ALL MATERIALS
 USE ADCN FE FOR FE58 IN ALL MATERIALS
 USE ADCN CR FOR CR50 IN ALL MATERIALS
 USE ADCN CR FOR CR52 IN ALL MATERIALS
 USE ADCN CR FOR CR53 IN ALL MATERIALS
 USE ADCN CR FOR CR54 IN ALL MATERIALS
 USE ADCN NI FOR NI58 IN ALL MATERIALS
 USE ADCN NI FOR NI60 IN ALL MATERIALS
 USE ADCN NI FOR NI61 IN ALL MATERIALS
 USE ADCN NI FOR NI62 IN ALL MATERIALS
 USE ADCN NI FOR NI64 IN ALL MATERIALS
 END

& UNIT 15

BEGIN SOURCE STRENGTH

& SOURCES SUPPLIED BY D. MAERKER

DIMENSIONS

23 38 19 1 1

SEPARABLE

COMPONENT X Y

| | | | | |
|-------------|-------------|-------------|-------------|-------------|
| 1.85750E+15 | 1.88139E+15 | 2.12459E+15 | 2.37558E+15 | 2.18132E+15 |
| 2.19150E+15 | 2.25963E+15 | 2.55529E+15 | 2.13517E+15 | 1.90959E+15 |
| 1.91846E+15 | 1.99254E+15 | 2.34192E+15 | 2.89716E+15 | 2.56099E+15 |
| 2.66330E+15 | 2.58761E+15 | 2.96464E+15 | 2.29931E+15 | 2.03235E+15 |
| 1.99446E+15 | 2.00898E+15 | 2.25052E+15 | 1.88080E+15 | 1.90694E+15 |
| 1.89072E+15 | 2.10078E+15 | 2.21289E+15 | 2.21689E+15 | 2.29723E+15 |
| 2.26076E+15 | 1.89395E+15 | 1.92714E+15 | 1.93628E+15 | 2.01383E+15 |
| 2.07804E+15 | 2.41892E+15 | 2.73580E+15 | 2.57229E+15 | 2.76605E+15 |
| 2.47693E+15 | 2.03423E+15 | 2.05723E+15 | 2.02042E+15 | 2.04177E+15 |
| 2.00659E+15 | 2.12126E+15 | 1.88825E+15 | 1.88011E+15 | 2.05201E+15 |
| 2.12606E+15 | 2.44136E+15 | 2.19677E+15 | 2.19313E+15 | 1.86745E+15 |
| 1.89719E+15 | 2.16866E+15 | 1.97721E+15 | 2.03743E+15 | 2.43409E+15 |
| 2.42880E+15 | 2.92103E+15 | 2.45714E+15 | 2.49493E+15 | 1.99295E+15 |
| 2.01611E+15 | 2.27100E+15 | 2.01755E+15 | 1.99771E+15 | 2.29700E+15 |
| 2.03142E+15 | 1.98450E+15 | 1.96723E+15 | 1.98269E+15 | 2.21871E+15 |
| 1.96008E+15 | 1.92234E+15 | 2.00792E+15 | 2.06227E+15 | 2.36573E+15 |
| 2.14435E+15 | 2.18896E+15 | 1.94055E+15 | 1.97772E+15 | 2.24105E+15 |
| 2.00488E+15 | 1.99605E+15 | 2.19172E+15 | 2.26078E+15 | 2.58870E+15 |
| 2.31764E+15 | 2.29080E+15 | 2.10804E+15 | 2.13866E+15 | 2.05478E+15 |
| 1.97806E+15 | 1.98432E+15 | 1.93526E+15 | 1.94361E+15 | 1.89828E+15 |

| | | | | |
|-------------|-------------|-------------|-------------|-------------|
| 2.04912E+15 | 2.14069E+15 | 2.14762E+15 | 2.23388E+15 | 2.23686E+15 |
| 1.93603E+15 | 1.97294E+15 | 1.96470E+15 | 2.00535E+15 | 2.00148E+15 |
| 2.23928E+15 | 2.36856E+15 | 2.37722E+15 | 2.46188E+15 | 2.40061E+15 |
| 2.11674E+15 | 2.14119E+15 | 2.35769E+15 | 2.20555E+15 | 1.92787E+15 |
| 1.88052E+15 | 1.88362E+15 | 2.09930E+15 | 2.31301E+15 | 2.11460E+15 |
| 2.12814E+15 | 2.20369E+15 | 2.51704E+15 | 2.16238E+15 | 1.93523E+15 |
| 1.92892E+15 | 1.97181E+15 | 2.24714E+15 | 2.54391E+15 | 2.35716E+15 |
| 2.37854E+15 | 2.45715E+15 | 2.75682E+15 | 2.18149E+15 | 2.21761E+15 |
| 2.11983E+15 | 1.94200E+15 | 1.92692E+15 | 1.87620E+15 | 1.87833E+15 |
| 1.83925E+15 | 2.04493E+15 | 2.14569E+15 | 2.15653E+15 | 2.24491E+15 |
| 2.23001E+15 | 1.91276E+15 | 1.94886E+15 | 1.94439E+15 | 1.99410E+15 |
| 2.00288E+15 | 2.26783E+15 | 2.42522E+15 | 2.44181E+15 | 2.53903E+15 |
| 2.46806E+15 | 2.46584E+15 | 2.18133E+15 | 2.11528E+15 | 1.89671E+15 |
| 1.87339E+15 | 2.08275E+15 | 1.83253E+15 | 1.80360E+15 | 1.99956E+15 |
| 2.06854E+15 | 2.38284E+15 | 2.15809E+15 | 2.17005E+15 | 1.88661E+15 |
| 1.91968E+15 | 2.18279E+15 | 1.97069E+15 | 1.99355E+15 | 2.26030E+15 |
| 2.37208E+15 | 2.73378E+15 | 2.45867E+15 | 2.41465E+15 | 2.06892E+15 |
| 1.83515E+15 | 1.80939E+15 | 2.00267E+15 | 2.04468E+15 | 2.30915E+15 |
| 2.04279E+15 | 1.99871E+15 | 1.80076E+15 | 1.84079E+15 | 2.10553E+15 |
| 1.90582E+15 | 1.92713E+15 | 2.11870E+15 | 2.14526E+15 | 2.41573E+15 |
| 2.14776E+15 | 2.12016E+15 | 2.11182E+15 | 2.14553E+15 | 2.41732E+15 |
| 2.14966E+15 | 2.11448E+15 | 1.84986E+15 | 1.86683E+15 | 1.83815E+15 |
| 2.05727E+15 | 2.13592E+15 | 2.11047E+15 | 2.14228E+15 | 2.06647E+15 |
| 1.83413E+15 | 1.88149E+15 | 1.88683E+15 | 1.94602E+15 | 1.95797E+15 |
| 2.13044E+15 | 2.20077E+15 | 2.16594E+15 | 2.20686E+15 | 2.14886E+15 |
| 2.10810E+15 | 2.13543E+15 | 2.10112E+15 | 2.12683E+15 | 2.08932E+15 |
| 1.85827E+15 | 1.87558E+15 | 2.10115E+15 | 2.36070E+15 | 2.14325E+15 |
| 2.12398E+15 | 2.15249E+15 | 2.37913E+15 | 2.08927E+15 | 1.87955E+15 |
| 1.88121E+15 | 1.93334E+15 | 2.21170E+15 | 2.37778E+15 | 2.14610E+15 |
| 2.12271E+15 | 2.15702E+15 | 2.40514E+15 | 2.33626E+15 | 2.06770E+15 |
| 2.03957E+15 | 2.06486E+15 | 2.32225E+15 | 1.92972E+15 | 1.95037E+15 |
| 1.91574E+15 | 2.14040E+15 | 2.22980E+15 | 2.19951E+15 | 2.24036E+15 |
| 2.15380E+15 | 1.88143E+15 | 1.92957E+15 | 1.92593E+15 | 1.97941E+15 |
| 1.97409E+15 | 2.08365E+15 | 2.15590E+15 | 2.12947E+15 | 2.17103E+15 |
| 2.11419E+15 | 2.04710E+15 | 2.06094E+15 | 2.03363E+15 | 2.06341E+15 |
| 2.04345E+15 | 2.26898E+15 | 2.01370E+15 | 1.97500E+15 | 2.18554E+15 |
| 2.23324E+15 | 2.51254E+15 | 2.22534E+15 | 2.16485E+15 | 1.90239E+15 |
| 1.94017E+15 | 2.19821E+15 | 1.96905E+15 | 1.95699E+15 | 2.02571E+15 |
| 2.06949E+15 | 2.34408E+15 | 2.08945E+15 | 2.06265E+15 | 1.99589E+15 |
| 1.99968E+15 | 2.25558E+15 | 2.01396E+15 | 2.00700E+15 | 2.87737E+15 |
| 2.40209E+15 | 2.41734E+15 | 1.93445E+15 | 1.92957E+15 | 2.15450E+15 |
| 1.90493E+15 | 1.87795E+15 | 2.02969E+15 | 2.04090E+15 | 2.27852E+15 |
| 1.99770E+15 | 1.94364E+15 | 1.81711E+15 | 1.84890E+15 | 2.11272E+15 |
| 1.91623E+15 | 1.95402E+15 | 2.09899E+15 | 2.16768E+15 | 2.47805E+15 |
| 2.22447E+15 | 2.20695E+15 | 2.54530E+15 | 2.71891E+15 | 2.41352E+15 |
| 1.97244E+15 | 1.96708E+15 | 1.92873E+15 | 1.94136E+15 | 1.91132E+15 |
| 2.05584E+15 | 2.10843E+15 | 2.05557E+15 | 2.06472E+15 | 1.98226E+15 |
| 1.83627E+15 | 1.87568E+15 | 1.88662E+15 | 1.95400E+15 | 1.99202E+15 |
| 2.14992E+15 | 2.25161E+15 | 2.24643E+15 | 2.30807E+15 | 2.25806E+15 |
| 2.64888E+15 | 2.55847E+15 | 2.90471E+15 | 2.23629E+15 | 1.95971E+15 |
| 1.92313E+15 | 1.93751E+15 | 2.17381E+15 | 2.31541E+15 | 2.07481E+15 |
| 2.03212E+15 | 2.03713E+15 | 2.24129E+15 | 2.07198E+15 | 1.86161E+15 |
| 1.87369E+15 | 1.94011E+15 | 2.25487E+15 | 2.44798E+15 | 2.23804E+15 |
| 2.23577E+15 | 2.28660E+15 | 2.55542E+15 | 2.57606E+15 | 2.75306E+15 |
| 2.44566E+15 | 2.00194E+15 | 2.00131E+15 | 1.96670E+15 | 1.98765E+15 |

| | | | | |
|-------------|-------------|-------------|-------------|-------------|
| 1.96298E+15 | 2.05899E+15 | 2.11392E+15 | 2.06416E+15 | 2.07506E+15 |
| 1.99538E+15 | 1.85157E+15 | 1.89324E+15 | 1.90743E+15 | 1.98155E+15 |
| 2.02789E+15 | 2.19302E+15 | 2.29607E+15 | 2.28508E+15 | 2.33957E+15 |
| 2.27123E+15 | 2.95349E+15 | 2.46829E+15 | 2.48489E+15 | 1.99447E+15 |
| 1.99875E+15 | 2.24247E+15 | 1.99721E+15 | 1.98633E+15 | 2.03306E+15 |
| 2.05858E+15 | 2.30137E+15 | 2.02006E+15 | 1.96950E+15 | 1.84575E+15 |
| 1.88258E+15 | 2.15876E+15 | 1.96992E+15 | 2.02465E+15 | 2.18432E+15 |
| 2.25446E+15 | 2.56502E+15 | 2.27922E+15 | 2.24074E+15 | 2.28917E+15 |
| 2.02491E+15 | 1.98306E+15 | 2.13803E+15 | 2.18320E+15 | 2.47856E+15 |
| 2.20785E+15 | 2.19879E+15 | 2.01833E+15 | 2.01301E+15 | 2.22880E+15 |
| 1.95075E+15 | 1.90030E+15 | 2.06767E+15 | 2.11892E+15 | 2.41503E+15 |
| 2.16730E+15 | 2.16113E+15 | 2.53719E+15 | 2.50050E+15 | 2.96881E+15 |
| 2.44589E+15 | 2.45418E+15 | 2.02565E+15 | 2.05010E+15 | 2.00822E+15 |
| 2.20753E+15 | 2.31105E+15 | 2.29823E+15 | 2.36253E+15 | 2.30871E+15 |
| 2.05121E+15 | 2.03975E+15 | 1.97376E+15 | 1.96565E+15 | 1.90587E+15 |
| 2.13601E+15 | 2.21899E+15 | 2.20718E+15 | 2.26712E+15 | 2.22879E+15 |
| 2.49865E+15 | 2.76881E+15 | 2.52171E+15 | 2.66463E+15 | 2.31023E+15 |
| 1.99060E+15 | 2.01612E+15 | 2.26497E+15 | 2.53073E+15 | 2.32177E+15 |
| 2.32093E+15 | 2.38041E+15 | 2.66257E+15 | 2.31215E+15 | 2.00827E+15 |
| 1.94836E+15 | 1.94161E+15 | 2.15269E+15 | 2.44542E+15 | 2.21695E+15 |
| 2.20731E+15 | 2.25756E+15 | 2.53609E+15 | 2.96622E+15 | 2.52079E+15 |
| 2.54315E+15 | 2.35419E+15 | 2.63186E+15 | 2.00871E+15 | 2.04095E+15 |
| 2.01541E+15 | 2.26921E+15 | 2.40710E+15 | 2.39968E+15 | 2.47694E+15 |
| 2.39628E+15 | 2.05748E+15 | 2.03410E+15 | 1.97398E+15 | 1.97178E+15 |
| 1.92431E+15 | 2.19771E+15 | 2.28037E+15 | 2.25955E+15 | 2.31288E+15 |
| 2.25418E+15 | 2.44349E+15 | 2.66327E+15 | 2.35367E+15 | 2.42038E+15 |
| 1.97774E+15 | 2.25553E+15 | 2.01035E+15 | 1.99933E+15 | 2.24697E+15 |
| 2.35058E+15 | 2.69512E+15 | 2.40978E+15 | 2.35519E+15 | 2.02551E+15 |
| 2.00011E+15 | 2.22196E+15 | 1.95463E+15 | 1.91951E+15 | 2.18218E+15 |
| 2.23265E+15 | 2.52689E+15 | 2.24634E+15 | 2.21666E+15 | 2.45218E+15 |
| 2.30888E+15 | 2.63101E+15 | 1.97746E+15 | 1.81094E+15 | 2.05650E+15 |
| 1.83193E+15 | 1.82550E+15 | 2.06762E+15 | 2.11503E+15 | 2.39285E+15 |
| 2.13022E+15 | 2.09459E+15 | 2.22134E+15 | 2.27320E+15 | 2.57785E+15 |
| 2.29576E+15 | 2.29517E+15 | 2.23515E+15 | 2.29191E+15 | 2.59071E+15 |
| 2.29672E+15 | 2.27129E+15 | 2.36241E+15 | 2.33586E+15 | 2.45375E+15 |
| 1.93487E+15 | 1.48011E+15 | 1.83203E+15 | 1.85659E+15 | 1.83500E+15 |
| 2.05217E+15 | 2.09871E+15 | 2.07373E+15 | 2.10736E+15 | 2.06907E+15 |
| 2.29353E+15 | 2.39904E+15 | 2.37800E+15 | 2.44154E+15 | 2.39169E+15 |
| 2.28936E+15 | 2.36153E+15 | 2.30686E+15 | 2.33783E+15 | 2.25311E+15 |
| 2.31572E+15 | 2.29661E+15 | 2.04088E+15 | 1.83314E+15 | 1.31289E+15 |
| 1.81469E+15 | 1.83615E+15 | 2.06241E+15 | 2.27064E+15 | 2.02344E+15 |
| 2.00202E+15 | 2.03119E+15 | 2.28391E+15 | 2.62053E+15 | 2.39611E+15 |
| 2.38418E+15 | 2.43692E+15 | 2.72201E+15 | 2.57645E+15 | 2.29497E+15 |
| 2.22889E+15 | 2.22172E+15 | 2.41488E+15 | 2.41408E+15 | 2.02638E+15 |
| 1.78396E+15 | 1.55734E+15 | 1.27412E+15 | 1.84764E+15 | 1.87234E+15 |
| 1.84504E+15 | 1.99621E+15 | 2.01463E+15 | 1.98692E+15 | 2.01550E+15 |
| 1.99108E+15 | 2.34299E+15 | 2.47120E+15 | 2.44395E+15 | 2.50320E+15 |
| 2.40144E+15 | 2.25728E+15 | 2.29873E+15 | 2.19821E+15 | 2.16170E+15 |
| 1.97280E+15 | 1.89750E+15 | 1.80805E+15 | 1.54737E+15 | 1.31258E+15 |
| 8.79700E+14 | 2.09742E+15 | 1.86781E+15 | 1.86016E+15 | 1.96234E+15 |
| 1.95155E+15 | 2.18902E+15 | 1.94455E+15 | 1.93347E+15 | 2.31981E+15 |
| 2.39973E+15 | 2.71671E+15 | 2.39418E+15 | 2.30259E+15 | 2.19362E+15 |
| 2.17730E+15 | 2.34999E+15 | 1.94086E+15 | 1.68848E+15 | 1.43561E+15 |
| 1.28548E+15 | 1.25771E+15 | 8.74314E+14 | 6.00154E+14 | 2.81540E+15 |
| 2.49486E+15 | 2.41760E+15 | 2.43192E+15 | 2.47949E+15 | 2.80133E+15 |

| | | | | |
|-------------|-------------|-------------|-------------|-------------|
| 2.47358E+15 | 2.42566E+15 | 2.42997E+15 | 2.49799E+15 | 2.78813E+15 |
| 2.43958E+15 | 2.31749E+15 | 2.20485E+15 | 2.16255E+15 | 2.26899E+15 |
| 1.80696E+15 | 1.38766E+15 | 0.00000E+00 | 0.00000E+00 | 0.00000E+00 |
| 0.00000E+00 | 0.00000E+00 | 2.33780E+15 | 2.57229E+15 | 2.46056E+15 |
| 2.45426E+15 | 2.38044E+15 | 2.27652E+15 | 2.34346E+15 | 2.38160E+15 |
| 2.37786E+15 | 2.44615E+15 | 2.18221E+15 | 2.35621E+15 | 2.20715E+15 |
| 2.09461E+15 | 2.06958E+15 | 1.84608E+15 | 1.67231E+15 | 1.20803E+15 |
| 0.00000E+00 | 0.00000E+00 | 0.00000E+00 | 0.00000E+00 | 0.00000E+00 |
| 2.32071E+15 | 2.22201E+15 | 2.64458E+15 | 2.63718E+15 | 2.15431E+15 |
| 2.22128E+15 | 2.08641E+15 | 2.48076E+15 | 2.43369E+15 | 1.97759E+15 |
| 2.01873E+15 | 1.87216E+15 | 2.18824E+15 | 2.06787E+15 | 1.75291E+15 |
| 1.56273E+15 | 1.38155E+15 | 1.14262E+15 | 0.00000E+00 | 0.00000E+00 |
| 0.00000E+00 | 0.00000E+00 | 0.00000E+00 | 2.04126E+15 | 2.26724E+15 |
| 2.15178E+15 | 2.11566E+15 | 2.01127E+15 | 1.89527E+15 | 1.90798E+15 |
| 1.90105E+15 | 1.85646E+15 | 1.87017E+15 | 1.60525E+15 | 1.73611E+15 |
| 1.59664E+15 | 1.49920E+15 | 1.47745E+15 | 1.30031E+15 | 1.12600E+15 |
| 7.65956E+14 | 0.00000E+00 | 0.00000E+00 | 0.00000E+00 | 0.00000E+00 |
| 0.00000E+00 | 2.17929E+15 | 1.91746E+15 | 1.83652E+15 | 1.81279E+15 |
| 1.79548E+15 | 1.98607E+15 | 1.65008E+15 | 1.50166E+15 | 1.33724E+15 |
| 1.30439E+15 | 1.42371E+15 | 1.18462E+15 | 1.09333E+15 | 1.01743E+15 |
| 9.72363E+14 | 9.97015E+14 | 7.16569E+14 | 5.03903E+14 | 0.00000E+00 |
| 0.00000E+00 | 0.00000E+00 | 0.00000E+00 | 0.00000E+00 | 1.55237E+15 |
| 1.38231E+15 | 1.34983E+15 | 1.25601E+15 | 1.21531E+15 | 1.28468E+15 |
| 1.06816E+15 | 8.87599E+14 | 0.00000E+00 | 0.00000E+00 | 0.00000E+00 |
| 0.00000E+00 | 0.00000E+00 | 0.00000E+00 | 0.00000E+00 | 0.00000E+00 |
| 0.00000E+00 | 0.00000E+00 | 0.00000E+00 | 0.00000E+00 | 0.00000E+00 |
| 0.00000E+00 | 0.00000E+00 | 0.00000E+00 | 0.00000E+00 | 0.00000E+00 |
| 0.00000E+00 | 0.00000E+00 | 1.13670E+15 | 1.14918E+15 | 1.11685E+15 |
| 1.02031E+15 | 9.72470E+14 | 8.92220E+14 | 8.19297E+14 | 6.53382E+14 |
| 0.00000E+00 | 0.00000E+00 | 0.00000E+00 | 0.00000E+00 | 0.00000E+00 |
| 0.00000E+00 | 0.00000E+00 | 0.00000E+00 | 0.00000E+00 | 0.00000E+00 |
| 0.00000E+00 | 0.00000E+00 | 0.00000E+00 | 0.00000E+00 | 0.00000E+00 |
| 9.09864E+14 | 9.12571E+14 | 9.99514E+14 | 8.91565E+14 | 7.46038E+14 |
| 6.81278E+14 | 6.10016E+14 | 5.40626E+14 | 0.00000E+00 | 0.00000E+00 |
| 0.00000E+00 | 0.00000E+00 | 0.00000E+00 | 0.00000E+00 | 0.00000E+00 |
| 0.00000E+00 | 0.00000E+00 | 0.00000E+00 | 0.00000E+00 | 0.00000E+00 |
| 0.00000E+00 | 0.00000E+00 | 0.00000E+00 | 0.00000E+00 | 0.00000E+00 |
| 6.74228E+14 | 5.90156E+14 | 5.59258E+14 | 5.08441E+14 | 4.40363E+14 |
| 3.29725E+14 | 0.00000E+00 | 0.00000E+00 | 0.00000E+00 | 0.00000E+00 |
| 0.00000E+00 | 0.00000E+00 | 0.00000E+00 | 0.00000E+00 | 0.00000E+00 |
| 0.00000E+00 | 0.00000E+00 | 0.00000E+00 | 0.00000E+00 | 0.00000E+00 |
| 0.00000E+00 | 5.40465E+14 | 4.64012E+14 | 4.45617E+14 | 3.81856E+14 |
| 3.55271E+14 | 3.67085E+14 | 2.71727E+14 | 2.07674E+14 | 0.00000E+00 |
| 0.00000E+00 | 0.00000E+00 | 0.00000E+00 | 0.00000E+00 | 0.00000E+00 |
| 0.00000E+00 | 0.00000E+00 | 0.00000E+00 | 0.00000E+00 | 0.00000E+00 |
| 0.00000E+00 | 0.00000E+00 | 0.00000E+00 | 0.00000E+00 | 0.00000E+00 |

COMPONENT Z

| | | | | |
|-------------|-------------|-------------|-------------|-------------|
| 1.20051E-03 | 2.01117E-03 | 2.54674E-03 | 2.79905E-03 | 2.87465E-03 |
| 2.85916E-03 | 2.94752E-03 | 2.96756E-03 | 2.92117E-03 | 2.98851E-03 |
| 3.03041E-03 | 3.02768E-03 | 2.98669E-03 | 3.06593E-03 | 3.09645E-03 |
| 2.96756E-03 | 2.88740E-03 | 2.54128E-03 | 1.69874E-03 | |

&FISSION FRACTIONS

PLUTONIUM
 FRACTION

&ROW H

69*0.412

&ROW G to C

115*0.412 115*0.412 115*0.412 115*0.412 115*0.412

&ROW B

8*0.412 5*0.195 5*0.150 5*0.0
8*0.412 5*0.195 5*0.150 5*0.0
8*0.412 5*0.195 5*0.150 5*0.0
8*0.412 5*0.195 5*0.150 5*0.0
8*0.412 5*0.195 5*0.150 5*0.0

&ROW A

3*0.521 5*0.617 15*0.0
3*0.521 5*0.617 15*0.0
3*0.521 5*0.617 15*0.0
3*0.521 5*0.617 15*0.0
3*0.521 5*0.617 15*0.0

&ROW H

69*0.412

&ROW G to C

115*0.412 115*0.412 115*0.412 115*0.412 115*0.412

&ROW B

8*0.412 5*0.195 5*0.150 5*0.0
8*0.412 5*0.195 5*0.150 5*0.0
8*0.412 5*0.195 5*0.150 5*0.0
8*0.412 5*0.195 5*0.150 5*0.0
8*0.412 5*0.195 5*0.150 5*0.0

&ROW A

3*0.521 5*0.617 15*0.0
3*0.521 5*0.617 15*0.0
3*0.521 5*0.617 15*0.0
3*0.521 5*0.617 15*0.0
3*0.521 5*0.617 15*0.0

&ROW H

69*0.412

&ROW G to C

115*0.412 115*0.412 115*0.412 115*0.412 115*0.412

&ROW B

8*0.412 5*0.195 5*0.150 5*0.0
8*0.412 5*0.195 5*0.150 5*0.0
8*0.412 5*0.195 5*0.150 5*0.0
8*0.412 5*0.195 5*0.150 5*0.0
8*0.412 5*0.195 5*0.150 5*0.0

&ROW A

3*0.521 5*0.617 15*0.0
3*0.521 5*0.617 15*0.0
3*0.521 5*0.617 15*0.0
3*0.521 5*0.617 15*0.0
3*0.521 5*0.617 15*0.0

&ROW H

69*0.412

&ROW G to C

115*0.412 115*0.412 115*0.412 115*0.412 115*0.412

&ROW B

8*0.412 5*0.195 5*0.150 5*0.0
8*0.412 5*0.195 5*0.150 5*0.0
8*0.412 5*0.195 5*0.150 5*0.0
8*0.412 5*0.195 5*0.150 5*0.0

8*0.412 5*0.195 5*0.150 5*0.0
&ROW A
3*0.521 5*0.617 15*0.0
3*0.521 5*0.617 15*0.0
3*0.521 5*0.617 15*0.0
3*0.521 5*0.617 15*0.0
3*0.521 5*0.617 15*0.0
&ROW H
69*0.412
&ROW G to C
115*0.412 115*0.412 115*0.412 115*0.412 115*0.412
&ROW B
8*0.412 5*0.195 5*0.150 5*0.0
8*0.412 5*0.195 5*0.150 5*0.0
8*0.412 5*0.195 5*0.150 5*0.0
8*0.412 5*0.195 5*0.150 5*0.0
8*0.412 5*0.195 5*0.150 5*0.0
&ROW A
3*0.521 5*0.617 15*0.0
3*0.521 5*0.617 15*0.0
3*0.521 5*0.617 15*0.0
3*0.521 5*0.617 15*0.0
3*0.521 5*0.617 15*0.0
&ROW H
69*0.412
&ROW G to C
115*0.412 115*0.412 115*0.412 115*0.412 115*0.412
&ROW B
8*0.412 5*0.195 5*0.150 5*0.0
8*0.412 5*0.195 5*0.150 5*0.0
8*0.412 5*0.195 5*0.150 5*0.0
8*0.412 5*0.195 5*0.150 5*0.0
8*0.412 5*0.195 5*0.150 5*0.0
&ROW A
3*0.521 5*0.617 15*0.0
3*0.521 5*0.617 15*0.0
3*0.521 5*0.617 15*0.0
3*0.521 5*0.617 15*0.0
3*0.521 5*0.617 15*0.0
&ROW H
69*0.412
&ROW G to C
115*0.412 115*0.412 115*0.412 115*0.412 115*0.412
&ROW B
8*0.412 5*0.195 5*0.150 5*0.0
8*0.412 5*0.195 5*0.150 5*0.0
8*0.412 5*0.195 5*0.150 5*0.0
8*0.412 5*0.195 5*0.150 5*0.0
8*0.412 5*0.195 5*0.150 5*0.0
&ROW A
3*0.521 5*0.617 15*0.0
3*0.521 5*0.617 15*0.0
3*0.521 5*0.617 15*0.0
3*0.521 5*0.617 15*0.0
3*0.521 5*0.617 15*0.0

&ROW H
69*0.412
&ROW G to C
115*0.412 115*0.412 115*0.412 115*0.412 115*0.412
&ROW B
8*0.412 5*0.195 5*0.150 5*0.0
8*0.412 5*0.195 5*0.150 5*0.0
8*0.412 5*0.195 5*0.150 5*0.0
8*0.412 5*0.195 5*0.150 5*0.0
8*0.412 5*0.195 5*0.150 5*0.0
&ROW A
3*0.521 5*0.617 15*0.0
3*0.521 5*0.617 15*0.0
3*0.521 5*0.617 15*0.0
3*0.521 5*0.617 15*0.0
3*0.521 5*0.617 15*0.0
&ROW H
69*0.412
&ROW G to C
115*0.412 115*0.412 115*0.412 115*0.412 115*0.412
&ROW B
8*0.412 5*0.195 5*0.150 5*0.0
8*0.412 5*0.195 5*0.150 5*0.0
8*0.412 5*0.195 5*0.150 5*0.0
8*0.412 5*0.195 5*0.150 5*0.0
8*0.412 5*0.195 5*0.150 5*0.0
&ROW A
3*0.521 5*0.617 15*0.0
3*0.521 5*0.617 15*0.0
3*0.521 5*0.617 15*0.0
3*0.521 5*0.617 15*0.0
3*0.521 5*0.617 15*0.0
&ROW H
69*0.412
&ROW G to C
115*0.412 115*0.412 115*0.412 115*0.412 115*0.412
&ROW B
8*0.412 5*0.195 5*0.150 5*0.0
8*0.412 5*0.195 5*0.150 5*0.0
8*0.412 5*0.195 5*0.150 5*0.0
8*0.412 5*0.195 5*0.150 5*0.0
8*0.412 5*0.195 5*0.150 5*0.0
&ROW A
3*0.521 5*0.617 15*0.0
3*0.521 5*0.617 15*0.0
3*0.521 5*0.617 15*0.0
3*0.521 5*0.617 15*0.0
3*0.521 5*0.617 15*0.0
&ROW H
69*0.412
&ROW G to C
115*0.412 115*0.412 115*0.412 115*0.412 115*0.412
&ROW B
8*0.412 5*0.195 5*0.150 5*0.0
8*0.412 5*0.195 5*0.150 5*0.0

8*0.412 5*0.195 5*0.150 5*0.0
8*0.412 5*0.195 5*0.150 5*0.0
8*0.412 5*0.195 5*0.150 5*0.0

&ROW A

3*0.521 5*0.617 15*0.0
3*0.521 5*0.617 15*0.0
3*0.521 5*0.617 15*0.0
3*0.521 5*0.617 15*0.0
3*0.521 5*0.617 15*0.0

&ROW H

69*0.412

&ROW G to C

115*0.412 115*0.412 115*0.412 115*0.412 115*0.412

&ROW B

8*0.412 5*0.195 5*0.150 5*0.0
8*0.412 5*0.195 5*0.150 5*0.0
8*0.412 5*0.195 5*0.150 5*0.0
8*0.412 5*0.195 5*0.150 5*0.0
8*0.412 5*0.195 5*0.150 5*0.0

&ROW A

3*0.521 5*0.617 15*0.0
3*0.521 5*0.617 15*0.0
3*0.521 5*0.617 15*0.0
3*0.521 5*0.617 15*0.0
3*0.521 5*0.617 15*0.0

&ROW H

69*0.412

&ROW G to C

115*0.412 115*0.412 115*0.412 115*0.412 115*0.412

&ROW B

8*0.412 5*0.195 5*0.150 5*0.0
8*0.412 5*0.195 5*0.150 5*0.0
8*0.412 5*0.195 5*0.150 5*0.0
8*0.412 5*0.195 5*0.150 5*0.0
8*0.412 5*0.195 5*0.150 5*0.0

&ROW A

3*0.521 5*0.617 15*0.0
3*0.521 5*0.617 15*0.0
3*0.521 5*0.617 15*0.0
3*0.521 5*0.617 15*0.0
3*0.521 5*0.617 15*0.0

&ROW H

69*0.412

&ROW G to C

115*0.412 115*0.412 115*0.412 115*0.412 115*0.412

&ROW B

8*0.412 5*0.195 5*0.150 5*0.0
8*0.412 5*0.195 5*0.150 5*0.0
8*0.412 5*0.195 5*0.150 5*0.0
8*0.412 5*0.195 5*0.150 5*0.0
8*0.412 5*0.195 5*0.150 5*0.0

&ROW A

3*0.521 5*0.617 15*0.0
3*0.521 5*0.617 15*0.0
3*0.521 5*0.617 15*0.0

3*0.521 5*0.617 15*0.0
3*0.521 5*0.617 15*0.0
&ROW H
69*0.412
&ROW G to C
115*0.412 115*0.412 115*0.412 115*0.412 115*0.412
&ROW B
8*0.412 5*0.195 5*0.150 5*0.0
8*0.412 5*0.195 5*0.150 5*0.0
8*0.412 5*0.195 5*0.150 5*0.0
8*0.412 5*0.195 5*0.150 5*0.0
8*0.412 5*0.195 5*0.150 5*0.0
&ROW A
3*0.521 5*0.617 15*0.0
3*0.521 5*0.617 15*0.0
3*0.521 5*0.617 15*0.0
3*0.521 5*0.617 15*0.0
3*0.521 5*0.617 15*0.0
&ROW H
69*0.412
&ROW G to C
115*0.412 115*0.412 115*0.412 115*0.412 115*0.412
&ROW B
8*0.412 5*0.195 5*0.150 5*0.0
8*0.412 5*0.195 5*0.150 5*0.0
8*0.412 5*0.195 5*0.150 5*0.0
8*0.412 5*0.195 5*0.150 5*0.0
8*0.412 5*0.195 5*0.150 5*0.0
&ROW A
3*0.521 5*0.617 15*0.0
3*0.521 5*0.617 15*0.0
3*0.521 5*0.617 15*0.0
3*0.521 5*0.617 15*0.0
3*0.521 5*0.617 15*0.0
&ROW H
69*0.412
&ROW G to C
115*0.412 115*0.412 115*0.412 115*0.412 115*0.412
&ROW B
8*0.412 5*0.195 5*0.150 5*0.0
8*0.412 5*0.195 5*0.150 5*0.0
8*0.412 5*0.195 5*0.150 5*0.0
8*0.412 5*0.195 5*0.150 5*0.0
8*0.412 5*0.195 5*0.150 5*0.0
&ROW A
3*0.521 5*0.617 15*0.0
3*0.521 5*0.617 15*0.0
3*0.521 5*0.617 15*0.0
3*0.521 5*0.617 15*0.0
3*0.521 5*0.617 15*0.0
&ROW H
69*0.412
&ROW G to C
115*0.412 115*0.412 115*0.412 115*0.412 115*0.412
&ROW B

```
8*0.412 5*0.195 5*0.150 5*0.0
8*0.412 5*0.195 5*0.150 5*0.0
8*0.412 5*0.195 5*0.150 5*0.0
8*0.412 5*0.195 5*0.150 5*0.0
8*0.412 5*0.195 5*0.150 5*0.0
&ROW A
3*0.521 5*0.617 15*0.0
3*0.521 5*0.617 15*0.0
3*0.521 5*0.617 15*0.0
3*0.521 5*0.617 15*0.0
3*0.521 5*0.617 15*0.0
&ROW H
69*0.412
&ROW G to C
115*0.412 115*0.412 115*0.412 115*0.412 115*0.412
&ROW B
8*0.412 5*0.195 5*0.150 5*0.0
8*0.412 5*0.195 5*0.150 5*0.0
8*0.412 5*0.195 5*0.150 5*0.0
8*0.412 5*0.195 5*0.150 5*0.0
8*0.412 5*0.195 5*0.150 5*0.0
&ROW A
3*0.521 5*0.617 15*0.0
3*0.521 5* 617 15*0.0
3*0.521 5* 617 15*0.0
3*0.521 5*0.617 15*0.0
3*0.521 5*0.617 15*0.0
END
& UNIT 10
BEGIN RESPONSE DATA
& INSERT IRDF-90 DOSIMETRY CROSS-SECTIONS HERE
END
& UNIT 11
BEGIN SENSITIVITY DATA
COMBINATIONS 6
2631 2
EXC 1 2
2631 2
INC 1 2
2631 4
EXC 1 2
2631 4
INC 1 2
1250296 3
TOTAL
825 3
TOTAL
GROUPS 15
14.6 10.0 6.06531 3.67879 2.23130
1.35335 0.82085 0.49787 0.30197 0.18316
0.11109 0.06738 0.04087 0.02480 0.01503
0.00912
END
```

FEW-CHANNEL UNFOLDING IN SHIELDING-THE SENSAK CODE*

A K McCracken

Radiation Physics & Shielding Group, Atomic Energy
Establishment, Atomic Energy Authority, Winfrith,
Dorchester, Dorset, United Kingdom.

1 INTRODUCTION

Information available for the unfolding of flux spectra from detector counting-rates will usually include some knowledge (albeit sometimes imprecise) of the nature of the spectrum sought. In the case of a Standard Field this knowledge may be of very high quality. In reactor work - and particularly in shielding - we shall usually have some calculation which, even using the best available methods, may be subject to quite large uncertainties.

An experienced worker will be able to give an estimate of this uncertainty - which is worth more than an uninformed guess. (Comparison of calculated and measured counting rates of detectors which span different energy ranges will in itself give a rough idea of the uncertainties in the calculated spectrum). The introduction of correlations between group fluxes in these difficult situations might seem unjustified but we do have the knowledge that calculated spectral shapes are roughly correct locally in energy and mutilation of these shapes during unfolding can be inhibited by the introduction of positive correlation coefficients of, say, 0.5 and 0.25 between first and second group flux neighbours. Although arbitrary, this is more sensible than treating calculated fluxes as independent.

Some tests with a prototype code SENSAK I using the above type of spectral information were carried out using numerical minimisation subroutines to derive unfolding spectra, and work on the estimation of uncertainties on the output spectrum by introducing Monte Carlo sampling of the probability density functions (p. d. f's) of the measured parameters was initiated. This approach which is obligatory in many-channel unfolding,

* Paper presented at the Third ASTM-EURATOM Symposium on Reactor Dosimetry held at Ispra, Italy in 1979.

is, however, considerably less efficient for few-channel unfolding than the purely algebraic method of Perey (1) employed in STAYSL. SENSAK II seeks to solve the same problem as SENSAK I with the efficiency inherent in the latter approach.

The speed and directness of this method have obvious appeal. Disadvantages are:-

- (i) With strong long-range correlations in the parameter covariance matrix (and with many detector results) the inversion of an ill-conditioned matrix may arise.
- (ii) The linear methods adopted are unsuitable without modification for dealing with large perturbations in an unfolding.

The latter implies some step-length limitation by scaling together with iteration. Only further experience with practical problems will show whether such a modification method is preferable to the method of 'black-box' minimisation with Monte Carlo sampling.

2 METHOD

The calculation of the saturation counting-rate C_i of the i th detector in a reactor irradiation experiment can be expressed by

$$C_i = S f_i \sum_j x_{ij} \phi_j = \sum_j x_{ij} \phi_j \quad 1$$

where S is a source-strength

f_i is the efficiency of the counting system to radiation from the i^{th} detector

x_{ij} is the reaction cross-section of detector i to flux in group j ,

ϕ_j is the calculated flux in group j per unit source strength.

The form of equation 1 recognises two things:-

- (i) We measure counting-rates - not reaction-rates
- (ii) We are normally given a fission-source per unit power to start a calculation; estimation of the power leads to uncertainty in the source strength S .

To each of the variables S f_i x_{ij} ϕ_j is ascribed a variance-covariance matrix V and it is presumed that the above variates are mutually independent.

From equation 1 we find

$$\delta C_i = f_i \sum_j x_{ij} \delta \phi_j + f_i \sum_j \delta x_{ij} \phi_j + \left[\frac{\delta f_i}{f_i} + \frac{\delta S}{S} \right] C_i \quad 2$$

which can be written

$$\delta \underline{C} = G \delta \underline{P} \quad 3$$

where \underline{P} is the vector of parameters to be adjusted in the unfolding.

The form of $G \delta \underline{P}$ (illustrated for two detectors) is

$$\begin{pmatrix} f_1 \underline{x}_1^T & f_1 \underline{\phi}^T & 0 & \underline{x}_1^T \underline{\phi} & 0 & f_1 \underline{x}_1^T \underline{\phi} \\ f_2 \underline{x}_2^T & 0 & f_2 \underline{\phi}^T & 0 & \underline{x}_2^T \underline{\phi} & f_2 \underline{x}_2^T \underline{\phi} \end{pmatrix} \begin{pmatrix} \delta \underline{\phi} \\ \delta \underline{x}_1 \\ \delta \underline{x}_2 \\ \delta \underline{f} \\ \frac{\delta S}{S} \end{pmatrix} \quad 4$$

Noting that $\langle \delta \underline{C} \delta \underline{C}^T \rangle = V_c$ where $\langle \quad \rangle$ denotes the expectation, the dispersion matrix of \underline{C} is found in terms of that of \underline{P} to be

$$V_c = G V_p G^T \quad 5$$

where V_p has the form (for two detectors)

$$V_p = \begin{bmatrix} V_s & & & & \\ & V_{x1} & & & \\ & & V_{x2} & & \\ & & & V_f & \\ & & & & V_s \end{bmatrix} \quad 6$$

This form of V_p shows the cross-sections of different detectors as independent - if information to the contrary is available the individual matrices V_{x_i} can be replaced by a single matrix V_x . V_s is simply $\sigma^2(S)/S^2$ and V_f will be taken as diagonal if correlations within a counting system are ignored or unknown.

Maximum likelihood agreement between calculation \underline{C} and measurement \underline{M} can now be sought by choosing $\delta\underline{P}$ and hence $\delta\underline{C}$ such that

$$\chi^2 = (\underline{C} - \underline{M} + \delta\underline{C})^T V_M^{-1} (\underline{C} - \underline{M} + \delta\underline{C}) + \delta\underline{C}^T V_C^{-1} \delta\underline{C} = \text{a minimum} \quad 7$$

where V_M^{-1} the inverse dispersion of matrix of \underline{M} is diagonal.

Setting the derivative w.r.t. $\delta\underline{C}$ of equation 7 equal to zero gives

$$\delta\underline{C} = -V_C (V_C + V_M)^{-1} (\underline{C} - \underline{M}) \quad 8$$

and \therefore

$$\delta\underline{P} = -G^{-1} (G V_P G^T) (V_C + V_M)^{-1} (\underline{C} - \underline{M}) = -V_P G^T (V_C + V_M)^{-1} (\underline{C} - \underline{M}) \quad 9$$

Writing $\hat{\underline{P}} = \underline{P} + \delta\underline{P}$ we find

$$\langle \hat{\underline{P}} \hat{\underline{P}}^T \rangle = V_{\hat{P}} = V_P - V_P G^T (V_C + V_M)^{-1} G V_P^T \quad 10$$

for the dispersion matrix of the adjusted variables \underline{P} whose first components are the unfolded group fluxes. Equations 7 and 8 give for the minimum value of χ^2

$$\chi_{MIN}^2 = (\underline{C} - \underline{M})^T (V_C + V_M)^{-1} (\underline{C} - \underline{M}) \quad 11$$

and if \underline{C} is an unbiased estimator of \underline{M}

$$\langle \chi_{MIN}^2 \rangle = N_M \quad \text{the number of independent measurements.} \quad 12$$

Thus $\hat{\underline{P}}(\hat{\phi}, \hat{x}, \hat{f}, \hat{S})$ and $V_{\hat{P}}$ are established.

In many practical reactor situations the improvement of an imprecise first estimate $\underline{\phi}$ to $\hat{\underline{\phi}}$ with its associated part of $V_{\hat{P}}$ will be the most important product of the adjustment with $\hat{\underline{f}}, \hat{\underline{x}}, \hat{S}$ regarded as slightly refined by-products.

If we require χ_{MIN}^2 to be equal to N_M all the variance matrices V_C , V_M and hence V_P can be scaled by the factor $\alpha = \chi_{MIN}^2 / N_M$ without changing the values of the unfolded parameters - this operation is performed in SENSACK II. With the exception of the scaling, which needs discussion, the above algorithm represents a simple - in some ways oversimple - solution to the few-channel unfolding problem.

An example of its use is now given before consideration, necessarily brief in this paper, of some of the implications of this type of unfolding in situations where accurate calculation is difficult.

3 AN UNFOLDING

Fourteen activation detectors were irradiated in the ASPIS facility of the NESTOR reactor operated in the Core Source mode with the fission-plate removed. The experimental shield comprised a boral sheet followed by 10 centimetres each of lead and water. The neutron flux spectrum in this position was calculated in twenty groups with ANISN in spherical geometry. Detector cross sections were taken from the SAND-II library with the exception of those for $^{103}\text{Rh}(n, n')$ $^{103\text{M}}\text{Rh}$ which were taken from the UK Nuclear Data Library (DFN 94).

Uncertainties in the detector cross-sections were taken from SAND-II values quoted by Zijp (2) and for lack of any other information first neighbours of group cross-sections were statistically related with a correlation coefficient of +0.5. Fractional standard deviations of 0.3 and 0.05 were ascribed to the source strength and detector counting efficiencies respectively and of 0.5 and 0.3 to the top-energy ten and bottom-energy ten groups respectively of the calculated fluxes which were statistically related to their first and second neighbours with correlation coefficients of +0.5 and +0.25 respectively. A fractional standard deviation of 0.05 was uniformly applied to all saturated counting rates - this number is a realistic rounding of observed standard deviations. Table 1 shows some of the principal results of two unfoldings in the first of which all fourteen detectors were included in the unfolding, and in the second of which seven detectors - arbitrarily chosen - were omitted.

Table 2 gives the group structures employed and the flux spectrum before and after unfolding which included all fourteen detectors. (All the input parameters were perturbed but generally by an insignificant amount; these and output dispersion matrices are not shown for lack of space). The value of χ^2 per measurement fell from 279 to 1.10 for the first unfolding and from 235 to 0.96 for the second unfolding.

The important thing about Table 1 is not the good agreement between measurement and calculation of those detectors which were included in the unfolding but the improvement, sometimes striking, in the ability to predict measurement of each of the seven detectors which were excluded from the unfolding. This is precisely what a foil unfolding code will be required to do in practice. The c. p. u. time taken on an IBM 3033 for the fourteen detector unfolding was 30 seconds and the storage requirement was 500 Kbytes.

TABLE 1
AGREEMENT OF CALCULATION AND MEASUREMENT
BEFORE AND AFTER UNFOLDING

| Reaction | Calculated/Measured
Reaction -Rates | | | Fractional S. D
on Calculations | |
|--|--|----------------------|----------------------|------------------------------------|----------------------|
| | Before | After ⁽¹⁾ | After ⁽²⁾ | Before | After ⁽²⁾ |
| $^{58}\text{Ni}(n,p)^{58}\text{Co}$ | 2.06 | 1.02 | 1.0 | | |
| * $^{197}\text{Au}(n,\gamma)^{198}\text{Au}$ | 0.60 | 0.98 | 0.64 | 0.41 | 0.25 |
| * $^{59}\text{Co}(n,\gamma)^{60}\text{Co}$ | 0.71 | 0.98 | 0.80 | 0.39 | 0.20 |
| $^{63}\text{Cu}(n,\gamma)^{64}\text{Cu}$ | 0.85 | 1.01 | 0.98 | | |
| * $^{54}\text{Fe}(n,p)^{54}\text{Mn}$ | 2.02 | 1.00 | 1.01 | 0.42 | 0.38 |
| * $\text{S}(n,p)$ | 1.58 | 0.98 | 0.80 | 0.42 | 0.42 |
| $^{24}\text{Mg}(n,p)$ | 2.51 | 0.99 | 1.00 | | |
| * $^{47}\text{Ti}(n,p)$ | 1.72 | 1.00 | 1.00 | 0.43 | 0.46 |
| $^{237}\text{Np}(n,f)$ | 1.06 | 0.98 | 0.98 | | |
| $^{238}\text{U}(n,f)$ | 1.54 | 1.01 | 1.01 | | |
| * $^{27}\text{Al}(n,\alpha)^{24}\text{Na}$ | 3.14 | 1.01 | 1.50 | 0.50 | 0.25 |
| $^{115}\text{In}(n,n')^{115\text{M}}\text{In}$ | 1.34 | 1.00 | 1.00 | | |
| $^{103}\text{Rh}(n,n')^{103\text{M}}\text{Rh}$ | 1.37 | 1.01 | 1.01 | | |
| * $^{235}\text{U}(n,f)$ | 0.75 | 0.99 | 0.82 | 0.34 | 0.13 |

- (1) All detectors included in the unfolding
(2) Detectors marked * not included in the unfolding

TABLE 2

AN UNFOLDING WITH FOURTEEN DETECTORS

| Group | Upper Energy MeV | Flux/Lethargy | | Ratio After/Before | Fractional S. D. | |
|-------|----------------------|---------------|-------|--------------------|------------------|-------|
| | | Before | After | | Before | After |
| 1 | 12.2 | 5.85 | 3.75 | 0.64 | 0.50 | 0.72 |
| 2 | 10.0 | 27.2 | 8.53 | 0.31 | 0.50 | 0.86 |
| 3 | 8.18 | 77.5 | 12.6 | 0.16 | 0.50 | 1.70 |
| 4 | 6.36 | 158 | 38.1 | 0.24 | 0.50 | 1.40 |
| 5 | 4.96 | 195 | 101 | 0.52 | 0.50 | 0.62 |
| 6 | 4.06 | 186 | 122 | 0.66 | 0.50 | 0.60 |
| 7 | 3.01 | 401 | 267 | 0.67 | 0.50 | 0.65 |
| 8 | 2.46 | 599 | 386 | 0.64 | 0.50 | 0.69 |
| 9 | 2.35 | 628 | 353 | 0.56 | 0.50 | 0.59 |
| 10 | 1.83 | 696 | 560 | 0.80 | 0.50 | 0.35 |
| 11 | 1.11 | 797 | 857 | 1.08 | 0.30 | 0.19 |
| 12 | 0.55 | 558 | 572 | 1.03 | 0.30 | 0.28 |
| 13 | 0.11 | 222 | 204 | 0.92 | 0.30 | 0.28 |
| 14 | 3.35, -3 | 184 | 196 | 1.06 | 0.30 | 0.24 |
| 15 | 5.83, -4 | 203 | 263 | 1.29 | 0.30 | 0.15 |
| 16 | 1.01, -4 | 222 | 273 | 1.23 | 0.30 | 0.21 |
| 17 | 2.90, -5 | 194 | 258 | 1.33 | 0.30 | 0.20 |
| 18 | 1.07, -5 | 210 | 327 | 1.55 | 0.30 | 0.10 |
| 19 | 3.06, -6 | 229 | 299 | 1.31 | 0.30 | 0.21 |
| 20 | 1.12, -6
0.41, -6 | 234 | 247 | 1.06 | 0.30 | 0.26 |

4 DISCUSSION

No attempt was made to provide a precisely modelled definitive calculation of the type that might have been achieved by extensive running of Monte Carlo for example. Nevertheless this calculation is of no worse quality than would be found in many shielding applications. The standard deviations ascribed to the calculated fluxes are little more than informed guesses based on the calculator's experience and a cursory inspection of the calculated to measured reaction-rate ratios. A more detailed inspection of the latter might have improved these guesses but the fact remains that in many situations we may reasonably expect V_x , V_f and V_s to be more soundly based statistically than V_ϕ . For the case where we feel that V_ϕ is as well-known as the other components of the covariance matrix of the parameters (in which case χ^2_{MIN} is unlikely to differ significantly from N_M) it is entirely reasonable to scale all the covariance matrices in the way described in Section 2 - the covariance matrix and the distribution means, are both estimated parts of an unknown joint probability density function and are subject to adjustment. When V_ϕ is not statistically soundly based we may choose to ascribe a discrepancy between χ^2_{MIN} and N_M entirely to a bias in the flux calculations. Uncertainties in the cross-sections of materials used in the calculation of the flux spectrum are the only source of uncertainty in ϕ which can be treated statistically - in this case by uncertainty analysis. Other important sources of error in a flux calculation - those due to modelling, method inadequacies etc. cause the calculations \underline{C} to be biased estimators of the measurements. This bias is properly attributed to V_ϕ and account may be taken of it in a rather simplistic manner as follows :-

$$\text{We have } (\underline{C} - \underline{M})^T (V_C + V_M)^{-1} (\underline{C} - \underline{M}) = \chi^2_{MIN} \quad 13$$

$$\text{postulate } (\underline{C} - \underline{M})^T (V'_C + V_M)^{-1} (\underline{C} - \underline{M}) = N_M$$

$$\therefore V'_C = \alpha (V_C + V_M) - V_M \quad \text{where } \alpha = \chi^2_{MIN} / N_M \quad 14$$

$$\text{Then } E = V'_C - V_C = (V_C + V_M)(\alpha - 1) \quad 15$$

is the matrix to be added to V_C .

V_M is left unaltered. We can isolate the 'statistical' part of V_C by writing

$$V_C = G_\phi V_\phi G_\phi^T + \sum_i G_{xi} V_{xi} G_{xi}^T + G_f V_f G_f^T + G_s V_s G_s^T \quad 16$$

where G_ϕ for example can be seen from equation 4 to be

$$\begin{pmatrix} f_1 & x_1^T \\ f_2 & x_2^T \\ \cdot & \cdot \end{pmatrix}$$

Now isolating V_ϕ as the source of the discrepancy between χ_{MIN}^2 and N_M we seek a correction matrix F to V_ϕ such that

$$G_\phi(V_\phi + F)G_\phi^T = G_\phi V_\phi G_\phi^T + E \quad 17$$

We find after a little manipulation

$$F = \frac{1}{\alpha - 1} [G_\phi^T (V_C + V_M)^{-1} G_\phi]^{-1} \quad 18$$

This type of variance updating is not at present incorporated in SENSACK pending further testing of unfoldings in difficult environments - highly improbable values of χ_{MIN}^2 will demand some such treatment.

It is interesting to note that only minor changes in the input/output format of SENSACK are required to adapt it to a philosophy previously proposed by the author (3) which, although limited in application and more expensive to carry out, appears to have marked advantages over the direct method of Section 2. In any situation where the sensitivities of the calculated count rates to the data used in the flux calculation can be found write

$$h_{ik} = \frac{\partial C_i}{\partial Z_k}$$

where h_{ik} is the sensitivity of the i th measurement to the k th item of data. In the sensitivity matrix G replace

$$G_\phi = \begin{pmatrix} f_1 & x_1^T \\ f_2 & x_2^T \\ \cdot & \cdot \end{pmatrix} \quad \text{by} \quad G_Z = \begin{pmatrix} h_1^T \\ h_2^T \\ \cdot \end{pmatrix}$$

and in V_ϕ replace V_ϕ by V_Z which will be derived from uncertainty files. The unfolding proceeds precisely as before but the output vector \underline{P} now contains \underline{Z} instead of an adjusted value of flux for its first elements.

The unfolded spectrum is now given by a flux calculation using updated data $\hat{\underline{Z}}$. The advantages of this approach are:

- (i) The replacement of V_ϕ by V_Z where the latter may be more soundly based statistically. In this case the term F would be added to V_Z before solution and would represent approximately those biases on the calculated reaction-rates caused solely by errors in the method of calculation. ($V_Z' = V_Z + F$ would not of course, be regarded as an improvement in V_Z)

- (ii) Where a few detectors provided rather incomplete coverage of the spectral energy range all parameters which are statistically based would be included and Z would vary over the whole energy range. At present only the correlations between calculated group fluxes which in some cases may be rather arbitrary cause adjustments of flux spectrum in energy regions of low detector information.

5 CONCLUSIONS

The unfoldings described included all the information available to the author; the calculation, by design, was not intended to match the quality of the measurements - a situation which will occur commonly in practice. The algebraic solution has worked well in these cases but some experience is needed in environments more hostile to accurate calculations - questions of scaling and iteration may well arise.

ACKNOWLEDGEMENTS

Mr A Packwood supplied the measurements and the initial calculations. Mr V Sumner is thanked for the efficient programming of SENS AK II. The influence of Dr F Perey through his writing and in discussions is gratefully acknowledged.

REFERENCES

- (1) Perey, F. G. 'Least-Squares Dosimetry Unfolding: The Program STAYSL'. ORNL/TM-6062, 1977.
- (2) Zijp, W. L. 'Review of Activation Methods for the Determination of Neutron Flux Density Spectra' R.M.G. Note 75/19, 1975.
- (3) McCracken, A. K. 'Foil Activation Detectors - Some Remarks on Unfolding of Flux Spectra' IAEA-208, 1976.

Distribution

D Spaar
(4 copies)

AEA Technology, Engineering Services, Inc.
241 Curry Hollow Road
Pittsburgh
Pennsylvania 15236-4696
USA

A Avery

301/A32 Winfrith

S J Chucas

341/A32 Winfrith

IJ Curl
(10 Copies)

357/A32 Winfrith

L J Neal (Database)

316/A32 Winfrith

AEAT Archive
(2 Copies)

Bdg 149 Harwell



AEA Technology